Design and development of novel nanocomposite based electrochemical sensors for quantification of antimalarial drugs and early detection of malaria

Mr. Zondi Nate

Student number: 218088171

2021

A thesis submitted to the School of Health Sciences, University of KwaZulu-Natal, Westville, South Africa, in fulfilment for the degree of Doctor of Philosophy in Pharmaceutical Chemistry

PREFACE

The experimental work described in this thesis was conducted under the supervision of Prof. Rajshekhar Karpoormath at the University of KwaZulu-Natal, college of health sciences, department of pharmaceutical sciences, from September 2018 to May 2021.

This thesis has been prepared according to Format 4 (Thesis by publications) as outlined in the guidelines of College of Health Sciences, University of KwaZulu-Natal. The thesis is divided into 7 chapters, the first chapter is a general introduction, rationale for the study, objectives of the study and the outline of the thesis. Five chapters are provided as two published articles and three research manuscripts. The final chapter provides concluding remarks and future work.

This thesis has not been submitted for any degree or examination in any other university.

Zondi Nate….[redacted]..... Date: 17/09/ 2021

As the candidate's supervisor I agree to the submission of the thesis:

Prof. Rajshekhar Karpoormat[redacted] Date…….....25/Sept./2021

DECLARATION 1 – PLAGIARISM

I, **Zondi Nate,** declare that

i. The research reported in this thesis, except where otherwise indicated, is my original work.

ii. This thesis has not been submitted for any degree or examination at any other university.

iii. This thesis does not contain other person' data, pictures, graphs or other information, unless specifically acknowledged as being sourced from other persons.

iv. This thesis does not contain other persons' writing, unless specifically acknowledged as being sourced from other researchers. Where other written sources have been quoted, then:
   a. Their words have been re-written but the general information attributed to them has been referenced
   b. Where their exact words have been used, then their writing has been placed in italics and inside quotation marks, and referenced.

v. Where I have reproduced a publication of which I am an author, co-author or editor, I have indicated in detail which part of the publication was actually written by me.

vi. This thesis does not contain text, graphics or tables copied and pasted from the internet, unless specifically acknowledged, and the source being detailed in the thesis and in the References sections.

Signed:  …… Date: 17/09/2021

DECLARATION 2 – PUBLICATION

Publications

Zondi Nate, Atal A.S Gill, Ruchika Chauhan, Suraj Shinde, Shaukatali N. Inamdar, Rajshekhar Karpoormath. A simple in-situ flame synthesis of nanocomposite (MWCNTs-Fe_2O_3) for electrochemical sensing of proguanil in pharmaceutical formulation. *Diamond and Related Materials*. (111). 2020. 108178. doi.org/10.1016/j.diamond.2020.108178

Contribution: I conceptualized this work, did all the experimental studies and wrote the manuscript. The co-authors assisted with corrections, editing and proof reading of the manuscript.

Zondi Nate, Atal A.S Gill, Ruchika Chauhan, Rajshekhar Karpoormath. Polyaniline-cobalt oxide nanofibers for simultaneous electrochemical determination of antimalarial drugs: Primaquine and proguanil. *Microchemical Journal*. (160). 2021. 105709. doi.org/10.1016/j.microc.2020.105709

Contribution: I conceptualized this work, did all the experimental studies and wrote the manuscript. The co-authors assisted with corrections, editing and proof reading of the manuscript.

Zondi Nate, Atal A.S Gill, Ruchika Chauhan, Rajshekhar Karpoormath. Recent progress in electrochemical sensors for detection of malaria and antimalarial drugs. *Microchimica Acta*. (Submitted).

Contribution: I conceptualized the review article, I did all the literature review and wrote the article. The co-authors assisted with corrections, editing and proof reading.

Zondi Nate, Atal A.S Gill, Ruchika Chauhan, Rajshekhar Karpoormath. Synthesis of amino functionalized copper metal organic framework (Cu-MOFs) for electrochemical detection of malaria biomarker (β−Hematin). *Electroanalysis*. (Under review).

Contribution: I conceptualized this work, did all the experimental studies and wrote the manuscript. The co-authors assisted with corrections, editing and proof reading of the manuscript.

Zondi Nate, Phindile Mthombo, Atal A.S Gill, Ruchika Chauhan, Rajshekhar Karpoormath, Lebogang Mogole, Makwena Justice Moloto. Electrospun polyethylene oxide-silica-Co_3O_4 nanofibers for electrochemical detection of *Plasmodium falciparum* histidine-rich protein 2. *Analytical Biochemistry*. (Submitted).

Contributions: I conceptualized this work, did all the experimental studies and wrote the manuscript. Phindile Mthombo and Lebogang Mogole assisted with the electrospinning technique. The other co-authors assisted with corrections, editing and proof reading of the manuscript

Other publications

Atal A.S. Gill, Sima Singh, Nikhil Agrawal, **Zondi Nate**, Tirivashe E. Chiwunze, Neeta Bachheti Thapliyal, Ruchika Chauhan, Rajshekhar Karpoormath. A poly(acrylic acid)-modified copper-organic framework for electrochemical determination of vancomycin. *Microchimica Acta*. 2020 Jan 2; 187(1):79.

Ruchika Chauhan, Atal Gill, **Zondi Nate**, Rajshekhar Karpoormath. Highly selective electrochemical detection of ciprofloxacin using reduced graphene oxide/poly(phenol red) modified glassy carbon electrode. *Journal of Electroanalytical Chemistry*. 2020, 114254.

Atal A.S. Gill, Sima Singh, **Zondi Nate**, Ruchika Chauhan, Neeta B. Thapliyal, Rajshekhar karpoormath. A novel copper-based 3D porous nanocomposite for electrochemical detection and inactivation of pathogenic bacteria. Sensors and Actuators B: Chemical. 2020. 128449.

DEDICATION

This thesis is dedicated to my parents (Laura Nate and Maria Nate) and the entire family.

ACKNOWLEDGEMENTS

The completion of this thesis is a milestone on my long academic journey. I would like to convey my sincere gratitude and appreciation to everyone who supported me. A special thank you to my supervisor Prof. Rajshekhar Karpoormath for giving me an opportunity to conduct this research, thank you for all your support, knowledge transfer and motivation. I would also like to appreciate the co-supervising efforts of Dr Ruchika Chauhan and Dr Atal Anudeep Singh Gill. It has been a great journey filled with growth, joy and love. To Dr Atal Anudeep Singh Gill, thank you for welcoming me to the group with a warm heart, I appreciate all the work that we did together and the friendship that we have formed. Synthetic and medicinal chemistry group (SMCRG) you made my days at lab so exciting for that I thank you.

All the glory goes to god, he has been with me throughout this journey, I draw strength and courage from him. I would like to thank my family (Laura Nate, Maria Nate, Mandinyo Nate, France Nate, Phindile Nate and Hlengiwe Nate) for the support and encouragement in all my life endeavours. My gratitude also goes to Lebogang mogole for her support, willingness to listen and give advises during this period. To my friend and brother Tsakani Mathebula thank you for the encouragement and support.

I would like to thank the National Research Foundation (NRF) and the College of Health Sciences (CHS) at the University of KwaZulu Natal for the financial support. Thank you to all the sponsors that have supported me from undergraduate to date (Gauteng city region academy, National Student Financial Aid Scheme, Vaal University of Technology New Generation of Scholars and National Research Foundation). A special mention to the following people; Sphiwe Sibisi, Mosses Sibisi, Leyanora Sibisi, Phindile Mthombo, Makwena Justice Moloto, Fanyana Mthunzi, Thokozani Xaba, Theophilus Selaelo, Vincent Okobayi, Usha Govinden, Danial Makanyane, Boitumelo Makgabutlane, Sithabile Mokeana, Majeed Ganai, Thabsum Khan Pathan, Elton Chiwunze, Mavela Mahlalela, Francis Kayamba, Sima Singh, Andile Nzimande, Precious Mahlambi, Suraj Shinde, Narvadeshwar kushwaha, Bethany Nathaniel, Akwasi Boadu, Pankaj Girase, Vishal Bhardwaj, Babita Kushwaha, Nisar Sayyad, John Alake, Darko Adu, Blessing Ike and Srinivas Reddy Merugu.

TABLE OF CONTENTS

Table of Contents

LIST OF FIGURES

LIST OF TABLES

LIST OF ABBREVIATIONS

A: Effective surface area

ASSURED: Affordable, sensitive, specific, user friendly, robust, rapid, equipment-free deliverable to end-user

AMMRA: Amorphous MOF-mediated recrystallization approach

ART: Artemisinin

AuNps: Gold nanoparticles

BSA: bovine serum albumin

C: Double layer capacitance

CHS: College of Health Sciences

CPE: Carbon paste electrode

CI: Confidence interval

CNTs: Carbon nanotubes

Co_3O_4: Cobalt oxide

CP: Conducting polymers

CPNs: Conducting polymers nanostructures

Cu-MOFs: Copper metal organic frameworks

CuNW: Copper nanowires

CTAB: Cetrimonium bromide

CV: Cyclic voltammetry

CWE: Coated wire electrode

D:	Diffusion coefficient
DHFR:	Dihydrofolate reductase
DPV:	Differential pulse voltammetry
EDC:	N-ethyl-N0-(3-dimethylaminopropyl carbodiimide)
EDX:	Energy-dispersive X-ray spectroscopy
Ep:	Peak potential
ΔEp:	Peak to peak separation potential
$Fe(CN)_6^{3-/4-}$:	Ferri/ferro cyanide
FeGd-MOF:	Iron-gadolinium metal organic framework
FE-SEM:	Field emission scanning electron microscopy
FTIR:	Fourier transform infrared spectroscopy
E^o:	Formal redox potential
EIS:	Electrochemical impedance spectroscopy
EP-EPPG:	Electrochemical pretreatment –edge-plane pyrolytic graphite
GCE:	Glassy carbon electrode
GDH:	Glutamate dehydrogenases
G:	Graphene
GO:	Graphene oxide
GO-CTs-ECH:	Graphene oxide –chitosan-epichlorohydrin)
HCl:	Hydrochloric acid
HRP:	Horse-redish peroxidase

HRP2:	Histidine-rich proteins 2
*h*LDH:	Human Lactate Dehydrogenase
Ip:	Peak current
Ipa/Ipc:	Ratio of the anodic and cathodic peak current
ITO:	Indium tin oxide
K^o:	Standard rate constant of the surface reaction
LOD:	Limit of detection
LSV:	Linear sweep voltammetry
MIC:	Molecularly imprinted composite
MIM:	Molecularly imprinted membrane
MIP:	Molecularly imprinted polymer
MP-dsSPCE:	Single microfluidic paper, double-sided screen-printed carbon electrode
MPA:	Mercaptopropionic acid
MWCNTs:	Multiwall carbon nanotubes
MOFs:	Metal organic frameworks
MONps:	Metal oxide nanoparticles
N:	Number of electrons
NADH:	Nicotinamide adenine dinucleotide
NaOH:	Sodium hydroxide
Nf:	Nanofibers
NHS:	N-hydroxysuccinimide

Nps:	Nanoparticles
NRF-SA:	National Research Foundation- South Africa
PANI:	Polyaniline
PB:	Phosphate buffer
PBS:	Phosphate buffer saline
PEO:	Polyethylene oxide
PHA:	Polyhydroxyalkanoate
P. aldolase:	*Plasmodium* aldolase
P.falciprum:	*Plasmodium falciparum:*
*Pf*GDH:	*Plasmodium falciparum* Glutamate dehydrogenase
*Pf*HRP2:	*Plasmodium falciparum* Histidine-Rich Protein 2
*Pf*LDH:	*Plasmodium falciparum* Lactate Dehydrogenase
pI:	Isoelectric point
*p*LDH:	*Plasmodium* Lactate Dehydrogenase
P.malariae:	*Plasmodium malariae*
POC:	Point of care
P.ovale:	*Plasmodium ovale*
P.vivax:	*Plasmodium vivax*
PCR:	Polymerase chain reaction
QDs:	Quantum dots
R:	Resistance of the electrolyte solution

Rct:	Charge resistance transfer
RTILs:	Room temperature ionic liquids
RGO:	Reduced graphene oxide
RBCs:	Red blood cells
SEM:	Scanning electron microscopy
SWCNTs:	Single-walled carbon nanotubes
SWV:	Square wave voltammetry
TEM:	Transmission electron microscopy
UKZN:	University of KwaZulu-Natal
Uv-vis:	Ultraviolet visible spectroscopy
W:	Warburg impedance
WHO:	World Health Organization
WHO-GSMS:	World health organization global surveillance and monitoring system
WS_2:	Tungsten disulfide
XRD:	X-ray diffraction patterns

ABSTRACT

This thesis reports the synthesis of different nanocomposites such as multiwall carbon nanotubes incorporated with iron oxide nanoparticles, polyaniline nanofibers incorporated with cobalt oxide nanoparticles, amino functionalized copper metal organic frameworks and polyethylene oxide-silica-cobalt oxide nanofibers. Different synthesis methods that includes in-situ flame synthesis, interfacial polymerization, precipitation oxidation, amorphous MOF-mediated recrystallization approach and electrospinning method were used. The characterization of these nanocomposites was carried out using Transmission Electron Microscopy (TEM), Scanning Electron Microscopy (SEM), Energy-Dispersive X-Ray Spectroscopy (EDX), X-Ray Diffraction Spectroscopy (XRD), Fourier Infrared Spectroscopy (FTIR), Ultraviolet-Visible Spectroscopy and Raman Spectroscopy. The synthesized nanocomposites were further used to develop electroanalytical methods for qualitative and quantitative analysis of malaria biomarker (β−Hematin, *Plasmodium falciparum* histidine-rich protein 2) and antimalarial drugs (primaquine, proguanil). All the electrochemical studies were done using a conventional three electrode electrochemical workstation. A glassy carbon electrode, platinum wire and Ag/AgCl/KCl were used as working, counter, and the reference electrode, respectively.

The first electroanalytical method was based on the application of multiwall carbon nanotubes-iron oxide nanocomposite for electrochemical detection of proguanil in pharmaceutical formulation. Differential Pulse Voltammetry (DPV) and Cyclic Voltammetry (CV) were used to study the electrochemical oxidation of proguanil. The selectivity of the sensor was investigated in the presence of organic and inorganic interfering agents. Furthermore, spiked human urine samples and pharmaceutical formulations were used to evaluate the utility of the sensor. Under optimum conditions, the sensor showed a detection limit of 1.96×10^{-8} M. The second part involved the fabrication of an electrochemical sensor with polyaniline-cobalt oxide nanofibers for simultaneous detection of antimalarial drugs (primaquine and proguanil) using Differential Pulse Voltammetry and Cyclic Voltammetry. Additionally, the practical applicability of the sensor was studied in human urine with different interfering agents. Under optimum conditions, this developed method gave a detection limit of 2.07 nM and 1.42 nM for primaquine and proguanil, respectively.

The third electroanalytical method involved the fabrication of amino functionalized copper metal organic frameworks for electrochemical detection of malaria biomarker (ß-Hematin).

Electrochemical studies were carried out using Electrochemical Impedance Spectroscopy (EIS), Cyclic Voltammetry and Diffractive Pulse Voltammetry. Additionally, the feasibility of the modified electrode was investigated in some organic and inorganic interfering species. Under optimum conditions, a detection limit of 4.08 μM was obtained. Lately the fourth part was based on the fabrication of electrospun polyethylene oxide silica cobalt oxide nanofibers for electrochemical detection of malaria biomarker (*Plasmodium falciparum* Histidine-Rich Protein 2). Electrochemical Impendence Spectroscopy was used to study the electrochemical behavior of the biosensor towards *Plasmodium falciparum* Histidine-Rich Protein 2. A detection limit of 12 ag/mL and 18.3 ag/mL was obtained for *Plasmodium falciparum* Histidine-Rich Protein 2 in phosphate buffer saline and sheep blood serum respectively.

All the developed electroanalytical methods showed good reproducibility, selectivity, and sensitivity towards the selected analytes.

CHAPTER ONE

1.1 INTRODUCTION

1.1.1 Overview of malaria cases

Malaria is a parasitic disease, which has become public health problem. This disease is mostly found in tropical and subtropical areas as shown in Figure 1:1. In the year 2000, the World Health Organization (WHO) reported approximately 262 million cases of malaria in which 839 000 resulted in death [1–3]. Fifteen years later in 2015, nearly 214 million cases of malaria were reported in which 469 000 resulted in death [2–4]. From the year 2000 to 2015 there is a decrease in the number of cases of about 48 million. Although the number of cases decreased, malaria is still a dominant disease in tropical and sub-tropical countries. In 2018 an estimated 228 million cases of malaria were reported worldwide, 405 000 cases resulted in death. Most of the malaria cases are reported in Africa with 213 million cases of which 380 700 resulted in death, nineteen countries with the world's biggest malaria problem are in sub-Sahara Africa and India, and account for 85% of the global burden[4,5]. Figure 1:2 represent the estimated number of cases and death caused by malaria.

Malaria can be prevented and treated using different strategies as recommended by WHO. However the lack of rapid diagnostic tools with good selectivity and sensitivity is still a challenge. Another problem is high prevalence of counterfeit antimalarial drugs. These drugs are dominant in most African countries since the cost of medicine is high and some countries lack good quality control and verification processes.

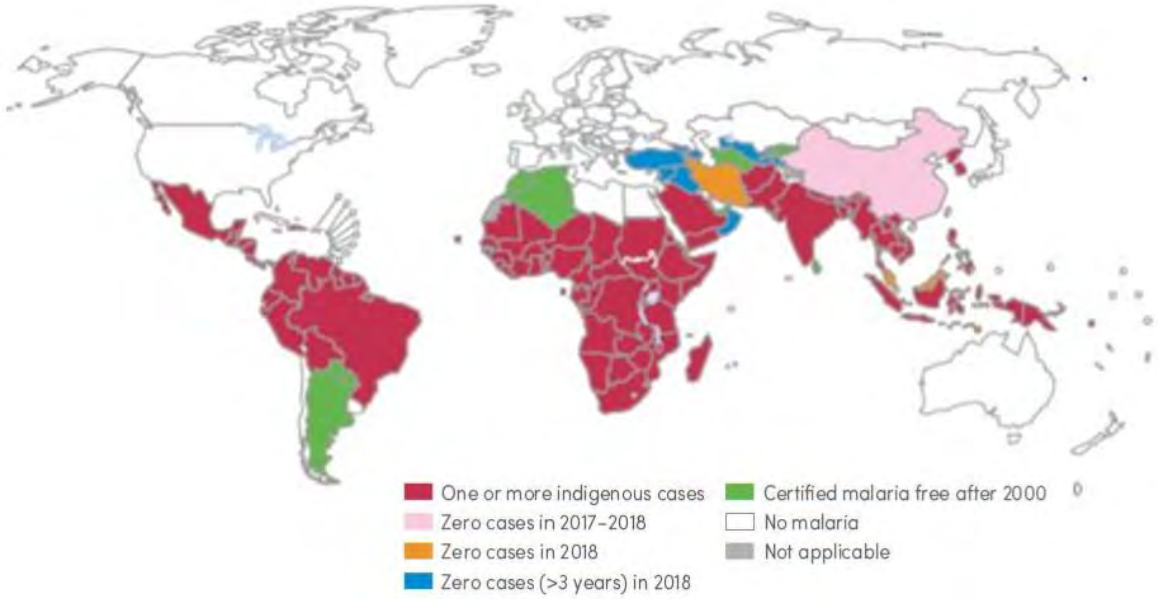

Figure 1:1 World malaria map [5]

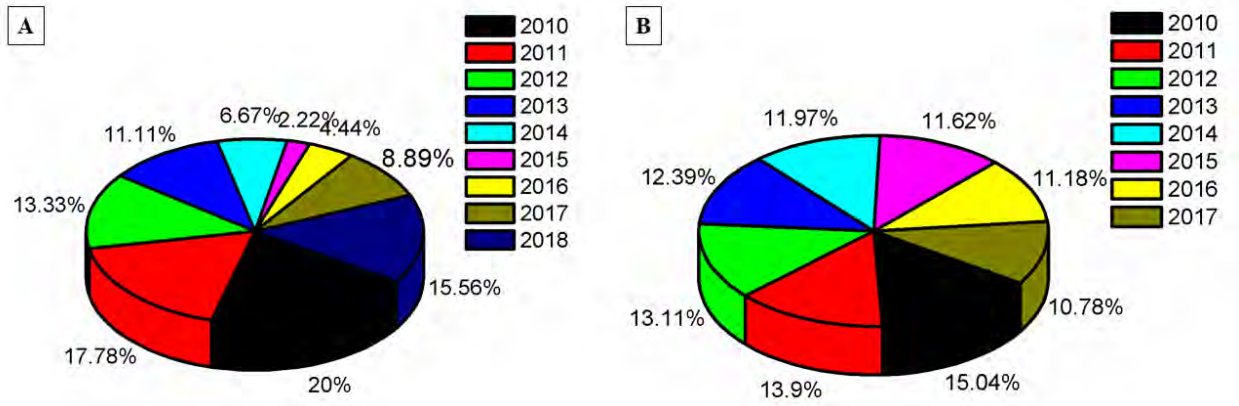

Figure 1:2 (A) 2010-2018 World Health Organization (WHO) global estimated malaria cases (B) global estimated malaria death [3,5]

1.1.2 Role of nanomaterials in electrochemical sensors

Several analytical methods have been reported for the detection and quantification of malaria and antimalarial drugs. For diagnosis of malaria WHO recommends the use of parasite-based diagnostic testing such as microscopy or rapid diagnostic tests. While quality control for antimalarial drugs is done using different methods such as reflectance and refractive index,

colorimetry, spectroscopic techniques, chromatography and mass spectroscopy. However most of these methods are time consuming and require tedious sample preparation methods. They also require a high level of technical expertise and complex laboratory equipment. Therefore, there is a need to develop a rapid, selective, and sensitive method for qualitative and quantitative analysis of malaria biomarkers and antimalarial drugs.

In the past decade, significant progress has been made in the development of nanomaterials-based electrochemical sensors for the detection of various diseases and pharmaceutical drugs. The interesting properties of nanomaterials that make them suitable to be used in electrochemical sensors include a high surface-to-volume ratio, high adsorption, and reactive capacity. Nanomaterials also provide platforms for immobilization of biomolecules, catalysis of electrochemical reactions, enhancement of electron transfer rate, and labeling of biomolecules [6–8]. These properties result in improved selectivity, sensitivity, reproducibility, and stability of electrochemical biosensors and chemical sensors.

Nanocomposites material have been studied in recent years because of their unique and fascinating properties. These unique properties arise from the synergistic effect of the individual components that make up the composite. The choice of individual materials is based on their unique physical, chemical and biological properties. In this thesis nanocomposites of different metal oxides nanoparticles (MONps), metal organic frameworks (MOFs), carbon nanotubes (CNTs), polymer nanofibers and conducting polymers (CP) were used to develop electrochemical sensors for quantification of selected antimalarial drugs and malaria biomarkers.

Metal organic frameworks were selected because of these properties: high porosity, high crystallinity, large surface to volume ratio, tunable pore size and are compatible for immobilization of biomolecules. Carbon nanotubes were selected because of their fast electron transfer rate, high surface area, and wide electrical potential window. Conducting polymers are known to have special properties such as flexibility, scalability, resistance to corrosion and they can be moulded for a particular need. These polymers have a wide range of electrical conductivity which is similar to that of metals. The unique properties of metal oxide nanoparticles includes higher surface area, mechanical strength, and lower melting point make them suitable to be used in electrochemical sensors. Metal oxide nanoparticles enhance the electron transfer between redox centers in proteins and electrode surface because they have good conductivity. The catalytic property of metal and

metal oxide nanoparticles is also useful in electrochemical sensors because they act as catalysts to increase electrochemical reactions.

1.1.3 Electrochemical techniques used in chemical and biosensors

In electrochemical methods, the detection occurs between the interface of the analytes and the modified working electrode. Cyclic Voltammetry (CV), Differential Pulse Voltammetry (DPV), Linear Sweep Voltammetry (LSV), Square Wave Voltammetry (SWV), and Electrochemical Impedance Spectroscopy (EIS) are among the commonly used electrochemical techniques during the development of an electrochemical sensor. These techniques have several advantages such as wide linear concentration range, consumption of small reagents, real-time monitoring of analytes and they are easy to use [9]. They also have high sensitivity with good precision and accuracy. Cyclic voltammetry is based on changing the applied potential of the working electrode in both the forward and reverse direction while measuring the corresponding current [9–11]. While differential pulse voltammetry uses a series of potential pulses with a fixed pulse amplitude that is superimposed on a slowly increasing potential staircase [9–11]. The current is measured just before and after the application of each pulse. In square wave voltammetry, the square is superimposed on a potential staircase [9–11]. The square wave pulse consists of a forward and reverse pulse. The difference between the forward and reverse currents is measured. In linear sweep voltammetry, the current is measured while the potential between the working and reference electrode is swept linearly in time [9]. In electrochemical impedance spectroscopy, the change in impendence on the surface of the working electrode is measured [11].

1.1.4 Properties of nanomaterials

The term nanotechnology was coined in 1974 by Professor Nario Taniguchi. This was inspired by the 1959 talk titled ‘‘there’s plenty of room at the bottom’’ given by the Noble laureate Richard Feynman at the American Physical Society Meeting [12]. Over the years, advances have been made in understanding the physical, chemical, and biological properties of nanomaterials. Nanotechnology is usually referred as a field that deals with the manipulation of matter at a scale that is within 1-100 nm [13–15]. Depending on the overall shape, nanomaterials can be classified as 0D, 1D, 2D, and 3D. There are different types of nanomaterials that have been reported to date. These nanomaterials can be grouped as organic, inorganic, and hybrid nanomaterials as shown in Figure 1:3. The unique properties of nanomaterials that make them different from their bulk

counterparts include high surface to volume ratio, size, shape, tunable pore size, crystallinity, solubility, and size distribution [16–20]. Also, nanomaterials have unique surface chemistry such as zeta potential, tension, charge, and reactive sites [16,18,20]. Thus these properties make them suitable for different applications such as diagnostic tools, wastewater treatment, energy, biological fields, and catalysis. Although nanomaterials are used in different fields, their properties are mostly influenced by the composition, degree of purity, size, shape, and agglomeration. These factors can be controlled by varying various parameters during the synthesis process.

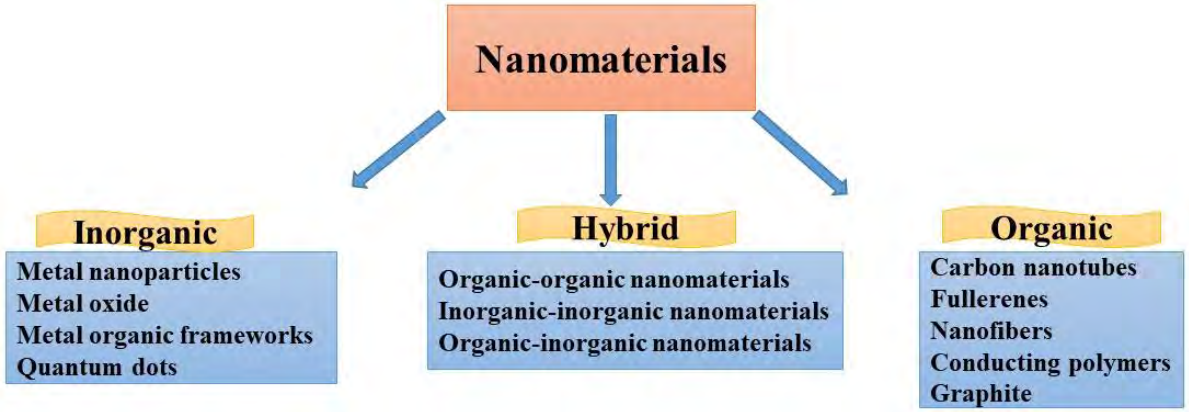

Figure 1:3 Classification of nanomaterials

1.1.5 Synthesis and properties of selected nanomaterials

Several methods can be used to synthesize nanomaterials. These methods can be categorized as the bottom-up and top-down approach. The top-down approach involves the breaking down of bulk material to required sizes and shapes [13,21]. This is normally done by lithographic processes such as grinding, sputtering, and laser ablation [13,21]. In the bottom-up approach, the required structures are formed molecule by molecule or atom by atom through supermolecular or covalent interactions [13,21,22]. Common methods for the synthesis of nanofibers, carbon nanotubes, metal organic frameworks, and conducting polymers are described below.

1.1.5.1 Nanofibers

Nanofibers are defined as solid fibers with diameters that range from a few hundred to nanometers [23]. These fibers are also long with lengths of up to several meters. The application of nanofibers in filters, food, energy, packaging, medicine, diagnostics, and textile is increasing due to their

special properties [24,25]. These properties include high specific surface area, controllable morphology, high porosity, and large aspect ratio [23]. They also have good encapsulation efficiency, biocompatibility, and high chemical and thermal stability. Several methods such as phase separation, electrospinning, mechanical drawing, met blowing, temple-assisted and self-assembly techniques are being used to fabricate nanofibers [26–31]. In this study, the electrospinning method was used because it is cost-effective, versatile, and produces continuous nanofibers. The morphology and diameter of the nanofibers can be controlled by changing spinning parameters such as applied voltage, tip to collector distance, flow rate, and needle diameter [32–34]. Also, the polymer viscosity, molecular weight, concentration, conductivity, and incorporation of nanomaterials play a crucial role. The electrospinning technique is made up of four components (high voltage power supply, syringe pump, needle, and conductive collector) as shown in Figure 1:4. The principle of electrospinning is based on applying a high voltage to a polymer solution inside a syringe pump which results in the ejection of continuous nanofibers from the tip of the needle to the conductive collector [35].

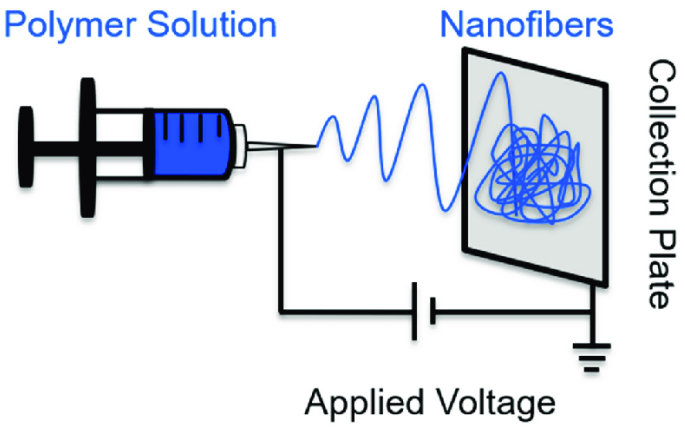

Figure 1:4 Typical electrospinning technique [36]

1.1.5.2 Metal-organic frameworks

Metal-organic frameworks (MOFs) are crystalline porous materials formed by coordination between metal ions and organic linkers. These materials have unique properties that make them be used in various applications such as sensing, catalysis, energy storage, wastewater treatment, biomedical imaging, and drug delivery [37–39]. The attractive features of MOFs include; high porosity, high crystallinity, large surface to volume ratio, and tunable pore sizes [20,40–42]. These

features of MOFs can be improved by compositional manipulation, pre-synthesis modulation, morphology control, and post-synthetic treatment. Metal-organic frameworks can be synthesized using several methods such as microwave, hydrothermal, electrochemical, and mechanochemical methods. During the synthesis process, the most important parameters include temperature, pH, concentration, solvent, metal ion, capping agent, and organic linkers [42–45]. In this study hydrothermal method was selected to synthesize MOFs. The hydrothermal method involves the use of an autoclave as shown in Figure 1:5. The autoclave is made up of a stainless steel chamber lined with Teflon material. This method has several advantages such as the ability to dissolve the reactant by adjusting the temperature and applied pressure. The size, shape, and size distribution can be preciously controlled by varying these reaction parameters. This approach is also a reliable method to produce crystalline nanomaterials.

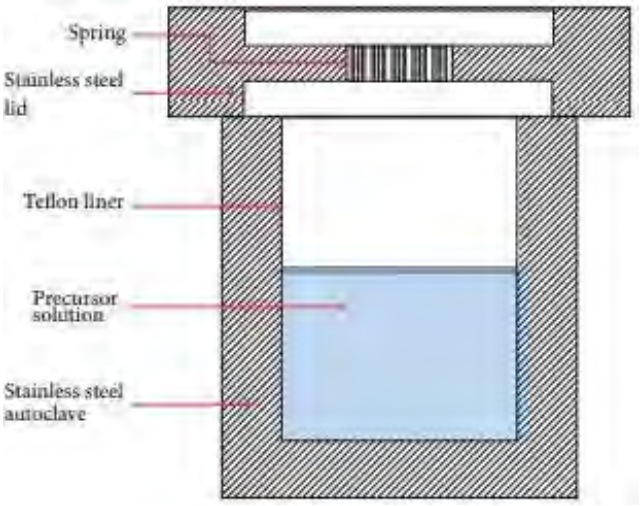

Figure 1:5 Diagram of the autoclave used in hydrothermal synthesis [46].

1.1.5.3 Carbon nanotubes

Carbon nanotubes (CNTs) are defined as cylindrical large molecules that are made up of the hexagonal arrangement of hybridized carbon atoms. Depending on the number of graphene sheets, carbon nanotubes can be categorized as single-walled, double-walled, and multi-walled. Single-walled and double-walled carbon nanotubes are made up of a single and a double layer of graphene sheet with a diameter of 1-3 nm respectively [47,48]. While multiwall carbon nanotubes are made up of multiple layers of graphene sheets with diameters ranging from 2-50 nm [47,48]. It is important to note that single-wall carbon nanotubes (SWCNTs) are more stable than multiwall

carbon nanotubes (MWCNTs). This is due to the undefined diameters and inbuilt structural defects in MWCNTs [47,49]. CNTs are used in different areas such as transistors, capacitors, biosensors, nanomedicine, and wastewater treatment [50–53]. This is because of their special properties such as small size, high aspect ratio, high specific surface area, lightweight, good thermal conductivity, and high electrocatalytic properties [47,53,54]. The method used to synthesis carbon nanotubes plays a significant role in their length and purity. Different methods such as flame synthesis, plasma-assisted growth, chemical vapor deposition, laser ablation, arc-discharge, and vapor phase growth have been used to produce SWCNTs and MWCNTs [47,53–55]. In this study a novel simply flame synthesis method was used as shown in Figure 1:6. The setup is made up of a source of fuel, an oxidizer, and a cooling system.

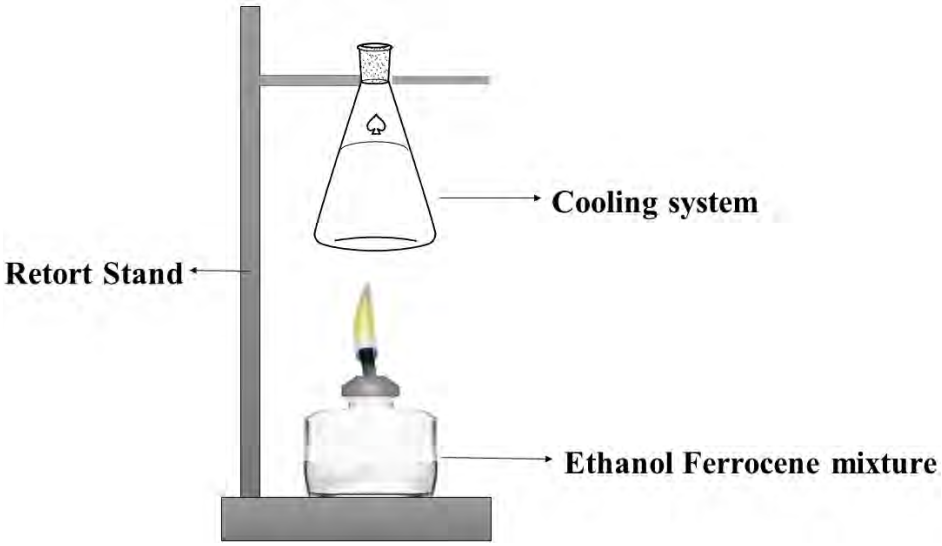

Figure 1:6 Novel simple flame synthesis of multiwall carbon nanotubes

1.1.5.4 Conducting polymers nanostructures

A polymer is defined as a large molecule built up by repetitive bonding together of many smaller units called monomers [56]. The unique properties of different polymers make them suitable to be used in different areas such as electrical and biological fields. In the electrical field, polymers are mostly used as insulators for electrical conducting wires [57]. However, there is a class of polymers that are called conducting polymers, these polymers have a wide range of electrical conductivity which is similar to that of metals. Conducting polymers (CP) are defined as a class of unique polymers that can conduct electricity via the extended conjugation present within their structure [57–59]. Some of the frequently used conducting polymers include polypyrrole,

poly(3,4-ethylenedioxythiophene), polyaniline, poly(para-phenylenevinylene), and polyacetylene. These polymers are characterized by the double bond along their backbone. Electron flow is possible within the structure of conducting polymers because the electrons in the conjugated systems are loosely bounded [60,61]. It of importance to note that charge carriers within a polymer structure play an important role because a conducting polymer is not conductive without the charge carriers. Since most organic conjugated polymers do not have elemental charge carriers, external charge carriers are introduced to the polymer structure by a doping process [57].

Conducting polymers are generally obtained by either chemical or electrochemical oxidative polymerization. Chemical polymerization is mostly used when a large quantity of the polymer is required. Electrochemical polymerization involves the direct deposition of the polymer on the electrode that facilitates the analysis. During this process, three stages occur. The first step is the formation of soluble oligomers in the diffusion layer by the oxidation of monomers at the anode, this is followed by the deposition of oligomers through nucleation and growth process. Lastly, the chain propagation by solid-state polymerization occurs [62].

Several studies have reported the synthesis of conducting polymers nanostructures (CPNs) using the hard-template, soft-template, and template-free methods [63–66]. CPNs have enhanced electrical, electrochemical, and mechanical properties compared to their bulk counterparts. They also have a larger surface area and short path lengths for ion transport [65–67]. Due to these properties conducting polymers nanostructures are applied in different fields such as diagnostic, energy-related systems, and wastewater treatment plants [65–67]. The hard-template method is usually used to synthesis well-controlled and orientated conducting polymers nanostructures [66]. This method involves the use of template membrane and can be applied in both chemical and electrochemical polymerization. The diameter, length, and thickness of the CPNs are dependent on the polymerization time, pores, or channels of the membrane. One of the drawbacks of this method is the post-treatment to remove the template. This may sometimes destroy the formed CPNs. Also, this method is not preferred for large-scale production since the quantity of the CPNs is determined by the template membrane.

The synthesis of CPNs by the soft-template method depends on molecular self-assembly. Several soft-template methods can be used to synthesize CNPs. These methods include reversed-microemulsion, microemulsion polymerization, block copolymer mediated, and layer by layer

self-assembly [65–69]. Template-free methods such as interfacial, electrospinning, radiolysis produces CNPs without the use of a template. This method has some advantages over template-based methods since there is no need for post-treatment. Also, it is rapid, reproducible, and scalable. In this study, interfacial polymerization was used.

1.2 RATIONAL FOR STUDY

1.2.1 Problem statement

Malaria is still a major disease in sub-Saharan Africa and South-East Asia. This is despite different interventions by the World Health Organization (WHO) such as the use of insecticide-treated mosquito net, antimalarial drugs, indoor residual spraying and rapid diagnostic tools. In 2018, the mortality rate due to malaria was estimated to be 405 000, with children under the age of 5 accounting for 67% of all malaria deaths. Malaria can be prevented and treated using different strategies as recommended by WHO. However the lack of rapid diagnostic tools with good selectivity and sensitivity is still a challenge. Another problem is high prevalence of counterfeit antimalarial drugs. These drugs are dominant in most African countries since the cost of medicine is high and some countries lack good quality control and verification processes.

1.2.2 Novelty statement

A new, economic method to synthesis multiwall carbon nanotubes (MWCNTs) impregnated with iron oxide nanoparticles was developed. The synthesized nanocomposite was used to modify the surface of glassy carbon electrode (GCE) for improved electrochemical detection of antimalarial drug; proguanil. Also in this thesis; for the first-time a method for simultaneous electrochemical detection of two antimalarial drugs; primaquine and proguanil was reported. A low-cost malaria biomarker (β−Hematin) was used to develop a highly sensitive electrochemical sensor for early diagnosis of malaria. β−Hematin is structurally and chemically similar to Hemozoin. An electrochemical biosensor for early diagnosis of *Plasmodium falciparum* Histidine-Rich Protein 2 (*Pf*HRP2) was developed. This sensor showed high sensitivity and selectivity with good detection limit. In this biosensor a new nanocomposite of polyethylene oxide (PEO), Silica and cobalt oxide (Co_3O_4) nanofibers was used.

1.3 AIM AND RESEARCH OBJECTIVES

In summary, the study focuses on the following aim and objectives:

1.3.1 Aim

To synthesis novel nanocomposites and their application in the development of ultra-sensitive electrochemical sensors for detection and quantification of selected malaria biomarkers and antimalarial drugs.

1.3.2 Objectives

Part 1: A simple In-situ flame synthesis of nanocomposite (MWCNTs-Fe_2O_3) for electrochemical sensing of proguanil in pharmaceutical formulation.

- To synthesize and characterize carbon nanotubes impregnated with iron oxide nanoparticles using novel flame synthesis method.
- To examine the electrochemical behavior of the modified glassy carbon electrode (MWCNTs-iron oxide/GCE) in potassium ferricyanide and ferrocyanide redox couple using Electrochemical Impedance Spectroscopy (EIS) and Cyclic Voltammetry (CV).
- To examine the electrochemical behavior of proguanil at MWCNTs-iron oxide/GCE.
- Method development and electrochemical detection of proguanil using MWCNTs-iron oxide/GCE. Various parameters will be investigated.
- To examine the practical applicability of the developed method in pharmaceutical formulations.

Part 2: Synthesis of polyaniline-cobalt oxide nanofibers for simultaneous electrochemical determination of antimalarial drugs: primaquine and proguanil.

- To synthesize and characterize cobalt oxide nanoparticles using precipitation oxidation method.
- To synthesize and characterize polyaniline (PANI) nanofibers using interfacial polymerization.
- To synthesize and characterize polyaniline-cobalt oxide nanofibers using interfacial polymerization.

- To examine the electrochemical behavior of the modified glassy carbon electrode PANI-Co_3O_4/GCE in potassium ferricyanide and ferrocyanide redox couple using Electrochemical Impedance Spectroscopy (EIS).
- To examine the electrochemical behavior of proguanil and primaquine at PANI-Co_3O_4/GCE.
- Method development and simultaneous electrochemical detection of primaquine and proguanil using PANI-Co_3O_4/GCE. Various parameters will be investigated.
- To examine the practical applicability of the developed method in human urine samples.

Part 3: Synthesis of amino functionalized copper metal organic framework (Cu-MOFs) for electrochemical detection of malaria biomarker (β−Hematin)

- To synthesize and characterize amino functionalized copper metal organic frameworks (Cu-MOFs) nanorods using an Amorphous MOF-Mediated Recrystallization Approach (AMMRA). The effect of pH on the size and shape of Cu-ABDC MOFs will be investigated.
- To synthesize and characterize a malaria biomarker (β−Hematin).
- To examine the electrochemical behavior of the modified glassy carbon electrode (Cu-MOFs/GCE) in potassium ferricyanide and ferrocyanide redox couple using Electrochemical Impedance Spectroscopy (EIS).
- Method development and electrochemical detection of β−Hematin using Cu-MOFs/GCE. Various parameters will be investigated.

Part 4: Electrospun polyethylene oxide-silica-Co_3O_4 nanofibers for electrochemical detection of *Plasmodium falciparum histidine*-rich protein 2.

- To fabricate 2D and 3D polyethylene oxide-silica-cobalt oxide nanofibers from colloidal solution using electrospinning technique.
- To evaluate the effect of calcination temperature on the morphology of polyethylene oxide-silica-cobalt oxide nanofibers.
- To examine the electrochemical behavior of the modified glassy carbon electrode (PEO-silica-Co_3O_4/GCE) in potassium ferricyanide and ferrocyanide redox couple using Electrochemical Impedance Spectroscopy (EIS).

- To functionalize the surface of the modified electrode using mercaptopropionic acid (MPA), N-hydroxysuccinimide and N-ethyl-N0-(3-dimethylaminopropyl carbodiimide).
- Immobilization of specific antibody for *Plasmodium falciparum* Histidine-Rich Protein II on the functionalized electrode. The concentration of the antibody will be optimized.
- Method development and electrochemical detection of *Plasmodium falciparum* Histidine-Rich Protein 2 using functionalized PEO-silica-Co_3O_4/GCE. Various parameters will be investigated.
- To examine the practical applicability of the developed method in sheep blood serum.

1.4 THESIS OUTLINE

- **Chapter one**: General introduction, rationale, objectives of the study and the outline of the thesis.
- **Chapter two:** Consist of the literature review about role of malaria biomarkers, recent developments in nanomaterial-based electrochemical and colorimetric biosensors. Also, electrochemical sensors for detection of different antimalarial drugs are discussed.
- **Chapter three:** Reports a simple in-situ flame synthesis of multiwall carbon nanotubes-iron oxide nanocomposite for electrochemical sensing of proguanil in pharmaceutical formulation.
- **Chapter four:** Is based on the synthesis of polyaniline-cobalt oxide nanofibers for simultaneous electrochemical determination of antimalarial drugs: primaquine and proguanil.
- **Chapter five:** focuses on the synthesis of amino functionalized copper metal organic framework for electrochemical detection of malaria biomarker (β−Hematin).
- **Chapter six:** Elaborates on electrospun polyethylene oxide-silica-Co_3O_4 nanofibers for electrochemical detection of *Plasmodium falciparum* histidine-rich protein 2.
- **Chapter seven:** Provides the summary, conclusions and future perspectives of present work.

1.5 REFERENCES

[1] M. Rai, A.P. Ingle, P. Paralikar, I. Gupta, S. Medici, C.A. Santos, Recent advances in use of silver nanoparticles as antimalarial agents, Int. J. Pharm. 526 (2017) 254–270. https://doi.org/https://doi.org/10.1016/j.ijpharm.2017.04.042.

[2] WHO, World malaria report in 2015, Geneva, 2015.

[3] World Health Organization, WHO | The World malaria report 2018, 2018. www.who.int/malaria%0Ahttps://apps.who.int/iris/bitstream/handle/10665/275867/9789241565653-eng.pdf?ua=1%0Ahttps://www.who.int/malaria/publications/world-malaria-report-2018/en/; consulté le 22/03/2019%0Ahttps://www.who.int/malaria/media/world-malaria-rep.

[4] WHO, World malaria report 2017, Geneva, 2017.

[5] WHO, World malaria report 2019, Geneva, 2019. https://www.who.int/publications/i/item/9789241565721.

[6] X. Luo, A. Morrin, A.J. Killard, M.R. Smyth, Application of Nanoparticles in Electrochemical Sensors and Biosensors, Electroanalysis. 18 (2006) 319–326. https://doi.org/https://doi.org/10.1002/elan.200503415.

[7] U. Hanefeld, L. Gardossi, E. Magner, Understanding enzyme immobilisation., Chem. Soc. Rev. 38 (2009) 453–468. https://doi.org/10.1039/b711564b.

[8] W. Putzbach, N.J. Ronkainen, Immobilization techniques in the fabrication of nanomaterial-based electrochemical biosensors: a review., Sensors (Basel). 13 (2013) 4811–4840. https://doi.org/10.3390/s130404811.

[9] N. Thapliyal, T.E. Chiwunze, R. Karpoormath, R.N. Goyal, H. Patel, S. Cherukupalli, Research progress in electroanalytical techniques for determination of antimalarial drugs in pharmaceutical and biological samples, RSC Adv. 6 (2016) 57580–57602. https://doi.org/10.1039/C6RA05025E.

[10] L. Qian, S. Durairaj, S. Prins, A. Chen, Nanomaterial-based electrochemical sensors and biosensors for the detection of pharmaceutical compounds, Biosens. Bioelectron. 175

(2021) 112836. https://doi.org/https://doi.org/10.1016/j.bios.2020.112836.

[11] A.A.S. Gill, S. Singh, N. Thapliyal, R. Karpoormath, Nanomaterial-based optical and electrochemical techniques for detection of methicillin-resistant Staphylococcus aureus: a review, Microchim. Acta. 186 (2019) 114. https://doi.org/10.1007/s00604-018-3186-7.

[12] R.P. Feynman, There's plenty of room at the bottom, Resonance. 16 (2011) 890. https://doi.org/10.1007/s12045-011-0109-x.

[13] P. Iqbal, J.A. Preece, P.M. Mendes, Nanotechnology: The "Top-Down" and "Bottom-Up" Approaches, Supramol. Chem. (2012). https://doi.org/https://doi.org/10.1002/9780470661345.smc195.

[14] A.X. Wang, X. Kong, Review of Recent Progress of Plasmonic Materials and Nano-Structures for Surface-Enhanced Raman Scattering., Mater. (Basel, Switzerland). 8 (2015) 3024–3052. https://doi.org/10.3390/ma8063024.

[15] J.N. Tiwari, R.N. Tiwari, K.S. Kim, Zero-dimensional, one-dimensional, two-dimensional and three-dimensional nanostructured materials for advanced electrochemical energy devices, Prog. Mater. Sci. 57 (2012) 724–803. https://doi.org/https://doi.org/10.1016/j.pmatsci.2011.08.003.

[16] A.B. Asha, R. Narain, Chapter 15 - Nanomaterials properties, in: R.B.T.-P.S. and N. Narain (Ed.), Elsevier, 2020: pp. 343–359. https://doi.org/https://doi.org/10.1016/B978-0-12-816806-6.00015-7.

[17] I. Khan, K. Saeed, I. Khan, Nanoparticles: Properties, applications and toxicities, Arab. J. Chem. 12 (2019) 908–931. https://doi.org/https://doi.org/10.1016/j.arabjc.2017.05.011.

[18] M.A. Gatoo, S. Naseem, M.Y. Arfat, A. Mahmood Dar, K. Qasim, S. Zubair, Physicochemical Properties of Nanomaterials: Implication in Associated Toxic Manifestations, Biomed Res. Int. 2014 (2014) 498420. https://doi.org/10.1155/2014/498420.

[19] T.A. Saleh, Nanomaterials: Classification, properties, and environmental toxicities, Environ. Technol. Innov. 20 (2020) 101067.

https://doi.org/https://doi.org/10.1016/j.eti.2020.101067.

[20] Y. He, Z. Wang, H. Wang, Z. Wang, G. Zeng, P. Xu, D. Huang, M. Chen, B. Song, H. Qin, Y. Zhao, Metal-organic framework-derived nanomaterials in environment related fields: Fundamentals, properties and applications, Coord. Chem. Rev. 429 (2021) 213618. https://doi.org/https://doi.org/10.1016/j.ccr.2020.213618.

[21] S. Kumar, P. Bhushan, S. Bhattacharya, Fabrication of Nanostructures with Bottom-up Approach and Their Utility in Diagnostics, Therapeutics, and Others BT - Environmental, Chemical and Medical Sensors, in: S. Bhattacharya, A.K. Agarwal, N. Chanda, A. Pandey, A.K. Sen (Eds.), Springer Singapore, Singapore, 2018: pp. 167–198. https://doi.org/10.1007/978-981-10-7751-7_8.

[22] L. Gritsch, D. Meng, A.R. Boccaccini, 20 - Nanostructured biocomposites for tissue engineering scaffolds, in: L.B.T.-B.C. (Second E. Ambrosio (Ed.), Woodhead Publ. Ser. Biomater., Woodhead Publishing, 2017: pp. 501–542. https://doi.org/https://doi.org/10.1016/B978-0-08-100752-5.00021-4.

[23] B.-T. Zhang, H. Liu, Y. Liu, Y. Teng, Application trends of nanofibers in analytical chemistry, TrAC Trends Anal. Chem. 131 (2020) 115992. https://doi.org/https://doi.org/10.1016/j.trac.2020.115992.

[24] A. Luraghi, F. Peri, L. Moroni, Electrospinning for drug delivery applications: A review, J. Control. Release. (2021). https://doi.org/https://doi.org/10.1016/j.jconrel.2021.03.033.

[25] X. Xie, Y. Chen, X. Wang, X. Xu, Y. Shen, A. ur R. Khan, A. Aldalbahi, A.E. Fetz, G.L. Bowlin, M. El-Newehy, X. Mo, Electrospinning nanofiber scaffolds for soft and hard tissue regeneration, J. Mater. Sci. Technol. 59 (2020) 243–261. https://doi.org/https://doi.org/10.1016/j.jmst.2020.04.037.

[26] N. Wongkaew, M. Simsek, C. Griesche, A.J. Baeumner, Functional Nanomaterials and Nanostructures Enhancing Electrochemical Biosensors and Lab-on-a-Chip Performances: Recent Progress, Applications, and Future Perspective, Chem. Rev. 119 (2019) 120–194. https://doi.org/10.1021/acs.chemrev.8b00172.

[27] J. Horne, L. McLoughlin, B. Bridgers, E.K. Wujcik, Recent developments in nanofiber-based sensors for disease detection, immunosensing, and monitoring, Sensors and Actuators Reports. 2 (2020) 100005. https://doi.org/https://doi.org/10.1016/j.snr.2020.100005.

[28] Y. Wen, M.D.R. Kok, J.P.V. Tafoya, A.B.J. Sobrido, E. Bell, J.T. Gostick, S. Herou, P. Schlee, M.-M. Titirici, D.J.L. Brett, P.R. Shearing, R. Jervis, Electrospinning as a route to advanced carbon fibre materials for selected low-temperature electrochemical devices: A review, J. Energy Chem. 59 (2021) 492–529. https://doi.org/https://doi.org/10.1016/j.jechem.2020.11.014.

[29] C.C. Lee, C. Grenier, E.W. Meijer, A.P.H.J. Schenning, Preparation and characterization of helical self-assembled nanofibers, Chem. Soc. Rev. 38 (2009) 671–683. https://doi.org/10.1039/B800407M.

[30] X. Xing, Y. Wang, B. Li, Nanofiber drawing and nanodevice assembly in poly(trimethylene terephthalate), Opt. Express. 16 (2008) 10815–10822. https://doi.org/10.1364/OE.16.010815.

[31] I. Alghoraibi, S. Alomari, Different Methods for Nanofiber Design and Fabrication BT - Handbook of Nanofibers, in: A. Barhoum, M. Bechelany, A. Makhlouf (Eds.), Springer International Publishing, Cham, 2018: pp. 1–46. https://doi.org/10.1007/978-3-319-42789-8_11-2.

[32] A. Haider, S. Haider, I.-K. Kang, A comprehensive review summarizing the effect of electrospinning parameters and potential applications of nanofibers in biomedical and biotechnology, Arab. J. Chem. 11 (2018) 1165–1188. https://doi.org/https://doi.org/10.1016/j.arabjc.2015.11.015.

[33] V. Beachley, X. Wen, Effect of electrospinning parameters on the nanofiber diameter and length, Mater. Sci. Eng. C. Mater. Biol. Appl. 29 (2009) 663–668. https://doi.org/10.1016/j.msec.2008.10.037.

[34] X. Shi, W. Zhou, D. Ma, Q. Ma, D. Bridges, Y. Ma, A. Hu, Electrospinning of Nanofibers and Their Applications for Energy Devices, J. Nanomater. 2015 (2015) 140716. https://doi.org/10.1155/2015/140716.

[35] J. Xue, T. Wu, Y. Dai, Y. Xia, Electrospinning and Electrospun Nanofibers: Methods, Materials, and Applications, Chem. Rev. 119 (2019) 5298–5415. https://doi.org/10.1021/acs.chemrev.8b00593.

[36] I.S. Kurtz, J.D. Schiffman, Current and Emerging Approaches to Engineer Antibacterial and Antifouling Electrospun Nanofibers., Mater. (Basel, Switzerland). 11 (2018). https://doi.org/10.3390/ma11071059.

[37] R.J. Kuppler, D.J. Timmons, Q.-R. Fang, J.-R. Li, T.A. Makal, M.D. Young, D. Yuan, D. Zhao, W. Zhuang, H.-C. Zhou, Potential applications of metal-organic frameworks, Coord. Chem. Rev. 253 (2009) 3042–3066. https://doi.org/https://doi.org/10.1016/j.ccr.2009.05.019.

[38] M.H. Yap, K.L. Fow, G.Z. Chen, Synthesis and applications of MOF-derived porous nanostructures, Green Energy Environ. 2 (2017) 218–245. https://doi.org/https://doi.org/10.1016/j.gee.2017.05.003.

[39] R. Ricco, C. Pfeiffer, K. Sumida, C.J. Sumby, P. Falcaro, S. Furukawa, N.R. Champness, C.J. Doonan, Emerging applications of metal–organic frameworks, CrystEngComm. 18 (2016) 6532–6542. https://doi.org/10.1039/C6CE01030J.

[40] A.E. Baumann, D.A. Burns, B. Liu, V.S. Thoi, Metal-organic framework functionalization and design strategies for advanced electrochemical energy storage devices, Commun. Chem. 2 (2019) 86. https://doi.org/10.1038/s42004-019-0184-6.

[41] T. Saeed, A. Naeem, I. Ud Din, M.A. Alotaibi, A.I. Alharthi, I. Wali Khan, N. Huma Khan, T. Malik, Structure, nomenclature and viable synthesis of micro/nanoscale metal organic frameworks and their remarkable applications in adsorption of organic pollutants, Microchem. J. 159 (2020) 105579. https://doi.org/https://doi.org/10.1016/j.microc.2020.105579.

[42] R. Seetharaj, P. V Vandana, P. Arya, S. Mathew, Dependence of solvents, pH, molar ratio and temperature in tuning metal organic framework architecture, Arab. J. Chem. 12 (2019) 295–315. https://doi.org/https://doi.org/10.1016/j.arabjc.2016.01.003.

[43] K.A.S. Usman, J.W. Maina, S. Seyedin, M.T. Conato, L.M. Payawan, L.F. Dumée, J.M. Razal, Downsizing metal–organic frameworks by bottom-up and top-down methods, NPG Asia Mater. 12 (2020) 58. https://doi.org/10.1038/s41427-020-00240-5.

[44] V.R. Remya, M. Kurian, Synthesis and catalytic applications of metal–organic frameworks: a review on recent literature, Int. Nano Lett. 9 (2019) 17–29. https://doi.org/10.1007/s40089-018-0255-1.

[45] L. Zou, C.-C. Hou, Z. Liu, H. Pang, Q. Xu, Superlong Single-Crystal Metal–Organic Framework Nanotubes, J. Am. Chem. Soc. 140 (2018) 15393–15401. https://doi.org/10.1021/jacs.8b09092.

[46] N. Asim, S. Ahmadi, M.A. Alghoul, F.Y. Hammadi, K. Saeedfar, K. Sopian, Research and Development Aspects on Chemical Preparation Techniques of Photoanodes for Dye Sensitized Solar Cells, Int. J. Photoenergy. 2014 (2014) 518156. https://doi.org/10.1155/2014/518156.

[47] S. Rathinavel, K. Priyadharshini, D. Panda, A review on carbon nanotube: An overview of synthesis, properties, functionalization, characterization, and the application, Mater. Sci. Eng. B. (2021) 115095. https://doi.org/https://doi.org/10.1016/j.mseb.2021.115095.

[48] H. He, L.A. Pham-Huy, P. Dramou, D. Xiao, P. Zuo, C. Pham-Huy, Carbon Nanotubes: Applications in Pharmacy and Medicine, Biomed Res. Int. 2013 (2013) 578290. https://doi.org/10.1155/2013/578290.

[49] M.S. Dresselhaus, G. Dresselhaus, J.C. Charlier, E. Hernández, Electronic, thermal and mechanical properties of carbon nanotubes., Philos. Trans. Ser. A, Math. Phys. Eng. Sci. 362 (2004) 2065–2098. https://doi.org/10.1098/rsta.2004.1430.

[50] M. Trojanowicz, Analytical applications of carbon nanotubes: a review, TrAC Trends Anal. Chem. 25 (2006) 480–489. https://doi.org/https://doi.org/10.1016/j.trac.2005.11.008.

[51] Z.A. ALOthman, S.M. Wabaidur, Application of carbon nanotubes in extraction and chromatographic analysis: A review, Arab. J. Chem. 12 (2019) 633–651. https://doi.org/https://doi.org/10.1016/j.arabjc.2018.05.012.

[52] E. Bekyarova, Y. Ni, E.B. Malarkey, V. Montana, J.L. McWilliams, R.C. Haddon, V. Parpura, Applications of Carbon Nanotubes in Biotechnology and Biomedicine, J. Biomed. Nanotechnol. 1 (2005) 3–17. https://doi.org/10.1166/jbn.2005.004.

[53] K.A. Shah, B.A. Tali, Synthesis of carbon nanotubes by catalytic chemical vapour deposition: A review on carbon sources, catalysts and substrates, Mater. Sci. Semicond. Process. 41 (2016) 67–82. https://doi.org/https://doi.org/10.1016/j.mssp.2015.08.013.

[54] N. Anzar, R. Hasan, M. Tyagi, N. Yadav, J. Narang, Carbon nanotube - A review on Synthesis, Properties and plethora of applications in the field of biomedical science, Sensors Int. 1 (2020) 100003. https://doi.org/https://doi.org/10.1016/j.sintl.2020.100003.

[55] N. Arora, N.N. Sharma, Arc discharge synthesis of carbon nanotubes: Comprehensive review, Diam. Relat. Mater. 50 (2014) 135–150. https://doi.org/https://doi.org/10.1016/j.diamond.2014.10.001.

[56] C.I. Awuzie, Conducting Polymers, Mater. Today Proc. 4 (2017) 5721–5726. https://doi.org/https://doi.org/10.1016/j.matpr.2017.06.036.

[57] N. Yi, M.R. Abidian, 10 - Conducting polymers and their biomedical applications, in: L. Poole-Warren, P. Martens, R.B.T.-B.P. for M.A. Green (Eds.), Woodhead Publ. Ser. Biomater., Woodhead Publishing, 2016: pp. 243–276. https://doi.org/https://doi.org/10.1016/B978-1-78242-105-4.00010-9.

[58] J. V Yakhmi, V. Saxena, D.K. Aswal, 2 - Conducting Polymer Sensors, Actuators and Field-Effect Transistors, in: S. Banerjee, A.K.B.T.-F.M. Tyagi (Eds.), Elsevier, London, 2012: pp. 61–110. https://doi.org/https://doi.org/10.1016/B978-0-12-385142-0.00002-7.

[59] R. Ravichandran, S. Sundarrajan, J.R. Venugopal, S. Mukherjee, S. Ramakrishna, Applications of conducting polymers and their issues in biomedical engineering, J. R. Soc. Interface. 7 Suppl 5 (2010) S559–S579. https://doi.org/10.1098/rsif.2010.0120.focus.

[60] E.J. Jelmy, S. Ramakrishnan, S. Devanathan, M. Rangarajan, N.K. Kothurkar, Optimization of the conductivity and yield of chemically synthesized polyaniline using a design of experiments, J. Appl. Polym. Sci. 130 (2013) 1047–1057.

https://doi.org/10.1002/app.39268.

[61] M. Gerard, A. Chaubey, B.D. Malhotra, Application of conducting polymers to biosensors, Biosens. Bioelectron. 17 (2002) 345–359. https://doi.org/https://doi.org/10.1016/S0956-5663(01)00312-8.

[62] J. Heinze, B.A. Frontana-Uribe, S. Ludwigs, Electrochemistry of Conducting Polymers—Persistent Models and New Concepts, Chem. Rev. 110 (2010) 4724–4771. https://doi.org/10.1021/cr900226k.

[63] L. Pan, H. Qiu, C. Dou, Y. Li, L. Pu, J. Xu, Y. Shi, Conducting Polymer Nanostructures: Template Synthesis and Applications in Energy Storage, Int. J. Mol. Sci. . 11 (2010). https://doi.org/10.3390/ijms11072636.

[64] S. Il Cho, S.B. Lee, Fast Electrochemistry of Conductive Polymer Nanotubes: Synthesis, Mechanism, and Application, Acc. Chem. Res. 41 (2008) 699–707. https://doi.org/10.1021/ar7002094.

[65] S. Ghosh, T. Maiyalagan, R.N. Basu, Nanostructured conducting polymers for energy applications: towards a sustainable platform, Nanoscale. 8 (2016) 6921–6947. https://doi.org/10.1039/C5NR08803H.

[66] L. Xia, Z. Wei, M. Wan, Conducting polymer nanostructures and their application in biosensors, J. Colloid Interface Sci. 341 (2010) 1–11. https://doi.org/https://doi.org/10.1016/j.jcis.2009.09.029.

[67] Y. Xue, S. Chen, J. Yu, B.R. Bunes, Z. Xue, J. Xu, B. Lu, L. Zang, Nanostructured conducting polymers and their composites: synthesis methodologies, morphologies and applications, J. Mater. Chem. C. 8 (2020) 10136–10159. https://doi.org/10.1039/D0TC02152K.

[68] K.-J. Ahn, Y. Lee, H. Choi, M.-S. Kim, K. Im, S. Noh, H. Yoon, Surfactant-Templated Synthesis of Polypyrrole Nanocages as Redox Mediators for Efficient Energy Storage, Sci. Rep. 5 (2015) 14097. https://doi.org/10.1038/srep14097.

[69] P. Anilkumar, M. Jayakannan, Divergent Nanostructures from Identical Ingredients:

Unique Amphiphilic Micelle Template for Polyaniline Nanofibers, Tubes, Rods, and Spheres, Macromolecules. 41 (2008) 7706–7715. https://doi.org/10.1021/ma801090f.

CHAPTER TWO

Recent progress in electrochemical sensors for detection of malaria and antimalarial drugs

Graphical Abstract

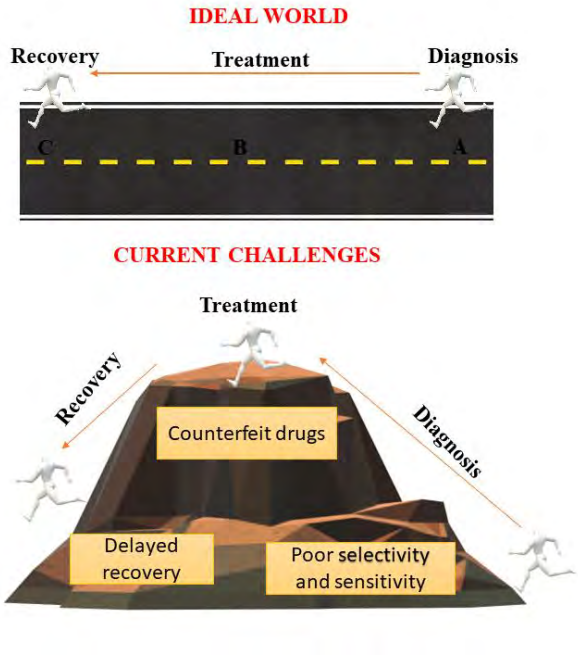

2.1 ABSTRACT

Malaria is still a major disease in sub-Saharan Africa and South-East Asia. This is despite different interventions by the World Health Organization (WHO) such as the use of insecticide-treated mosquito net, antimalarial drugs, indoor residual spraying, and rapid diagnostic tools. In 2018, the mortality rate due to malaria was estimated to be 405 000, with children under the age of 5 accounting for 67% of all malaria deaths. Malaria can be prevented and treated using different strategies as recommended by WHO. However, the lack of rapid diagnostic tools with good selectivity and sensitivity is still a challenge. Another problem is the high prevalence of counterfeit antimalarial drugs. These drugs are dominant in most African countries since the cost of medicine is high and some countries lack good quality control and verification processes. Therefore there is a need to develop rapid, low-cost, and portable analytical methods for the quantification of malaria and antimalarial drugs. This review focuses on the role of malaria biomarkers in diagnosis; *Plasmodium falciparum* Lactate Dehydrogenase (*Pf*LDH), *Plasmodium* aldolase, *Plasmodium falciparum* Histidine-Rich Protein 2 (*Pf*HRP2) and *Plasmodium falciparum* Glutamate dehydrogenase (*Pf*GDH) and Hemozoin. Recent developments in nanomaterial-based electrochemical and colorimetric biosensors for malaria diagnosis are discussed. Also, electrochemical sensors for qualitative and quantitative analysis of different antimalarial compounds (Quinoline-related compounds, artemisinin derivatives, antifolates, and antibiotics), which have been approved by the World Health Organization are covered. Finally, the closing remarks and future perspectives of electrochemical sensors and biosensors conclude the review.

Keywords: Malaria, antimalarial drugs, biosensor, nanomaterials, biomarkers.

2.2 MALARIA

2.2.1 The life cycle of malaria

Malaria is caused by a protozoan parasite that belongs to the *Plasmodium genus* [1,2]. Among all the *Plasmodium genus* species, only four are responsible for the presence of malaria in humans; these species include *Plasmodium malariae (P.malariae)*, *Plasmodium ovale (P.ovale)*, *Plasmodium vivax (P.vivax)*, and *Plasmodium falciparum (P.falciprum)* [3]. The most prevalent malaria species globally is *Plasmodium falciparum* which accounts for 99.9% of malaria cases in Africa, 50% in South-East Asia, 71% in the Eastern Mediterranean Region, and 65% in the Western Pacific Region [4]. Malaria cases that are due to *Plasmodium vivax* are mostly dominant in South-East Asia and the Americas [4]. The other malaria species can cause severe illness but the mortality rate is low [5]. The four species are transmitted to the human body through a single bite from a female mosquito. Since malaria affects human beings, it is important to understand the life cycle of malaria; Figure 2:1 shows the life cycle of the malaria. The events that occurs include the exoerythrocytic, erythrocytic, and sporogonic cycle.

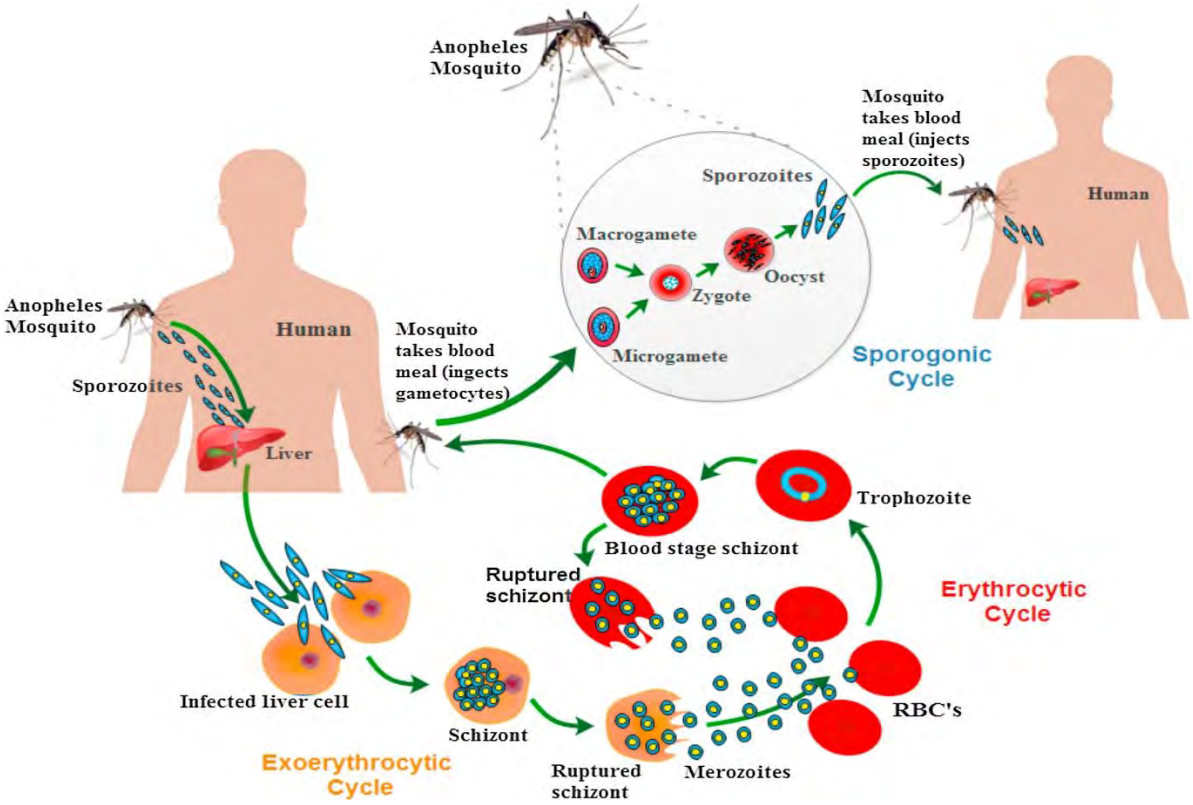

Figure 2:1 Malaria life cycle [3].

The human infection starts in the exoerythrocytic cycle where the mosquito injects the sporozoites during the blood meal. The injected sporozoites travel to the liver cell where they overcome the liver cells, during this stage thousands of merozoites are generated by asexual replication. The replication stage is referred to as exoerythrocytic schizogony. Schizogony is defined as a replication process where merozoites are formed, to achieve this, sporozoites undergo many divisions followed by budding or segmentation. The merozoites are released into the bloodstream after they rapture liver cells [3,6,7].

The second stage is the erythrocytic cycle, at this stage, the merozoites defeat the erythrocytes and form trophozoites through asexual replication, here another round of schizogony is initiated. This process takes place repeatedly and in the end causes malaria. As the infection continues, the peripheral blood is concentrated with female and male gametocytes that are formed by young merozoites. Therefore when the mosquito feeds it injects the gametocytes into itself [6]. In the sporogonic cycle, as shown in Figure 2:1, the gametocytes develop into macrogametes and microgametes. The gametes are fertilized within the mosquito midgut to form ookinetes. These ookinetes penetrate the gut wall and develop oocytes. The oocytes result in the formation of sporozoites [3,6].

2.2.2 Role of Biomarkers in malaria diagnosis

Since malaria affects most people in developing and tropical countries, early detection of this disease is important. Early diagnosis will have several advantages such as early treatment of malaria. As a result, the spread of the disease will be prevented; thus the mortality rate will be reduced. Currently, conventional methods such as nucleic acid-based analytical techniques, immunobased rapid diagnostic test kits and microscopic analysis are being used for the diagnosis of malaria [6]. These conventional methods have some drawbacks such as multi-step analysis, lack of onsite applicability and they are time-consuming. Due to these drawbacks, there is a need for a simple, rapid, cheap, sensitive, and onsite-applicable point of care device for the detection of malaria. To achieve this several malaria biomarkers are used to develop diagnostic sensors.

To develop a selective and sensiitve biosensor for the early detection of malaria, it is important to understand the various malaria-related biomarkers. A biomarker is defined as a naturally occurring molecule, gene, or characteristics in which a particular pathological or physiological process or disease can be identified [8,9]. The advantage of using biomarkers in diagnostic tools is their

sensitivity towards a specific disease pathogen [10]. Biomarkers that are mostly used in malaria-related detection devices are shown in Figure 2:2. The most used biomarker for developing rapid and reliable detection systems is *Plasmodium falciparum* Lactate Dehydrogenase (PfLDH) and *Plasmodium falciparum* Histidine-Rich Protein 2 (*Pf*HRP2).

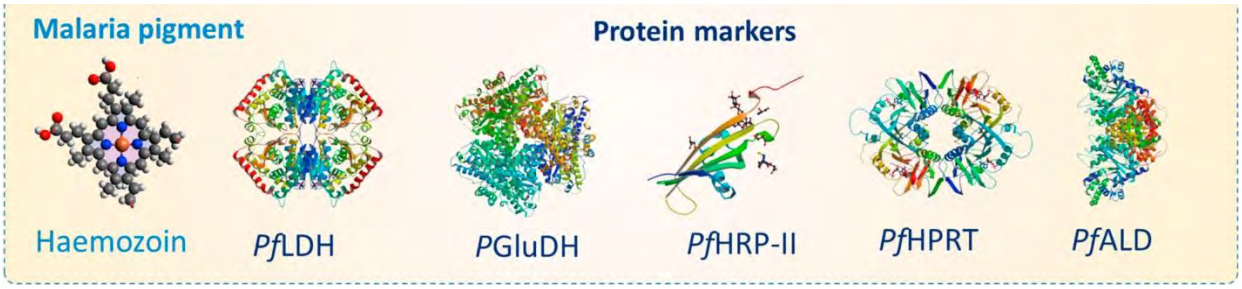

Figure 2:2 Commonly used markers for the diagnosis of malaria [6]

2.2.2.1 Histidine-Rich Protein 2

Histidine-rich proteins 2 (HRP2) is a frequently used biomarker in the development of malaria diagnostic tools. HRP2 is a unique protein that is produced by *P. falciparum* [11]. In total composition of HRP2, 37% of its amino acid sequence is histidine, and a repeat of histidine plus alanine covers 85% of its sequence [8,12]. HRP2 is released from infected erythrocytes as a water-soluble protein into the red blood cells cytosol through a mosquito bite [13]. HRP2 is found in food vacuole [14], digestive vacuole [15], and membrane surface of the infected red blood cells [16]. It is also found in cerebrospinal fluid, serum plasma, and urine of infected patients [8]. HRP2 is mostly used as a biomarker in the development of antimalarial drugs and rapid diagnostic tests because it shows high sensitivity towards *P. falciparum* compared to other biomarkers such as *P. falciparum lactate dehydrogenase* and *P. Glutamate Dehydrogenase*.

2.2.2.2 Lactate Dehydrogenase

Plasmodium Lactate Dehydrogenase (*p*LDH) is a common biomarker that is found in all *Plasmodium* species, the main function of *p*LDH is to convert pyruvate to lactate by using a cofactor reduced nicotinamide adenine dinucleotide (NADH) [10,17]. High levels of *p*LDH are produced during the asexual intraerythrocytic cycle; this is because the *Plasmodium* parasite depends on anaerobic metabolism to generate energy [18,19]. *p*LDH is useful as a malaria biomarker since it has structural features that are different from the human Lactate Dehydrogenase (*h*LDH). The main difference between *p*LDH and *h*LDH is the presence of Leu 163 on *p*LDH

instead of Ser 163 that is found in *h*LDH [17,20]. *p*LDH is used in malaria case management because the circulation of this enzyme in the host environment clears within 24 hours after successful treatment. Thus false-positive diagnosis after the elimination of the infection is reduced.

2.2.2.3 Hemozoin

Blood-feeding parasite species such as *Plasmodium spp.* produces an insoluble brown microcrystalline product during the digestion of blood called hemozoin [8,10]. Hemozoin is a crystal structure that is made up of hemes that are linked by carboxylate side group oxygen and the central ferric ion as shown in Figure 2:3. Hemozoin is used as malaria pigment during the development of antimalarial drugs and diagnostic tools; this is because hemozoin is important for the parasite survival in the host. The red blood cells of the host are infected during the intra-erythrocytic cycle at this stage amino acids, and toxic-free heme that were released from the digestion of hemoglobin are polymerized to hemozoin [21,22]. 80% of hemoglobin in infected red blood cells is digested by the parasite [23].

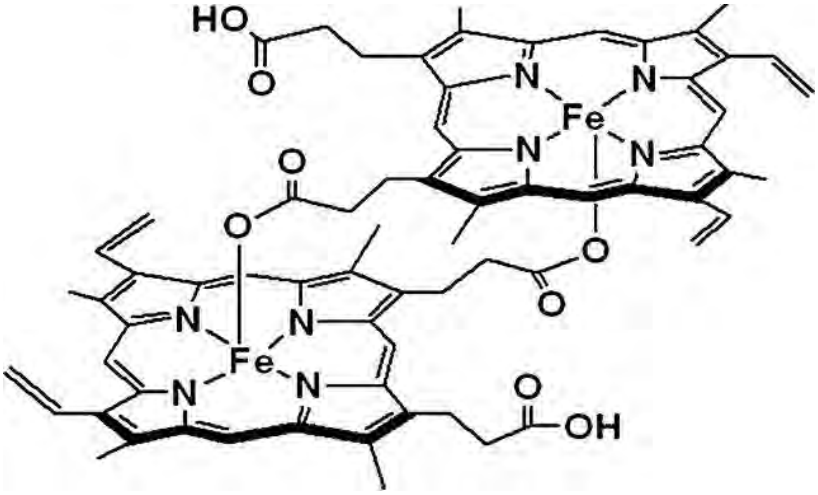

Figure 2:3 Structure of hemozoin

2.2.2.4 Aldolase

Aldolase is a homotetrameric protein with each subunit of approximately 40kDa [8,24]. This protein is used as a malaria biomarker since it is found in both *P. falciparum* and *P. vivax*, also the sequence of *Plasmodium* aldolase (*P.* aldolase) is different from the human aldolase. The amino acid sequence of aldolase in *P. vivax* and *P. falciparum* are both 369 in length, and they are conserved [25,26]. Aldolase is present in its active and soluble form at the cytoplasm of the

parasite. In its insoluble form, it is associated with the membrane fraction. During the glycolytic pathway aldolase act as a catalyst to cleavage fructose-1,6-bisphosphate to form glyceraldehyde-3-phosphate and dihydroxyacetone phosphate. HRP2 is mostly used as a biomarker for the detection of *P. falciparum* instead of *P.* aldolase; this is due to the poor sensitivity of aldolase in commercially available rapid diagnostic tools [27,28]. The poor sensitivity is mostly attributed to low concentrations of the antigen in infected erythrocytes. Another disadvantage of using aldolase is that the *P. falciparum* aldolase shares a 61-68% sequence with eukaryotic aldolase [29].

2.2.2.5 *Plasmodium falciparum* Glutamate dehydrogenase

The branch point between the carbon and nitrogen metabolism is occupied by ubiquitous enzymes called Glutamate dehydrogenases (GDH). *Plasmodium falciparum* Glutamate dehydrogenase is a common malaria biomarker that is present throughout the intra-erythrocytic cycle of the parasite. This enzyme is absent in the host red blood cells and it has different kinetics, structure, location, and sequence compared to GDH of the host; thus it is attracting interest from researchers to be used as a malaria biomarker [30–32]. *Plasmodium falciparum* expresses three different genes encoding potential GDH proteins, namely GDHa (PF 14-0164), GDHb (PF 14-0286), and GDHc (PF08-0132) [33]. GDHa and GDHb are found in chromosome 14, and GDHc is in chromosome 8 [10,33]. The function of glutamate dehydrogenase is to facilitate the conversion of L-glutamate to α-ketoglutarate and ammonia by using NADP (H) or NAD (H) as cofactors [33].

2.3 CHALLENGES FOR MALARIA DIAGNOSTIC TOOLS

2.3.1 Conventional methods

Diagnosis of malaria using traditional methods such as light microscopy, empirical/syndromic, and clinical diagnosis are still widely used in malaria-endemic countries. Empirical/syndromic clinical diagnosis is based on patient medical history, signs, and symptoms such as headache, fever, dizziness, nausea, diarrhea, chills, weakness, vomiting, and myalgia among others. The World Health Organization (WHO) is against the use of this approach in the area where adequate laboratory diagnostic tools are available. This is mainly due to some limitations that are associated with this approach such as incorrect diagnosis that results in an increase in resistance to available antimalarial drugs, non-specificity, and significant clinical overlap with other pyretic diseases.

Therefore microscopic method remains a gold standard in most developing countries since it is cost-effective, readily available in most laboratories, can accurately identify the infecting species

and mixed infections, the microscopy has multiple applications, and can be used to determine the density of the parasite in the blood [34–36]. However the following drawbacks are associated with this approach; it is time-consuming, unreliable at low parasite densities, and experts are required to operate the microscopy and interpret the results effectively [5,37,38]. The ability to detect mixed malaria infections at low-level parasitemia using Polymerase chain reaction (PCR)-based diagnostic method (RFLP-dHPLC) was compared with the microscopic method by Steenkeste et al [39]. The PCR-based method was found to be more sensitive, also the presence of *Plasmodium falciparum* and *Plasmodium vivax* were found to be approximately 59% and 15% respectively while 28% and 5% was obtained for the microscopy method. The PCR-based method detected 11.2% and 1.3 % of *Plasmodium ovale* and *Plasmodium malariae* respectively. No cases were found when the microscopic method was used. In another study, Hopkins et al [40] used 272 blood samples to compare the sensitivity of a new loop-mediated Isothermal Amplification kit with microscopy and single-well nested PCR. Compared with 3-well nested PCR, the sensitivity of both the new loop-mediated Isothermal Amplification and single-well nested PCR was found to be 90% and 51% for the microscopy method.

To improve the sensitivity of the microscopy method, Davis et al [41] investigated the effect of passive gravitational sedimentation of peripheral blood on the sensitivity of microscopic detection of malaria. 205 samples were analyzed using three methods; conventional thin smear preparation, centrifuged samples, and gravitational sedimented samples. A sensitivity of 25.39%, 30.24%, and 30.24% was observed for traditional, centrifuged, and sedimented blood respectively. Thus the two methods were found to be more sensitive compared to conventional thin smear preparation. Berzosa et al [42] compared microscopy, rapid diagnostic test, and PCR for detection of the malaria parasite in representative samples. 1724 blood samples were analyzed, 19.4% and 13.3% false-negative results were obtained for microscopy and rapid diagnostic test respectively.

Since light microscopy is still considered the gold standard for malaria diagnosis, efforts are being made to overcome some of the drawbacks such as the need for lab-based microscopy. A handheld light microscopy for diagnosis of malaria due to *Plasmodium falciparum* was reported by Coulibaly et al [43]. 223 samples were used, the sensitivity and specificity was found to be 80.2% (95% Confidence interval [Cl]: 73.1-85.9%) and 100% (95% Cl: 92.6-100%) respectively. Several

innovative strategies to improve the selectivity and sensitivity of light microscopy for malaria diagnosis have been reported as shown in Table 2:1.

Table 2:1 Some of the innovative light microscopy for detection of malaria

Technique	**Sensitivity**	**Benefits**	**Ref**
Handheld light microscopy with mobile phone attachment	80.2% (95% Confidence interval [Cl]: 73.1-85.9%)	Portable quality laboratory testing of malaria in remote settings	[43]
Light Emission Diode fluorescence microscopy	Sensitivity and specificity of 71.2% and 96.3% respectively	highly specific in comparison to Light microscopy	[44]
Polarized microscope designed using a cell phone.	Device Resolution is sufficient for observing birefringence from hemozoin crystals	Low cost and it is adaptable to multiple mobile devices	[45]
Mobile phone mounted light microscopy	Device resolution is sufficient to accurately capture images of malaria-infected red blood cells from both thick and thin blood smears	Cheap, fast and field applicable microscopic evaluation of malaria patients.	[46]

2.3.2 Electrochemical biosensors

A biosensor is a device that is made up of a biological receptor, transducer, signal amplification, and output unit [36]. Biosensors can be classified as electrochemical, optical, magnetic, thermometric, and piezoelectric. Ideal biosensors consist of the following 12 key features; high sensitivity, high selectivity, reproducibility, rapid response time, multiplexing, multimode, high stability, easy to use, disposable, easy manufactured, cost-effectiveness and autonomous [47,48]. In recent years several studies have reported the use of biosensors in malaria diagnosis. Most of the reported biosensors use nanocomposites to improve their sensitivity, selectivity, and reproducibility. Nanocomposites are solid materials that consist of multiple phase domains, and at least one of these domains has nanoscale structures. Nanocomposites material have been studied in recent years because of their unique and fascinating properties. These unique properties arise from the synergistic effect of the individual components that make up the composite. The

application of nanocomposites in the fabrication of sensors has some advantages such as high surface to volume ratio, reactive capacity, biocompatibility, and high adsorption [49,50]. Nanocomposites are responsible for catalysis of electrochemical reactions, easy immobilization of biomolecules, labelling of biomolecules, and enhancement of electron transfer rate [51–54]. Nanocomposites that are mostly used to modify the surface of the electrode are made up of conducting polymers (CP), metal-organic frameworks (MOFs), graphene (G), nanofibers (Nf), carbon nanotubes (CNTs), and nanoparticles (Nps).

A tri-inlet device integrated with an electrode, used as a diagnostic tool for electrochemical detection of *Plasmodium vivax* in human whole blood samples was reported by Singh et al [55] as shown in Figure 2:4. Reduced graphene oxide (RGO) gold nanocomposite was used to modify the surface of the electrode followed by conjugation with *Plasmodium vivax* antibody. The interaction of the electrode with the infected red blood cells (RBCs) resulted in a decrease in current charge density. The sensor showed good selectivity and sensitivity with a detection limit of 40 vivax infected RBCs/ 10 ul blood. This study demonstrated the use of a disposable type sensor kit for onsite analysis of *Plasmodium vivax* within 5 minutes.

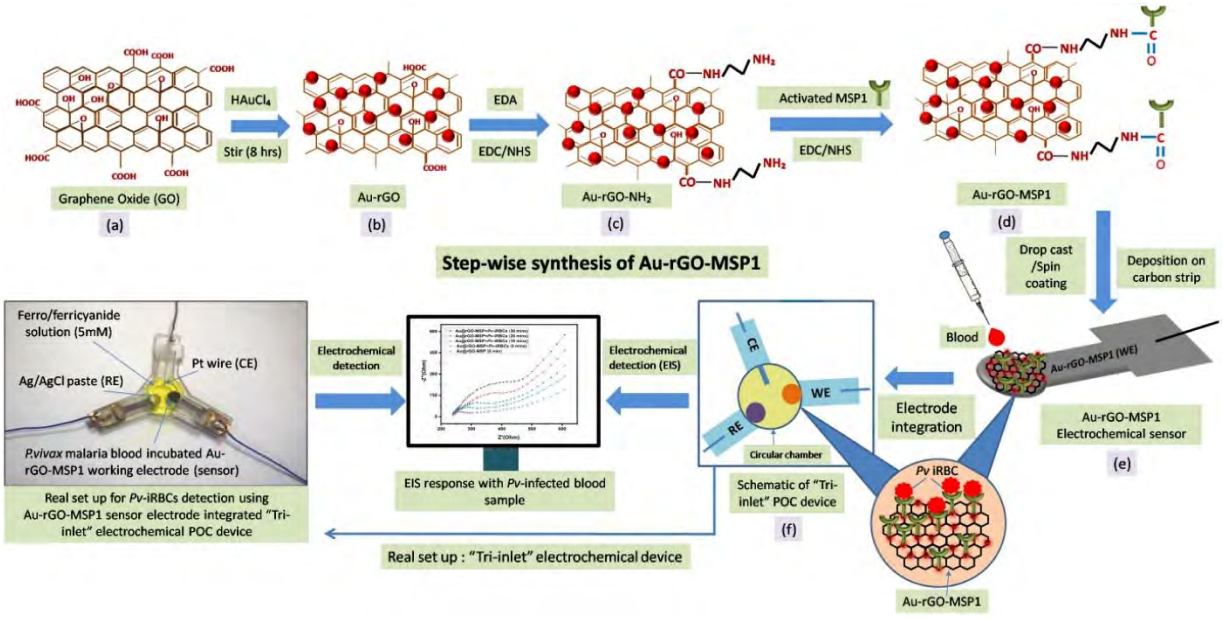

Figure 2:4 Electrochemical detection of *Plasmodium vivax*-infected RBCs in whole blood using a tri-inlet device integrated with the modified electrode [55].

Since most malaria cases in Africa are due to *Plasmodium falciparum*, it is important to develop diagnostic tools that are sensitive and selective to this malaria species. It is important to note that DNA aptamers and antibodies are usually used to improve the selectivity of the biosensor. DNA aptamers are defined as short oligonucleotide chains that can bind to a target with high specificity and affinity. DNA aptamers have high stability at elevated temperature and humidity compared to conventional antibody thus they are suitable for point of care devices in tropical areas. Gabriel et al [56] reported an aptamer-based electrochemical biosensor for malaria with an adjustable dynamic response range of up to 10 nM under variable environmental conditions. 2008s aptamer was used as a recognition molecule and *Pf*LDH as the target protein. Ferri/Ferro cyanide ($Fe(CN)_6^{3-/4-}$) was used as a redox probe. The adjustable dynamic response range was made possible by the isoelectric point (pI) of *Pf*LDH (Figure 2:5). At pH<pI a decrease in interface impendence was observed since the negative $Fe(CN)_6^{3-/4-}$ was attracted towards the surface. However, at pH>pI the interface impendence increased since $Fe(CN)_6^{3-/4-}$ was repealed. A detection limit of 0.84 pM was obtained, this was attributed to the electrostatic properties of the protein and the good selectivity of the 2008s aptamer. The sensor was found to be selective to *Pf*LDH when compared with other proteins such as L-LDH from muse muscle and human LDH, HAS, and bovine serum albumin (BSA). The main advantage of this biosensor is its low detection limit and its reusability since it can be reused by simply rinsing it with 6M urea. Jain et al [57] reported an aptamer-graphene oxide sensor for dual electrochemical detection of *Plasmodium falciparum* lactate dehydrogenase (*Pf*LDH). The dual detection was carried out using electrochemical impedance spectroscopy (EIS) and differential pulse voltammetry (DPV). During the EIS measurement, the charge resistance transfer (Rct) was found to be directly proportional to the concentration of (*Pf*LDH). The lowest detectable concentration was found to be 0.5 fM. DPV was used to confirm the specificity of the sensor; HAS, BSA, and lysozyme were used. No current response was obtained for the three proteins. While Singh et al [30] used *Plasmodium falciparum* glutamate dehydrogenase as a biomarker to develop a capacitive malaria aptasensor (Figure 2:6). A limit of detection of 0.77 pM with a dynamic range of 100fM- 100 nM in human serum was obtained. Also because of the specificity of the thiolated ssDNA aptamer (NG_3) to *Pf*GDH, interference from LDH and HRP2 was negligible.

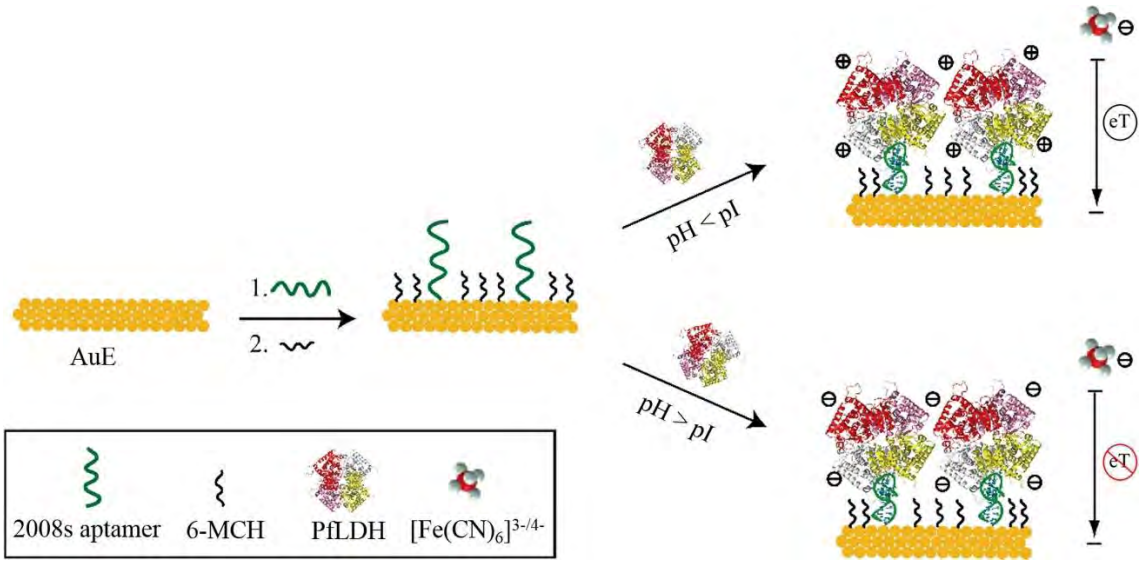

Figure 2:5 Stepwise fabrication of an aptasensor for detection of *Pf*LDH in two different pH environment [56].

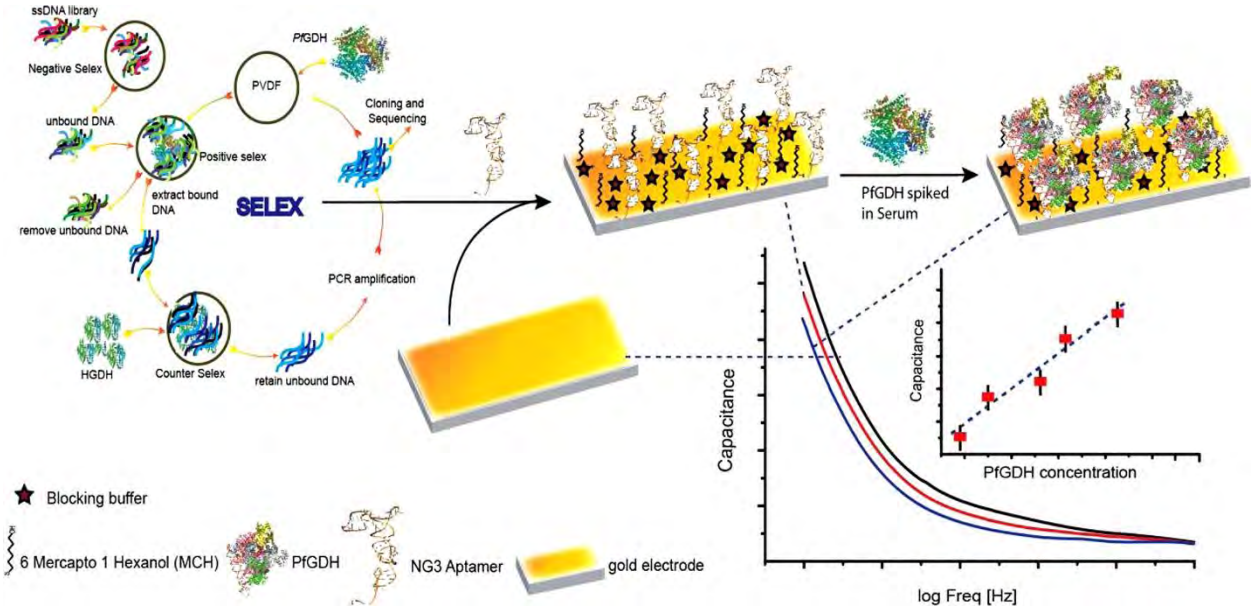

Figure 2:6 Development of aptamer through SELEX for electrochemical detection of *Pf*GDH [30].

Another study by Paul et al [1] fabricated an ultrasensitive biosensor for the detection of *Plasmodium falciparum* histidine-rich protein-2 (Figure 2:7). The sensor was found to have a limit of detection of 6.8 ag/mL. This low limit of detection is due to the complementary effect of copper

doped zinc oxide and mercaptopropylphosphonic acid. The acid increases the functional groups required for immobilizing antibody, while the doped metal oxide enhance the conductivity and pre-concentrate the target analyte.

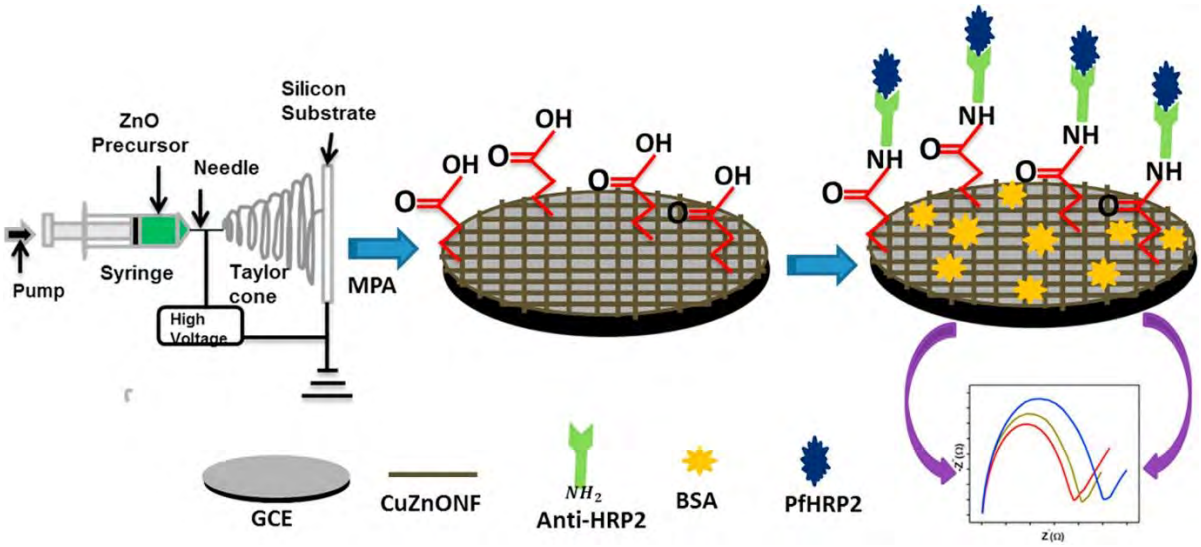

Figure 2:7 Stepwise fabrication of electrochemical sensor for detection of *Plasmodium falciparum* histidine-rich protein-2 using Copper doped zinc oxide nanofiber [1].

Diagnostic tools that require little user intervention are needed in low resource settings for rapid and accurate diagnosis of malaria. One such device was reported by Vega et al [58], in this study a fast and simple point of care (POC) electrochemical sensor for detection and quantification of *Plasmodium falciparum* lactate dehydrogenase (*Pf*LDH) in lysed whole blood was reported. The POC device was made up of the following components; single microfluidic paper, double-sided screen-printed carbon electrode (MP-dsSPCE), a magnet, a whole-blood filtration unit, and an adsorbent as shown in Figure 2:8. The sensitivity of this device was evaluated, with a detection limit of 200 ng/mL. This is close to the WHO recommendation for clinical diagnosis of malaria. Also, this method is fast since the *Pf*LDH was detected in lysed whole blood in less than 20 min.

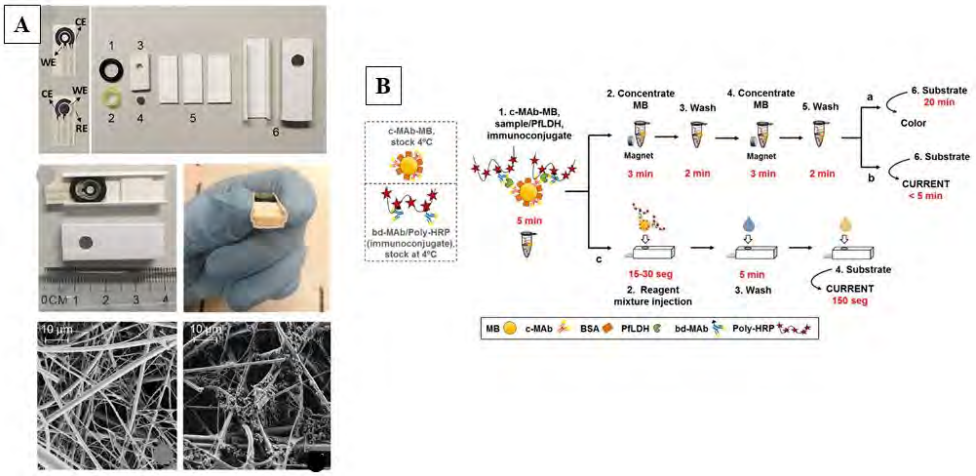

Figure 2:8 (A) Production of the MP-dsSPCE POC device, (B) Different formats of the single-step magneto-immunoassay [58].

Lillehoj et al [59] reported the onsite diagnosis of *Plasmodium falciparum* histidine-rich 2 protein (*Pf*HRP2) using an electrochemical platform integrated with a mobile phone (Figure 2:9). The system was made up of several components such as the capillary flow which was used for sample loading, processing, and pumping; microfluidic chips which are responsible for fluidic handling and biosensing; and a circuit for signal processing and data analysis. *Plasmodium falciparum* histidine-rich 2 protein was successfully detected in human serum within 15 min, a detection limit of 16 ng/mL was obtained. The device was also found to be specific to *Pf*HRP2 in the presence of 5 different proteins. This device can be used in remote and rural areas because of its compact size and good selectivity and sensitivity. Some of the recently reported electrochemical biosensors for the detection of malaria are listed in Table 2:2.

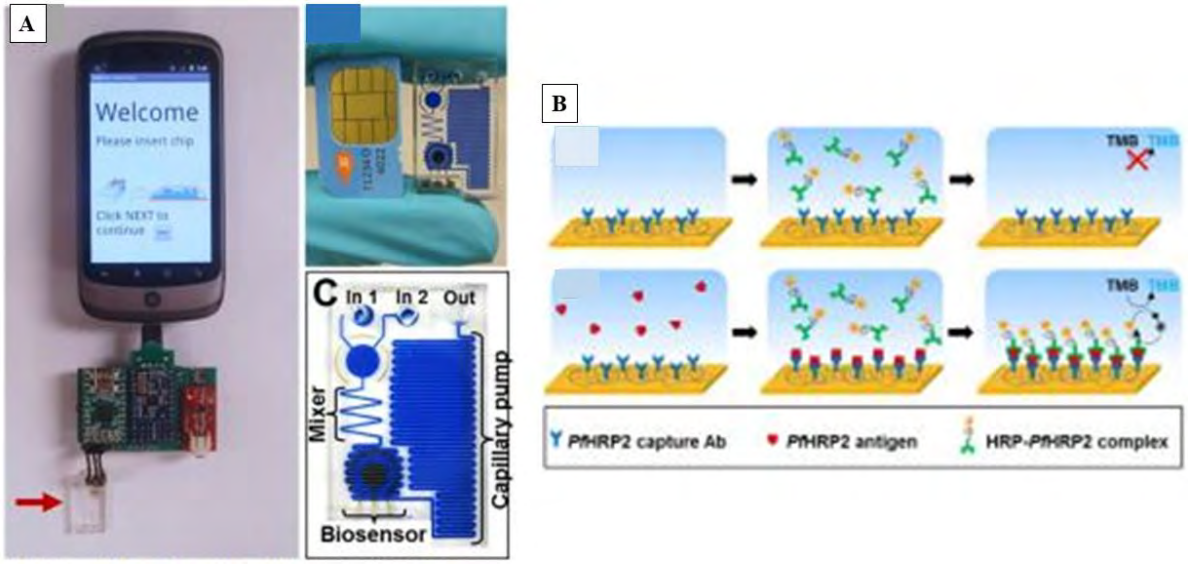

Figure 2:9 (A) Image of the designed prototype device. (B) Scheme for electrochemical detection of *Pf*HRP2 [59].

Table 2:2 Some of the selected electrochemical biosensors for malaria diagnosis.

Biosensor description	**Biomarker/ malaria species**	**Detection limit**	**Time**	**Benefits**	**Ref**
A tri-inlet device integrated with nanocomposite (reduced graphene oxide gold nanoparticles) and *Plasmodium vivax* modified electrode	*Plasmodium vivax*	40 vivax infected RBCs/ 10 ul blood	5 min	Rapid and easily Disposable type sensor kit for onsite analysis of *Plasmodium vivax*.	[55]
4-mercaptobenzoic acid-modified gold SPR chip immobilized with Ag and malaria antibodies	*Pf*HRP2	5.6 pg	-	High sensitivity due to the use of 4-mercaptobenzoic acid which has a lesser thickness and fast electron transfer compared to dextain	[60]
Dual electrochemical analysis of malaria using aptamer-graphene oxide biosensor	*Plasmodium falciparum* lactate dehydrogenase (PfLDH)	0.5 fM	-	dual electrochemical detection of *Pf*LDH	[57]
Magneto immunoassay strategy for detection of malaria based on magnetic nanoparticles	*Pf*HRP2	0.36 ng/mL	-	Application for onsite diagnosis of malaria and it uses disposable screen-printed magneto electrodes	[61]
aptamer-based electrochemical biosensor for malaria with an adjustable dynamic response range	*Pf*LDH	0.84 pM	-	High selectivity, low detection limit, and it is reusable.	[56]
Electrochemical immunosensor based on methylene blue and the electro-oxidation of hydrazine on Pt nanoparticles	*Pf*HRP2	2.2 pg/mL	-	High sensitivity and ability to detect PfHRP2 in unadulterated saliva samples	[62]
Malara Immunosensor based on chronoamperometry	*Pf*HRP2	2.14 ng/mL and 2.95 ng/mL	-	Cost-effective, sensitive, and easy to use. Ideal for onsite application.	[63]

Electrochemical impendence spectroscopy-based malaria aptasensor	*Pf*HRP2	3.15 pM	-	High sensitivity and selectivity because of the novel ssDNA aptamer	[64]
Copper doped zinc oxide nanofibers modified electrode for the detection of malaria.	*Pf*HRP2	6.8 ag/mL	-	High sensitivity and a new surface modification method for adding functional groups to improve the selectivity of the biosensor.	[1]
capacitive malaria aptasensor	*Pf*GDH	0.77 pM	-	High selectivity due to specificity of the thiolated ssDNA aptamer (NG_3) to PfGDH,	[30]
Electrochemical detection of malaria in whole blood using a wash-free, label-free immunoassay	*Pf*HRP2	Not available however detection range from 100ng/mL - 100ug/mL was given	5min	Rapid with excellent specificity and reproducibility	[65]
Detection of *Plasmodium* lactate dehydrogenase using an aptasensor.	*Pf*LDH *Pv*LDH	120,1 fM and 108.5 fM for *Pf*LDH and *Pv*LDH respectively	-	Simple rapid and highly sensitive sensor with an aptamer that selectively bound to both PfLDH and PvLDH	[66]
Gold nanoparticles based biosensor for detection of malaria	*Pf*LDH	19 pg/mL 23 pg/mL	-	Rapid and cost-effective point of care immunoassay with high sensitivity and reproducibility	[67]
Screen-printed electrode modified with gold nanoparticles-multi-wall carbon nanotubes and *Pf*-HRP2 antibody	*Pf*HRP2	8 ng/mL	-	Disposable Amperometric immunosensor with high sensitivity	[7]

				compared to commercial Paracheck Pf test	
Point of care (POC) electrochemical sensor for detection and quantification of malaria in lysed whole blood	*Pf*LDH	200 ng/mL	20 min	Rapid Quantitation in lysed whole blood. Single-step magneto-immunoassay for PfLDH.	[58]
Mobile based electrochemical biosensor for quantification of malaria in low resource settings.	*Pf*HRP2	20 ng/mL	-	Simple and cost-effective hands held device.	[68]
electrochemical platform integrated with a mobile phone	*Pf*HRP2	16 ng/mL	15 min	This device can be used in remote and rural areas because of its compact size and good selectivity and sensitivity.	[59]
Chemiresistive biosensor for detection of malaria using multi-walled carbon nanotubes-zinc oxide nanofibers	*Pf*HRP2	0.97 fg/mL	-	Good reproducibility and specificity with a sensitivity of 8.29 $K\Omega g^{-1}$ mL	[69]

2.3.3 Colorimetric biosensors

Recently several studies have reported the development of colorimetric biosensors that meet the WHO recommendations for point of care devices. According to the WHO, the world needs diagnostic tools that are affordable, sensitive, specific, user friendly, robust, rapid, equipment-free, and deliverable to end-user (ASSURED) [70,71]. Therefore several colorimetric malaria biosensors are being reported. These biosensors use the change in color which can be identified by the human naked eye to confirm the presence of a malaria biomarker. Also uses optical detectors for quantitative measurements. To improve the performance of these biosensors, nanomaterials such as nanoparticles and quantum dots are being used. This is due to their unique physical and chemical properties such as high surface-to-volume ratio, excellent capacity for reaction catalysis, visual color transition, and optical properties [72,73]. It is essential to note that the properties of nanomaterials depend on their size, shape, and degree of agglomeration. Cationic polymers and gold nanoparticles were used to develop a colorimetric aptasensor for diagnosis of malaria by Jeon et al [74] *Plasmodium falciparum* lactate dehydrogenase and pL_1 were used as biomarker and aptamer respectively. The principle of this biosensor was based on cationic polymers (poly (diallyldimethylammonium chloride) and poly (allylamine hydrochloride)) which aggregate gold nanoparticles (AuNps) thus a color change was observed from red to blue. This color change depends on the concentration of *Plasmodium falciparum* lactate dehydrogenase (Figure 2:10). A detection limit of 8.7 pM and 8.3 pM was obtained for *Plasmodium vivax* lactate dehydrogenase when (poly (diallyldimethylammonium chloride) and poly (allylamine hydrochloride)) were used respectively. The same sensor was used for the measure *Plasmodium falciparum* lactate dehydrogenase and a detection limit of 125 pM and 10.3 pM was obtained for poly (allylamine hydrochloride)) and (poly (diallyldimethylammonium chloride) respectively. A similar study was conducted by Lee et al [75] where a cationic surfactant was used as shown in Figure 2:11. A detection limit of 2.94 pM and 1.25 pM was obtained for *Pf*LDH and *Pv*LDH respectively. While Jain et al [76] reported the use of aromatic surfactant (benzalkonium chloride) as aggregating agent for aptamer (P38) gold nanoparticles based detection of *Plasmodium* lactate dehydrogenase. A detection limit of 281±11 pM was obtained.

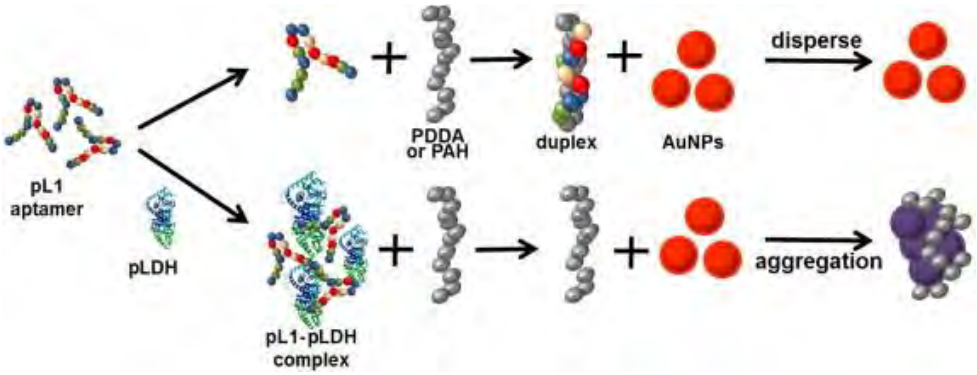

Figure 2:10 Representation of the aptasensor for pLDH detection [74].

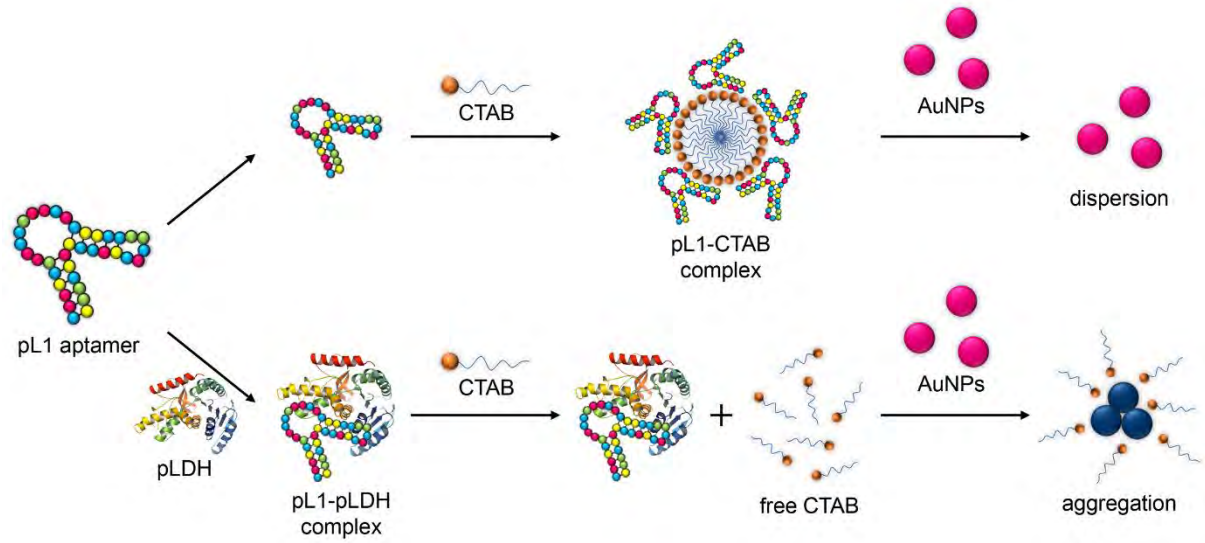

Figure 2:11 Detection of pLDH based on the surfactant-induced aggregation of AuNPs [75].

In another study, a simple colorimetric point of care device for the diagnosis of malaria was reported by Dirkzwager et al [77]. This POC device was made of a paper-based syringe test and a magnetic bead-based well test. *Pf*LDH and 2008s-biotin were used as biomarker and aptamer respectively. Both methods were found to be sensitive to *Pf*LDH. However, the syringe method was more sensitive with a wider linear range and a detection limit of 4.9 ng/mL. A novel and sensitive carbon nanofibers grown on glass micro balloons immunosensor was reported by Gikunoo et al [78] for detection of *Pf*HRP2 a detection limit of 0.025 ng/mL was obtained.

2.4 ELECTROCHEMICAL DETECTION OF ANTIMALARIAL DRUGS

One of the main factors that contribute to the high mortality rate in malaria cases is substandard or falsified drugs. According to the WHO report on global surveillance and monitoring system for substandard and falsified medical products; counterfeit medicine is a global problem as shown in Figure 2:12. Several factors contribute to high volumes of substandard drugs, these include; high cost of medicine in most countries, failure to adhere to good manufacturing practice, and lack of quality control and verification process [79,80]. The use of these drugs contributes negatively to the health system since they result in poisoning, early death, treatment failure, drug-resistant, social, and economic effects [79].

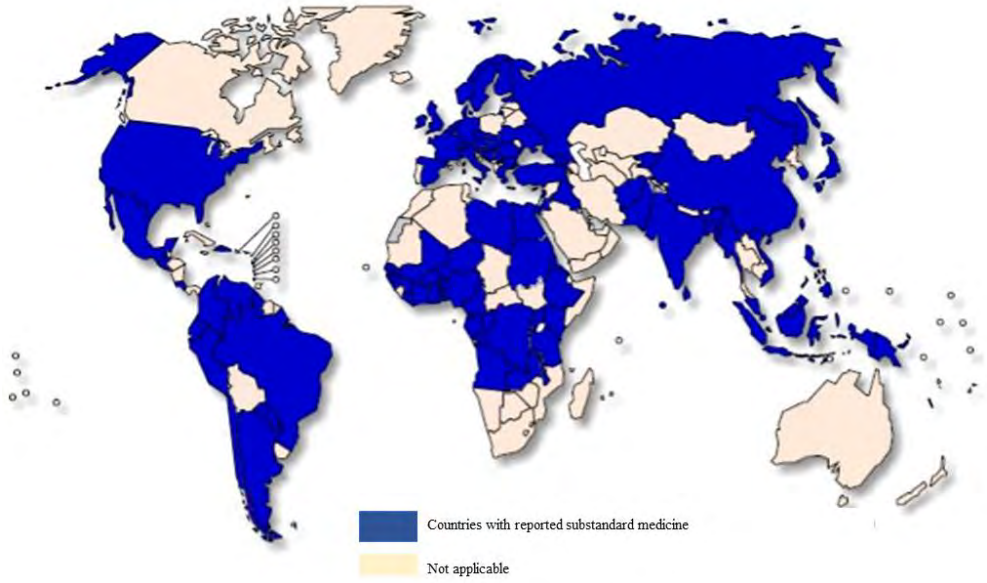

Figure 2:12 Countries with reported substandard and falsified medical products, WHO GSMS, 2013–2017 [79].

Malaria can be treated using different antimalarial drugs. These drugs can be classified as quinoline-related compounds, artemisinin derivatives, antifolates, and antibiotics. Some of these compounds are listed in Table 2:3. Although malaria can be treated, the effectiveness of these antimalarial drugs is compromised by substandard medicine. A practical example of the impact of counterfeit drugs was reported in Southeast Asia, where some malaria species developed resistance to artemisinin [79,81,82]. This resistance was attributed to counterfeit drugs since 38-90% of artemisinin was found to be substandard.

Table 2:3 List of WHO recommended antimalarial drugs

Antimalarial drug	Classification
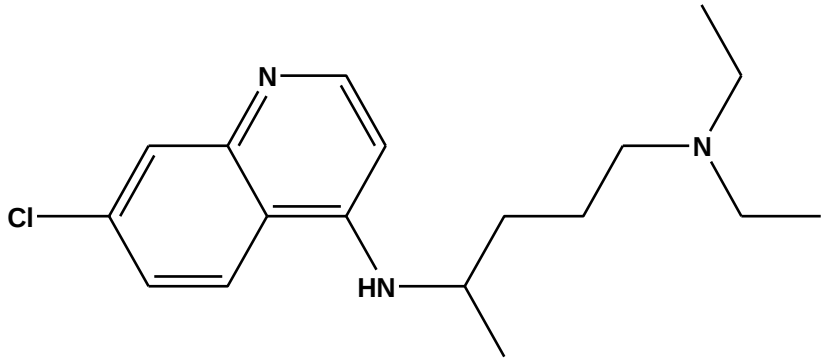 Chloroquine 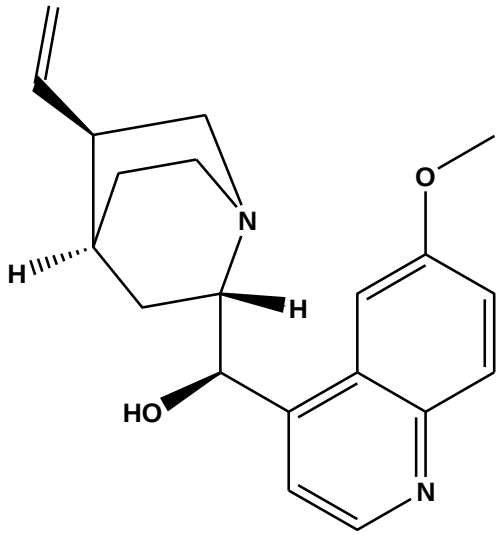 Quinine	Quinoline-related compounds

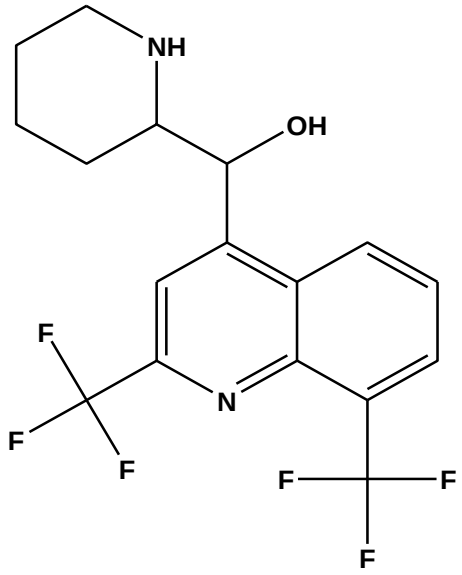

Mefloquine

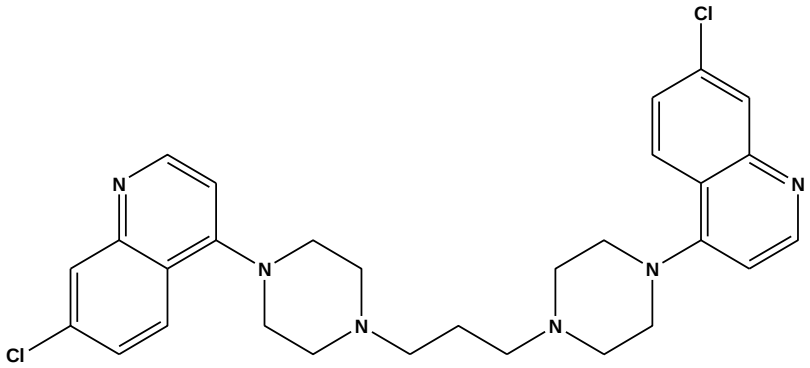

Piperaquine

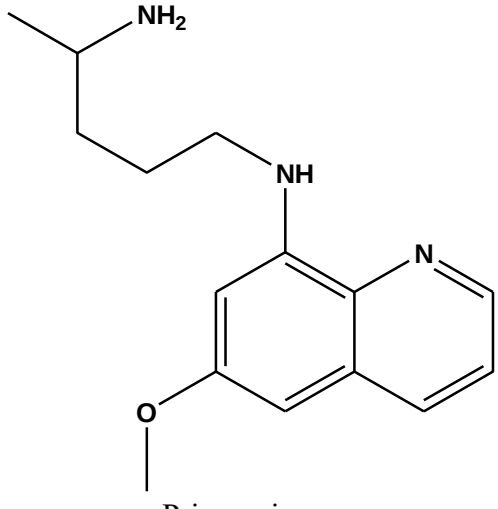

Primaquine

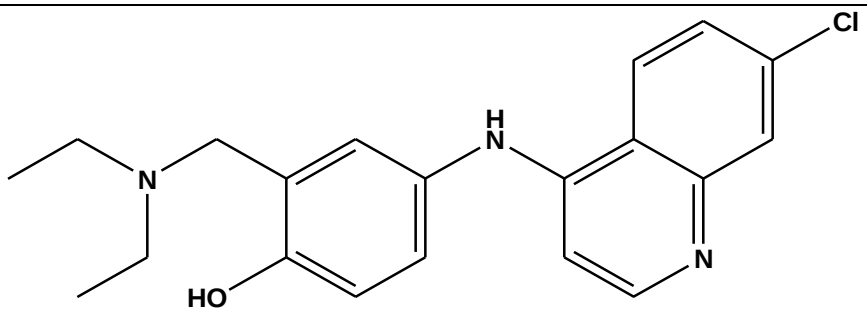 Amodiaquine	
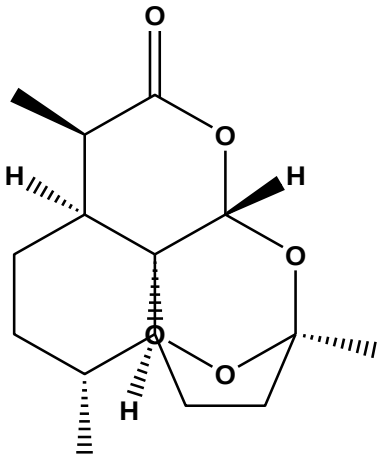 Artemisinin 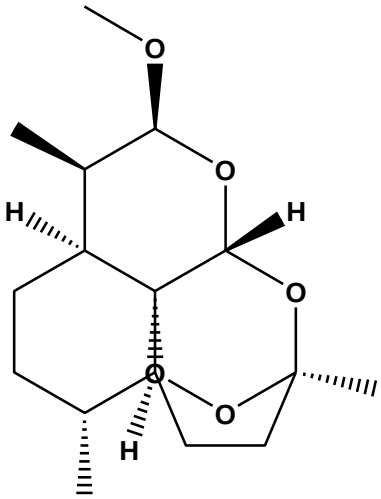 Artemether	Artemisinin derivatives

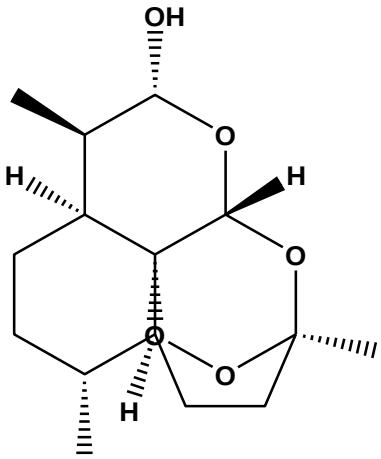 Dihydroartemisinin 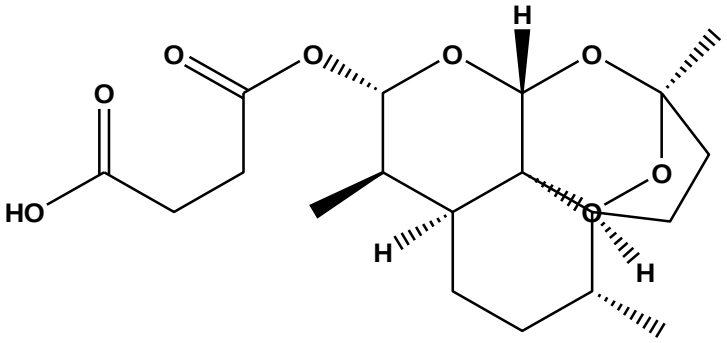 Artesunate	
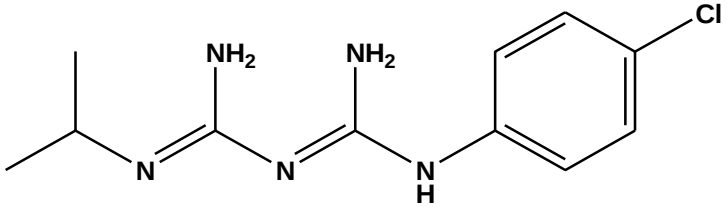 Proguanil 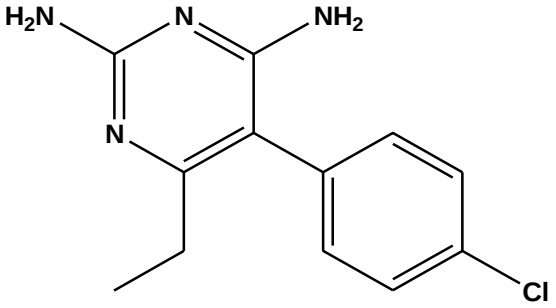 Pyrimethamine	Antifolates

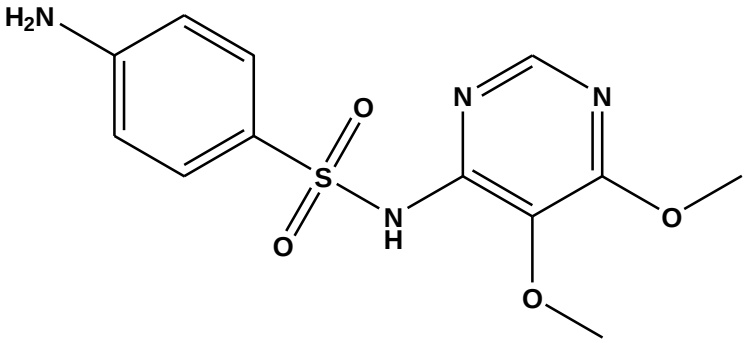 Sulfadoxine	
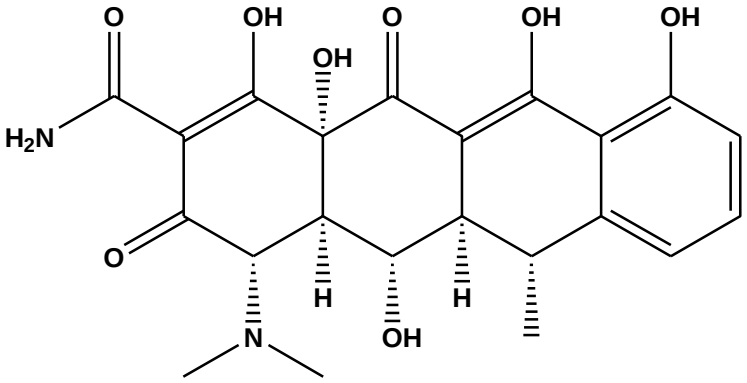 Doxycycline 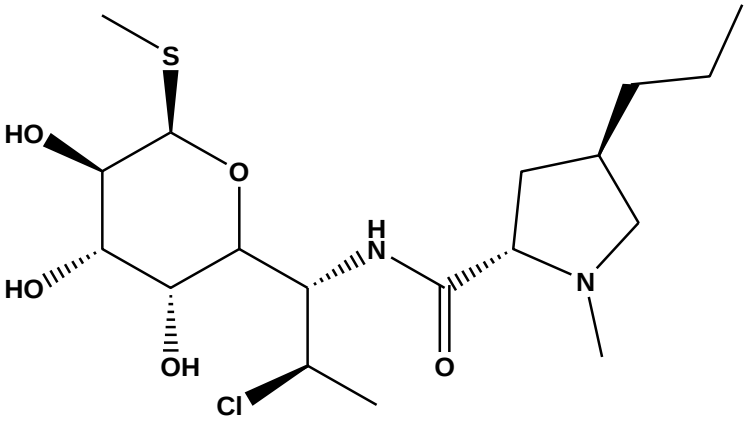 Clindamycin	Antibiotics

2.4.1 Quinoline-related compounds

The pharmacological activity of the quinoline scaffold is well reported in several studies. Quinine, chloroquine, mefloquine, piperaquine, primaquine, and amodiaquine are referred to as quinoline-related compounds (Table 2:3). These compounds are frequently used as antimalarial drugs. The mechanism of action is not fully known. However, it is postulated that quinolines interfere with

the hemoglobin in the blood stages of the malaria life cycle. This is achieved by the inhibition of heme polymerization and by preventing the disposal of polymers from the food vacuole to the cytoplasm where hemozoin is formed. Thus this results in the intraparastic accumulation of heme [83,84]. Other quinoline targets include DNA, tyrosine kinase, phospholipases, and hemoglobin degradation proteases [83,85,86]. Cyclic voltammetry and differential pulse voltammetry were used to evaluate the sensitivity and selectivity of a glassy carbon electrode modified with graphene oxide (GO)-tungsten disulfide (WS_2) quantum dots (QDs) for detection of chloroquine in pharmaceutical formulation by Srivastava et al [87]. A wide linear range, detection limit and good sensitivity of 0.5- 82 uM, 0.04 uM, and 0.143-0.90 $uA.uM^{-1}$ cm^{-2} was obtained respectively. The proposed mechanism for chloroquine oxidation on the surface of the modified electrode is shown in Figure 2:13. While Azadmehr et al [88] fabricated an imprinted electrochemical for detection of quinine using a glassy carbon electrode modified with L-tyrosine, 3-methyl-4-nitrophenol, and gold nanoparticles. The mechanism of detection was based on the signal reduction of the Fe^{2+} probe with an increase in quinine concentration. A detection limit of 0.05 pM with a linear range of 0.1 to 1000 pM was obtained. In another study by Chiwunze et al [89], the surface of a glassy carbon electrode was modified using gold nano-urchin for the determination of mefloquine. Gold nanoparticles were synthesized using the seed-mediated method, and the fabrication of the sensor was done by the drop-coating method. The modified electrode showed two linear response ranges with a detection limit of 1.4 nM.

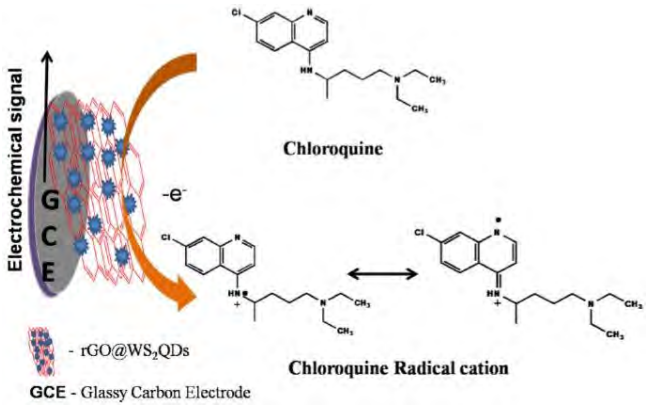

Figure 2:13 Plausible mechanism for electrooxidation of chloroquine on rGO@WS2 QDs modified GCE [87].

2.4.2 Artemisinin derivatives

Since there is high resistance of malaria to chloroquine and sulfadoxine-pyrimethamine, the world health organization recommends the use of Artemisinin-based combination therapy as a first-line treatment option for malaria. Artemisinin-based combination therapy is among the few strategies that result in diminished parasite recrudescence, reduced treatment time, and lower probability of resistance development [90–92]. *Artenisia aunua L* (sweet wormwood) a natural plant that belongs to the *Asteraceae* family was first used in 1972 to isolate artemisinin. In 1979 the first molecular structure was assigned. Over the year's artemisinin and its derivatives (Artemether, dihydroartemisinin, and Artesunate) (Table 2:3) have proven to be useful anticancer, anti-inflammatory, and antimalarial agents. The antimalarial activity of these compounds is proposed to be through the unspecific modification of multiple targets like proteins and heme in the digestive vacuole. This is achieved by the presence of an endoperoxide linkage (a peroxide bridge), the endoperoxide bridge is cleaved by an intraparasital iron-II source to yield carbon-centered radicals [90,93]. An electrochemical sensor for the detection of artemisinin that does not require the use of complex electrode modification or high oxidation potential was reported by Wang et al [94]. This was based on the electrochemical detection of aminophenol which is produced by the reaction artemisinin with *p*-aminophenylboronic acid as shown in Figure 2:14a. A detection limit of 0.8 uM with a linear range of 2- 200 uM was obtained. Artemisinin was further detected in spiked naphthoquine phosphate tablet samples, a recovery from 101.7- 107.6% was obtained.

Bai et al [95] used a glassy electrode modified with graphene and in-situ polymerized molecular imprinted membrane for sensitive and selective determination of artemisinin (Figure 2:14b). Graphene was used because of its specific surface area, exceptional electrocatalytic and electrical properties. A detection limit of 2×10^{-9} M and a linear range of 4×10^{-5} - 1×10^{-8} M was obtained. The sensor was found to be highly selective to artemisinin in the presence of artemether, dihydroartemisinin, and artesunate. This was attributed to the presence of molecular imprinted polymers. In another study, a novel electrochemical sensor based on inhibition of redox for hemin caused by artemisinin was reported by Jiang et al [96] (Figure 2:15). A glassy carbon electrode modified with multiwall carbon nanotubes, bimetallic organic frameworks, and hemin was used. Under optimum conditions, a limit of detection of 0.17 uM was reported. The sensor was further used to evaluate its practical applicability using dried *Artemisia apiacea*, recovery in the range of 99.5- 104.34% was obtained.

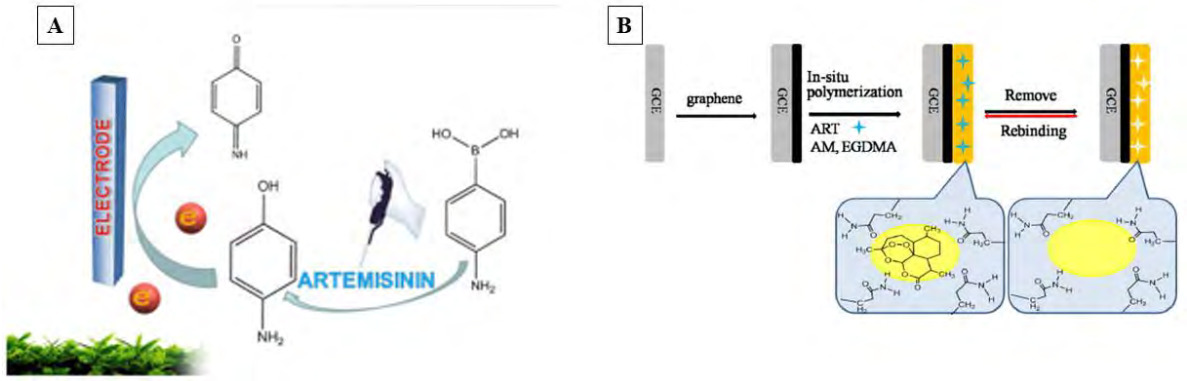

Figure 2:14 (A) illustration of the reaction between artemisinin and p-aminophenylboronic acid at the surface of the electrode [94], (B) Representation of the ART-MIM/G/GCE sensor [95].

Figure 2:15 Artemisinin detection based on signal inhibition for the reduction of hemin [96].

2.4.3 Antifolates

Antifolates compounds such as proguanil, pyrimethamine, and sulfadoxine are used as antimalarial drugs (Table 2:3). The main function of these compounds is to inhibit the folate mechanism of the parasite, both in the synthesis and use of folate cofactors. To achieve this, two key enzymes are targeted; dihydropteroate synthase which is inhibited by the sulfa compounds, and dihydrofolate reductase which is inhibited by cycloguanil, pyrimethamine, and other inhibitors [97,98]. However, most antifolates are susceptive to resistance because of the mutation in the targeted enzymes. To solve this challenge, antifolates compounds are used with other antimalarial drugs

such as primaquine and atovaquone. A recent study by Nate et al [99] reported the simultaneous electrochemical determination of proguanil and primaquine. Differential pulse voltammetry and cyclic voltammetry with a potential window of 0 to 1.5 V were used. From the CV plots, oxidation peaks at 0.5 and 1.2 V were obtained for primaquine and proguanil respectively. The electrochemical active site of these drugs was proposed to be the irreversible oxidation of 4-Chloroaniline and 7-methoxyamino quinolone moiety with a detection limit of 1.42 nM and 2.07 nM in proguanil and primaquine, respectively (Figure 2:16). In another study by Abdel-Haleem [100], phosphotungstic acid was used as a modifier to investigate the sensitivity of five electrodes (PVC membrane, screen printed, coated wire, carbon paste, and modified carbon base) towards proguanil. A detection limit of 7.94×10^{-6} M, 1×10^{-5} M, 1×10^{-6} M, 7.07×10^{-6} M, and 2.5×10^{-6} M were obtained respectively.

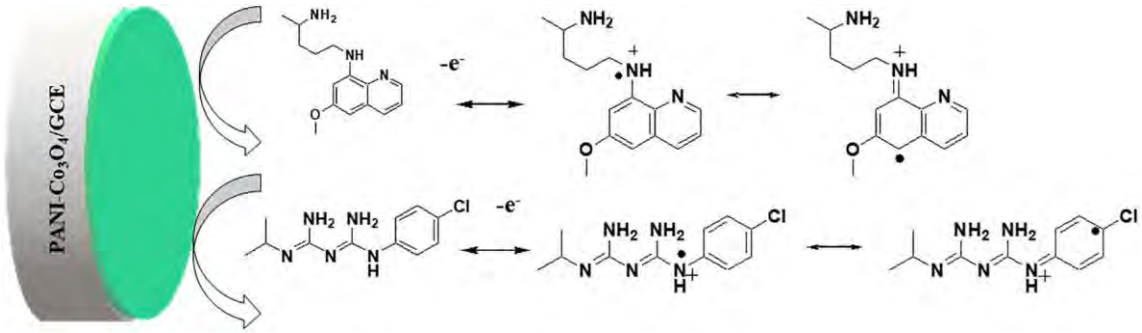

Figure 2:16 Illustration for simultaneous electrochemical detection of proguanil and primaquine [99].

2.4.4 Antibiotics

In areas where *Plasmodium falciparum* is resistant to chloroquine and sulfadoxine-pyrimethamine, antibiotics such as tetracycline and its derivatives (doxycycline) in combination with other antimalarial drugs are used for malaria treatment (Table 2:3). The main function of doxycycline is to inhibit the pathogen protein synthesis by reversibly inhibiting the 30S ribosomal subunit. The sensitivity of doxycycline to *Plasmodium* ribosomes is high since there is a significant difference between the mammalian ribosomes and the *Plasmodium* ribosomes. However, doxycycline is not recommended for pregnant women and children under 8 years. While clindamycin a derivative of lincomycin is not frequently used because it is expensive and more toxic than other antibiotics

alternatives. An electrochemical sensor based on multi-walled carbon nanotubes and molecular imprinted polymers was fabricated for the determination of doxycycline by Xu et al [101]. The presence of MWCNTs improved the current response, this was attributed to the high surface to volume ratio and good electrocatalytic activity of MWCNTs. While molecular imprinted polymers provided selective recognition sites for doxycycline. A detection limit of 1.3×10^{-2} umol/L with a linear range of 0.05 umol/L- 0.5 umol/L was obtained. While Gurler et al [102] determined doxycycline in pharmaceutical formulation using molecular imprinted polypyrrole modified electrode. Differential pulse voltammetry was used. A detection limit of 4.35×10^{-5} M was obtained and the recovery of doxycycline in two commercial products was found to be 96.30 % and 61.18 % with a relative standard deviation of 0.46 and 0.54 respectively.

A sensitive and selective molecular imprinted polymer electrochemical sensor for the detection of clindamycin was fabricated by Zhang et al [103]. Au electrode modified with multi-wall carbon nanotubes and thin sol-gel film of the molecular imprinted polymer was used. A detection limit of 2.44×10^{-8} M with a linear range of $5\times 10^{-7} – 8\times 10^{-5}$ M was obtained. In another study, Wong et al [104] reported an electrochemical method for the quantification of clindamycin in pharmaceutical formulation using graphene oxide and gold nanoparticles within a film of crosslinked chitosan with epichlorohydrin modified electrode. Using square wave voltammetry a wide linear concentration range ($9.5\times 10^{-7} – 1.4\times 10^{-4}$ mol/L) with a detection limit of 2.9×10^{-7} mol/L was obtained. Some of the recently reported electrochemical sensors for the detection of antimalarial drugs are listed in table 2:4.

Table 2:4 Some of the selected electrochemical sensors for detection of antimalarial drugs

Sensor description	**Antimalarial drug**	**Electrochemical method**	**Detection limit (µM)**	**Linear range (µM)**	**Ref**
MIP– MIC-AuNPs/MWCNT-chitosan/PGE	quinine	DPV	5.0×10^{-8}	1.0×10^{-7} –1.0 $\times10^{-3}$	[88]
Glassy carbon electrode modified with 4-amino-3-hydroxynaphthalene sulfonic acid	quinine	SWV	0.0142	0.1–10	[105]

polypyrrolepentacyanonitrosylferrate/ platinum electrode	quinine	CV	10.8	1000-9000	[106]
hanging mercury drop electrode	quinine	SWV	0.132 $ng \cdot mL^{-1}$	30-230 $ng \cdot mL^{-1}$	[107]
pretreated pencil graphite electrode	quinine	DPV	0.2	0.5-100	[108]
MIP/GCE	quinine	Amperometric	0.02	0.8-260	[109]
MWCNTs-RTIL/GCE	quinine	SWV	0.44	3-100	[110]
rGO@WS2/GCE	chloroquine	DPV CV	0.04 0.04	0.5 - 82.4	[87]
Boron-Doped Diamond Electrode	chloroquine	SWV	0.002	0.01–0.25	[111]
dsDNA/CPE	chloroquine	DPV CV	0.03	0.1–10	[112]
CuNW/CPE	chloroquine	DPV	0.02	0.13-13.3	[113]
Gold Nanourchin modified glassy carbon electrode	Mefloquine	SWV	1.42×10^{-3}	2.0×10^{-3} - 1.0 1.0- 1000	[114]
Hanging mercury drop electrode	Mefloquine	DPV SWV	0.454 0.261	6-80	[115]
MWCNTs/GCE	Primaquine	SWV	0.028	0.1-5.0	[116]
Gold nanourchins /GCE	Primaquine	DPV SWV	3.52×10^{-3} 9.91×10^{-4}	0.01-1.0 1.0×10^{-3} - 1.0	[117]
CuNW/CPE	Primaquine	DPV	0.25 μg mL^{-1}	0.58–5.89 μg mL^{-1}	[113]
GCE	Primaquine	LSV DPV SWV	36.2 16.2 6.94	30 - 10000 30 - 100 30 - 100	[118]
functionalized fullerene (C60)-based imprinted polymer composite/pencil graphite electrode	Primaquine	Differential pulse anodic stripping voltammetry	8×10^{-4}	2.7×10^{-3} - 0.8485	[119]

Pencil graphite electrode	Amodiaquine	DPV	3.0×10^{-4}	0.001–0.2	[120]
multi-walled carbon nanotubes/ poly(methyl orange) /GCE	Amodiaquine	DPV	0.089	0.10–3.5	[121]
Hemin modified electrode	Amodiaquine	SWV	7.04	19–100	[122]
Polyvinyl chloride membrane sensors	Amodiaquine	Potentiometric	-	3.2 - 20000	[123]
o-phenylenediamine MIPs/Au wire	Artemisinin	CV SWV	0.01 buffer 0.02 Plant matrix	-	[124]
PHA/AuNPs/HRP/ITO	Artemisinin	DPV	0.0035 μg mL^{-1}	0.01–0.08 $\mu g mL^{-1}$	[125]
ART-MIM/G/GCE	Artemisinin	DPV	2×10^{-3}	40 – 0.01	[126]
GCE	Artemisinin	SWV	0.8	2- 200	[127]
[FeT(o-glu)PPCl]/Au/GCE	Artemisinin	Amperometric	1.7×10^{-3}	0.18–1.7×10^{-3}	[128]
hemin immobilized on titanium oxide-modified silica/ carbon paste electrode	Artemisinin	Amperometric	0.015	0.05 – 1.0	[129]
FeGd-MOF/Hemin/MWCNTs/GCE	Artemisinin	DPV	0.17	0.3–350	[130]
GrO/PANI/HRP/ITO	artesunate	SWV	0.012 ng/mL	0.05-0.40 ng/mL	[131]
GCE in presence of CTAB	artesunate	SWV and DPV	0.034 and 0.491 ug/ mL in tablet 0.245 & 3.942 ug/ mL in serum 0.120 & 2.753 ug/ mL in Plasma	4.0–40 ug/mL	[132]

			0.066 & 0.970 ug/ mL in urine		
MWCNTs-Fe_2O_3/GCE	Proguanil	DPV	0.0196	0.7- 1.9	[133]
PANI-Co_3O_4/GCE	Primaquine and Proguanil	DPV	2.07×10^{-3} 1.42×10^{-3}	20-36 16-28	[99]
Renewable silver amalgam film	Proguanil	SWV	0.029	0.1- 6	[134]
CWE/phosphotungstic Acid	Proguanil	Potentiometric	1.00	10-10000	[100]
GCE	Sulfadoxine	DPV	0.01 µg ml^{-1}.	0.310 - 4.34 µg ml^{-1}	[135]
Graphene-polyaniline/screen-printed carbon electrode	Sulfadoxine	Amperometric	9.65×10^{-3}	0.0325 – 35	[136]
Carbon paste electrode/α-cyclodextrine-multi-walled carbon nanotube/tricresylphosphate Carbon paste electrode/α-cyclodextrine-multi-walled carbon Nanotube/ o-nitrophenyloctylether	Doxycycline	Potentiometric	0.1 0.122	0.1-10000 0.122-10000	[137]
molecularly imprinted polymer/MWCNTs/GCE	doxycycline	DPV	1.3×10^{-2}	0.05- 0.5	[138]
pencil graphite electrode/ Molecularly imprinted-polypyrrole	doxycycline	DPV	42.5	50-500	[102]
Au electrode/ MWCNTs/ imprinted	clindamycin	Amperometric	0.0244	0.5 - 80	[103]

sol gel					
AuNPs-GO-CTS-ECH/GCE	clindamycin	SWV	0.29	0.95- 140	[104]
carbon paste electrode	clindamycin	DPV SWV	0.0861 0.164	0.17-1.02 0.34-2.04	[139]
EP-EPPG	clindamycin	CV DPV	0.06 0.01	0.2–16.0 0.03–3.2	[140]

Abbreviations; MIP (molecularly imprinted polymer), MIC (molecularly imprinted composite), MWCNTs (multiwall carbon nanotubes), AuNps (gold nanoparticles), DPV (differential pulse voltammetry), SWV (square wave voltammetry, LSV (linear sweep voltammetry) CV (cyclic voltammetry), GCE, glassy carbon electrode, RTILs (room temperature ionic liquids), rGO (reduced graphene oxide, WS2 (tungsten disulfide), CPE (carbon paste), CuNW (copper nanowires), PHA (polyhydroxyalkanoate), HRP (horse-redish peroxidase), ITO (indium tin oxide), ART (artemisinin), MIM (molecularly imprinted membrane), G (graphene), [FeT(o-glu)PPCl] (5,10,15,20-tetrakis[2-(2,3,4,6-tetraacetyl-β-d-glucopyranosyl)-1-O-phenyl]porphyrin (T(o-glu)PPH), FeGd-MOF (iron-gadolinium metal organic framework), GrO (graphene oxide), PANI (polyaniline), CTAB (cetrimonium bromide), CWE (coated wire electrode), GO-CTs-ECH (graphene oxide –chitosan-epichlorohydrin), EP-EPPG (electrochemical pretreatment –edge-plane pyrolytic graphite).

2.5 SUB-CONCLUSION AND FUTURE PERSPECTIVES

A number of electroanalytical methods have been reported for the analysis of malaria and antimalarial drugs. For diagnosis of malaria WHO recommends the use of parasite-based diagnostic testing such as microscopy or rapid diagnostic tests. While quality control for antimalarial drugs is done using different methods. The selectivity and sensitivity of some of these analytical methods are poor. Therefore, there is a need to develop diagnostic tools that are affordable, sensitive, specific, user-friendly, robust, rapid, equipment-free, and deliverable to the end-user (ASSURED). More studies still need to be done that to improve the analytical performance of electrochemical biosensors in real-world malaria samples. Since the WHO recommends the use of artemisinin-based combination therapy more electrochemical studies for qualitative and quantitative analysis of these drugs need to be carried out. Also, the application of various nanomaterials to fabricate electrochemical sensors for the diagnosis of malaria and antimalarial drugs is limited thus more research focus is needed.

2.6 REFERENCES

[1] K. Brince Paul, S. Kumar, S. Tripathy, S.R.K. Vanjari, V. Singh, S.G. Singh, A highly sensitive self assembled monolayer modified copper doped zinc oxide nanofiber interface for detection of Plasmodium falciparum histidine-rich protein-2: Targeted towards rapid, early diagnosis of malaria, Biosens. Bioelectron. 80 (2016) 39–46. https://doi.org/https://doi.org/10.1016/j.bios.2016.01.036.

[2] N. Thapliyal, T.E. Chiwunze, R. Karpoormath, R.N. Goyal, H. Patel, S. Cherukupalli, Research progress in electroanalytical techniques for determination of antimalarial drugs in pharmaceutical and biological samples, RSC Adv. 6 (2016) 57580–57602. https://doi.org/10.1039/C6RA05025E.

[3] M. Rai, A.P. Ingle, P. Paralikar, I. Gupta, S. Medici, C.A. Santos, Recent advances in use of silver nanoparticles as antimalarial agents, Int. J. Pharm. 526 (2017) 254–270. https://doi.org/https://doi.org/10.1016/j.ijpharm.2017.04.042.

[4] WHO, World malaria report 2019, Geneva, 2019. https://www.who.int/publications/i/item/9789241565721.

[5] N. Tangpukdee, C. Duangdee, P. Wilairatana, S. Krudsood, Malaria diagnosis: a brief review., Korean J. Parasitol. 47 (2009) 93–102. https://doi.org/10.3347/kjp.2009.47.2.93.

[6] K. V Ragavan, S. Kumar, S. Swaraj, S. Neethirajan, Advances in biosensors and optical assays for diagnosis and detection of malaria, Biosens. Bioelectron. 105 (2018) 188–210. https://doi.org/https://doi.org/10.1016/j.bios.2018.01.037.

[7] M.K. Sharma, V.K. Rao, G.S. Agarwal, G.P. Rai, N. Gopalan, S. Prakash, S.K. Sharma, R. Vijayaraghavan, Highly sensitive amperometric immunosensor for detection of Plasmodium falciparum histidine-rich protein 2 in serum of humans with malaria: comparison with a commercial kit., J. Clin. Microbiol. 46 (2008) 3759–3765. https://doi.org/10.1128/JCM.01022-08.

[8] P. Jain, B. Chakma, S. Patra, P. Goswami, Potential Biomarkers and Their Applications for Rapid and Reliable Detection of Malaria, Biomed Res. Int. 2014 (2014) 852645. https://doi.org/10.1155/2014/852645.

[9] R. Mayeux, Biomarkers: potential uses and limitations, NeuroRx. 1 (2004) 182–188. https://doi.org/10.1602/neurorx.1.2.182.

[10] V.B. Mathema, K. Na-Bangchang, A brief review on biomarkers and proteomic approach for malaria research, Asian Pac. J. Trop. Med. 8 (2015) 253–262. https://doi.org/https://doi.org/10.1016/S1995-7645(14)60327-8.

[11] H. Noedl, W.H. Wernsdorfer, R.S. Miller, C. Wongsrichanalai, Histidine-rich protein II: a novel approach to malaria drug sensitivity testing, Antimicrob. Agents Chemother. 46 (2002) 1658–1664. https://doi.org/10.1128/aac.46.6.1658-1664.2002.

[12] P. Pal, B.P. Daniels, A. Oskman, M.S. Diamond, R.S. Klein, D.E. Goldberg, Plasmodium falciparum Histidine-Rich Protein II Compromises Brain Endothelial Barriers and May Promote Cerebral Malaria Pathogenesis., MBio. 7 (2016). https://doi.org/10.1128/mBio.00617-16.

[13] M.E. Parra, C.B. Evans, D.W. Taylor, Identification of Plasmodium falciparum histidine-rich protein 2 in the plasma of humans with malaria, J. Clin. Microbiol. 29 (1991) 1629–1634. https://doi.org/10.1128/JCM.29.8.1629-1634.1991.

[14] V. Desakorn, A.M. Dondorp, K. Silamut, W. Pongtavornpinyo, D. Sahassananda, K. Chotivanich, P. Pitisuttithum, A.M. Smithyman, N.P.J. Day, N.J. White, Stage-dependent production and release of histidine-rich protein 2 by Plasmodium falciparum, Trans. R. Soc. Trop. Med. Hyg. 99 (2005) 517–524. https://doi.org/10.1016/j.trstmh.2004.11.014.

[15] D.J.J. Sullivan, I.Y. Gluzman, D.E. Goldberg, Plasmodium hemozoin formation mediated by histidine-rich proteins., Science. 271 (1996) 219–222. https://doi.org/10.1126/science.271.5246.219.

[16] E.P. Rock, K. Marsh, A.J. Saul, T.E. Wellems, D.W. Taylor, W.L. Maloy, R.J. Howard, Comparative analysis of the Plasmodium falciparum histidine-rich proteins HRP-I, HRP-II and HRP-III in malaria parasites of diverse origin., Parasitology. 95 (Pt 2) (1987) 209–227. https://doi.org/10.1017/s0031182000057681.

[17] C.F. Markwalter, K.M. Davis, D.W. Wright, Immunomagnetic capture and colorimetric

detection of malarial biomarker Plasmodium falciparum lactate dehydrogenase., Anal. Biochem. 493 (2016) 30–34. https://doi.org/10.1016/j.ab.2015.10.003.

[18] E.E. Dzakah, K. Kang, C. Ni, S. Tang, J. Wang, J. Wang, Comparative performance of aldolase and lactate dehydrogenase rapid diagnostic tests in Plasmodium vivax detection, Malar. J. 13 (2014) 272. https://doi.org/10.1186/1475-2875-13-272.

[19] R.M. Dirkzwager, A.B. Kinghorn, J.S. Richards, J.A. Tanner, APTEC: aptamer-tethered enzyme capture as a novel rapid diagnostic test for malaria., Chem. Commun. (Camb). 51 (2015) 4697–4700. https://doi.org/10.1039/c5cc00438a.

[20] D. Turgut-Balik, D.K. Shoemark, K.M. Moreton, R.B. Sessions, J.J. Holbrook, Over-production of lactate dehydrogenase from Plasmodium falciparum opens a route to new antimalarials, Biotechnol. Lett. 23 (2001) 917–921. https://doi.org/10.1023/A:1010555803606.

[21] S. Mohapatra, A. Ghosh, R. Singh, D.P. Singh, B. Sharma, J.C. Samantaray, M. Deb, R. Gaind, Hemozoin Pigment: An Important Tool for Low Parasitemic Malarial Diagnosis., Korean J. Parasitol. 54 (2016) 393–397. https://doi.org/10.3347/kjp.2016.54.4.393.

[22] T. Hänscheid, T. Carvalho, M.P. Grobusch, Hemozoin Detection for Human Malaria Diagnosis Investigated in Rodent Models: How Similar Is Similar?, Trends Parasitol. 32 (2016) 94–96. https://doi.org/10.1016/j.pt.2015.11.012.

[23] M. Olivier, K. Van Den Ham, M.T. Shio, F.A. Kassa, S. Fougeray, Malarial pigment hemozoin and the innate inflammatory response., Front. Immunol. 5 (2014) 25. https://doi.org/10.3389/fimmu.2014.00025.

[24] H. Döbeli, A. Trzeciak, D. Gillessen, H. Matile, I.K. Srivastava, L.H. Perrin, P.E. Jakob, U. Certa, Expression, purification, biochemical characterization and inhibition of recombinant Plasmodium falciparum aldolase, Mol. Biochem. Parasitol. 41 (1990) 259–268. https://doi.org/https://doi.org/10.1016/0166-6851(90)90189-S.

[25] N. Lee, J. Baker, D. Bell, J. McCarthy, Q. Cheng, Assessing the genetic diversity of the aldolase genes of Plasmodium falciparum and Plasmodium vivax and its potential effect on

performance of aldolase-detecting rapid diagnostic tests, J. Clin. Microbiol. 44 (2006) 4547–4549. https://doi.org/10.1128/JCM.01611-06.

[26] N. Cloonan, K. Fischer, Q. Cheng, A. Saul, Aldolase genes of Plasmodium species., Mol. Biochem. Parasitol. 113 (2001) 327–330. https://doi.org/10.1016/s0166-6851(01)00226-2.

[27] J. Maltha, P. Gillet, J. Jacobs, Malaria rapid diagnostic tests in endemic settings., Clin. Microbiol. Infect. Off. Publ. Eur. Soc. Clin. Microbiol. Infect. Dis. 19 (2013) 399–407. https://doi.org/10.1111/1469-0691.12151.

[28] K.G. Le Roch, J.R. Johnson, L. Florens, Y. Zhou, A. Santrosyan, M. Grainger, S.F. Yan, K.C. Williamson, A.A. Holder, D.J. Carucci, J.R. 3rd Yates, E.A. Winzeler, Global analysis of transcript and protein levels across the Plasmodium falciparum life cycle., Genome Res. 14 (2004) 2308–2318. https://doi.org/10.1101/gr.2523904.

[29] J.C. Mouatcho, J.P.D. Goldring, Malaria rapid diagnostic tests: challenges and prospects., J. Med. Microbiol. 62 (2013) 1491–1505. https://doi.org/10.1099/jmm.0.052506-0.

[30] N.K. Singh, S.K. Arya, P. Estrela, P. Goswami, Capacitive malaria aptasensor using Plasmodium falciparum glutamate dehydrogenase as target antigen in undiluted human serum, Biosens. Bioelectron. 117 (2018) 246–252. https://doi.org/10.1016/j.bios.2018.06.022.

[31] N.K. Singh, B. Chakma, P. Jain, P. Goswami, Protein-Induced Fluorescence Enhancement Based Detection of Plasmodium falciparum Glutamate Dehydrogenase Using Carbon Dot Coupled Specific Aptamer, ACS Comb. Sci. 20 (2018) 350–357. https://doi.org/10.1021/acscombsci.8b00021.

[32] N.K. Singh, P.D. Thungon, P. Estrela, P. Goswami, Development of an aptamer-based field effect transistor biosensor for quantitative detection of Plasmodium falciparum glutamate dehydrogenase in serum samples, Biosens. Bioelectron. 123 (2019) 30–35. https://doi.org/https://doi.org/10.1016/j.bios.2018.09.085.

[33] J. Storm, J. Perner, I. Aparicio, E.-M. Patzewitz, K. Olszewski, M. Llinas, P.C. Engel, S. Müller, Plasmodium falciparum glutamate dehydrogenase a is dispensable and not a drug

target during erythrocytic development, Malar. J. 10 (2011) 193. https://doi.org/10.1186/1475-2875-10-193.

[34] M.L. Wilson, Laboratory diagnosis of malaria: conventional and rapid diagnostic methods., Arch. Pathol. Lab. Med. 137 (2013) 805–811. https://doi.org/10.5858/arpa.2011-0602-RA.

[35] A. Mbanefo, N. Kumar, Evaluation of Malaria Diagnostic Methods as a Key for Successful Control and Elimination Programs, Trop. Med. Infect. Dis. 5 (2020) 102. https://doi.org/10.3390/tropicalmed5020102.

[36] S.L. Rei Yan, F. Wakasuqui, C. Wrenger, Point-of-care tests for malaria: speeding up the diagnostics at the bedside and challenges in malaria cases detection, Diagn. Microbiol. Infect. Dis. 98 (2020) 115122. https://doi.org/https://doi.org/10.1016/j.diagmicrobio.2020.115122.

[37] S.N. Mukry, M. Saud, G. Sufaida, K. Shaikh, A. Naz, T.S. Shamsi, Laboratory Diagnosis of Malaria: Comparison of Manual and Automated Diagnostic Tests., Can. J. Infect. Dis. Med. Microbiol. = J. Can. Des Mal. Infect. La Microbiol. Medicale. 2017 (2017) 9286392. https://doi.org/10.1155/2017/9286392.

[38] S. Kasetsirikul, J. Buranapong, W. Srituravanich, M. Kaewthamasorn, A. Pimpin, The development of malaria diagnostic techniques: a review of the approaches with focus on dielectrophoretic and magnetophoretic methods, Malar. J. 15 (2016) 358. https://doi.org/10.1186/s12936-016-1400-9.

[39] N. Steenkeste, W.O. Rogers, L. Okell, I. Jeanne, S. Incardona, L. Duval, S. Chy, S. Hewitt, M. Chou, D. Socheat, F.-X. Babin, F. Ariey, C. Rogier, Sub-microscopic malaria cases and mixed malaria infection in a remote area of high malaria endemicity in Rattanakiri province, Cambodia: implication for malaria elimination, Malar. J. 9 (2010) 108. https://doi.org/10.1186/1475-2875-9-108.

[40] H. Hopkins, I.J. González, S.D. Polley, P. Angutoko, J. Ategeka, C. Asiimwe, B. Agaba, D.J. Kyabayinze, C.J. Sutherland, M.D. Perkins, D. Bell, Highly sensitive detection of malaria parasitemia in a malaria-endemic setting: performance of a new loop-mediated isothermal amplification kit in a remote clinic in Uganda., J. Infect. Dis. 208 (2013) 645–

652. https://doi.org/10.1093/infdis/jit184.

[41] R. Davis, T. Flanigan, E. Wilson, Passive gravitational sedimentation of peripheral blood increases the sensitivity of microscopic detection of malaria., Asian Pac. J. Trop. Med. 6 (2013) 552–555. https://doi.org/10.1016/S1995-7645(13)60095-4.

[42] P. Berzosa, A. de Lucio, M. Romay-Barja, Z. Herrador, V. González, L. García, A. Fernández-Martínez, M. Santana-Morales, P. Ncogo, B. Valladares, M. Riloha, A. Benito, Comparison of three diagnostic methods (microscopy, RDT, and PCR) for the detection of malaria parasites in representative samples from Equatorial Guinea., Malar. J. 17 (2018) 333. https://doi.org/10.1186/s12936-018-2481-4.

[43] J.T. Coulibaly, M. Ouattara, J. Keiser, B. Bonfoh, E.K. N'Goran, J.R. Andrews, I.I. Bogoch, Evaluation of Malaria Diagnoses Using a Handheld Light Microscope in a Community-Based Setting in Rural Côte d'Ivoire, Am. Soc. Trop. Med. Hyg. 95 (n.d.) 831–834. https://doi.org/10.4269/ajtmh.16-0328.

[44] R. Hathiwala, P.R. Mehta, G. Nataraj, S. Hathiwala, LED fluorescence microscopy: Novel method for malaria diagnosis compared with routine methods., J. Infect. Public Health. 10 (2017) 824–828. https://doi.org/10.1016/j.jiph.2017.01.001.

[45] C.W. Pirnstill, G.L. Coté, Malaria Diagnosis Using a Mobile Phone Polarized Microscope, Sci. Rep. 5 (2015) 13368. https://doi.org/10.1038/srep13368.

[46] D.N. Breslauer, R.N. Maamari, N.A. Switz, W.A. Lam, D.A. Fletcher, Mobile Phone Based Clinical Microscopy for Global Health Applications, PLoS One. 4 (2009) e6320. https://doi.org/10.1371/journal.pone.0006320.

[47] G. Dutta, S. Nagarajan, L.J. Lapidus, P.B. Lillehoj, Enzyme-free electrochemical immunosensor based on methylene blue and the electro-oxidation of hydrazine on Pt nanoparticles, Biosens. Bioelectron. 92 (2017) 372–377. https://doi.org/10.1016/j.bios.2016.10.094.

[48] N. Bhalla, Y. Pan, Z. Yang, A.F. Payam, Opportunities and Challenges for Biosensors and Nanoscale Analytical Tools for Pandemics: COVID-19, ACS Nano. 14 (2020) 7783–7807.

https://doi.org/10.1021/acsnano.0c04421.

[49] S. Shrivastava, N. Jadon, R. Jain, Next-generation polymer nanocomposite-based electrochemical sensors and biosensors: A review, TrAC Trends Anal. Chem. 82 (2016) 55–67. https://doi.org/https://doi.org/10.1016/j.trac.2016.04.005.

[50] B. John, Polymer Nanocomposite-Based Electrochemical Sensors and Biosensors, Nanorods and Nanocomposites. (2020). https://doi.org/10.5772/intechopen.86826.

[51] X. Luo, A. Morrin, A.J. Killard, M.R. Smyth, Application of Nanoparticles in Electrochemical Sensors and Biosensors, Electroanalysis. 18 (2006) 319–326. https://doi.org/https://doi.org/10.1002/elan.200503415.

[52] U. Hanefeld, L. Gardossi, E. Magner, Understanding enzyme immobilisation., Chem. Soc. Rev. 38 (2009) 453–468. https://doi.org/10.1039/b711564b.

[53] W. Putzbach, N.J. Ronkainen, Immobilization techniques in the fabrication of nanomaterial-based electrochemical biosensors: a review., Sensors (Basel). 13 (2013) 4811–4840. https://doi.org/10.3390/s130404811.

[54] R. Batool, A. Rhouati, M.H. Nawaz, A. Hayat, J.L. Marty, A Review of the Construction of Nano-Hybrids for Electrochemical Biosensing of Glucose, Biosens. . 9 (2019). https://doi.org/10.3390/bios9010046.

[55] P. Singh, M. Chatterjee, K. Chatterjee, R.K. Arun, N. Chanda, Design of a point-of-care device for electrochemical detection of P.vivax infected-malaria using antibody functionalized rGO-gold nanocomposite, Sensors Actuators, B Chem. 327 (2021) 128860. https://doi.org/10.1016/j.snb.2020.128860.

[56] G. Figueroa-Miranda, L. Feng, S.C.-C. Shiu, R.M. Dirkzwager, Y.-W. Cheung, J.A. Tanner, M.J. Schöning, A. Offenhäusser, D. Mayer, Aptamer-based electrochemical biosensor for highly sensitive and selective malaria detection with adjustable dynamic response range and reusability, Sensors Actuators B Chem. 255 (2018) 235–243. https://doi.org/https://doi.org/10.1016/j.snb.2017.07.117.

[57] P. Jain, S. Das, B. Chakma, P. Goswami, Aptamer-graphene oxide for highly sensitive dual

electrochemical detection of Plasmodium lactate dehydrogenase, Anal. Biochem. 514 (2016) 32–37. https://doi.org/10.1016/j.ab.2016.09.013.

[58] G. Ruiz-Vega, K. Arias-Alpízar, E. de la Serna, L.N. Borgheti-Cardoso, E. Sulleiro, I. Molina, X. Fernàndez-Busquets, A. Sánchez-Montalvá, F.J. del Campo, E. Baldrich, Electrochemical POC device for fast malaria quantitative diagnosis in whole blood by using magnetic beads, Poly-HRP and microfluidic paper electrodes, Biosens. Bioelectron. 150 (2020). https://doi.org/10.1016/j.bios.2019.111925.

[59] P.B. Lillehoj, M.-C. Huang, N. Truong, C.-M. Ho, Rapid electrochemical detection on a mobile phone, Lab Chip. 13 (2013) 2950–2955. https://doi.org/10.1039/C3LC50306B.

[60] B. Sikarwar, P.K. Sharma, A. Srivastava, G.S. Agarwal, M. Boopathi, B. Singh, Y.K. Jaiswal, Surface plasmon resonance characterization of monoclonal and polyclonal antibodies of malaria for biosensor applications, Biosens. Bioelectron. 60 (2014) 201–209. https://doi.org/10.1016/j.bios.2014.04.025.

[61] M. De Souza Castilho, T. Laube, H. Yamanaka, S. Alegret, M.I. Pividori, Magneto immunoassays for plasmodium falciparum histidine-rich protein 2 related to malaria based on magnetic nanoparticles, Anal. Chem. 83 (2011) 5570–5577. https://doi.org/10.1021/ac200573s.

[62] G. Dutta, S. Nagarajan, L.J. Lapidus, P.B. Lillehoj, Enzyme-free electrochemical immunosensor based on methylene blue and the electro-oxidation of hydrazine on Pt nanoparticles, Biosens. Bioelectron. 92 (2017) 372–377. https://doi.org/https://doi.org/10.1016/j.bios.2016.10.094.

[63] A. Hemben, J. Ashley, I.E. Tothill, Development of an Immunosensor for Pf HRP 2 as a biomarker for malaria detection, Biosensors. 7 (2017) 28. https://doi.org/10.3390/bios7030028.

[64] B. Chakma, P. Jain, N.K. Singh, P. Goswami, Development of Electrochemical Impedance Spectroscopy Based Malaria Aptasensor Using HRP-II as Target Biomarker, Electroanalysis. 30 (2018) 1839–1846. https://doi.org/10.1002/elan.201800142.

[65] G. Dutta, P.B. Lillehoj, Wash-free, label-free immunoassay for rapid electrochemical detection of PfHRP2 in whole blood samples, Sci. Rep. 8 (2018) 1–8. https://doi.org/10.1038/s41598-018-35471-8.

[66] S. Lee, K.M. Song, W. Jeon, H. Jo, Y.B. Shim, C. Ban, A highly sensitive aptasensor towards Plasmodium lactate dehydrogenase for the diagnosis of malaria, Biosens. Bioelectron. 35 (2012) 291–296. https://doi.org/10.1016/j.bios.2012.03.003.

[67] A. Hemben, J. Ashley, I.E. Tothill, An immunosensor for parasite lactate dehydrogenase detection as a malaria biomarker – Comparison with commercial test kit, Talanta. 187 (2018) 321–329. https://doi.org/10.1016/j.talanta.2018.04.086.

[68] A. Nemiroski, D.C. Christodouleas, J.W. Hennek, A.A. Kumar, E.J. Maxwell, M.T. Fernández-Abedul, G.M. Whitesides, Universal mobile electrochemical detector designed for use in resource-limited applications, Proc. Natl. Acad. Sci. U. S. A. 111 (2014) 11984–11989. https://doi.org/10.1073/pnas.1405679111.

[69] B. Paul, A.K. Panigrahi, V. Singh, S.G. Singh, A multi-walled carbon nanotube-zinc oxide nanofiber based flexible chemiresistive biosensor for malaria biomarker detection, Analyst. 142 (2017) 2128–2135. https://doi.org/10.1039/c7an00243b.

[70] C.M. Silveira, T. Monteiro, M.G. Almeida, Biosensing with Paper-Based Miniaturized Printed Electrodes–A Modern Trend, Biosens. . 6 (2016). https://doi.org/10.3390/bios6040051.

[71] C.S. Kosack, A.L. Page, P.R. Klatser, A guide to aid the selection of diagnostic tests, Bull. World Health Organ. 95 (2017) 639–645. https://doi.org/10.2471/BLT.16.187468.

[72] Q.H. Nguyen, M. Il Kim, Nanomaterial-mediated paper-based biosensors for colorimetric pathogen detection, Trends Analyt. Chem. 132 (2020) 116038. https://doi.org/10.1016/j.trac.2020.116038.

[73] B. Liu, J. Zhuang, G. Wei, Recent advances in the design of colorimetric sensors for environmental monitoring, Environ. Sci. Nano. 7 (2020) 2195–2213. https://doi.org/10.1039/D0EN00449A.

[74] W. Jeon, S. Lee, D.H. Manjunatha, C. Ban, A colorimetric aptasensor for the diagnosis of malaria based on cationic polymers and gold nanoparticles., Anal. Biochem. 439 (2013) 11–16. https://doi.org/10.1016/j.ab.2013.03.032.

[75] S. Lee, D.H. Manjunatha, W. Jeon, C. Ban, Cationic Surfactant-Based Colorimetric Detection of Plasmodium Lactate Dehydrogenase, a Biomarker for Malaria, Using the Specific DNA Aptamer, PLoS One. 9 (2014) e100847. https://doi.org/10.1371/journal.pone.0100847.

[76] P. Jain, B. Chakma, N.K. Singh, S. Patra, P. Goswami, Aromatic Surfactant as Aggregating Agent for Aptamer-Gold Nanoparticle-Based Detection of Plasmodium Lactate Dehydrogenase, Mol. Biotechnol. 58 (2016) 497–508. https://doi.org/10.1007/s12033-016-9946-x.

[77] R.M. Dirkzwager, S. Liang, J.A. Tanner, Development of Aptamer-Based Point-of-Care Diagnostic Devices for Malaria Using Three-Dimensional Printing Rapid Prototyping, ACS Sensors. 1 (2016) 420–426. https://doi.org/10.1021/acssensors.5b00175.

[78] E. Gikunoo, A. Abera, E. Woldesenbet, A novel carbon Nanofibers grown on glass microballoons immunosensor: A tool for early diagnosis of Malaria, Sensors (Switzerland). 14 (2014) 14686–14699. https://doi.org/10.3390/s140814686.

[79] WHO, WHO Global Surveillance and Monitoring System for substandard and falsified medical products, Geneva, 2017. https://www.who.int/medicines/regulation/ssffc/publications/gsms-report-sf/en/.

[80] E.A. Blackstone, J.P.J. Fuhr, S. Pociask, The health and economic effects of counterfeit drugs., Am. Heal. Drug Benefits. 7 (2014) 216–224.

[81] P. Newton, S. Proux, M. Green, F. Smithuis, J. Rozendaal, S. Prakongpan, K. Chotivanich, M. Mayxay, S. Looareesuwan, J. Farrar, F. Nosten, N.J. White, Fake artesunate in southeast Asia., Lancet (London, England). 357 (2001) 1948–1950. https://doi.org/10.1016/S0140-6736(00)05085-6.

[82] S. Sengaloundeth, M.D. Green, F.M. Fernández, O. Manolin, K. Phommavong, V.

Insixiengmay, C.Y. Hampton, L. Nyadong, D.C. Mildenhall, D. Hostetler, L. Khounsaknalath, L. Vongsack, S. Phompida, V. Vanisaveth, L. Syhakhang, P.N. Newton, A stratified random survey of the proportion of poor quality oral artesunate sold at medicine outlets in the Lao PDR - implications for therapeutic failure and drug resistance., Malar. J. 8 (2009) 172. https://doi.org/10.1186/1475-2875-8-172.

[83] K. Kaur, M. Jain, R.P. Reddy, R. Jain, Quinolines and structurally related heterocycles as antimalarials, Eur. J. Med. Chem. 45 (2010) 3245–3264. https://doi.org/https://doi.org/10.1016/j.ejmech.2010.04.011.

[84] S. Kapishnikov, T. Staalsø, Y. Yang, J. Lee, A.J. Pérez-Berná, E. Pereiro, Y. Yang, S. Werner, P. Guttmann, L. Leiserowitz, J. Als-Nielsen, Mode of action of quinoline antimalarial drugs in red blood cells infected by Plasmodium falciparum revealed in vivo, Proc. Natl. Acad. Sci. 116 (2019) 22946 LP – 22952. https://doi.org/10.1073/pnas.1910123116.

[85] A. Sharma, N.C. Mishra, Inhibition of a protein tyrosine kinase activity in Plasmodium falciparum by chloroquine., Indian J. Biochem. Biophys. 36 (1999) 299–304.

[86] M. Kubo, K.Y. Hostetler, Mechanism of cationic amphiphilic drug inhibition of purified lysosomal phospholipase A1, Biochemistry. 24 (1985) 6515–6520. https://doi.org/10.1021/bi00344a031.

[87] M. Srivastava, P. Tiwari, V.K. Mall, S.K. Srivastava, R. Prakash, Voltammetric determination of the antimalarial drug chloroquine using a glassy carbon electrode modified with reduced graphene oxide on WS2 quantum dots, Microchim. Acta. 186 (2019). https://doi.org/10.1007/s00604-019-3525-3.

[88] F. Azadmehr, K. Zarei, Fabrication of an imprinted electrochemical sensor from L-tyrosine, 3-methyl-4-nitrophenol and gold nanoparticles for quinine determination, Bioelectrochemistry. 127 (2019) 59–67. https://doi.org/10.1016/j.bioelechem.2019.01.001.

[89] T.E. Chiwunze, N.B. Thapliyal, V.N. Palakollu, R. Karpoormath, A Simple, Efficient and Ultrasensitive Gold Nanourchin Based Electrochemical Sensor for the Determination of an Antimalarial Drug: Mefloquine, Electroanalysis. 29 (2017) 2138–2146.

https://doi.org/doi:10.1002/elan.201700154.

[90] O.P.S. Patel, R.M. Beteck, L.J. Legoabe, Exploration of artemisinin derivatives and synthetic peroxides in antimalarial drug discovery research, Eur. J. Med. Chem. 213 (2021) 113193. https://doi.org/https://doi.org/10.1016/j.ejmech.2021.113193.

[91] M.A. Corsello, N.K. Garg, Synthetic chemistry fuels interdisciplinary approaches to the production of artemisinin., Nat. Prod. Rep. 32 (2015) 359–366. https://doi.org/10.1039/c4np00113c.

[92] L.Y. Kong, R.X. Tan, Artemisinin, a miracle of traditional Chinese medicine., Nat. Prod. Rep. 32 (2015) 1617–1621. https://doi.org/10.1039/c5np00133a.

[93] D.H.J. Cheong, D.W.S. Tan, F.W.S. Wong, T. Tran, Anti-malarial drug, artemisinin and its derivatives for the treatment of respiratory diseases, Pharmacol. Res. 158 (2020) 104901. https://doi.org/https://doi.org/10.1016/j.phrs.2020.104901.

[94] C. Wang, Y.T. Zholudov, A. Nsabimana, G. Xu, J. Li, Sensitive and selective electrochemical detection of artemisinin based on its reaction with p-aminophenylboronic acid, Anal. Chim. Acta. 937 (2016) 39–42. https://doi.org/https://doi.org/10.1016/j.aca.2016.07.026.

[95] H. Bai, C. Wang, J. Chen, J. Peng, Q. Cao, A novel sensitive electrochemical sensor based on in-situ polymerized molecularly imprinted membranes at graphene modified electrode for artemisinin determination, Biosens. Bioelectron. 64 (2015) 352–358. https://doi.org/https://doi.org/10.1016/j.bios.2014.09.034.

[96] T. Jiang, X. Sun, L. Wei, M. Li, Electrochemical determination of artemisinin based on signal inhibition for the reduction of hemin, Anal. Bioanal. Chem. 413 (2021) 565–576. https://doi.org/10.1007/s00216-020-03028-2.

[97] Y. Yuthavong, Antifolate Drugs BT - Encyclopedia of Malaria, in: M. Hommel, P.G. Kremsner (Eds.), Springer New York, New York, NY, 2021: pp. 1–12. https://doi.org/10.1007/978-1-4614-8757-9_2-1.

[98] A. Gregson, C. V Plowe, Mechanisms of resistance of malaria parasites to antifolates.,

Pharmacol. Rev. 57 (2005) 117–145. https://doi.org/10.1124/pr.57.1.4.

[99] Z. Nate, A.A.S. Gill, R. Chauhan, R. Karpoormath, Polyaniline-cobalt oxide nanofibers for simultaneous electrochemical determination of antimalarial drugs: Primaquine and proguanil, Microchem. J. 160 (2021) 105709. https://doi.org/10.1016/j.microc.2020.105709.

[100] F.M. Abdel-Haleem, M. Saad, M.S. Rizk, Development of new potentiometric sensors for the determination of proguanil hydrochloride in serum and urine, Chinese Chem. Lett. 27 (2016) 857–863. https://doi.org/https://doi.org/10.1016/j.cclet.2016.01.027.

[101] Z. Xu, X. Jiang, S. Liu, M. Yang, Sensitive and selective molecularly imprinted electrochemical sensor based on multi-walled carbon nanotubes for doxycycline hyclate determination, Chinese Chem. Lett. 31 (2020) 185–188. https://doi.org/https://doi.org/10.1016/j.cclet.2019.04.026.

[102] B. Gürler, S.P. Özkorucuklu, E. Kir, Voltammetric behavior and determination of doxycycline in pharmaceuticals at molecularly imprinted and non-imprinted overoxidized polypyrrole electrodes, J. Pharm. Biomed. Anal. 84 (2013) 263–268. https://doi.org/10.1016/j.jpba.2013.06.009.

[103] Z. Zhang, Y. Hu, H. Zhang, S. Yao, Novel layer-by-layer assembly molecularly imprinted sol-gel sensor for selective recognition of clindamycin based on Au electrode decorated by multi-wall carbon nanotube, J. Colloid Interface Sci. 344 (2010) 158–164. https://doi.org/10.1016/j.jcis.2009.12.022.

[104] A. Wong, C.A. Razzino, T.A. Silva, O. Fatibello-Filho, Square-wave voltammetric determination of clindamycin using a glassy carbon electrode modified with graphene oxide and gold nanoparticles within a crosslinked chitosan film, Sensors Actuators, B Chem. 231 (2016) 183–193. https://doi.org/10.1016/j.snb.2016.03.014.

[105] A. Geto, M. Amare, M. Tessema, S. Admassie, Polymer-modified glassy carbon electrode for the electrochemical detection of quinine in human urine and pharmaceutical formulations, Anal. Bioanal. Chem. 404 (2012) 525–530. https://doi.org/10.1007/s00216-012-6171-8.

[106] S. Awasthi, A. Srivastava, M.L. Singla, Voltammetric determination of citric acid and quinine hydrochloride using polypyrrole-pentacyanonitrosylferrate/platinum electrode, Synth. Met. 161 (2011) 1707–1712. https://doi.org/10.1016/j.synthmet.2011.06.009.

[107] R.A. Dar, P.K. Brahman, S. Tiwari, K.S. Pitre, Electrochemical studies of quinine in surfactant media using hanging mercury drop electrode: A cyclic voltammetric study, Colloids Surfaces B Biointerfaces. 98 (2012) 72–79. https://doi.org/10.1016/j.colsurfb.2012.04.035.

[108] M. Buleandra, A.A. Rabinca, M.C. Cheregi, A.A. Ciucu, Rapid voltammetric method for quinine determination in soft drinks, Food Chem. 253 (2018) 1–4. https://doi.org/10.1016/j.foodchem.2018.01.130.

[109] L. Liu, X. Tan, X. Fang, Y. Sun, F. Lei, Z. Huang, Electrochemical Sensor Based on Molecularly Imprinted Polymer Film Prepared with Functional Abietic-Type Acids as Cross-Linker for the Determination of Quinine, Electroanalysis. 24 (2012) 1647–1654. https://doi.org/10.1002/elan.201200085.

[110] X.M. Zhan, L.H. Liu, Z.N. Gao, Electrocatalytic oxidation of quinine sulfate at a multiwall carbon nanotubes-ionic liquid modified glassy carbon electrode and its electrochemical determination, J. Solid State Electrochem. 15 (2011) 1185–1192. https://doi.org/10.1007/s10008-010-1184-8.

[111] G.G. Oliveira, D.C. Azzi, T.A. Silva, P.R. de Oliveira, O. Fatibello-Filho, B.C. Janegitz, Sensitive Voltammetric Detection of Chloroquine Drug by Applying a Boron-Doped Diamond Electrode, C. 6 (2020) 75. https://doi.org/10.3390/c6040075.

[112] A. Radi, Accumulation and trace measurement of chloroquine drug at DNA-modified carbon paste electrode, Talanta. 65 (2005) 271–275. https://doi.org/10.1016/j.talanta.2004.05.024.

[113] M.H. Mashhadizadeh, M. Akbarian, Voltammetric determination of some anti-malarial drugs using a carbon paste electrode modified with Cu(OH)2 nano-wire, Talanta. 78 (2009) 1440–1445. https://doi.org/https://doi.org/10.1016/j.talanta.2009.02.040.

[114] T.E. Chiwunze, N.B. Thapliyal, V.N. Palakollu, R. Karpoormath, A Simple, Efficient and Ultrasensitive Gold Nanourchin Based Electrochemical Sensor for the Determination of an Antimalarial Drug: Mefloquine, Electroanalysis. 29 (2017) 2138–2146. https://doi.org/https://doi.org/10.1002/elan.201700154.

[115] B. Uslu, B. Doğan, S.A. Özkan, H.Y. Aboul-Enein, Voltammetric investigation and determination of mefloquine, Electroanalysis. 17 (2005) 1563–1570. https://doi.org/10.1002/elan.200403255.

[116] M.J. Pedrozo-Peñafiel, J.M.S. Almeida, C.A.T. Toloza, D.G. Larrudé, W.F. Pacheco, R.Q. Aucelio, Square-wave voltammetric determination of primaquine in urine using a multi-walled carbon nanotube modified electrode, Microchem. J. 150 (2019) 104201. https://doi.org/10.1016/j.microc.2019.104201.

[117] N.B. Thapliyal, T.E. Chiwunze, R. Karpoormath, S. Cherukupalli, Fabrication of highly sensitive gold nanourchins based electrochemical sensor for nanomolar determination of primaquine, Mater. Sci. Eng. C. 74 (2017) 27–35. https://doi.org/10.1016/j.msec.2016.12.126.

[118] M.L.P.M. Arguelho, M.V.B. Zanoni, N.R. Stradiotto, Electrochemical Oxidation and Voltammetric Determination of the Antimalaria Drug Primaquine, Anal. Lett. 38 (2005) 1415–1425. https://doi.org/10.1081/AL-200062218.

[119] B.B. Prasad, A. Kumar, R. Singh, Molecularly imprinted polymer-based electrochemical sensor using functionalized fullerene as a nanomediator for ultratrace analysis of primaquine, Carbon N. Y. 109 (2016) 196–207. https://doi.org/10.1016/j.carbon.2016.07.044.

[120] S. Karakaya, B. Kartal, Y. Dilgin, Ultrasensitive voltammetric detection of an antimalarial drug (amodiaquine) at a disposable and low cost electrode, Monatshefte Fur Chemie. 151 (2020) 1019–1026. https://doi.org/10.1007/s00706-020-02637-y.

[121] T.E. Chiwunze, V.N. Palakollu, A.A.S. Gill, F. Kayamba, N.B. Thapliyal, R. Karpoormath, A highly dispersed multi-walled carbon nanotubes and poly(methyl orange) based electrochemical sensor for the determination of an anti-malarial drug: Amodiaquine., Mater.

Sci. Eng. C. Mater. Biol. Appl. 97 (2019) 285–292. https://doi.org/10.1016/j.msec.2018.12.018.

[122] C.O. Valente, C.A.B. Garcia, J.P.H. Alves, M.V.B. Zanoni, N.R. Stradiotto, M.L.P. Arguelho, Electrochemical Determination of Antimalarial Drug Amodiaquine in Maternal Milk Using a Hemin-Based Electrode, ECS Trans. 43 (2019) 297–304. https://doi.org/10.1149/1.4704970.

[123] T.K. Malongo, B. Blankert, O. Kambu, K. Amighi, J. Nsangu, J.M. Kauffmann, Amodiaquine polymeric membrane electrode, J. Pharm. Biomed. Anal. 41 (2006) 70–76. https://doi.org/10.1016/j.jpba.2005.10.014.

[124] A.F.T. Waffo, C. Yesildag, G. Caserta, S. Katz, I. Zebger, M.C. Lensen, U. Wollenberger, F.W. Scheller, Z. Altintas, Fully electrochemical MIP sensor for artemisinin, Sensors Actuators, B Chem. 275 (2018) 163–173. https://doi.org/10.1016/j.snb.2018.08.018.

[125] P. Phukon, K. Radhapyari, B.K. Konwar, R. Khan, Natural polyhydroxyalkanoate-gold nanocomposite based biosensor for detection of antimalarial drug artemisinin, Mater. Sci. Eng. C. 37 (2014) 314–320. https://doi.org/10.1016/j.msec.2014.01.019.

[126] H. Bai, C. Wang, J. Chen, J. Peng, Q. Cao, A novel sensitive electrochemical sensor based on in-situ polymerized molecularly imprinted membranes at graphene modified electrode for artemisinin determination, Biosens. Bioelectron. 64 (2015) 352–358. https://doi.org/10.1016/j.bios.2014.09.034.

[127] C. Wang, Y.T. Zholudov, A. Nsabimana, G. Xu, J. Li, Sensitive and selective electrochemical detection of artemisinin based on its reaction with p-aminophenylboronic acid, Anal. Chim. Acta. 937 (2016) 39–42. https://doi.org/10.1016/j.aca.2016.07.026.

[128] F.C. Gong, Z.D. Xiao, Z. Cao, D.X. Wu, A selective artemisinin-sensor using metalloporphyrin as a recognition element entrapped in the Au-nanoparticles-chitosan modified electrodes, Talanta. 72 (2007) 1453–1457. https://doi.org/10.1016/j.talanta.2007.01.056.

[129] J.R.M. Reys, P.R. Lima, A.G. Cioletti, A.S. Ribeiro, F.C. de Abreu, M.O.F. Goulart, L.T.

Kubota, An amperometric sensor based on hemin adsorbed on silica gel modified with titanium oxide for electrocatalytic reduction and quantification of artemisinin, Talanta. 77 (2008) 909–914. https://doi.org/10.1016/j.talanta.2008.07.043.

[130] T. Jiang, X. Sun, L. Wei, M. Li, Electrochemical determination of artemisinin based on signal inhibition for the reduction of hemin, Anal. Bioanal. Chem. 413 (2021) 565–576. https://doi.org/10.1007/s00216-020-03028-2.

[131] K. Radhapyari, P. Kotoky, M.R. Das, R. Khan, Graphene-polyaniline nanocomposite based biosensor for detection of antimalarial drug artesunate in pharmaceutical formulation and biological fluids, Talanta. 111 (2013) 47–53. https://doi.org/10.1016/j.talanta.2013.03.020.

[132] R. Jain, Vikas, Voltammetric behaviour of antimalarial drug artesunate in solubilized systems, Colloids Surfaces B Biointerfaces. 88 (2011) 729–733. https://doi.org/10.1016/j.colsurfb.2011.08.008.

[133] Z. Nate, A.A.S. Gill, S. Shinde, R. Chauhan, S.N. Inamdar, R. Karpoormath, A simple in-situ flame synthesis of nanocomposite (MWCNTs-Fe2O3) for electrochemical sensing of proguanil in pharmaceutical formulation, Diam. Relat. Mater. 111 (2020) 108178. https://doi.org/10.1016/j.diamond.2020.108178.

[134] S. Smarzewska, S. Skrzypek, W. Ciesielski, Voltammetric Determination of Proguanil in Malarone and Spiked Urine with a Renewable Silver Amalgam Film Electrode, Electroanalysis. 24 (2012) 1966–1972. https://doi.org/10.1002/elan.201200312.

[135] N.M. Gokavi, S.T. Nandibewoor, Voltammetric determination of sulfadoxine and its application in pharmaceuticals and urine samples, Anal. Bioanal. Chem. Res. 2 (2015) 119–128. https://doi.org/10.22036/abcr.2015.11540.

[136] N. Thammasoontaree, P. Rattanarat, N. Ruecha, W. Siangproh, N. Rodthongkum, O. Chailapakul, Ultra-performance liquid chromatography coupled with graphene/polyaniline nanocomposite modified electrode for the determination of sulfonamide residues, Talanta. 123 (2014) 115–121. https://doi.org/10.1016/j.talanta.2014.02.004.

[137] T.A. Ali, G.G. Mohamed, A.Z. El-Sonbati, M.A. Diab, A.M. Elkfass, A Potentiometric

Sensor for Determination of Doxycycline Hydrochloride in Pharmaceutical Preparation and Biological Fluids, Russ. J. Electrochem. 54 (2018) 1081–1095. https://doi.org/10.1134/S1023193518120029.

[138] Z. Xu, X. Jiang, S. Liu, M. Yang, Sensitive and selective molecularly imprinted electrochemical sensor based on multi-walled carbon nanotubes for doxycycline hyclate determination, Chinese Chem. Lett. 31 (2019) 185–188. https://doi.org/10.1016/j.cclet.2019.04.026.

[139] I.H.I. Habib, M.S. Rizk, T.R. El-Aryan, Determination of clindamycin in dosage forms and biological samples by adsorption stripping voltammetry with carbon paste electrode, Pharm. Chem. J. 44 (2011) 705–710. https://doi.org/10.1007/s11094-011-0548-4.

[140] M. Hadi, E. Honarmand, Application of anodized edge-plane pyrolytic graphite electrode for analysis of clindamycin in pharmaceutical formulations and human urine samples, Russ. J. Electrochem. 53 (2017) 380–390. https://doi.org/10.1134/S1023193517040061.

CHAPTER THREE

A simple *In-situ* flame synthesis of nanocomposite (MWCNTs-Fe_2O_3) for electrochemical sensing of proguanil in pharmaceutical formulation

Graphical Abstract

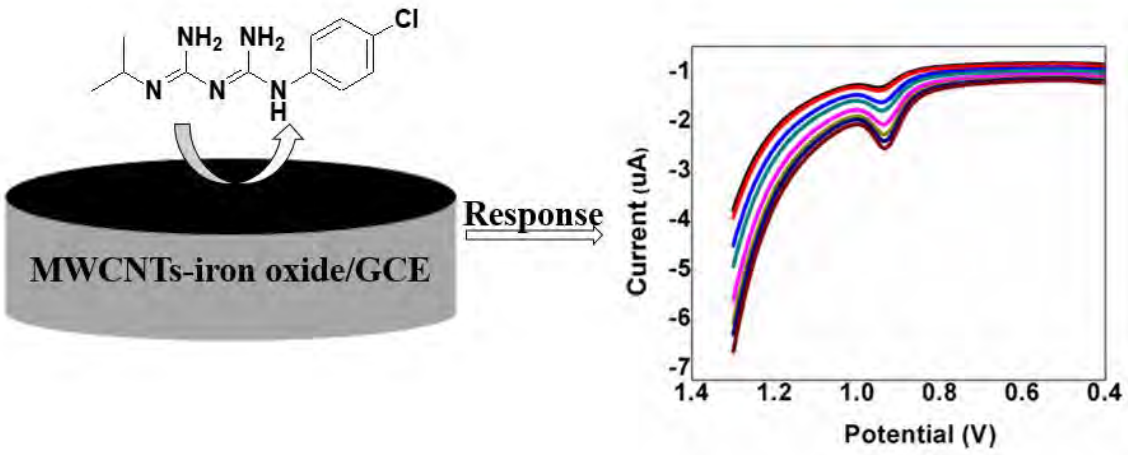

ARTICLE IN PRESS

Diamond & Related Materials xxx (xxxx) xxx

Contents lists available at ScienceDirect

Diamond & Related Materials

journal homepage: www.elsevier.com/locate/diamond

A simple in-situ flame synthesis of nanocomposite (MWCNTs-Fe_2O_3) for electrochemical sensing of proguanil in pharmaceutical formulation

Zondi Nate, Atal A.S. Gill, Suraj Shinde, Ruchika Chauhan, Shaukatali N. Inamdar, Rajshekhar Karpoormath*

Department of Pharmaceutical Chemistry, College of Health Sciences, University of KwaZulu Natal, Westville Campus, Durban 4000, South Africa

ARTICLE INFO

Keywords:
Proguanil
Carbon nanotubes
Iron oxide nanoparticles
Flame synthesis
Differential pulse voltammetry

ABSTRACT

Multiwall carbon nanotubes incorporated with iron oxide nanoparticles (MWCNTs-iron oxide) were prepared using a cheap, facile in-situ flame synthesis method. The nanocomposites were characterized using scanning electron microscopy, energy-dispersive X-ray spectroscopy, transmission electron microscopy, X-ray powder diffractometry, and Raman spectroscopy. MWCNTs-iron oxide nanocomposite was used to fabricate a sensitive electrochemical sensor for the detection and quantification of proguanil. The fabrication of the sensor was done by modifying a glassy carbon electrode with multiwall carbon nanotubes-iron oxide nanocomposite (MWCNTs-iron oxide). Differential pulse voltammetry (DPV) and cyclic voltammetry (CV) were used to study the electrochemical oxidation of proguanil. The selectivity of the sensor was investigated in the presence of organic and inorganic interfering agents. Furthermore, spiked human urine samples and pharmaceutical formulation were used to evaluate the utility of the sensor. A detection limit of 1.96×10^{-8} M was obtained under optimum conditions. MWCNTs-iron oxide nanocomposite can, therefore, be used to fabricate electrochemical sensors for quality control purposes.

3.1 ABSTRACT

Multiwall carbon nanotubes incorporated with iron oxide nanoparticles (MWCNTs-iron oxide) were prepared using a cheap, facile *In-situ* flame synthesis method. The nanocomposites were characterized using Scanning Electron Microscopy (SEM), Energy-Dispersive X-Ray Spectroscopy (EDX), Transmission Electron Microscopy (TEM), X-Ray Powder Diffractometry (XRD), and Raman Spectroscopy. MWCNTs-iron oxide nanocomposite was used to fabricate a sensitive electrochemical sensor for the detection and quantification of proguanil. The fabrication of the sensor was done by modifying a glassy carbon electrode with multiwall carbon nanotubes-iron oxide nanocomposite (MWCNTs-iron oxide). Differential Pulse Voltammetry (DPV) and Cyclic Voltammetry (CV) were used to study the electrochemical oxidation of proguanil. The selectivity of the sensor was investigated in the presence of organic and inorganic interfering agents. Furthermore, spiked human urine samples and pharmaceutical formulation were used to evaluate the utility of the sensor. A detection limit of 1.96×10^{-8} M was obtained under optimum conditions. MWCNTs-iron oxide nanocomposite can, therefore, be used to fabricate electrochemical sensors for quality control purposes.

Keywords: Proguanil, Carbon nanotubes, Iron oxide nanoparticles, Flame synthesis, Differential pulse voltammetry

3.2 INTRODUCTION

The application of carbon nanotubes in different fields, such as energy management, chemical sensors, and clinical diagnostic tools is increasing. This is mainly due to their unique physical and chemical properties. Some of these properties include a high surface area to volume ratio, ultra-lightweight, fast electron transfer rate, and biocompatibility [1–4]. In the past two decades, the properties of carbon nanotubes have been improved by the incorporation of metal oxide nanoparticles such as iron oxide and zinc oxide [5–8]. Also, other studies have reported the synthesis of carbon nanotubes with conducting polymers and metal nanoparticles [9–11]. Various methods, such as flame pyrolysis [12,13], arc discharge [14], laser ablation[15], sol-gel [16], and chemical vapor deposition [16,17] have been reported for the synthesis of different carbon nanotubes composites. However, most of these methods require sophisticated instrumentation, further purification steps, and are time-consuming. A cheap simple method is needed for the synthesis of carbon nanotubes. The ability of the flame to provide the required heat and chemical reaction environment for the production of carbon nanotubes, makes flame pyrolysis to be among the frequently used methods. This approach is economical, simpler and fast for making carbon nanotubes. Inamdar et al. [18] used a simple flame synthesis method to prepare maghemite nanoparticles. In another study by Bhattacharjya et al. [19], N-doped carbon particles were synthesized by direct burning of acetonitrile as nitrogen and carbon source.

Therefore in the present work, a simple, less time consuming, cheap method for synthesis of carbon nanotubes with iron oxide nanoparticles is reported. This methods allows for a direct one step synthesis of the MWCNTs-iron oxide nanocomposites, thus no further purification step is required. Iron oxide nanoparticles possess good adsorption affinity, biocompatibility and high electrocatalytic activity [20,21]. These properties are different from their bulk counterparts. However iron oxide nanoparticles have some drawbacks that limits their application in electrochemical sensors. These include poor dispersibility and high degree of agglomeration [20]. To overcome these drawbacks, iron oxide nanoparticles are incorporated into multiwall carbon nanotubes. Also, the synergistic effect of iron oxide nanoparticles and multiwall carbon nanotubes improves the electrocatalytic activity of the nanocomposite [22]. The presence of iron oxide nanoparticles will improve the selectivity of the sensor since it has high affinity to towards amine functional groups. In this method, ethanol, atmospheric air, and cold water were used as the source of fuel, oxidizer, and cooling system, respectively. Ferrocene was selected as a precursor because

of its dual function; it acts as a source of iron (Fe) and carbon. The process for the formation of MWCNTs-iron oxide nanocomposite begins at temperatures above 400 ℃, where ferrocene is vaporized to hydrocarbons (CH_4 and C_5H_6) and Fe [23,24]. In this reaction, the л electrons of C_5H_6 interact with Fe atoms. As the temperature increases above 500 ℃, the formation of MWCNTs-iron oxide nanocomposite takes place during the carbonization process [25]. Further, the synthesized nanocomposite was employed to carry out electrochemical detection of proguanil in human urine and pharmaceutical samples.

Proguanil is an antimalarial drug that is used in combination with other drugs. Among these, a synergistic combination of proguanil with atovaquone is widely used for malaria treatment in high-income countries. The high-cost factor of proguanil has contributed to a prevalence of counterfeit antimalarial drugs in Sub-Saharan Africa. Hence, there is a need to trace or encounter such counterfeit drugs available in the markets. Proguanil plays a significant role in the treatment of malaria; its function is to stop the reproduction of the parasite in the red blood cells by inhibiting the folic acid metabolism [26]. To achieve this, the active metabolite of the drug binds with dihydrofolate reductase (DHFR) enzyme of the parasite.

Several analytical methods have been reported for the detection and quantification of pharmaceutical drugs. These methods include; High-performance liquid chromatography [27–29], capillary electrophoresis [30–32], micellar electrokinetic chromatography [33,34], electrochemical [35,36], and spectroscopic methods. Most of these methods require tedious sample extraction processes and are time-consuming. Therefore, there is a need to develop a fast, sensitive, and selective method for qualitative and quantitative analysis of proguanil. As far as we could possibly know, just two investigations are reported for the electroanalytical detection of proguanil. A few notable limitations of the electrochemical methods include slow electron transfer, low selectivity, and sensitivity. Hence there is a need to modify the bare electrodes to avoid such limitations mentioned above. The use of nanocomposites carbon nanotubes with nanoparticle would be beneficial in this regard because of their enhanced electrical conductivity, high surface area, and fast electron transfer rate, which ultimately improve the selectivity and sensitivity of the modified electrode [37,38].

3.3 EXPERIMENTAL

3.3.1 Apparatus and chemicals

Field Emission Scanning Microscopy (FE-SEM) (ZEISS ultra plus, Germany) and Transmission Electron Microscopy (TEM) (JEOL 101, USA) were used for morphological studies of the nanocomposite. For SEM analysis, aluminium stub sample holder was coated with carbon tape. The nanocomposite was then added on to the carbon tape and it was gold coated three times. Prior to TEM analysis, the nanocomposite was dispersed in ethanol and sonicated for 15 minutes. A copper grid was immersed into the solution. The gird was dried under infrared lamp. The elemental composition was determined using Energy-Dispersive X-Ray Spectroscopy (EDX). A Bruker D2 diffractometer at 40 kV and 50 mA was used to record the X-ray diffraction patterns. The measurements were taken at high angle 2θ in a range of 5˚–90˚ with a scan speed of 0.01° 2θ s^{-1} using a secondary graphite monochromated Co K alpha radiation (l = 1.7902 A˚). Raman spectroscopy studies were done using a DeltaNu Advantage 532 high performance Raman spectrometer with a 532 nm solid state frequency doubled Nd:YAG laser with a peak power of 200 mW and a 35 μ m diameter focused beam. Its resolution ranges from 8-10 cm^{-1} and the spectral range from 200-3400 cm^{-1}. CHI660E electrochemical workstation (CH instrument, USA) and a conventional three-electrode system were used for all electrochemical measurements. A glassy carbon electrode (3.0 mm), platinum wire and Ag/AgCl/KCl (3.0 $molL^{-1}$) were used as working, counter, and the reference electrode, respectively. pH measurements were performed using the EXTECH PH60 pH meter (China). Ferrocene, ethanol, potassium ferricyanide, proguanil, and primaquine were purchased from Sigma Aldrich. Monosodium dihydrogen orthophosphate and sodium phosphate dibasic were purchased from Merck. Deionized water was used throughout the experiment.

3.3.2 Flame synthesis of MWCNTs-iron oxide nanocomposite

The experimental setup used in this study is shown in Figure 3:1. Briefly, 0.5g of ferrocene in ethanol was stirred for 30 min at room temperature. The mixture was transferred in a glassy spirit lamp with a cotton wick and ignited. After 4 hours, MWCNTs-iron oxide nanocomposites were collected at the bottom of the cotton wick.

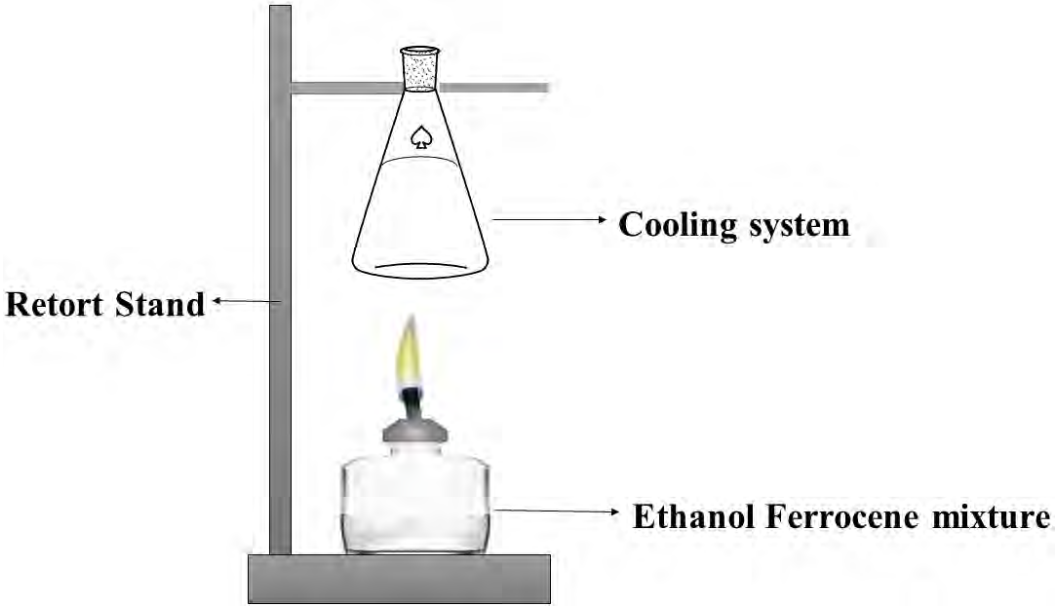

Figure 3:1 Flame synthesis of MWCNTs-iron oxide nanocomposite

3.3.3 Fabrication of MWCNTs-iron oxide modified electrode

The alumina slurry with a size of 0.05 Microns was used to polish the surface of the glassy carbon electrode (GCE) followed by washing with deionized water to remove any adsorbed alumina particles. A suspension of 5 µL (1 mg.mL^{-1}) MWCNTs-iron oxide was drop cast on the surface of the clean GCE. The electrode was dried under an IR lamp for 15 min. The modified electrode denoted (MWCNTs-iron oxide/GCE) was utilized for all electrochemical measurements. All electrochemical measurements were done using CHI660E electrochemical workstation. Electrochemical impendence spectroscopy measurements were taken at frequency range of 1-10000 Hz with 5 mV amplitude. 2.5 mM $[Fe(CN)_6]^{3-}/[Fe(CN)_6]^{4-}$ in 0.1 M KCl was used.

3.3.4 Preparation of pharmaceutical and human urine samples

Proguanil tablets (Mozitec) containing 100 mg proguanil hydrochloride were finely powdered using a mortar and pestle. A suitable stock solution was prepared using powdered tablets. DPV of proguanil in the presence of pharmaceutical excipients were recorded by using diluted aliquots that are within the linear concentration range.

Urine sample was diluted 100 times with 0.1M phosphate buffer (PB) (pH 5.5) to reduce the matrix effects. The sample was spiked with proguanil prior to analysis. MWCNTs-iron oxide/GCE was then used to detect proguanil in spiked urine samples.

3.4 RESULTS AND DISCUSSION

3.4.1 Morphological characterization

The formation of MWCNTs-iron oxide nanocomposite was confirmed by Raman spectroscopy as shown in Figure 3:2A. The peaks at 1338 and 1604 cm^{-1} were attributed to D and G band respectively. The D band is due to the defects in the sidewalls and ends of MWCNTs, while the G band is mainly due to the tangential stretching of the carbon-carbon bond. Second-order modes at 2301-2445 cm^{-1} and the G' (2759 cm^{-1}) were also observed. The structural quality of MWCNTs was estimated using the intensity ratio of the Raman D and G band (I_d/I_g) [39]. Both the D and G band were found to have similar intensities; thus, the density of defects was estimated to be high. The (I_d/I_g) ratio was found to be 0.98, the high (I_d/I_g) is attributed to the growth in multiple layers of MWCNTs. Raman spectroscopy was further used to confirm the presence of iron oxide in the MWCNTs- nanocomposite. The bands at 350, 482 and 686 cm^{-1} are assigned to maghemite nanoparticles [40]. While bands at 221, 240, 297, 416, 525, 620 cm^{-1} are assigned to hematite nanoparticles [41], as shown in Figure 3:2B.

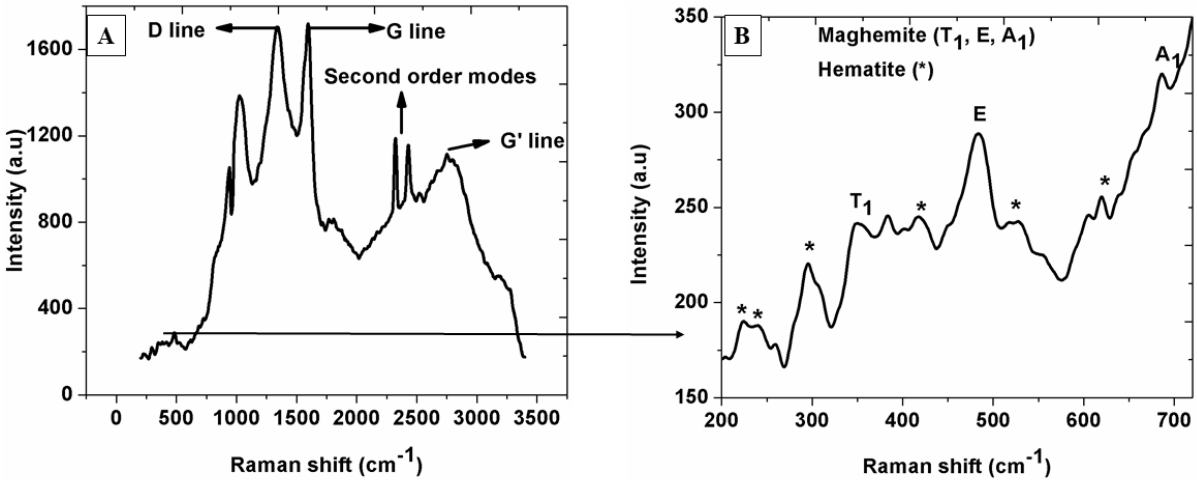

Figure 3:2 Raman spectra of MWCNTs-iron oxide nanocomposite

The morphological analysis of MWCNTs-iron oxide nanocomposite was studied using FE-SEM, as shown in Figure 3:3A. Carbon nanotubes with an average diameter of 84 nm were obtained. The presence of iron oxide particles around the MWCNT was also observed. The presence of small iron oxide nanoparticles on the surface of MWCNTs were also confirmed with TEM (Figure 3:3B). EDX analysis was used to confirm the presence of carbon (81.27 Wt %), iron (4.19 Wt %), and

oxygen (14.54 Wt %). No peaks of impurities were observed (Figure 3:3C). Iron oxide nanoparticles were evenly distributed on the surface of CNT, as shown in Figure 3:3D.

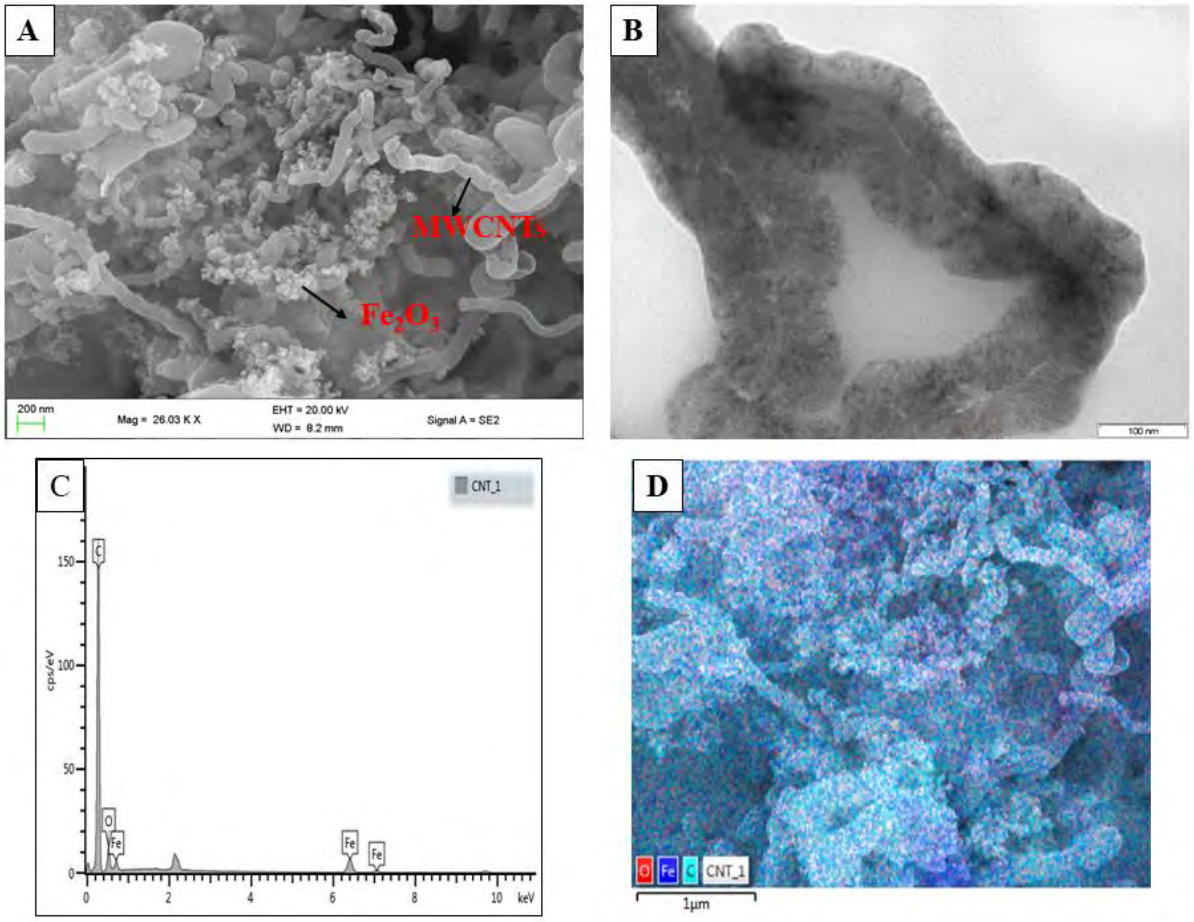

Figure 3:3 (A) SEM, (B) TEM, (C) EDX and (D) EDX mapping of MWCNTs-iron oxide nanocomposite

The XRD pattern of MWCNTs-iron oxide nanocomposite is shown in Figure 3:S1. Two distinct diffraction peaks at 2Θ 26 and 42.7 were indexed to (002) and (100) plane of graphite structure[42]. The other peaks at 2Θ 29, 35, 43, 53, 56, 62 and 77 are indexed to (220), (311), (400), (422), (511), (440) and (533) plane of cubic maghemite (JCPDS: 01-089-3850). As confirmed in the Raman spectroscopy, peaks of hematite were also observed in the XRD patterns at 2Θ 23.94, 40.33, 54.77, 56.95, and 62.48. These peaks were assigned to (012), (113), (116), (018), and (214) plane of rhombohedral hematite (JCPDS: 00-033-0664). The area ratio of the crystalline peak to all peaks was used to estimate the degree of crystallinity [43]. The percentage crystallinity values for

MWCNTs, maghemite, and hematite nanoparticles were found to be 34.63, 7.89, and 13.69% respectively.

3.4.2 Electrochemical characterization

To investigate the electron transfer properties of the modified electrode; Electrochemical Impendence Spectroscopy (EIS) studies were done. $[Fe(CN)_6]^{3-}/[Fe(CN)_6]^{4-}$ (2.5 mM) in 0.1 KCl was used as the electrolyte. A frequency range of 1-10000 Hz with 5 mV amplitude was used to take the measurements. EIS data was fitted using Randles equivalent circuit (Figure 3:S2 inset). The values for each element of the Randles equivalent circuit are given in Table 3:S1. As shown in Figure 3:S2, a well-defined semi-circle with charge transfer resistance (Rct) value of 222.2 Ω was obtained for the bare GCE. This high Rct value suggests that the diffusion of $[Fe(CN)_6]^{3-}/[Fe(CN)_6]^{4-}$ towards the electrode is low. Thus to improve this Rct value, it is necessary to modify the electrode with MWCNTs-iron oxide nanocomposite. Upon modification with MWCNTs-iron oxide nanoparticles; the semi-circle diminished, and the Rct value of 0.001 Ω was obtained. The decrease in Rct value signifies a high electron rate transfer between the modified electrode and the $[Fe(CN)_6]^{3-}/[Fe(CN)_6]^{4-}$. This is attributed to the unique properties of carbon nanotubes and iron oxide nanoparticles, such as high surface area and good conductivity.

Cyclic Voltammetry (CV) was used to investigate further the electron transport properties of MWCNTs-iron oxide nanocomposite-modified electrode using $Fe(CN)_6]^{3-}/[Fe(CN)_6]^{4-}$ as the redox probe. A well-defined redox couple (Figure 3:S3A) that is due to $[Fe(CN)_6]^{3-}/[Fe(CN)_6]^{4-}$ was obtained for both the bare electrode and MWCNTs-iron oxide/GCE electrode. However, the current increased on the modified electrode compared to the bare electrode, as shown in Table 3:1, which can be attributed to the high surface area of nanocomposite. Thus more sites for electron transfer were available. Also, the ratio of the anodic and cathodic peak current (I_{pa}/I_{pc}) was calculated to be ~1.0 (Table 3:1). This indicates a reversible electrochemical process [44]. Peak to peak separation potential (ΔEp) for bare and MWCNTs-iron oxide/GCE electrodes were found to be 100 mV and 72 mV, respectively. The decrease in ΔEp indicates a faster electron transfer rate at the modified electron.

Table 3:1 CV data obtained for MWCNTs-iron oxide/GCE electrode in 2.5 mM $[Fe(CN)_6]^{-3/-4}$

Electrode	Ipa (uA)	Ipc (uA)	Ipa/Ipc	Epa (mV)	Epc (mV)	ΔEp (mV)
GCE	4.45	4.39	1.01	288	188	100
GCE/MWCNTs-iron oxide	4.98	4.78	1.04	274	202	72

Randles Sevcik equation was used to calculate the effective surface area of the bare and modified electrode at 2.5 mM $Fe(CN)_6]^{3-}/[Fe(CN)_6]^{4-}$ solution while varying the scan rate as shown in Figure 3:S3B. The inset on Figure S3:3B displays a plot of peak current versus square root of scan rate with a linear regression Ip=0.0065$\sqrt{v}$ – 0.015

$$I_p = 2 \cdot 69 \times 10^5 A \sqrt{D} \left(\sqrt{n}\right)^3 \sqrt{\gamma}\, C_0 \qquad (1)$$

Where Ip represent the peak current, n= number of electrons involved in the charge transfer (n=1), D= diffusion coefficient (D= 7.6×10^{-6} cm^2s^{-1}), A= effective surface area (cm^2), C= concentration of $Fe(CN)_6]^{3-}/[Fe(CN)_6]^{4-}$ ($mol.cm^{-3}$) and υ = is the scan rate ($V.s^{-1}$). The effective surface area was calculated to be 0.0324 and 0.040 cm^2 for bare and MWCNTs-iron oxide modified electrode respectively.

3.4.3 Electrochemical Behavior of Proguanil at MWCNTs-iron oxide/GCE

CV was used to investigate the electrochemical behavior of MWCNTs-iron oxide/GCE electrode towards 0.1 mM proguanil in 0.1 mM PBS at pH 5.5, as illustrated in Figure 3:4A. One anodic peak at 1.02 V and 1.0 V was observed for GCE and MWCNTs-iron oxide/GCE respectively. No peaks were observed for MWCNTs-iron oxide/GCE in plan electrolyte. The anodic peak indicates that proguanil undergoes one irreversible oxidation process; thus, no reverse peak was obtained. A plausible mechanism for the electrochemical detection of proguanil is shown in Figure 3:7. The anodic peak at 1.0 V is due to the irreversible oxidation 4-Chloroaniline moiety in proguanil. The MWCNTs-iron oxide/GCE showed better sensitivity towards proguanil compared to bare GCE. This is attributed to the unique properties of the synthesized nanocomposite such as high electrocatalytic activity and good conductivity; thus the electron transfer rate is enhanced. The high surface to volume ratio and good affinity of iron oxide nanoparticles towards amine functional groups that are present in proguanil improves the sensitivity and selectivity of the sensor.

The effect of scan rate was conducted to investigate the electrochemical reaction mechanism of proguanil. Cyclic voltammograms (Figure 3:4B) were recorded with different scan rates (20-200 $mV.s^{-1}$). A linear relationship between peak currents and square root of scan rate was observed (Figure 3:5A). This relationship is represented by the equation $Ip= 0.4014v^{1/2} - 0.124$ ($R^2= 0.9842$). Therefore the oxidation of proguanil at MWCNTs-iron oxide/GCE is a diffusion controlled process [45]. This was further confirmed by the linear relation between the logarithm of scan rate and logarithm of peak current (Figure 3:5B) ($\log Ip= 0.486\log v - 0.386$ ($R^2= 0.9761$)). The slope was found to be 0.49 thus it is close to the theoretical value of a diffusion controlled process [46]. The potential of the oxidation peak was also influenced by the change in scan rate. The peak potential shifted to more positive values as the scan rate was increased (Figure 3:6). This further confirms the irreversibility of the oxidation process. The linear relationship between log v and Ep can be expressed as $Ep= 0.081\log v + 0.884$ ($R^2= 0.9892$).

The number of electrons involved in the oxidation of proguanil was calculated using the Laviron equation, which defines the relationship between Ep and logv as:

$$Ep = E° + \left[2.303\frac{RT}{\alpha nF}\right][\log(RTk°/\alpha nF)] + [\left(2.303\frac{RT}{\alpha nF}\right)\log \nu] \quad (2)$$

Where E^o= formal redox potential, n= number of electrons involved K^o= standard rate constant of the surface reaction, α= electron transfer coefficient. Other symbols have their usual meaning [47]. As illustrated in Figure 3:6, a linear relationship was observed between Ep and logv, which is represented by the equation $Ep= 0.081\log v + 0.884$ ($R^2= 0.9892$). The value of αn was calculated by using the following constants; R= 8.314 JK mol, T=298 K, and F=96480 C mol^{-1}. The value of α was then calculated using the Bard and Faulkner equation below:

$$\alpha = 47.7/(\mathrm{E_p} - \mathrm{E_{p^{1/2}}}) \quad (3)$$

Where $Ep_{1/2}$ is half of the peak potential. The number of electrons (n) involved in the oxidation of proguanil was found to be ~1.

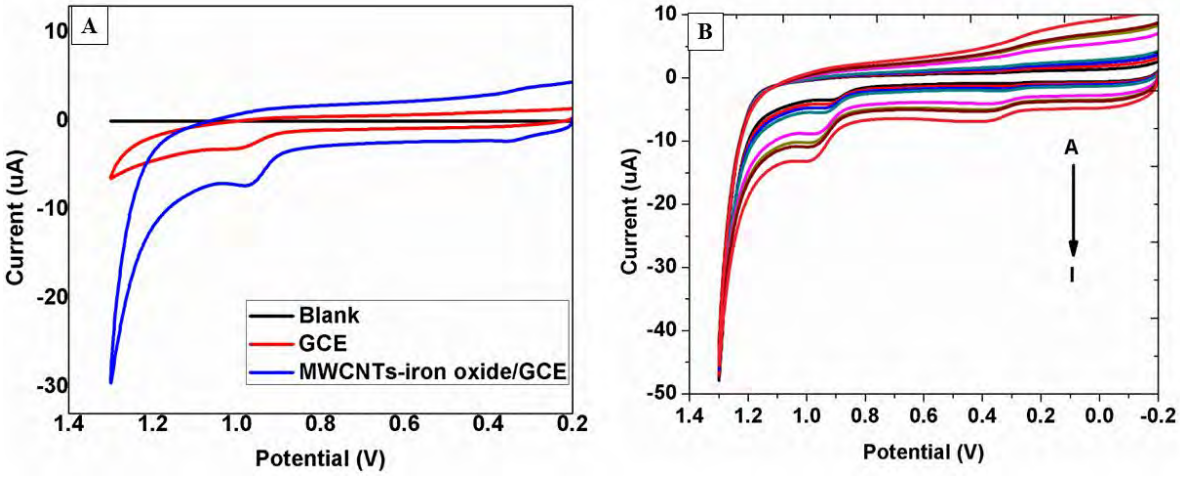

Figure 3:4 : (A) Cyclic voltammograms of MWCNTs-iron oxide/GCE in plain electrolyte, bare GCE and MWCNTs-iron oxide/GCE in 0.1 mM proguanil (pH 5.5) at a scan rate of 100 mV/s; (B) Cyclic voltammograms of MWCNTs-iron oxide/GCE with change in scan rate

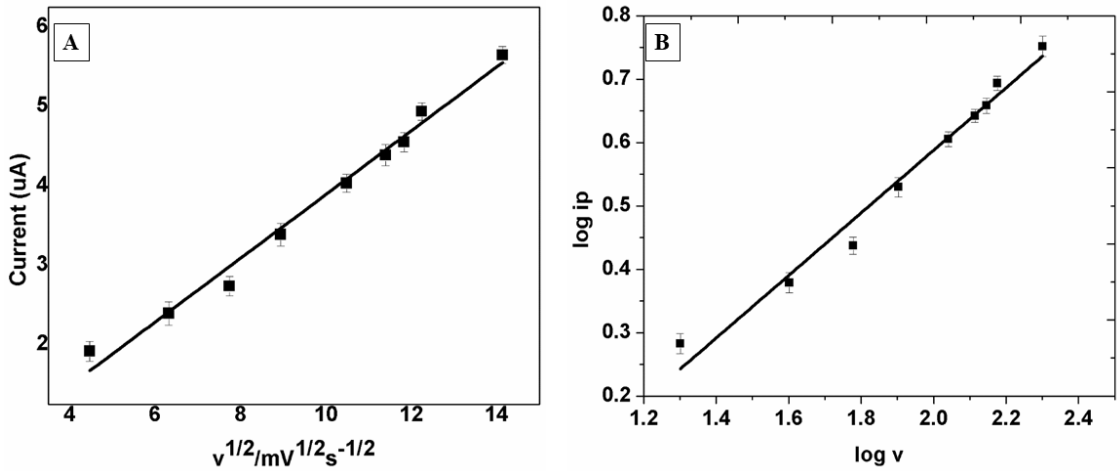

Figure 3:5 (A) Relation between square root of scan rate and current for MWCNTs-iron oxide/GCE in proguanil (0.1 M); (B) Relation between log v and log ip

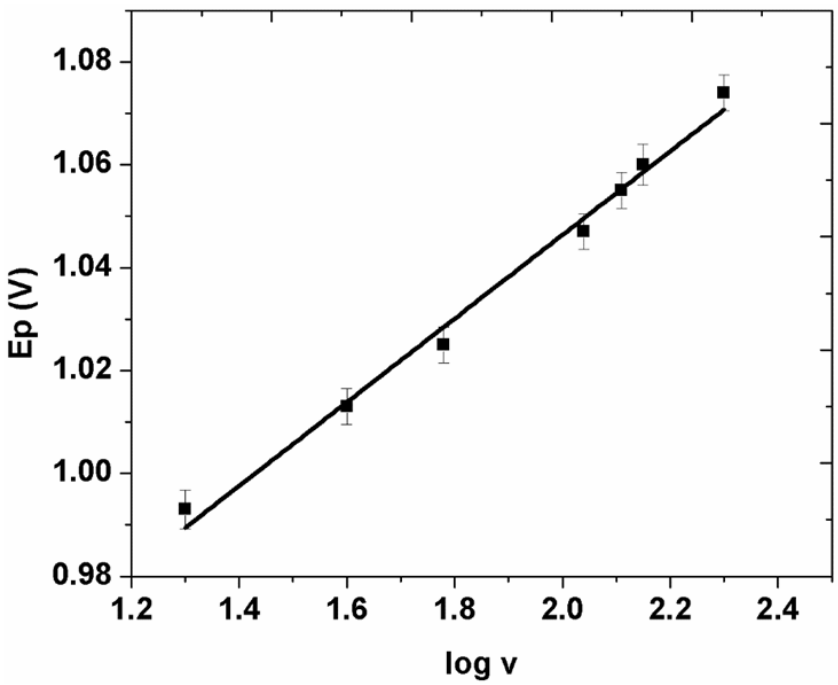

Figure 3:6 Plot between peak potential vs log of scan rate for MWCNTs-iron oxide/GCE in proguanil (0.1 M)

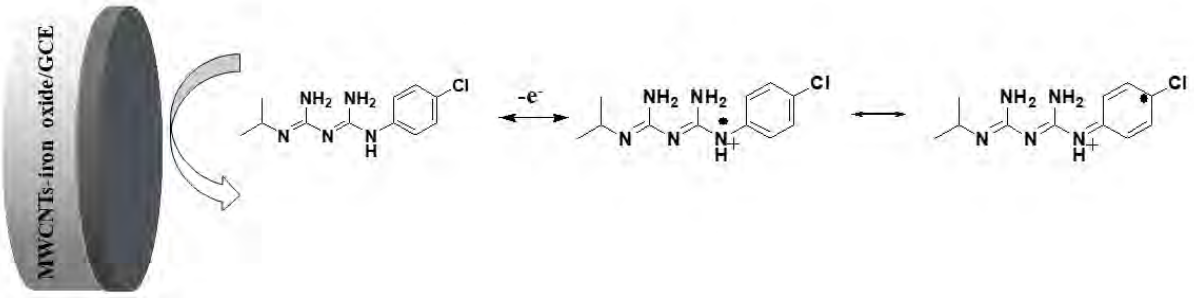

Figure 3:7 Schematic representation of a plausible mechanism for electrochemical detection of proguanil

3.4.4 DPV optimization and influence of pH

Before Differential Pulse Voltammetry (DPV) analysis, parameters such as step potential, pulse width, and pulse amplitude were optimized (Figure 3:S4). All Measurements were done three times. A pulse amplitude of 50 mV and a pulse width of 50 ms was used while varying the step potential (3-8 mV). An increase in current with the potential step was observed (Figure 3:S4A). This is due to a faster change in potential, thus a larger scan rate. The most repeatable peak current

was obtained at 5 mV. A pulse amplitude of 50 mV and the optimum step potential (5 mV) was used to investigate the effect of pulse width (10-60 ms). A decrease in peak current with an increase in pulse width was observed (Figure 3:S4B). This is due to a decrease in scan rate; the most repeatable current was obtained at 40 ms. The pulse width (40 ms) and potential step (5 mV) were used to study the influence of pulse amplitude (10-70 mV). An increase in current with pulse amplitude was observed (Figure 3:S4C). The most repeatable pulse amplitude was found to be 50 mV. The effect of pH on the oxidation of 0.1 mM proguanil in 0.1 M PBS was investigated using Differential Pulse Voltammetry (DPV), as shown in Figure 3:8A. A pH range of 5-8.5 was selected. A linear relationship between Ep vs pH was observed (Figure 3:8B). The linear regression is shown below:

$$Ep = 1.185 - 0.05pH. \quad (4)$$

Since the slope is close to the theoretical Nernstian value of 0.059 V/pH at 25 °C; an equal number of protons and electrons are involved in the electro-oxidation of proguanil at MWCNTs-iron oxide/GCE [48]. The peak potential shifted towards less positive potentials as the solution became more basic. This indicates the presence of a proton-coupled electron transfer reaction. The optimum pH was 5.5, and it was used for all further studies.

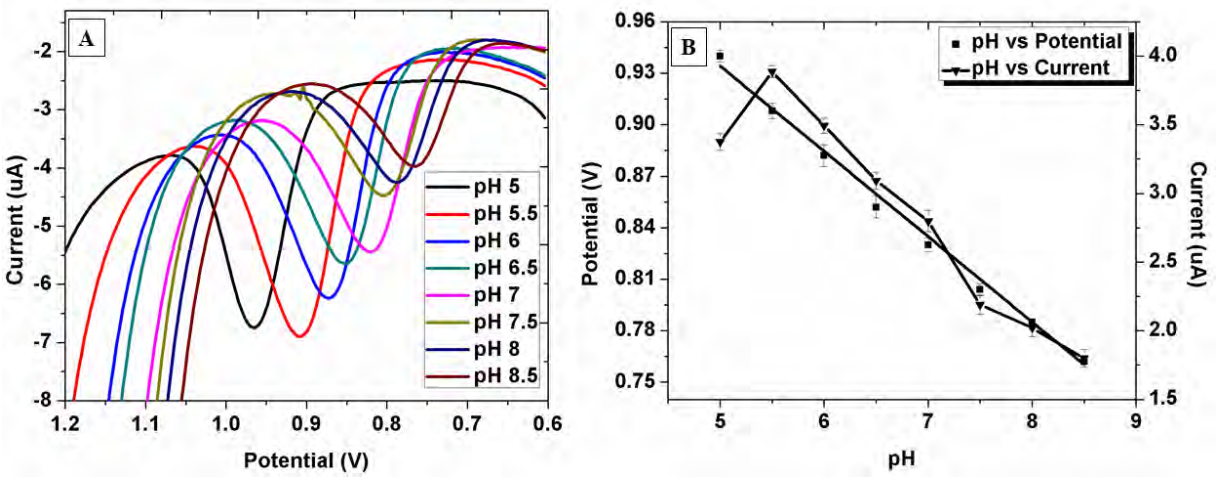

Figure 3:8 Differential pulse voltammograms of proguanil with different pH; (B) The plot of current vs pH and potential vs pH at MWCNTs-iron oxide/GCE

3.4.5 Analytical performance

DPV was used under optimum conditions to investigate the analytical performance of MWCNTs-iron oxide/GCE (figure 3:9A). A linear relationship between the peak current and concentration was observed in the range of 0.7×10^{-6} -1.9×10^{-6} M (Figure 3:9B). The equation below represents the corresponding linear regression:

$$Ip=0.4479C-0.0204 \quad (5)$$

Where C= concentration of proguanil and Ip= peak current. The relation between 3S/N and 10S/N was used to calculate the limit of detection (LOD) and limit of quantification (LOQ) respectively. The LOD and LOQ for proguanil at GCE/MWCNTs-iron oxide were calculated to be 1.96×10^{-8} M and 6.54×10^{-8} M respectively. The present work was compared with other reported electroanalytical methods for detection of proguanil (Table 3:2). The proposed method shows better sensitivity for detection of proguanil.

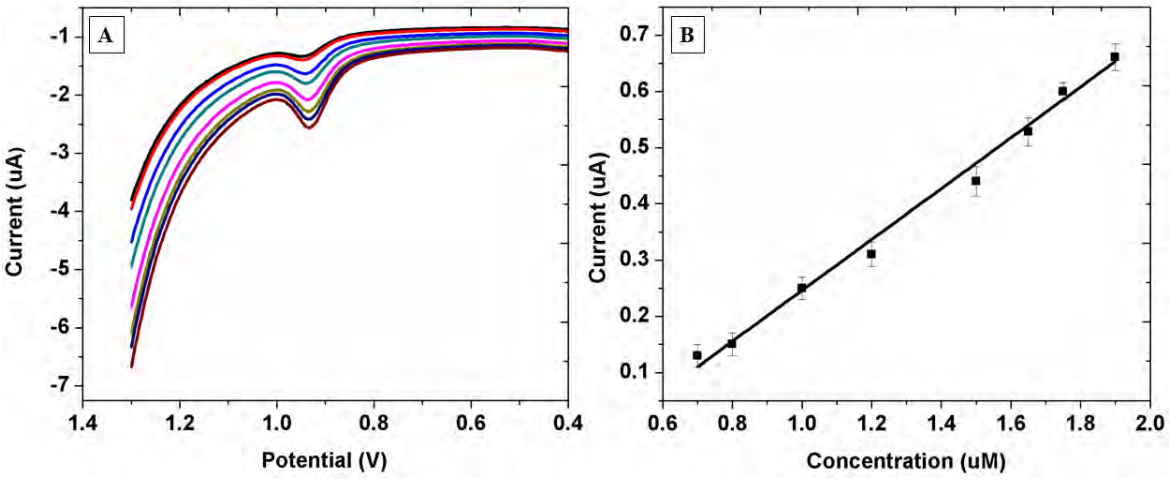

Figure 3:9 (A) DP voltammograms of proguanil at different concentrations in 0.1M PBS (pH 5.5); (B) calibration plots for proguanil in 0.1 M PBS (pH 5.5) MWCNTs-iron oxide/GCE

Table 3:2 A comparison of the present study with other reported methods for electrochemical determination of proguanil.

Electrode	Concentration range (mol.L^{-1})	LOD (mol.L^{-1})	Ref
Renewable silver amalgam film	1×10^{-7}-6×10^{-6}	2.9×10^{-8}	[49]
CWE/phosphotugnestic acid	1×10^{-5}-1×10^{-2}	1×10^{-6}	[26]
MWCNTs-iron oxide/GCE	0.7×10^{-6} -1.9×10^{-6}	1.96×10^{-8}	Present work

3.4.6 Interference study and reproducibility

The selectivity of MWCNTs-iron oxide/GCE towards proguanil was investigated in the presence of 200 fold concentration of primaquine, inorganic (Na^+, Mg^{2+}, Cl^- SO_4^-) and organic (uric acid, ascorbic acid) interfering species using DPV under optimum conditions (Figure 3:S5). The peak current slightly decreased in the presence of interfering species. The deviation was less than the accepted tolerance of 5%. Thus the proposed sensor showed good selectivity towards proguanil. The reproducibility of the sensor was evaluated using three identically prepared electrodes. The relative standard deviation was calculated to be 2.4%, this demonstrate good reproducibility.

3.4.7 Real sample analysis

DPV studies were carried out under optimum conditions to determine the content of proguanil in commercially available pharmaceutical tablets. The proposed sensor demonstrated good selectively towards proguanil in the presence of pharmaceutical excipients (Table 3:3). The recovery percentages were calculated using standard addition method (Figure 3:S6). A bias of less than 2.3% was obtained. Additionally proguanil was determined in 100 fold dilution of human urine under optimum conditions. The recovery results were found to be in the range of 99-104 % (Table 3:4). The proposed sensor is selective and practically applicable for the analysis of proguanil in pharmaceutical formulations and urine samples.

Table 3:3 Results from proguanil tablet at MWCNTs-iron oxide/GCE

S No	Expected (uM)	Detected	Recovery	Bias (%)	RSD (%) (n=3)
1	1.2	1.2093	100.8	0.8	0.26
2	1.4	1.423	101.6	1.6	0.83
3	1.6	1.5646	97.8	2.2	0.52
4	1.8	1.7631	98	2	1.23
5	2	2.0384	101.92	1.92	0.33

Table 3:4 Recovery results for proguanil in spiked human urine sample at MWCNTs-iron oxide/GCE

S No	Amount added (uM)	Found (uM)	Recovery (%)	Bias (%)
1	2.00	1.98	99.0	1
2	2.50	2.54	101.6	1.6
3	3.00	3.12	104.0	4

3.5 SUB-CONCLUSION

A simple method for *in-situ* flame synthesis of MWCNTs-iron oxide nanocomposite was successfully developed. Raman spectroscopy and X-ray diffraction confirmed the presence of MWCNTs and iron oxide nanoparticles in the composite material. SEM and TEM images proved the formation of MWCNTs-iron oxide nanocomposite. Electrochemical detection of proguanil was carried out using MWCNTs-iron oxide/GCE. A detection limit of 1.96×10^{-8} M with a linear range of 0.7×10^{-6} -1.9×10^{-6} M was obtained, this was found to be better when compared with the reported literature. The modified electrode showed satisfactory selectivity and sensitivity towards proguanil in the presence of different sample matrix such as pharmaceutical formulation and urine sample. Thus, MWCNTs-iron oxide nanocomposites have proven to be useful in the fabrication of electrochemical sensor for quality control purposes.

3.6 REFERENCES

[1] N. Anzar, R. Hasan, M. Tyagi, N. Yadav, J. Narang, Carbon nanotube - A review on Synthesis, Properties and plethora of applications in the field of biomedical science, Sensors Int. 1 (2020) 100003. https://doi.org/https://doi.org/10.1016/j.sintl.2020.100003.

[2] R.H. Baughman, A.A. Zakhidov, W.A. de Heer, Carbon nanotubes--the route toward applications., Science. 297 (2002) 787–792. https://doi.org/10.1126/science.1060928.

[3] J. Li, R. Yuan, Y. Chai, X. Che, Fabrication of a novel glucose biosensor based on Pt nanoparticles-decorated iron oxide-multiwall carbon nanotubes magnetic composite, J. Mol. Catal. B Enzym. 66 (2010) 8–14. https://doi.org/https://doi.org/10.1016/j.molcatb.2010.03.005.

[4] N.P. Shetti, D.S. Nayak, S.J. Malode, R.R. Kakarla, S.S. Shukla, T.M. Aminabhavi, Sensors based on ruthenium-doped TiO2 nanoparticles loaded into multi-walled carbon nanotubes for the detection of flufenamic acid and mefenamic acid, Anal. Chim. Acta. 1051 (2019) 58–72. https://doi.org/https://doi.org/10.1016/j.aca.2018.11.041.

[5] C. YX, L. YJ, H. JJ, K. Li, X. YZ, W. Zhang, J. LT, Amperometric tyrosinase biosensor based on Fe3O4 nanoparticles-coated carbon nanotubes nanocomposite for rapid detection of coliforms, Electrochim. Acta. 54 (2009) 2588–2594. https://doi.org/10.1016/j.electacta.2008.10.072.

[6] Y. Fan, F. Su, K. Li, C. Ke, Y. Yan, Carbon nanotube filled with magnetic iron oxide and modified with polyamidoamine dendrimers for immobilizing lipase toward application in biodiesel production, Sci. Rep. 7 (2017) 45643. https://doi.org/10.1038/srep45643.

[7] J. de O. Marques Neto, C.R. Bellato, D. de C. Silva, Iron oxide/carbon nanotubes/chitosan magnetic composite film for chromium species removal, Chemosphere. 218 (2019) 391–401. https://doi.org/https://doi.org/10.1016/j.chemosphere.2018.11.080.

[8] M. Madhusudhana Reddy, G. Ramanjaneya Reddy, K. Chennakesavulu, E. Sundaravadivel, S.S. Prasath, A.M. Rabel, J. Sreeramulu, Synthesis of zinc oxide and carbon nanotube composites by CVD method: photocatalytic studies, J. Porous Mater. 24 (2017) 149–156. https://doi.org/10.1007/s10934-016-0247-3.

[9] E.M. Elnaggar, K.I. Kabel, A.A. Farag, A.G. Al-Gamal, Comparative study on doping of polyaniline with graphene and multi-walled carbon nanotubes, J. Nanostructure Chem. 7 (2017) 75–83. https://doi.org/10.1007/s40097-017-0217-6.

[10] L.M. Hoyos-Palacio, D.P. Cuesta Castro, I.C. Ortiz-Trujillo, L.E. Botero Palacio, B.J. Galeano Upegui, N.J. Escobar Mora, J.A. Carlos Cornelio, Compounds of carbon nanotubes decorated with silver nanoparticles via in-situ by chemical vapor deposition (CVD), J. Mater. Res. Technol. 8 (2019) 5893–5898. https://doi.org/https://doi.org/10.1016/j.jmrt.2019.09.062.

[11] Z. Yang, L. Tang, J. Ye, D. Shi, S. Liu, M. Chen, Hierarchical nanostructured α-Fe2O3/polyaniline anodes for high performance supercapacitors, Electrochim. Acta. 269 (2018) 21–29. https://doi.org/https://doi.org/10.1016/j.electacta.2018.02.144.

[12] G. Zhao, H.-Y. Liu, X. Du, H. Zhou, Z. Pan, Y.-W. Mai, Y.-Y. Jia, W. Yan, Flame synthesis of carbon nanotubes on glass fibre fabrics and their enhancement in electrical and thermal properties of glass fibre/epoxy composites, Compos. Part B Eng. 198 (2020) 108249. https://doi.org/https://doi.org/10.1016/j.compositesb.2020.108249.

[13] H. Hong, N.K. Memon, Z. Dong, B.H. Kear, S.D. Tse, Flame synthesis of gamma-iron-oxide (γ-Fe2O3) nanocrystal films and carbon nanotubes on stainless-steel substrates, Proc. Combust. Inst. 37 (2019) 1249–1256. https://doi.org/https://doi.org/10.1016/j.proci.2018.06.098.

[14] N. Arora, N.N. Sharma, Arc discharge synthesis of carbon nanotubes: Comprehensive review, Diam. Relat. Mater. 50 (2014) 135–150. https://doi.org/https://doi.org/10.1016/j.diamond.2014.10.001.

[15] R.A. Ismail, M.H. Mohsin, A.K. Ali, K.I. Hassoon, S. Erten-Ela, Preparation and characterization of carbon nanotubes by pulsed laser ablation in water for optoelectronic application, Phys. E Low-Dimensional Syst. Nanostructures. 119 (2020) 113997. https://doi.org/https://doi.org/10.1016/j.physe.2020.113997.

[16] B. V Basheer, J.J. George, S. Siengchin, J. Parameswaranpillai, Polymer grafted carbon nanotubes—Synthesis, properties, and applications: A review, Nano-Structures & Nano-

Objects. 22 (2020) 100429. https://doi.org/https://doi.org/10.1016/j.nanoso.2020.100429.

[17] R. Andrews, D. Jacques, D. Qian, T. Rantell, Multiwall Carbon Nanotubes: Synthesis and Application, Acc. Chem. Res. 35 (2002) 1008–1017. https://doi.org/10.1021/ar010151m.

[18] S.N. Inamdar, S.K. Haram, Synthesis and Characterization of Uncapped -Fe2O3 Nanoparticles Prepared by Flame Pyrolysis of Ferrocene in Ethanol, J. Nanosci. Nanotechnol. 6 (n.d.) 2155–2158. https://www.ingentaconnect.com/content/asp/jnn/2006/00000006/00000007/art00042.

[19] D. Bhattacharjya, H.-Y. Park, M.-S. Kim, H.-S. Choi, S.N. Inamdar, J.-S. Yu, Nitrogen-Doped Carbon Nanoparticles by Flame Synthesis as Anode Material for Rechargeable Lithium-Ion Batteries, Langmuir. 30 (2014) 318–324. https://doi.org/10.1021/la403366e.

[20] N.P. Shetti, D.S. Nayak, G.T. Kuchinad, R.R. Naik, Electrochemical behavior of thiosalicylic acid at γ-Fe2O3 nanoparticles and clay composite carbon electrode, Electrochim. Acta. 269 (2018) 204–211. https://doi.org/https://doi.org/10.1016/j.electacta.2018.02.170.

[21] G. Manasa, A.K. Bhakta, Z. Mekhalif, R.J. Mascarenhas, Voltammetric Study and Rapid Quantification of Resorcinol in Hair Dye and Biological Samples Using Ultrasensitive Maghemite/MWCNT Modified Carbon Paste Electrode, Electroanalysis. 31 (2019) 1363–1372. https://doi.org/doi:10.1002/elan.201900143.

[22] V. Erady, R.J. Mascarenhas, A.K. Satpati, S. Detriche, Z. Mekhalif, J. Dalhalle, A. Dhason, Sensitive detection of Ferulic acid using multi-walled carbon nanotube decorated with silver nano-particles modified carbon paste electrode, J. Electroanal. Chem. 806 (2017) 22–31. https://doi.org/https://doi.org/10.1016/j.jelechem.2017.10.045.

[23] Wulan, Praswasti PDK, Rivai, Ghassan Tsabit, Synthesis of carbon nanotube using ferrocene as carbon source and catalyst in a vertical structured catalyst reactor, E3S Web Conf. 67 (2018) 3038. https://doi.org/10.1051/e3sconf/20186703038.

[24] C.S. Yah, G.S. Simate, K. Moothi, M.K. S, S.E. Iyuke, Synthesis of large carbon nanotube from ferrocene.The chemical vapour deposition process, Trends Appl. Sci. Res. 6 (2011)

1270–1279.

[25] T.M. Keller, M. Laskoski, S.B. Qadri, Ferrocene Catalyzed Carbon Nanotube Formation in Carbonaceous Solid, J. Phys. Chem. C. 111 (2007) 2514–2519. https://doi.org/10.1021/jp0665527.

[26] F.M. Abdel-Haleem, M. Saad, M.S. Rizk, Development of new potentiometric sensors for the determination of proguanil hydrochloride in serum and urine, Chinese Chem. Lett. 27 (2016) 857–863. https://doi.org/https://doi.org/10.1016/j.cclet.2016.01.027.

[27] S. Kombath, I.B. Balde, S. Carret, S. Kabiche, S. Cisternino, J.E. Fontan, J. Schlatter, Stability-Indicating HPLC Assay for Determination of Idebenone in Pharmaceutical Forms, J. Anal. Methods Chem. 2015 (2015) 6–11. https://doi.org/10.1155/2015/835986.

[28] N.M. Hosny, K. Huddersman, S.M. El-Gizawy, N.N. Atia, New approach for simultaneous analysis of commonly used antigout drugs by HPLC/UV method; Application in pharmaceutical and biological analysis, Microchem. J. 147 (2019) 717–728. https://doi.org/https://doi.org/10.1016/j.microc.2019.03.080.

[29] Y.S. Endoh, H. Yoshimura, N. Sasaki, Y. Ishihara, H. Sasaki, S. Nakamura, Y. Inoue, M. Nishikawa, High-performance liquid chromatographic determination of pamaquine, primaquine and carboxy primaquine in calf plasma using electrochemical detection, J. Chromatogr. B Biomed. Sci. Appl. 579 (1992) 123–129. https://doi.org/https://doi.org/10.1016/0378-4347(92)80370-6.

[30] M. Heller, L. Vitali, M.A. Siqueira, A.V.F. Sako, M. Piovezan, G.A. Micke, Capillary Electrophoresis with UV Detection to Determine Cocaine on Circulated Banknotes, ISRN Anal. Chem. 2013 (2013) 489705. https://doi.org/10.1155/2013/489705.

[31] M. Rambla-Alegre, J. Peris-Vicente, J. Esteve-Romero, M.-E. Capella-Peiró, D. Bose, Capillary electrophoresis determination of antihistamines in serum and pharmaceuticals, Anal. Chim. Acta. 666 (2010) 102–109. https://doi.org/https://doi.org/10.1016/j.aca.2010.03.041.

[32] Y. Huang, W. Pan, M. Guo, S. Yao, Capillary electrophoresis with end-column

electrochemiluminescence for the analysis of chloroquine phosphate and the study on its interaction with human serum albumin, J. Chromatogr. A. 1154 (2007) 373–378. https://doi.org/https://doi.org/10.1016/j.chroma.2007.02.029.

[33] R.B. Taylor, R.G. Reid, A.S. Low, Analysis of proguanil and its metabolites by application of the sweeping technique in micellar electrokinetic chromatography, J. Chromatogr. A. 916 (2001) 201–206. https://doi.org/https://doi.org/10.1016/S0021-9673(00)01035-9.

[34] M.E. El-Kommos, N.A. Mohamed, A.F. Abdel Hakiem, Selective micellar electrokinetic chromatographic method for simultaneous determination of some pharmaceutical binary mixtures containing non-steroidal anti-inflammatory drugs, J. Pharm. Anal. 3 (2013) 53–60. https://doi.org/10.1016/j.jpha.2012.07.005.

[35] A. Afkhami, H. Ghaedi, T. Madrakian, M. Ahmadi, H. Mahmood-Kashani, Fabrication of a new electrochemical sensor based on a new nano-molecularly imprinted polymer for highly selective and sensitive determination of tramadol in human urine samples, Biosens. Bioelectron. 44 (2013) 34–40. https://doi.org/https://doi.org/10.1016/j.bios.2012.11.030.

[36] T.E. Chiwunze, V.N. Palakollu, A.A.S. Gill, F. Kayamba, N.B. Thapliyal, R. Karpoormath, A highly dispersed multi-walled carbon nanotubes and poly(methyl orange) based electrochemical sensor for the determination of an anti-malarial drug: Amodiaquine., Mater. Sci. Eng. C. Mater. Biol. Appl. 97 (2019) 285–292. https://doi.org/10.1016/j.msec.2018.12.018.

[37] A.A. Ensafi, H. Karimi-Maleh, A Voltammetric Sensor Based on Modified Multiwall Carbon Nanotubes for Cysteamine Determination in the Presence of Tryptophan Using p-Aminophenol as a Mediator, Electroanalysis. 22 (2010) 2558–2568. https://doi.org/doi:10.1002/elan.201000270.

[38] N. Sattarahmady, H. Heli, An electrocatalytic transducer for l-cysteine detection based on cobalt hexacyanoferrate nanoparticles with a core–shell structure, Anal. Biochem. 409 (2011) 74–80. https://doi.org/https://doi.org/10.1016/j.ab.2010.09.032.

[39] L. Thi Mai Hoa, Characterization of multi-walled carbon nanotubes functionalized by a mixture of HNO3/H2SO4, Diam. Relat. Mater. 89 (2018) 43–51.

https://doi.org/https://doi.org/10.1016/j.diamond.2018.08.008.

[40] Y. El Mendili, J.-F. Bardeau, N. Randrianantoandro, J.-M. Greneche, F. Grasset, Structural behavior of laser-irradiated γ-Fe(2)O(3) nanocrystals dispersed in porous silica matrix : γ-Fe(2)O(3) to α-Fe(2)O(3) phase transition and formation of ε-Fe(2)O(3), Sci. Technol. Adv. Mater. 17 (2016) 597–609. https://doi.org/10.1080/14686996.2016.1222494.

[41] L. Slavov, M. V Abrashev, T. Merodiiska, C. Gelev, R.E. Vandenberghe, I. Markova-Deneva, I. Nedkov, Raman spectroscopy investigation of magnetite nanoparticles in ferrofluids, J. Magn. Magn. Mater. 322 (2010) 1904–1911. https://doi.org/https://doi.org/10.1016/j.jmmm.2010.01.005.

[42] K.S. Khashan, G.M. Sulaiman, R. Mahdi, A. kadhim, The effect of laser energy on the properties of carbon nanotube—iron oxide nanoparticles composite prepared via pulsed laser ablation in liquid, Mater. Res. Express. 5 (2018) 105004. https://doi.org/10.1088/2053-1591/aadabc.

[43] H. Park, T. Kim, J. Huh, M. Kang, J.E. Lee, H. Yoon, P.E.T. Al, Anisotropic Growth Control of Polyaniline Nanostructures and Their Morphology-Dependent Electrochemical Characteristics, (2012) 7624–7633.

[44] O.R. Obisesan, A.S. Adekunle, J.A.O. Oyekunle, T. Sabu, T.T.I. Nkambule, B.B. Mamba, Development of Electrochemical Nanosensor for the Detection of Malaria Parasite in Clinical Samples., Front. Chem. 7 (2019) 89. https://doi.org/10.3389/fchem.2019.00089.

[45] Allen J. Bard, L.R. Faulkner, Electrochemical Methods: Fundamentals and Applications, 2nd Edition, John Wiley & Sons, Ltd, New York, 1980.

[46] David K Gosser, Cyclic voltammetry: simulation and analysis of reaction mechanisms., VCH, New York, 1993.

[47] E. Laviron, General expression of the linear potential sweep voltammogram in the case of diffusionless electrochemical systems, J. Electroanal. Chem. Interfacial Electrochem. 101 (1979) 19–28. https://doi.org/https://doi.org/10.1016/S0022-0728(79)80075-3.

[48] L. Zhang, J. Zhang, 3D hierarchical bayberry-like Ni@carbon hollow nanosphere/rGO

hybrid as a new interesting electrode material for simultaneous detection of small biomolecules, Talanta. 178 (2018) 608–615. https://doi.org/https://doi.org/10.1016/j.talanta.2017.09.086.

[49] S. Smarzewska, S. Skrzypek, W. Ciesielski, Voltammetric Determination of Proguanil in Malarone and Spiked Urine with a Renewable Silver Amalgam Film Electrode, Electroanalysis. 24 (2012) 1966–1972. https://doi.org/10.1002/elan.201200312.

CHAPTER FOUR

Polyaniline-cobalt oxide nanofibers for simultaneous electrochemical determination of antimalarial drugs: primaquine and proguanil

Graphical Abstract

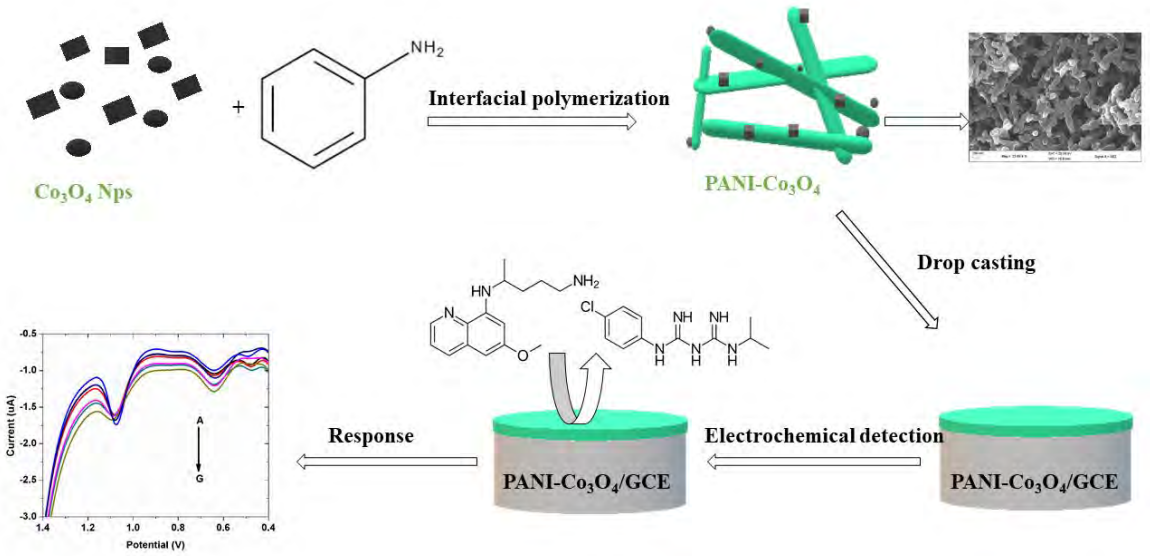

Microchemical Journal 160 (2021) 105709

Contents lists available at ScienceDirect

Microchemical Journal

journal homepage: www.elsevier.com/locate/microc

Polyaniline-cobalt oxide nanofibers for simultaneous electrochemical determination of antimalarial drugs: Primaquine and proguanil

Zondi Nate, Atal A.S. Gill, Ruchika Chauhan, Rajshekhar Karpoormath*

Department of Pharmaceutical Chemistry, College of Health Sciences, University of KwaZulu-Natal, Westville Campus, Durban 4000, South Africa

ARTICLE INFO

Keywords:
Primaquine
Proguanil
Simultaneous detection
Cobalt oxide
Polyaniline nanofibers

ABSTRACT

Quality control of antimalarial drugs is essential due to the prevalence of counterfeit medicines. In this work, polyaniline-cobalt oxide nanofibers were synthesized using precipitation oxidation and interfacial polymerization. The nanocomposites were characterized using UV–Vis spectroscopy, Fourier transform infrared spectroscopy (FTIR), transmission electron microscopy (TEM), scanning electron microscopy (SEM), Energy-dispersive X-ray spectroscopy (EDX), and X-ray diffraction (XRD). Morphological studies confirmed the formation of PANI nanofibers. The presence of Co_3O_4 in the composite was confirmed by XRD and EDX. Differential pulse voltammetry (DPV) and cyclic voltammetry (CV) were used to study the simultaneous electrochemical detection of primaquine and proguanil using a glassy carbon electrode modified with polyaniline nanofibers incorporated with cobalt oxide nanoparticles (PANI-Co_3O_4/GCE). The optimum pH for the response of the sensor was found to be 3.5 for both drugs. A limit of detection (LOD) of 2.07 nM and 1.42 nM with a linear range of 0.020–0.036 and 0.016–0.028 mM was obtained for primaquine and proguanil, respectively. Additionally, the practical applicability of PANI-Co_3O_4/GCE was studied in human urine with different interfering agents, good recovery of both drugs ranging within 94–105% was achieved. PANI-Co_3O_4 nanocomposite can therefore be used to fabricate electrochemical sensors for quality control purposes.

4.1 ABSTRACT

Quality control of antimalarial drugs is essential due to the prevalence of counterfeit medicines. In this work, polyaniline-cobalt oxide nanofibers were synthesized using precipitation oxidation and interfacial polymerization. The nanocomposites were characterized using Ultraviolet Visible Spectroscopy, Fourier Transform Infrared Spectroscopy (FTIR), Transmission Electron Microscopy (TEM), Scanning Electron Microscopy (SEM), Energy-Dispersive X-Ray Spectroscopy (EDX), and X-Ray Diffraction Spectroscopy (XRD). Morphological studies confirmed the formation of PANI nanofibers. The presence of Co_3O_4 in the composite was confirmed by XRD and EDX. Differential Pulse Voltammetry (DPV) and Cyclic Voltammetry (CV) were used to study the simultaneous electrochemical detection of primaquine and proguanil using a glassy carbon electrode modified with polyaniline nanofibers incorporated with cobalt oxide nanoparticles (PANI-Co_3O_4/GCE). The optimum pH for the response of the sensor was found to be 3.5 for both drugs. A limit of detection (LOD) of 2.07 nM and 1.42 nM with a linear range of 0.020-0.036 and 0.016-0.028 mM was obtained for primaquine and proguanil, respectively. Additionally, the practical applicability of PANI-Co_3O_4/GCE was studied in human urine with different interfering agents, good recovery of both drugs ranging within 94-105 % was achieved. PANI-Co_3O_4 nanocomposite can therefore be used to fabricate electrochemical sensors for quality control purposes.

Keywords: Primaquine, Proguanil, Simultaneous detection, Cobalt oxide, Polyaniline nanofibers.

4.2 INTRODUCTION

Malaria is one of the most common protozoan parasitic diseases, which has become a great public health concern in tropical and subtropical areas [1–3]. In 2017 an estimated 219 million malaria cases were reported worldwide; 435 000 cases resulted in death [4]. Most malaria cases in Africa are due to *Plasmodium falciparum,* while in the North and South America regions, *Plasmodium vivax* is dominant [4–7]. The application of combination therapy in the treatment of malaria due to *Plasmodium falciparum*, *Plasmodium vivax*, and *Plasmodium ovale* is increasing. A combination of primaquine and proguanil is usually recommended to treat uncomplicated malaria due to *Plasmodium vivax* [8]. N-(6-methoxyquinolin-8-yl)pentane-1,4-diamine, commonly known as primaquine (Figure 4:1A), is an FDA approved antimalarial drug. Its main function is to eliminate hypnozoites and schizonts of *Plasmodium ovale* and *Plasmodium vivax* [9–11]. Another antimalarial drug that is mostly used is (1E)-1-[amino-(4-chloroanilino)methylidene]-2-propan-2-yl guanidine commonly known as proguanil (Figure 4:1B). This drug effectively treats *Plasmodium vivax* when combined with other antimalarial drugs such as atovaquone and primaquine. Proguanil plays a crucial role in treating malaria; its function is to stop the reproduction of the parasite in the red blood cells by inhibiting folic acid metabolism [12].

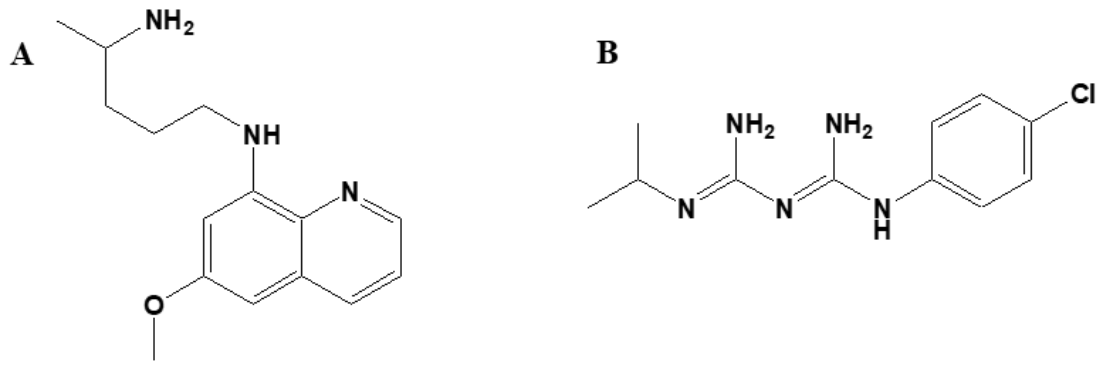

Figure 4:1 (A) Primaquine and (B) Proguanil structure

Quality control of these antimalarial drugs is essential due to the prevalence of counterfeit drugs [13–15]. Different analytical methods have been reported for qualitative and quantitative analysis of primaquine and proguanil. These methods include ultra-performance liquid chromatography [16,17], capillary electrophoresis [18,19] and mass spectrometry [20,21]. However, these methods involve multi-step analysis procedures, which are time-consuming. Electrochemical methods are

gaining interest in pharmaceutical drug analysis because they are rapid, sensitive, and selective to the targeted drug. Several electrochemical methods have been reported to detect primaquine and proguanil; however, these methods focus on individual detection [10,11,22]. To the best of our knowledge, this is the first study to report on the simultaneous electrochemical detection of primaquine and proguanil. This approach is less time consuming and economical since two analytes are analyzed at the same time.

The low cost, thermal stability, high conductivity, and its ability to form nanostructured nanoparticles makes polyaniline to be amongst the commonly used conducting polymers [23]. In recent years, the application of nanostructured conducting polymers such as polyaniline in electrochemical sensors is increasing. This is due to their unique physical and chemical properties that are different from their bulk counterparts. These properties include high surface to volume ratio, flexibility, high porosity, and fast electron transfer rate [24,25]. The morphology of nanostructured polyaniline plays a crucial role in their application in electrochemical sensors. Nanofibers have more active sites available than other morphologies; thus, the sensor's sensitivity is improved since the interaction between the analytes and the polymer occurs close to the underlying electrode [26]. Park et al [27] investigated the effect of shape on the electrochemical properties of nanostructured polyaniline. Nanofibers, nanorods, and nanospheres were used for electrochemical applications. Faster electron kinetics were obtained for nanofibers compared with nanorods and nanospheres. The electrical properties of polyaniline nanofibers can be improved by incorporating metal nanoparticles such as cobalt oxide, silver, and gold [28–31]. Cobalt oxide is a p-type semiconducting material that has good electrocatalytic activity. Co_3O_4 facilitates the oxidation of different pharmaceutical drugs by its ability to change oxidation states [32,33]. Sandhya et al [34] improved PANI shrubs' electron transfer rate by incorporating cobalt oxide nanoparticles.

Several methods have been reported for the synthesis of polyaniline nanostructures [35–38]. In this study, an interfacial polymerization method was used to synthesize well-defined polyaniline nanofibers incorporated with cobalt oxide nanoparticles. The addition of cobalt oxide nanoparticles into polyaniline nanofibers provides several advantages such as good conductivity, higher surface area, and better catalytic activity. The solubility of the nanocomposite is also improved. This study presents a method for synthesizing polyaniline nanofibers incorporated with

cobalt oxide nanoparticles (PANI-Co_3O_4). The prepared nanocomposite was used to modify a glassy carbon electrode (GCE) for simultaneous electrochemical detection of primaquine and proguanil.

4.3 EXPERIMENTAL

4.3.1 Apparatus and chemicals

The optical properties were studied using a UV spectrophotometer (UV-1800, Shimadzu, South Africa). The functional groups of PANI were confirmed by Fourier Transform Infrared Spectroscopy (Bruker® Alpha-P ATR–FT-IR, Germany). Morphological studies were done using Transmission Electron Microscopy (TEM) (JEOL 101, USA) and Field Emission Scanning Electron Microscopy (FE-SEM) (ZEISS ultra plus, Germany). The elemental composition of the nanocomposite was recorded using Energy-Dispersive X-Ray Spectroscopy (EDX). X-ray diffraction patterns were recorded using a Bruker D2 diffractometer at 40.00 kV and 50.00 mA. The measurements were taken at high angle 2θ in a range of 5˚–90˚ with a scan speed of 0.01° 2θ s^{-1} using secondary graphite monochromated Co K alpha radiation (l = 1.79 A˚). CHI660E electrochemical workstation (CH instrument, USA) and a standard three-electrode system were used for all electrochemical measurements. A glassy carbon electrode (3.00 mm), platinum wire, and Ag/AgCl/NaCl (3.00 $molL^{-1}$) were used as working, counter, and reference electrode respectively. pH measurements were performed using the EXTECH PH60 pH meter (China). All the chemicals used in this study were purchased from Sigma Aldrich. Throughout the experiment distilled water was used.

4.3.2 Synthesis of cobalt oxide nanoparticles

For the synthesis of cobalt oxide nanoparticles, the precipitation oxidation method was used with slight modification [39]. Briefly, two solutions were prepared; solution A was made by dissolving 5.00 g of cobalt acetate in 20 ml water and 0.91 g hydrogen peroxide. Solution B was prepared by adding 100 ml water to 1.27 g sodium hydroxide (NaOH) followed by the addition of 20 ml butanol. Solution A was added to solution B, and the mixture was stirred for 16 hours at 85 ℃. After 16 hours, the mixture was washed with 2.00 M hydrochloric acid (HCl) to dissolve the unreacted cobalt hydroxide. The product was further centrifuged with methanol and dried at room temperature.

4.3.3 Synthesis of polyaniline-cobalt oxide (PANI-Co_3O_4) nanocomposite

For the synthesis of PANI-Co_3O_4 nanocomposite, interfacial polymerization was used with some modifications, two solutions were used [38]. Solution A was made up of 4.00 mmol ammonium persulfate in 20 ml HCl and solution B was made up of 4.00 mmol aniline in 20 ml chloroform. 6 mg of Co_3O_4 nanoparticles powder with an average size of 4 nm was added to Solution B. The mixture was stirred for 5 min; solution A was then added to the mixture. The mixture was left undisturbed at room temperature for 24 hours. After 24 hours, a green precipitate was filtered and dried at room temperature. The same procedure was followed for the synthesis of PANI nanofibers without the addition of Co_3O_4 nanoparticles. A yield of 67% and 63% was obtained for PANI and PANI-Co_3O_4, respectively.

4.3.4 Fabrication of PANI-Co_3O_4 modified electrode

The surface of the glassy carbon electrode (GCE) was mechanically polished using 0.05 Microns of alumina slurry followed by rinsing with distilled water to remove any adsorbed alumina particles. A suspension of 5 µL PANI-Co_3O_4 was drop cast on the surface of the clean GCE. The electrode was dried under an IR lamp for 30 min. The modified electrode denoted PANI-Co_3O_4/GCE was used for all electrochemical measurements. All electrochemical measurements were done using the CHI660E electrochemical workstation. Electrochemical impendence spectroscopy measurements were taken at a frequency range of 1- 10000 Hz with 5 mV amplitude, 2.5 mM $[Fe(CN)_6]^{3-}/[Fe(CN)_6]^{4-}$ in 0.1 M KCl was used. Cyclic voltammetry and differential pulse voltammetry measurements were taken using a potential window of 0 to 1.5V and scan rate of 0.1 V in phosphate buffer pH 3.5

4.3.5 Preparation of urine samples

The prepared PANI-Co_3O_4/GCE electrode was tested in real samples; urine samples were collected from a healthy laboratory personnel. The sample was diluted 100 times with 0.1 M phosphate buffer (pH 3.5) to reduce the matrix effect. The diluted samples were spiked with different concentrations of primaquine and proguanil before analysis. The PANI-Co_3O_4/GCE was then used to simultaneously detect primaquine and proguanil in spiked urine samples.

4.4 RESULTS AND DISCUSSION

4.4.1 Material characterization

The optical properties of cobalt oxide nanoparticles were studied using Uv-vis spectroscopy, as shown in Figure 4:S1A. Two absorption peaks at 410 nm and 700 nm were obtained. These peaks are blue-shifted compared to the bulk cobalt oxide which absorbs at 554 nm and 838 nm [40,41]. The peaks at 410 and 700 nm are due to $O^{2-} \rightarrow Co^{2+}$ and $O^{2-} \rightarrow Co^{3+}$ transitions, respectively. Figure 4:S1B shows the X-ray diffraction pattern of cobalt oxide nanoparticles. The peaks at 2Ѳ 19.66, 31.20, 36.05, 45.86, 54.59, 59.71, 65.01 are attributed to (111), (220), (311), (222), (400), (511) and (440) planes respectively of face-centered cubic structure (JCPD: 042-1467). No peaks of impurities were obtained; thus, the prepared cobalt oxide nanoparticles are of high purity. The size and shape of cobalt oxide nanoparticles were confirmed by TEM, as shown in Figure 4:S1C. Cubic particles with an average size of 4.00 nm and narrow size distribution (Figure 4:S1D) were obtained. The smaller size of Co_3O_4 nanoparticles provides a higher surface area; this leads to better electro-catalytic activity. Also, the shape of Co_3O_4 nanoparticles plays a crucial role in their properties since different Miller indices are found in various shapes.

The oxidation levels of the polyaniline nanocomposite were investigated using Uv-vis spectroscopy as shown in Figure 4:S2A. Absorption peaks at 286, 340, and 435 nm were obtained for both the pristine PANI and PANI-Co_3O_4 nanocomposite. These peaks are attributed to л-л* (phenyl ring), л-л* (within benzenoid segment) and polaron- л* transition, respectively. The presence of the 435 nm peak confirms the formation of emeraldine salt PANI [42]. The slight hyper-chromic shift in PANI-Co_3O_4 is due to the presence of cobalt oxide. Figure 4:S2B shows the FTIR spectra of PANI and PANI-Co_3O_4 nanocomposite. The peak at 780 is attributed to (C-H out of plane bending vibration), 1108 (C-H stretch from both quinoid and benzenoid rings), 1279 (C-N stretching mode of secondary aromatic amines), 1557 (C-C bond in quinoid), 1650 (C-C bond in benzenoid ring) and 3350 cm^{-1} (N-H stretching). The addition of cobalt oxide resulted in a peak at 560 and 660 cm^{-1}, these are attributed to metal oxide stretching vibration of the Co^{3+}-O and Co^{2+}-O bands, respectively. Also cobalt oxide interacts with PANI through the qunoid ring and N-H groups, this is shown by a slight shift in peak position to lower wavenumbers. Figure 4:S2C-D shows the SEM images of PANI and PANI-Co_3O_4, nanofibers with an average diameter of 60 nm, and 118 nm, respectively, were obtained. The presence of cobalt oxide nanoparticles did not affect the morphology of PANI nanofibers.

Figure 4:S3A-B shows the XRD pattern of PANI and PANI-Co_3O_4 nanocomposite, the peaks at 2Ɵ 20.73, 25.81, 26.38, and 27.30 are indexed to (020), (220), (111), and (121) planes of conducting PANI [42]. Additionally, cobalt oxide peaks that correspond to a face-centered cubic structure (JCPD: 042-1467) were present in PANI-Co_3O_4. The presence of Co_3O_4 did not affect the crystal structure of PANI. The sharp peak at 2Ɵ 33.3 might be due to the metal sample holder [43]. The area ratio of the crystalline peak to all peaks was used to estimate the degree of crystallinity [44]. The percentage crystallinity values for PANI and PANI-Co_3O_4 were found to be 6.40 % and 7.79 %, respectively. EDX analysis (Figure 4:S3C-D) was done to confirm the presence of C (32.79), N (14.16), O (10.57), S (5.90), Cl (6.16), and Co (0.41) in PANI and PANI-Co_3O_4.

4.4.2 Electrochemical characterization

The Electrochemical Impedance Spectroscopy (EIS) was used for electrochemical characterization of the modified electrode. (EIS) measurements were taken at a frequency range of 1-10000 Hz with a 5 mV amplitude, as shown in Figure 4:S4. The charge resistance transfer (Rct) values for bare GCE, PANI, and PANI-Co_3O_4 were found to be 239.40 Ω, 0.001 Ω, and 0.001 Ω, respectively. These Rct values were obtained from the EIS plot using the standard Randles equivalent circuit (figure inset). The high Rct value for the bare GCE suggests that the diffusion of $[Fe(CN)_6]^{3-}$ /$[Fe(CN)_6]^{4-}$ towards the electrode is low. Thus there is low electro-catalytic activity. The electrode surface was improved by modification with PANI and PANI-Co_3O_4. The semi-circle that was observed in the bare GCE diminished thus a low Rct value was obtained. The decrease in Rct value signifies a high electron transfer rate between the modified electrode and $[Fe(CN)_6]^{3-}$/$[Fe(CN)_6]^{4-}$ .The decrease in Rct value is attributed to the conducting nature of PANI and the high electro-catalytic activity of Co_3O_4 nanoparticles.

4.4.3 Electrochemical behavior

The electrochemical behavior of 0.10 mM primaquine and proguanil in 0.10 M phosphate buffer solution (pH 3.50) at GCE, PANI/GCE, and PANI-Co_3O_4/GCE was investigated by cyclic voltammetry, as shown in Figure 4:2A. A potential window of 0 to 1.50 V was used. No peaks were observed at bare GCE; upon modification with PANI anodic peaks at 0.56 V and 1.20 V were obtained. These anodic peaks are attributed to the oxidation of primaquine and proguanil respectively. No corresponding reduction peak was observed for both drugs; therefore, the

electrode process is an irreversible reaction. A plausible mechanism for the simultaneous electrochemical detection of primaquine and proguanil is shown in Figure 4:3. The anodic peaks at 0.56 V and 1.20 V are due to the irreversible oxidation of 7-methoxyamino quinolone and 4-Chloroaniline moiety in primaquine and proguanil, respectively. The introduction of Co_3O_4 nanoparticles during the chemical polymerization of PANI enhanced the electrochemical performance of the composite; as a result, an increase in anodic peak current was observed at PANI-Co_3O_4/GCE. This increase in peak current is due to fast electron transfer kinetics of the modified electrode.

CV was further used to investigate the effect of scan rate on the oxidation of primaquine and proguanil at PANI-Co_3O_4/GCE, as shown in figure 4:2B. CV voltammograms were recorded by changing the scan rate from 30 to 120 mV/s. An increase in peak current with scan rate was observed. As shown in figure 4:4A-B, a linear relationship between peak current and root of scan rate was observed. Therefore the simultaneous oxidation of primaquine and proguanil at PANI-Co_3O_4/GCE is a diffusion-controlled process [45]. The equation for peak current vs root of scan rate can be expressed as:

$$Ip = 0.01x + 0.17 \ (R^2 = 0.99) \quad (1)$$

$$Ip = 0.40x + 3.10 \ (R^2 = 0.98) \quad (2)$$

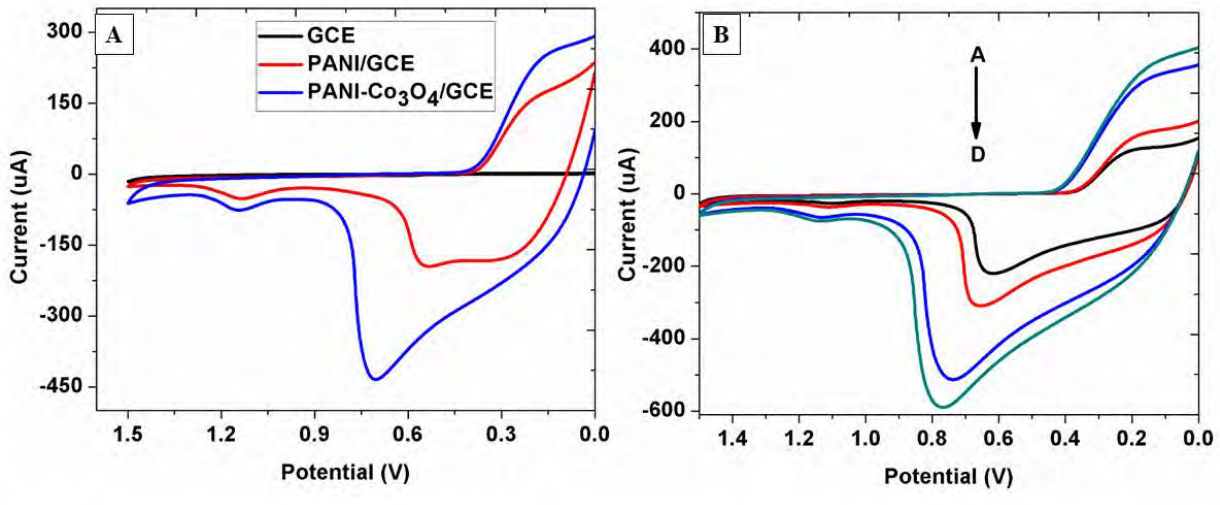

Figure 4:2 (A) Cyclic voltammograms of bare GCE, PANI and PANI-Co3O4/GCE in 0.1 mM proguanil and primaquine (pH 3.5) at a scan rate of 100 mV/s; (B) Cyclic voltammograms of PANI-Co3O4/GCE with change in scan rate

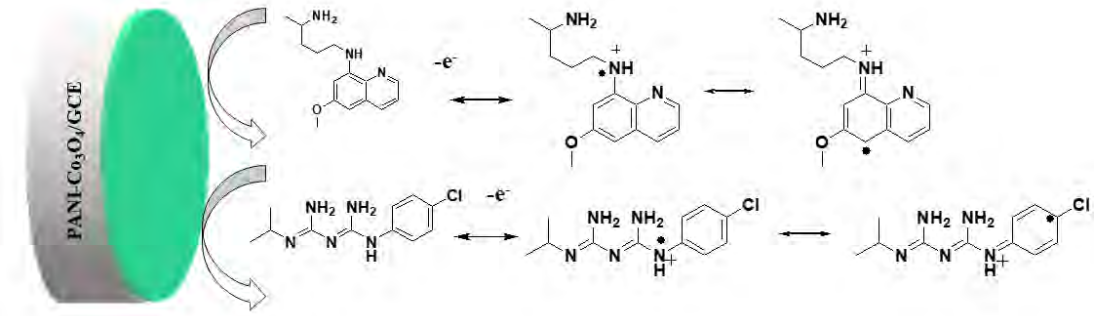

Figure 4:3 Schematic representation of a plausible mechanism for simultaneous electrochemical detection of primaquine and proguanil

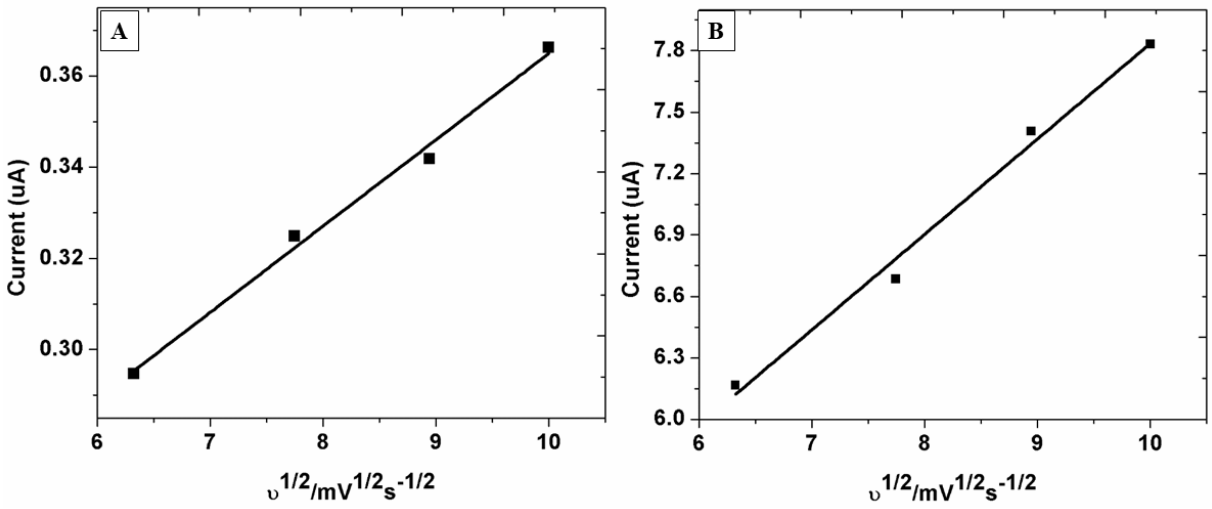

Figure 4:4 Relation between scan rate and current for PANI-Co3O4/GCE in primaquine (A) and proguanil (B)

4.4.4 Influence of pH

The influence of pH on the oxidation of primaquine and proguanil at PANI-Co_3O_4/GCE was investigated using Differential Pulse Voltammetry (DPV), as shown in Figure 4:S5A. The anodic peak current for primaquine decreased between pH 2.00 and pH 3.00. An increase in peak current at pH 3.50 was observed. The current continued to decrease between pH 4.00 and pH 4.50, as shown in Figure 4:S5B. In the case of proguanil, the anodic peak was found to alternate with a change in pH (Figure 4:S5C); the optimum current was also obtained at pH 3.50. For both drugs, the peak potential shifted towards less positive potential as the solution became less acidic. This indicates the presence of a proton-coupled electron transfer reaction. The linear relationship between pH and Ep (V) is expressed using the following regression equation:

$Ep(V)= -0.040x + 0.750$ $(R^2= 0.99)$ primaquine (3)

$Ep(V)= -0.034x + 1.231$ $(R^2= 0.99)$ proguanil (4)

The slope of Ep (V) vs pH for both primaquine and proguanil was calculated to be 0.04 and 0.03 V/pH, respectively. The slope values are biased from the Nernstain slope of 0.059 V/pH. Thus the simultaneous electro-catalytic oxidation of primaquine and proguanil is more complex. The slope values also indicate that an unequal number of protons and electrons are involved in the oxidation of both drugs at PANI-Co_3O_4/GCE.

4.4.5 Analytical performance

The analytical performance of PANI-Co_3O_4/GCE for simultaneous detection of primaquine and proguanil was investigated using Differential Pulse Voltammetry (DPV) under optimum conditions (Figures 4:5A and Figure 4:6A). When the concentration of proguanil was kept constant, a linear relationship between current and primaquine concentration was observed in the range of 0.020-0.036 mM (Figure 4:5B) with a limit of detection (LOD) of 2.07 nM. When the primaquine concentration was kept constant while varying the concentration of proguanil, a linear relationship in the range of 0.016-0.028 mM (Figure 4:6B) with LOD of 1.42 nM was obtained. The equations below represent the corresponding linear regression:

$Ip = 12.05C - 0.07$ $(R^2 = 0.99)$ primaquine (5)

$Ip = 6.10C + 0.59$ $(R^2 = 0.99)$ proguanil (6)

Where C=Concentration of the drug and Ip= peak current. To the best of our knowledge, this is the first study to report on the simultaneous electrochemical detection of primaquine and proguanil. However, the present work was compared with previously reported studies for the detection of primaquine and proguanil separately (Table 4:1). The proposed method shows good sensitivity for the simultaneous detection of the selected drugs.

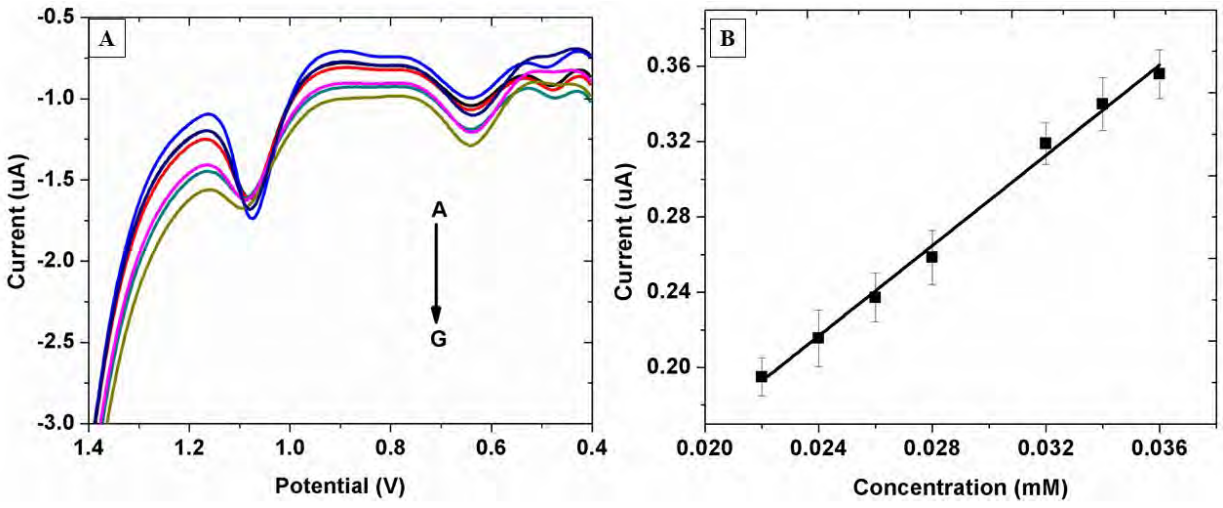

Figure 4:5 (A) DPV voltammogram of primaquine at different concentrations in 0.10 M PBS (pH 3.50) (B) calibration plot for primaquine in 0.10 M PBS (pH 3.50) PANI-Co3O4/GCE

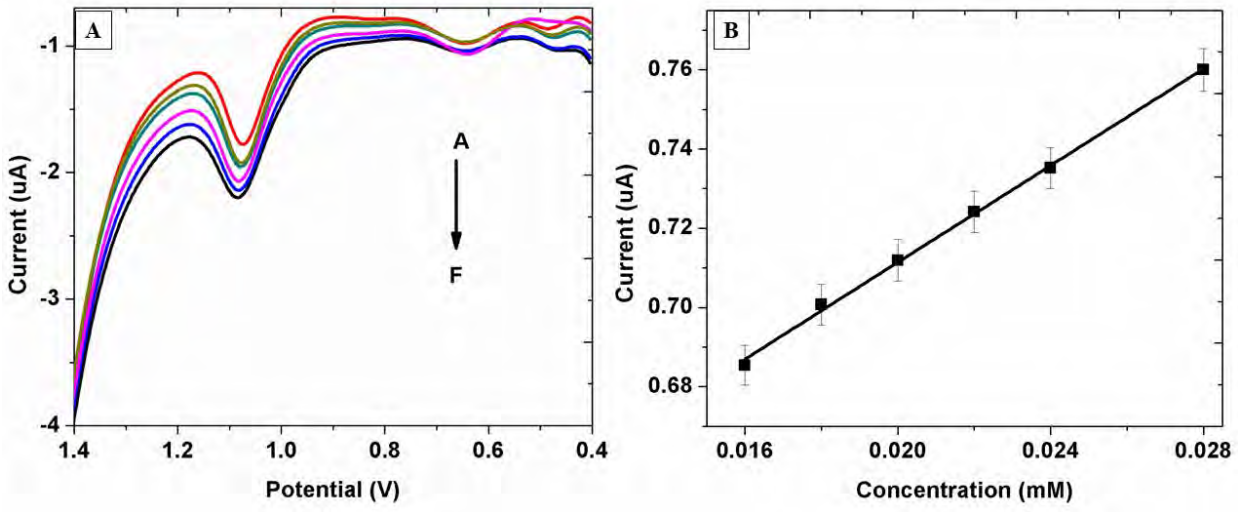

Figure 4:6 (A) DPV voltammogram of proguanil at different concentrations in 0.10 M PBS (pH 3.50) (B) calibration plot for primaquine in 0.10 M PBS (pH 3.50) PANI-Co3O4/GCE

Table 4:1 A comparison of the present study with other reported methods for the electrochemical determination of primaquine and proguanil

Electrode	**Concentration range (mol.L^{-1})**	**Analyte**	**LOD (mol.L^{-1})**	**Ref**
Renewable silver amalgam film	1×10^{-7}-6×10^{-6}	proguanil	2.9×10^{-8}	[22]
CWE/phosphotugnestic acid	1×10^{-5}-1×10^{-2}	proguanil	1×10^{-6}	[12]
Cu-NW/CPE	22.4×10^{-7}-22.7×10^{-6}	primaquine	0.96×10^{-6}	[46]
GCE	3×10^{-5}-1×10^{-4}	primaquine	1.62×10^{-5}	[47]
AuNu/GCE	1×10^{-8}-1×10^{-6}	primaquine	3.52×10^{-9}	[10]
PANI-Co_3O_4/GCE	2×10^{-5}-3.6×10^{-5} 1.6×10^{-5}-2.8×10^{-5}		2.07×10^{-9} 1.42×10^{-9}	Present work

4.4.6 Interference, reproducibility, and real sample

The selectivity of PANI-Co_3O_4/GCE towards primaquine and proguanil was investigated using DPV, as shown in Figure 4:S6. A 200-fold dilution of amodiaquine, a mixture of organic (ascorbic acid, glucose, citric acid, and uric acid) and inorganic (K^+, Cl^-, Mg^{2+}, SO_4^{2-} and Na^+) species were used as interfering agent. During the simultaneous detection of primaquine and proguanil, the modified electrode was found to be selective to primaquine with a deviation that is within the accepted tolerance of 5%. There was interference of more than 5% in the case of proguanil. The

reproducibility of the modified electrode was evaluated using four identically prepared electrodes. Relative standard deviations of 1.90 % and 2.30 % were obtained for primaquine and proguanil, respectively. Thus the modified electrode shows good reproducibility. The practical applicability of the modified electrode was evaluated using a 100-fold dilution of human urine. As shown in Tables 4:2 and 4:3, the recovery results were found to be in the range of 95-104 % and 94.40-105.00 % for primaquine and proguanil, respectively.

Table 4:2 Recovery results for primaquine in the spiked human urine sample

S No	Amount added (mM)	Found (mM)	Recovery (%)	Bias (%)
1	0.02	0.019	95.00	5
2	0.025	0.026	104.00	4
3	0.03	0.031	103.30	3.3

Table 4:3 Recovery results for proguanil in the spiked human urine sample

S No	Amount added (uM)	Found (uM)	Recovery (%)	Bias (%)
1	0.018	0.017	94.40	5.6
2	0.020	0.021	105.00	5
3	0.022	0.023	104.50	4.5

4.5 SUB-CONCLUSION

Precipitation-oxidation and interfacial polymerization methods were successfully employed to prepare PANI-Co_3O_4 nanocomposite. X-Ray Diffraction Spectroscopy and Energy-Dispersive X-Ray Spectroscopy confirmed the presence of cobalt oxide nanoparticles in the composite material. The formation of PANI nanofibers was confirmed by SEM. Simultaneous electrochemical detection of primaquine and proguanil was done using PANI-Co_3O_4/GCE. A detection limit of 2.07 nM and 1.42 nM was obtained for primaquine and proguanil, respectively. Additionally, the practical applicability of the modified electrode was evaluated in human urine and in the presence of different interfering agents. The modified electrode showed good reproducibility, selectivity, and sensitivity. Thus, PANI-Co_3O_4 nanocomposite can be used to fabricate electrochemical sensors for quality control purposes. As far as we could possibly know, this is the first study to report simultaneous electro-oxidation of primaquine and proguanil.

4.6 REFERENCES

[1] G. Figueroa-Miranda, L. Feng, S.C.C. Shiu, R.M. Dirkzwager, Y.W. Cheung, J.A. Tanner, M.J. Schöning, A. Offenhäusser, D. Mayer, Aptamer-based electrochemical biosensor for highly sensitive and selective malaria detection with adjustable dynamic response range and reusability, Sensors Actuators, B Chem. 255 (2018) 235–243. https://doi.org/10.1016/j.snb.2017.07.117.

[2] B. Kumar, V. Bhalla, R.P. Singh Bhadoriya, C.R. Suri, G.C. Varshney, Label-free electrochemical detection of malaria-infected red blood cells, RSC Adv. 6 (2016) 75862–75869. https://doi.org/10.1039/c6ra07665c.

[3] M.E. Casas, M. Hansen, K.A. Krogh, B. Styrishave, E. Björklund, Analytical sample preparation strategies for the determination of antimalarial drugs in human whole blood, plasma and urine, J. Chromatogr. B Anal. Technol. Biomed. Life Sci. 962 (2014) 109–131. https://doi.org/10.1016/j.jchromb.2014.02.048.

[4] WHO, World Malaria Report 2018, Geneva, 2018.

[5] D.E. Loy, W. Liu, Y. Li, G.H. Learn, L.J. Plenderleith, S.A. Sundararaman, P.M. Sharp, B.H. Hahn, Out of Africa: origins and evolution of the human malaria parasites Plasmodium falciparum and Plasmodium vivax, Int. J. Parasitol. 47 (2017) 87–97. https://doi.org/10.1016/j.ijpara.2016.05.008.

[6] WHO, World malaria report 2017, Geneva, 2017.

[7] WHO, World malaria report in 2015, Geneva, 2015.

[8] J. Recht, E.A. Ashley, N.J. White, Use of primaquine and glucose-6-phosphate dehydrogenase deficiency testing: Divergent policies and practices in malaria endemic countries, PLoS Negl. Trop. Dis. 12 (2018) e0006230. https://doi.org/10.1371/journal.pntd.0006230.

[9] D.R. Hill, J.K. Baird, M.E. Parise, L.S. Lewis, E.T. Ryan, A.J. Magill, Primaquine: Report from CDC expert meeting on malaria chemoprophylaxis I, Am. J. Trop. Med. Hyg. 75 (2006) 402–415. https://doi.org/10.4269/ajtmh.2006.75.402.

[10] N.B. Thapliyal, T.E. Chiwunze, R. Karpoormath, S. Cherukupalli, Fabrication of highly sensitive gold nanourchins based electrochemical sensor for nanomolar determination of primaquine, Mater. Sci. Eng. C. 74 (2017) 27–35. https://doi.org/10.1016/j.msec.2016.12.126.

[11] M.J. Pedrozo-Peñafiel, J.M.S. Almeida, C.A.T. Toloza, D.G. Larrudé, W.F. Pacheco, R.Q. Aucelio, Square-wave voltammetric determination of primaquine in urine using a multi-walled carbon nanotube modified electrode, Microchem. J. 150 (2019) 104201. https://doi.org/10.1016/j.microc.2019.104201.

[12] T.D. If, F.M.A. Td, M. Saad, T.D. If, M.S. Rizk, Development of new potentiometric sensors for the determination of proguanil hydrochloride in serum and urine, 27 (2016) 857–863.

[13] K. Karunamoorthi, The counterfeit antimalarial is a crime against humanity: a systematic review of the scientific evidence, Malar. J. 13 (2014) 209. https://doi.org/10.1186/1475-2875-13-209.

[14] L. Mhando, M.B. Jande, A. Liwa, S. Mwita, K.J. Marwa, Public Awareness and Identification of Counterfeit Drugs in Tanzania: A View on Antimalarial Drugs, Adv. Public Heal. 2016 (2016) 6254157. https://doi.org/10.1155/2016/6254157.

[15] WHO, A study on the public health and socioeconomic impact of substandard and falsified medical products, Geneva, 2017.

[16] T.A. Miranda, P.H.R. Silva, G.A. Pianetti, I.C. César, Simultaneous quantitation of chloroquine and primaquine by UPLC-DAD and comparison with a HPLC-DAD method, (2015) 1–7. https://doi.org/10.1186/s12936-015-0570-1.

[17] V.G. Dongre, P.P. Karmuse, P.P. Rao, A. Kumar, Development and validation of UPLC method for determination of primaquine phosphate and its impurities, J. Pharm. Biomed. Anal. 46 (2008) 236–242. https://doi.org/https://doi.org/10.1016/j.jpba.2007.09.012.

[18] M. Heller, L. Vitali, M.A. Siqueira, A.V.F. Sako, M. Piovezan, G.A. Micke, Capillary Electrophoresis with UV Detection to Determine Cocaine on Circulated Banknotes, ISRN

Anal. Chem. 2013 (2013) 1–7. https://doi.org/10.1155/2013/489705.

[19] M. Rambla-alegre, J. Peris-vicente, J. Esteve-romero, M. Capella-peiró, D. Bose, Analytica Chimica Acta Capillary electrophoresis determination of antihistamines in serum and pharmaceuticals, 666 (2010) 102–109. https://doi.org/10.1016/j.aca.2010.03.041.

[20] I. Brondz, D. Mantzilas, U. Klein, D. Ekeberg, E. Hvattum, M.N. Lebedeva, F.S. Mikhailitsyn, G.D. Souleimanov, J. Røe, Nature of the main contaminant in the anti malaria drug primaquine diphosphate: A qualitative isomer analysis, J. Chromatogr. B Anal. Technol. Biomed. Life Sci. 800 (2004) 211–223. https://doi.org/10.1016/j.jchromb.2003.09.042.

[21] K. Na, B. Etienne, A. Guirou, Determination of Primaquine in Whole Blood and Finger - Pricked Capillary Blood Dried on Filter Paper Using HPLC and LCMS / MS, (2014) 561–569. https://doi.org/10.1007/s10337-014-2639-3.

[22] S. Smarzewska, S. Skrzypek, W. Ciesielski, Voltammetric Determination of Proguanil in Malarone and Spiked Urine with a Renewable Silver Amalgam Film Electrode, Electroanalysis. 24 (2012) 1966–1972. https://doi.org/10.1002/elan.201200312.

[23] H. Wang, P.-H. Yang, H.-H. Cai, J. Cai, Constructions of polyaniline nanofiber-based electrochemical sensor for specific detection of nitrite and sensitive monitoring of ascorbic acid scavenging nitrite, Synth. Met. 162 (2012) 326–331. https://doi.org/https://doi.org/10.1016/j.synthmet.2011.12.013.

[24] R. Li, Z. Chen, J. Li, C. Zhang, Q. Guo, Effective synthesis to control the growth of polyaniline nanofibers by interfacial polymerization, Synth. Met. 171 (2013) 39–44. https://doi.org/https://doi.org/10.1016/j.synthmet.2013.02.020.

[25] Y. Shen, Z. Qin, T. Li, F. Zeng, Y. Chen, N. Liu, Boosting the supercapacitor performance of polyaniline nanofibers through sulfonic acid assisted oligomer assembly during seeding polymerization process, Electrochim. Acta. 356 (2020) 136841. https://doi.org/https://doi.org/10.1016/j.electacta.2020.136841.

[26] C.O. Baker, X. Huang, W. Nelson, R.B. Kaner, Polyaniline nanofibers: broadening

applications for conducting polymers, Chem. Soc. Rev. 46 (2017) 1510–1525. https://doi.org/10.1039/C6CS00555A.

[27] H.-W. Park, T. Kim, J. Huh, M. Kang, J.E. Lee, H. Yoon, Anisotropic Growth Control of Polyaniline Nanostructures and Their Morphology-Dependent Electrochemical Characteristics, ACS Nano. 6 (2012) 7624–7633. https://doi.org/10.1021/nn3033425.

[28] M. Xu, Y. Song, Y. Ye, C. Gong, Y. Shen, L. Wang, L. Wang, A novel flexible electrochemical glucose sensor based on gold nanoparticles/polyaniline arrays/carbon cloth electrode, Sensors Actuators B Chem. 252 (2017) 1187–1193. https://doi.org/https://doi.org/10.1016/j.snb.2017.07.147.

[29] Z. Lu, W. Dai, B. Liu, G. Mo, J. Zhang, J. Ye, J. Ye, One pot synthesis of dandelion-like polyaniline coated gold nanoparticles composites for electrochemical sensing applications, J. Colloid Interface Sci. 525 (2018) 86–96. https://doi.org/https://doi.org/10.1016/j.jcis.2018.04.065.

[30] F.M. Zahed, B. Hatamluyi, F. Lorestani, Z. Es'haghi, Silver nanoparticles decorated polyaniline nanocomposite based electrochemical sensor for the determination of anticancer drug 5-fluorouracil, J. Pharm. Biomed. Anal. 161 (2018) 12–19. https://doi.org/https://doi.org/10.1016/j.jpba.2018.08.004.

[31] J. Lei, Y. Zhu, C. Shi, Q. Xu, X. Tao, Appropriate amount of polyaniline coated Co3O4 nanofibers and their excellent electrochemical properties, Phys. E Low-Dimensional Syst. Nanostructures. 117 (2020) 113836. https://doi.org/https://doi.org/10.1016/j.physe.2019.113836.

[32] P.T. Mafuwe, M. Moyo, T. Mugadza, M. Shumba, S. Nyoni, Cobalt oxide nanoparticles anchored polyaniline-appended cobalt tetracarboxy phthalocyanine, modified glassy carbon electrode for facile electrocatalysis of amitrole, J. Solid State Electrochem. 23 (2019) 285–294. https://doi.org/10.1007/s10008-018-4131-8.

[33] M. Houshmand, A. Jabbari, H. Heli, M. Hajjizadeh, A.A. Moosavi-Movahedi, Electrocatalytic oxidation of aspirin and acetaminophen on a cobalt hydroxide nanoparticles modified glassy carbon electrode, J. Solid State Electrochem. 12 (2008) 1117–1128.

https://doi.org/10.1007/s10008-007-0454-6.

[34] S. C.P, R. Baig E, S. Pillai, M. C, A. Aravind, S. J. Devaki, Polyaniline-cobalt oxide nano shrubs based electrodes for supercapacitors with enhanced electrochemical performance, Electrochim. Acta. 324 (2019) 134876. https://doi.org/https://doi.org/10.1016/j.electacta.2019.134876.

[35] T. Li, Y. Zhou, B. Liang, D. Jin, N. Liu, Z. Qin, M. Zhu, One–pot synthesis and electrochemical properties of polyaniline nanofibers through simply tuning acid–base environment of reaction medium, Electrochim. Acta. 249 (2017) 33–42. https://doi.org/https://doi.org/10.1016/j.electacta.2017.07.177.

[36] J. Bhadra, N.J. Al-Thani, S. Karmakar, N.K. Madi, Photo-reduced route of polyaniline nanofiber synthesis with embedded silver nanoparticles, Arab. J. Chem. 12 (2019) 4848–4860. https://doi.org/https://doi.org/10.1016/j.arabjc.2016.10.001.

[37] S. Chen, B. Liu, Y. Wang, H. Cheng, X. Zhang, S. Xu, H. Liu, W. Liu, C. Hu, Excellent Electrochemical Performances of Intrinsic Polyaniline Nanofibers Fabricated by Electrochemical Deposition, J. Wuhan Univ. Technol. Sci. Ed. 34 (2019) 216–222. https://doi.org/10.1007/s11595-019-2038-6.

[38] A. Abdolahi, E. Hamzah, Z. Ibrahim, S. Hashim, Synthesis of Uniform Polyaniline Nanofibers through Interfacial Polymerization, (2012) 1487–1494. https://doi.org/10.3390/ma5081487.

[39] E.L. Viljoen, M.J. Moloto, P.M. Thabede, Impact of acetate ions on the shape of Co3O4 nanoparticles, Dig. J. Nanomater. Biostructures. 12 (2017) 571–577.

[40] Q. Yuanchun, Z. Yanbao, W. Zhishen, Preparation of cobalt oxide nanoparticles and cobalt powders by solvothermal process and their characterization, Mater. Chem. Phys. 110 (2008) 457–462. https://doi.org/https://doi.org/10.1016/j.matchemphys.2008.03.001.

[41] S. Farhadi, M. Javanmard, G. Nadri, Characterization of Cobalt Oxide Nanoparticles Prepared by the Thermal Decomposition of [Co(NH3)5(H2O)](NO3)3 Complex and Study of Their Photocatalytic Activity., Acta Chim. Slov. 63 (2016) 335–343.

[42] V. Kumar, R. Mahajan, I. Kaur, K.-H. Kim, Simple and Mediator-Free Urea Sensing Based on Engineered Nanodiamonds with Polyaniline Nanofibers Synthesized in Situ, ACS Appl. Mater. Interfaces. 9 (2017) 16813–16823. https://doi.org/10.1021/acsami.7b01948.

[43] X. Shang, M. De Luca, G. Pettinari, G. Bisognin, L. Amidani, E. Fonda, F. Boscherini, M. Berti, G. Ciatto, Quantitative determination of in clustering in In-rich InxGa1-xN thin films, J. Phys. D. Appl. Phys. 47 (2014). https://doi.org/10.1088/0022-3727/47/41/415301.

[44] H. Park, T. Kim, J. Huh, M. Kang, J.E. Lee, H. Yoon, P.E.T. Al, Anisotropic Growth Control of Polyaniline Nanostructures and Their Morphology-Dependent Electrochemical Characteristics, (2012) 7624–7633.

[45] S.N. Prashanth, K.C. Ramesh, J. Seetharamappa, Electrochemical Oxidation of an Immunosuppressant, Mycophenolate Mofetil, and Its Assay in Pharmaceutical Formulations, Int. J. Electrochem. 2011 (2011) 1–7. https://doi.org/10.4061/2011/193041.

[46] M.H. Mashhadizadeh, M. Akbarian, Talanta Voltammetric determination of some antimalarial drugs using a carbon paste electrode modified with Cu (OH) 2 nano-wire, 78 (2009) 1440–1445. https://doi.org/10.1016/j.talanta.2009.02.040.

[47] M.L.P.M. Arguelho, M. Valnice, B. Zanoni, R. Nelson, Electrochemical Oxidation and Voltammetric Determination of the Antimalaria Drug Primaquine, 2719 (2007). https://doi.org/10.1081/AL-200062218.

CHAPTER FIVE

Synthesis of amino functionalized copper metal organic framework (Cu-MOFs) for electrochemical detection of malaria biomarker (β−Hematin)

Graphical Abstract

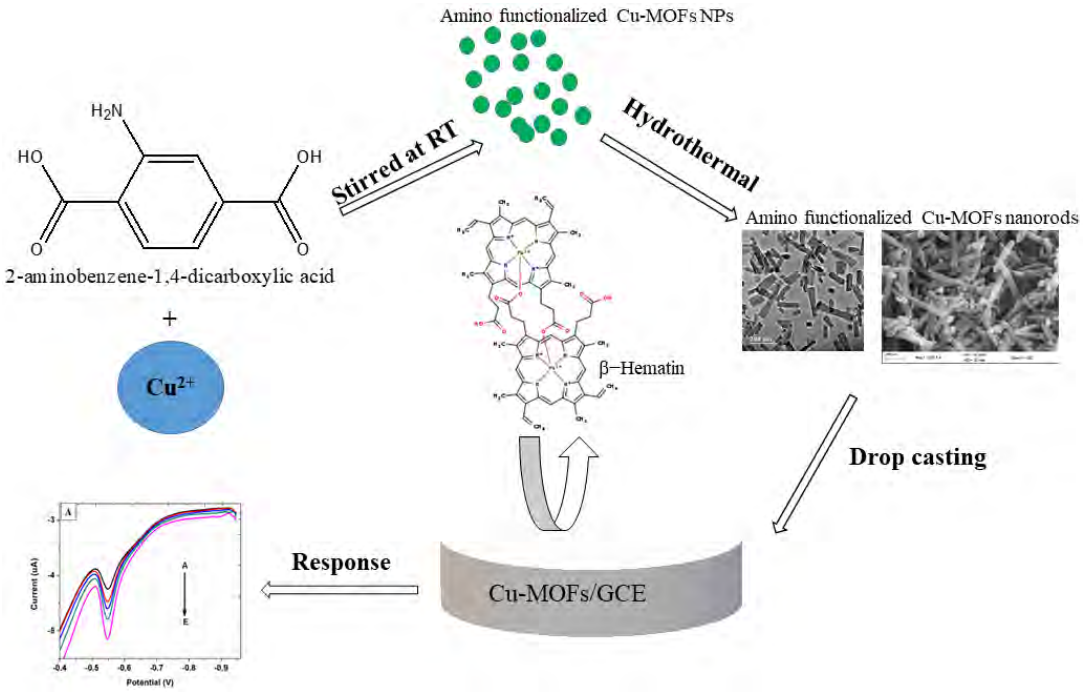

5.1 ABSTRACT

According to the World Health Organization 2019 malaria report, approximately 228 million cases of malaria were reported in which 405 000 resulted in death. Malaria can be detected using different biomarkers; thus, this study was aimed at developing a cheap electrochemical sensor (Cu-MOFs/GCE) for detection and quantification of β−Hematin. β−Hematin is structurally and chemically similar to hemozoin, which is a malaria biomarker. Amino functionalized copper-metal organic frameworks (Cu-MOFs) were synthesized using an Amorphous MOF-Mediated Recrystallization Approach (AMMRA), and the influence of pH on the formation of MOFs was investigated. Cu-MOFs were characterized using Fourier Infrared Spectroscopy (FTIR), Transmission Electron Microscopy (TEM), Ultraviolet Visible Spectroscopy, Scanning Electron Microscopy (SEM) and X-Ray Diffraction Spectroscopy (XRD). Cu-MOFs synthesized at pH 7 were selected as optimum since long nanorods with sharp edges were obtained. Electrochemical studies were carried out using Diffractive Pulse Voltammetry (DPV), Electrochemical Impedance Spectroscopy (EIS) and Cyclic Voltammetry (CV). Additionally, the feasibility of the modified electrode was investigated in some organic and inorganic interfering species. Under optimum conditions, a detection limit of 4.08 μM with a linear range of 0.05 to 0.45 mM was obtained. The present study demonstrated the use of cheap biomarkers (β−Hematin) for the diagnosis of malaria.

Keywords: Malaria, β−Hematin, Copper metal organic frameworks, diffractive pulse voltammetry, cyclic voltammetry.

5.2 INTRODUCTION

Metal-organic frameworks (MOFs) are crystalline porous materials formed by coordination between metal ions and organic linkers. These materials have unique properties that make them be used in various applications such as sensing, catalysis, biomedical imaging, and drug delivery [1,2]. The attractive features of MOFs include; high porosity, high crystallinity, large surface to volume ratio, and tunable pore size. However, these features are dependent on several reaction parameters such as temperature, concentration, solvent, metal ion, capping agent and organic linkers [2,3]. Also the choice of the synthesis method plays a crucial role. Metal organic frameworks can be synthesized using several methods such as microwave, hydrothermal, electrochemical and mechanochemical methods. Jiang et al. [4] investigated the effect of temperature on the synthesis of Co-MOF-74. From the XRD results, it was observed that the change in temperature does not have a significant impact on the formation of Co-MOF-74 crystals. However, temperature plays a vital role in the size and shape of Co-MOF-74. In another study by Zou et al. [3], the effect of solvent on the formation of super long crystal MOFs nanotubes was investigated. Water was found to be an ideal solvent for the formation of MOF nanotubes.

Several studies have reported the influence of pH on the synthesis of MOFs [5,6]. The pH value of a reaction system plays an important role during the synthesis of MOFs, this is because the coordination mode of carboxylic acid ligands such as 2-aminoteraphilic acid are determined by the pH value of the reaction system. Recently, the synthesis of functionalized metal organic frameworks is gaining interest. The presence of these functional groups such as $–NH_2$, -OH and Br improves the physical and chemical properties of the MOFs. Functionalized MOFs can be prepared by in situ synthesis, post modification and physical mixing. Ming et al [7] synthesized the amino functionalized copper based metal organic frameworks using solvothermal method. Spherical MOFs with an average diameter of 236.79 nm was obtained. While Lin et al [8] developed a method for the direct synthesis of amino functionalized MIL-101 (Cr) nanoparticles with an average size of 50 nm. Huo et al [9] reported the synthesis of spherical amino functionalized copper based metal organic frameworks with an average size of 400 nm.

Thus, in the present work the effect of pH value on the synthesis of amino functionalized copper based MOFs using an amorphous MOF-mediated recrystallization approach (AMMRA) was investigated. The synthesized amino functionalized copper MOFs were further used to modify the

surface of a glassy carbon electrode for electrochemical detection of β−Hematin. This is because of the unique electrocatalytic activity of copper MOFs and the affinity of copper to hemozoin. Also the presence of amino functional group will enhance the interaction of the Cu-MOFs with hemozoin. Several studies have shown that hemozoin is chemically and structurally similar to β−Hematin [10–12]. Hemozoin is produced by blood-feeding parasites such as *Plasmodium spp* during the digestion of blood. It is crucial for parasite survival in the host. β−Hematin is cheaper than the two commonly used malaria biomarker for developing detection systems (*Plasmodium falciparum* Lactate Dehydrogenase (PfLDH) and *Plasmodium falciparum* Histidine-rich proteins II (*Pf*HRP-II). To the best of our knowledge, only Obisesan et al. [12] has reported the electrochemical detection and quantification of β−Hematin. However this method showed a poor detection limit and selectivity since agglomerated metal oxide (CuO, Fe_2O_3, and Al_2O_3) nanoparticles were used. Therefore the physical and chemical properties of these metal oxide nanoparticles was compromised. Thus, in this study metal organic frameworks with well-defined morphologies were used.

5.3 EXPERIMENTAL

5.3.1 Apparatus and chemicals

The optical properties and functional groups present in β−Hematin and Cu-MOFs were studied using a UV spectrophotometer (UV-1800, Shimadzu, South Africa) and Fourier Transform Infrared Spectroscopy (Bruker® Alpha-P ATR–FT-IR, Germany) respectively. XRD patterns were recorded using X-ray diffraction (PanAlytical Empyrean, Germany). Morphological studies were done using Transmission Electron Microscopy (TEM) (JEOL 101, USA) and Field Emission Scanning Microscopy (FE-SEM) (ZEISS ultra plus, Germany). CHI660E electrochemical workstation (CH instrument, USA) and a standard three-electrode system were used for all electrochemical measurements. A glassy carbon electrode (3.0 mm), platinum wire, and Ag/AgCl/NaCl (3.0 molL−1) were used as working, counter, and reference electrode, respectively. pH measurements were performed using the EXTECH PH60 pH meter (China). All the chemicals used in this study were purchased from Sigma Aldrich. Throughout the experiment, distilled water was used.

5.3.2 Synthesis of β−Hematin

A method adapted from Obisesan et al [12] was used without any modification, as shown in equation 1. Briefly, hemin chloride (7.9 mM) was dissolved using 8 mL of 0.1 M NaOH solution. The solution was refluxed at 60 ℃ for 10 min, then 1.45 mL of HCl (1 M) was added, and the solution was further stirred for 4 min. after 4 min, 8.825 mL of acetic acid was added, and the solution was stirred for 32 min. After 32 min, the mixture was kept in the dark undisturbed for 24 hours. The solution was then washed with methanol followed by water then dried at room temperature.

$$2Cl - Fe(III)PPIX + CH_3COOH \rightarrow (Fe(III)PPIX)_2 + CH_3COOH^+Cl^- \quad (1)$$

Hemin chloride Acetic acid β−Hematin

5.3.3 Synthesis of amino functionalized copper metal organic frameworks (Cu-MOFs)

An Amorphous MOF-Mediated Recrystallization Approach (AMMRA) was used to synthesize Cu-MOFs nanorods [3]. Briefly, solution A was prepared by dissolving 4 mmol copper acetate in 100 mL methanol. Solution B was prepared by dissolving 1.5 mmol 2-aminoteraphilic acid in 50 mL methanol. Solution B was added slowly to solution A, and the mixture was stirred for 3 hours at room temperature. The final precipitate marked at Cu-MOFs nanoparticles was centrifuged and washed with methanol and water. The Cu-MOF nanoparticles were dispersed in 50 mL water, the pH of the dispersed nanoparticles was adjusted to various pH values (3, 5, 7, 9, 11) using 0.5 M HCl and 0.5 M NaOH. The solution was then transferred into a Teflon-lined autoclave and placed in an oven at 175 ℃ for 12 hours. The solution was then cooled at room temperature and centrifuged using methanol and water. The final product was marked as Cu-MOF nanorods.

5.3.4 Fabrication of Cu-MOF nanorods modified electrode

The surface of the glassy carbon electrode (GCE) was mechanically polished using 0.3 µm and 0.05 µm of alumina slurry followed by rinsing with distilled water to remove any adsorbed alumina particles. Aqueous aliquots (1 mg/mL) of Cu-MOF nanorods that were synthesized at different pH values were prepared. These aliquots were used to modify the surface of GCE. Briefly, a suspension of 5 µL Cu-MOF from the respective aliquots was drop cast on the surface of the clean GCE. The electrode was dried under an IR lamp for 15 min. The modified electrode denoted (Cu-

MOF/GCE) was used for all electrochemical measurements. The electrode was kept at room temperature when not in use.

5.4 RESULTS AND DISCISSION

5.4.1 Characterization of beta hematin

Uv-Vis spectroscopy was used to confirm the formation of β−Hematin from hemin chloride, as shown in Figure 5:1A. An absorption peak at 380 nm was obtained for hemin chloride. The formation of β−Hematin was confirmed by the presence of a peak at 625 nm and a double soret band at 400 nm [12–14]. The peak at 500 nm may be due to the partially altered heme porphyrin [15]. The FTIR spectra of β−Hematin is shown in Figure 5:1B, peaks at 1215 cm^{-1} and 1690 cm^{-1} were obtained for both hemin chloride and β−Hematin. These peaks are due to C-O and C=O stretching of the carboxylate group attached to the Fe(II) centre. Although the peak position for the spectra is the same, intense peaks were obtained for β−Hematin, this indicates a reduction in intermolecular hydrogen bonding. The obtained results are in agreement with previously reported studies [10,16,17].

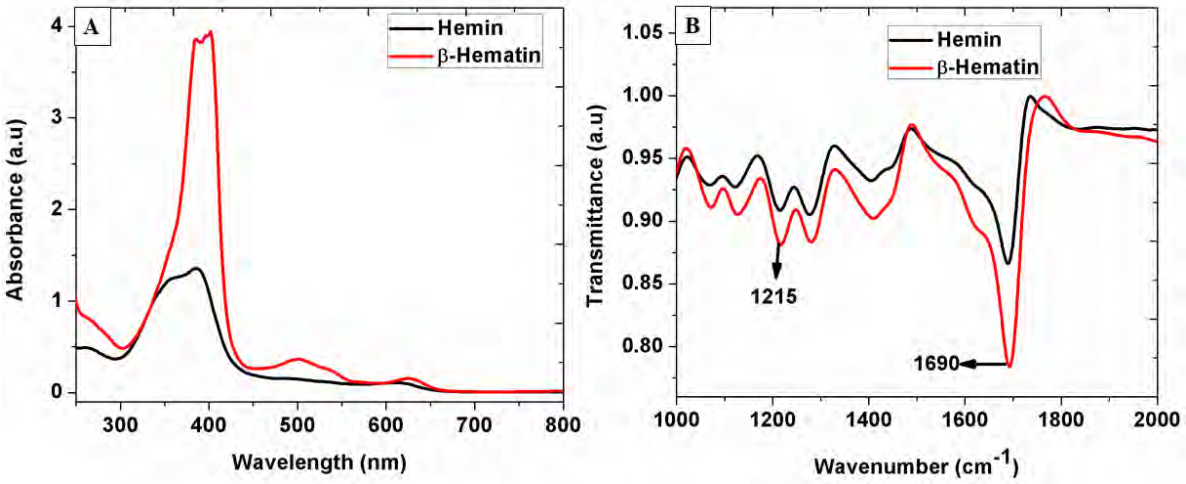

Figure 5:1 (A) Uv-vis (B) FTIR spectra of hemin and β−Hematin

5.4.2 Analysis of Effect of pH on amino functionalized (Cu-MOFs)

During the synthesis of metal-organic frameworks, the pH value of the reaction media plays an important role. This is because the coordination modes of carboxylic acid ligands, such as 2-aminoteraphilic acid are determined by the pH value of the reaction system. Thus the effect of pH value on the synthesis of Cu-MOFs was investigated. The optical properties of Cu-MOFs were

evaluated using Uv-Vis spectroscopy, as shown in Figure 5:2A. An absorption peak at 257, 259, 270, 278, and 322 nm were obtained for pH 3, pH 5, pH 7, pH 9, and pH 11, respectively. These peaks are attributed to a ligand to metal charge transfer transition from oxygen to copper ions [18]. The peaks red-shifted as the solution became more basic. The influence of pH on the synthesis of Cu-MOFs was further confirmed by the change in colour of the solution, as shown in Figure 5:2B. At pH 3, a dark olive green solution was observed; this is due to the protonation of the ligand. A light olive green solution was noted for pH 5; this is attributed to the partial deprotonation of the ligand. As the pH solution became more basic, the ligand was fully deprotonated; thus, a pale green, reddish-brown, and black solution were observed for pH 7, pH 9, and pH 11, respectively.

The FTIR spectra of Cu-MOFs at different pH values is shown in Figure 5:3A. Peaks in the range of 3200-3400 cm^{-1} are observed for pH 3, pH 5, and pH 7. These peaks are attributed to –N-H stretching vibration of $–NH_2$. As the solution becomes more basic, the NH_2 group is deprotonated; thus, no peaks of $–NH_2$ were observed at pH 9 and pH 11. The peaks at 1670 and 1500 cm^{-1} are due to the symmetric and asymmetric stretching vibration of C=O. The coordination of copper with the ligand was confirmed by the presence of a peak at 650 cm^{-1} for pH 3, pH 5, and pH 7. However, this peak was not present at pH 9 and pH 11. This might be due to the dissolving of precursor Cu-MOFs nanoparticles at more basic solutions; thus, the coordination of copper with ligand did not occur [3]. Figure 5:3B shows the XRD patterns of Cu-MOFs at different pH values. The XRD patterns for pH 3, pH 5, and pH 7 are in agreement with the reported literature for Cu-MOFs [19]. pH 9 and pH 11 did not give the predicted simulation. This might be due to the poor complexation of copper with the ligand at higher pH.

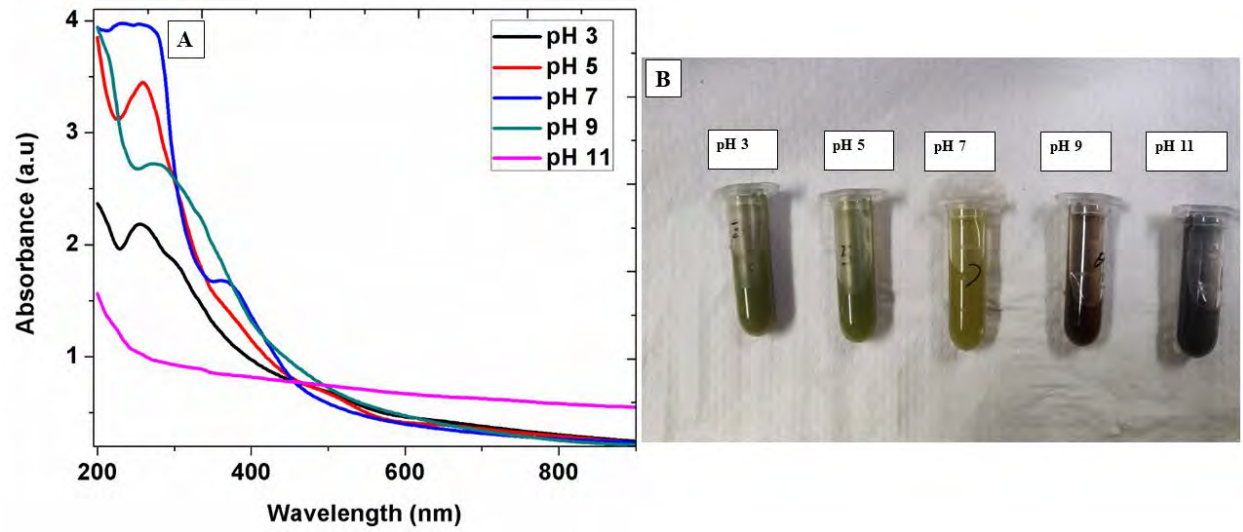

Figure 5:2 (A) Uv-vis spectra (B) images of Cu-MOFs

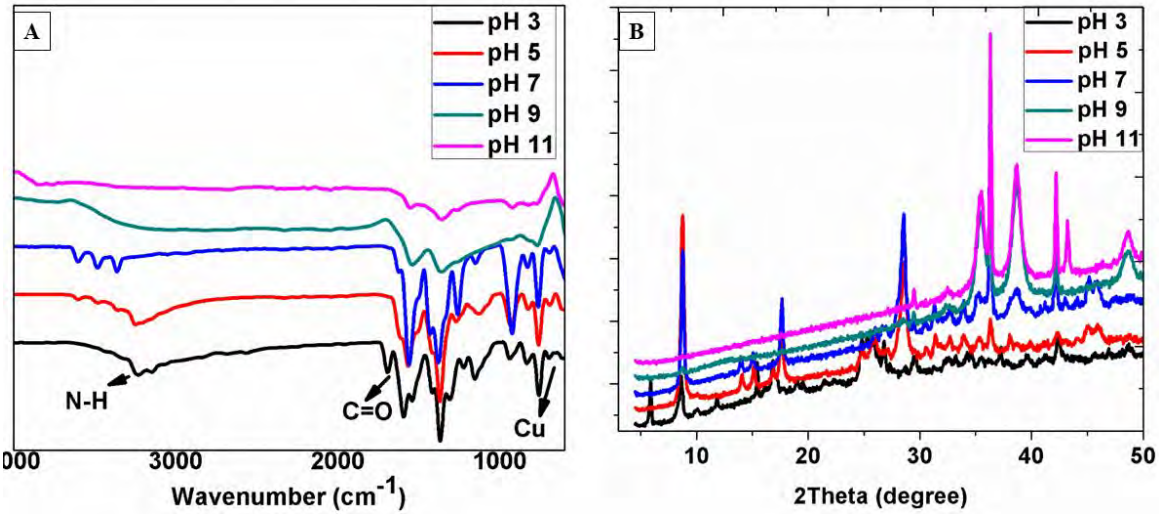

Figure 5:3 (A) FTIR spectra, (B) XRD of Cu-MOFs

The morphological studies of Cu-MOFs were evaluated using SEM and TEM, as shown in Figure 5:4 and 5:5 respectively. At pH 3, nanoflakes were obtained, as the solution become less acidic (pH 5); well defined short rods were obtained. A further increase in pH to 7 resulted in the formation of long rods with sharp edges. At more basic pH values, agglomerated rods started to form. This change in morphology is caused by the dissolving of precursor Cu-MOFs nanoparticles. A similar trend was observed in TEM images.

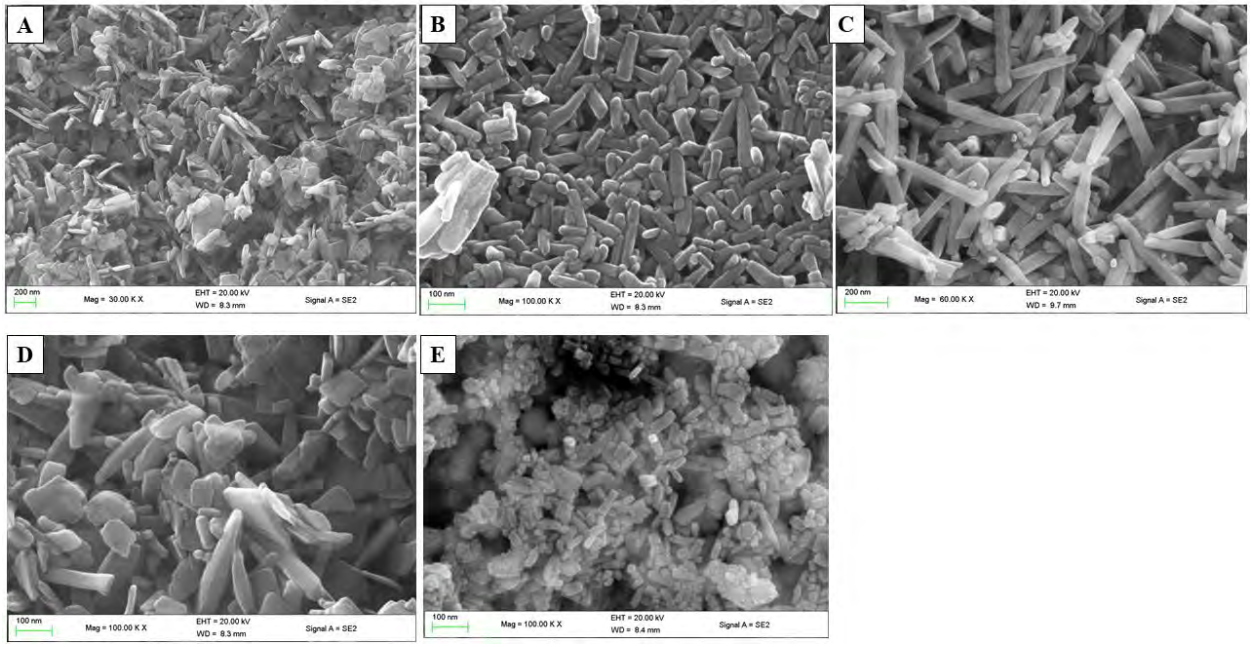

Figure 5:4 SEM images of Cu-MOFs at (A) pH 3, (B) pH 5, (C) pH 7, (D) pH 9, and (E) pH 11

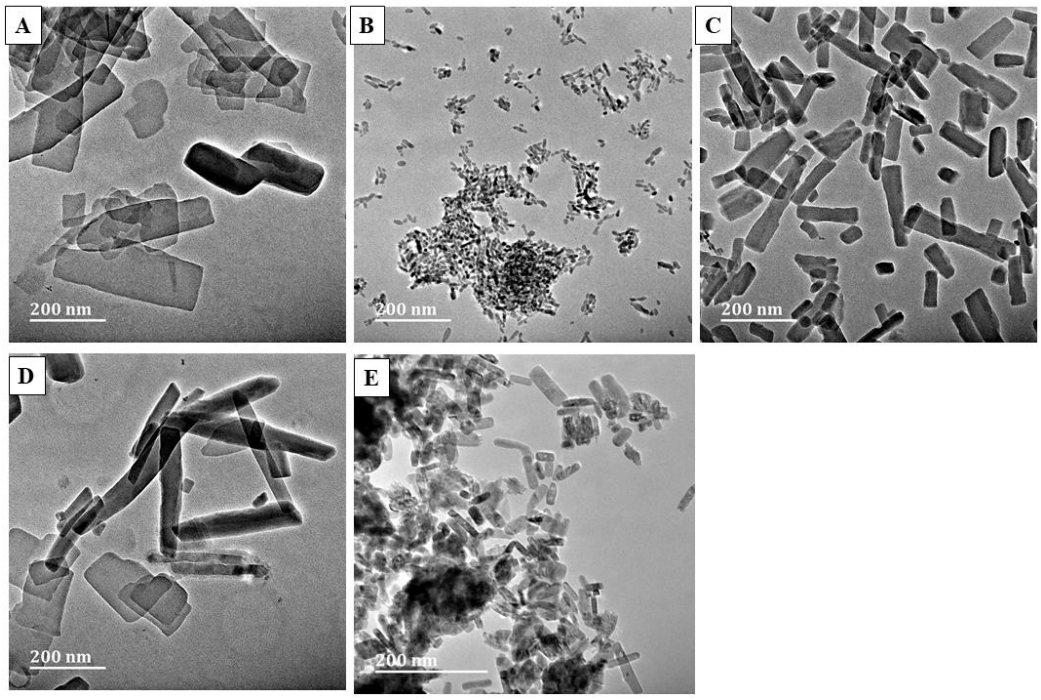

Figure 5:5 TEM images of Cu-MOFs at (A) pH 3, (B) pH 5, (C) pH 7, (D) pH 9, and (E) pH 11

5.4.3 Electrochemical characterization

The electron transfer rate of the modified electrode was investigated using Electrochemical Impedance Spectroscopy (EIS), as shown in Figure 5:6. $[Fe(CN)_6]^{3-}/[Fe(CN)_6]^{4-}$ (2.5 mM) in 0.1 M KCl was used as the redox probe. The EIS data was fitted using the Randles equivalent circuit (insert). A charge transfer resistance (Rct) of 191.9 Ω was obtained for the bare glassy carbon electrode (GCE). This indicates a slow electron transfer between the surface of the electrode and the redox couple. Upon modification with Cu-MOFs synthesized at different pH values, a decrease in Rct was observed for pH 3, pH 5, and pH 7, as shown in Table 5:1. This is attributed to high surface area and ordered pore structures of Cu-MOFs; thus, the electron transfer rate was improved. The size, shape, and degree of agglomeration affect the electrochemical properties of Cu-MOFs. This was confirmed by the increase in Rct values when pH 9 and pH 11 Cu-MOFs were used, as shown in Table 5:1.

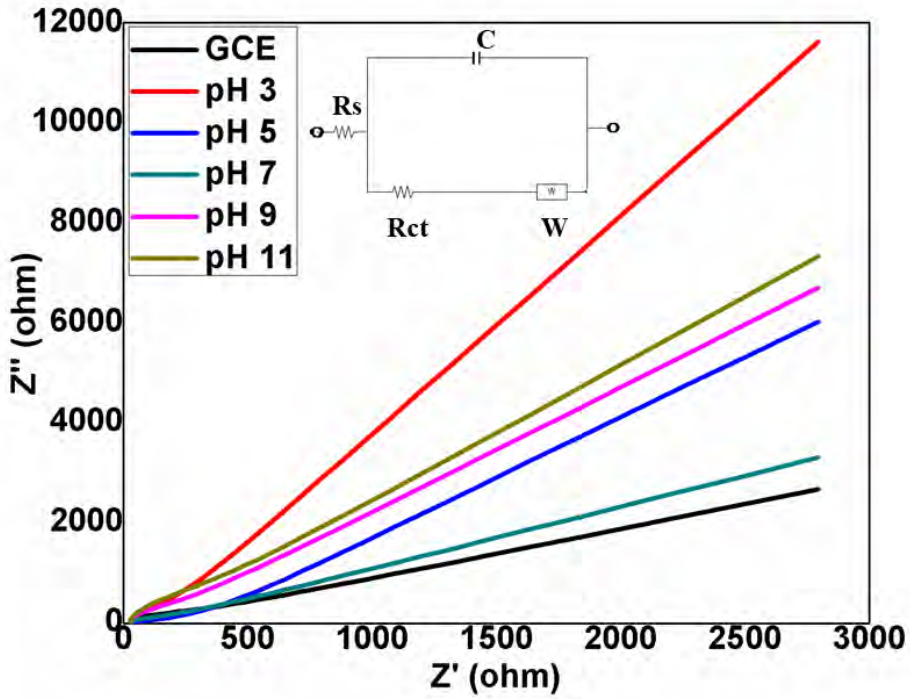

Figure 5:6 EIS measurement of Cu-MOFs/GCE in 2.5 mM $Fe(CN)_6]^{3-}/[Fe(CN)_6]^{4-}$. The inset shows the Randles equivalent circuit (C, W, Rct and Rs represents the double layer capacitance, Warburg impedance, charge-transfer resistance and resistance of the electrolyte solution respectively)

Table 5:1 EIS data obtained for Cu-MOFs/GCE in 2.5 mM $Fe(CN)_6]^{3-}/[Fe(CN)_6]^{4-}$

Electrode	Rs (Ω)	Rct (Ω)	W (Ω)	C (Farad)
GCE	26.04	191.9	0.0001051	8.482×10^{-7}
Cu-MOFs pH 3/GCE	25.44	74.97	2.432×10^{-5}	4.397×10^{-7}
Cu-MOFs pH 5/GCE	38.57	0.113	4.54×10^{-5}	3.68×10^{-7}
Cu-MOFs pH 7/GCE	26.27	0.001	0.0001142	3.72×10^{-7}
Cu-MOFs pH 9/GCE	27.16	255.8	4.21×10^{-5}	4.54×10^{-7}
Cu-MOFs pH 11/GCE	28.02	591.9	3.861×10^{-5}	3.943×10^{-7}

5.4.4 Electrochemical behaviour

The electrochemical behaviour of Cu-MOFs/GCE towards 0.1 mM β−Hematin in 0.1 mM phosphate buffer solution (pH 7.4) was investigated using Cyclic Voltammetry (CV), as shown in Figure 5:7A. For the unmodified GCE, a reduction peak at 0.55 V with a current of 1.411 μA was obtained. This peak was attributed to the reduction of β−Hematin [(Fe (III) protoporphyrin IX)] to [(Fe (II) protoporphyrin IXα]. The modification of the GCE with Cu-MOFs (pH 3, pH 5, and pH 7) resulted in an increase in current as shown in Table 5:2. The increase in current is attributed to high surface area and highly ordered porous structure of Cu-MOFs, which contribute in accumulating β−Hematin towards its pores; therefore, this leads to better sensitivity and selectivity. Also, the morphology of Cu-MOFs plays a crucial role in the electrochemical response of the modified electrode, since well-defined long nanorods (pH 7) shows a better response compared to nanoflakes (pH 3) and short nanorods (pH 5). This is because different miller indices are found in various shapes. This trend can be explained using index facets, long nanorods have high surface energy thus, they have a high density of reactive sites compared to nanoflakes and short nanorods. When Cu-MOFs (pH 9 and pH 11) were used, a decrease in current was observed, as shown in Table 5:2. Thus, Cu-MOFs (pH 7)/GCE was selected for further electrochemical studies.

The electrochemical reaction mechanism of β−Hematin at Cu-MOFs (pH 7)/GCE was investigated by changing the scan rate from 20mV/s to 80mV/s, as shown in Figure 5:7B. An increase in peak current with scan rate was observed. The reduction of β−Hematin at Cu-MOFs (pH 7)/GCE is an adsorption-controlled process. This is supported by a linear relationship between the scan rate and the reduction current (Figure 5:8). The equation for the linear relationship can be expressed as

Ip= 0.0025x + 0.8381 (R^2= 0.9881) (2)

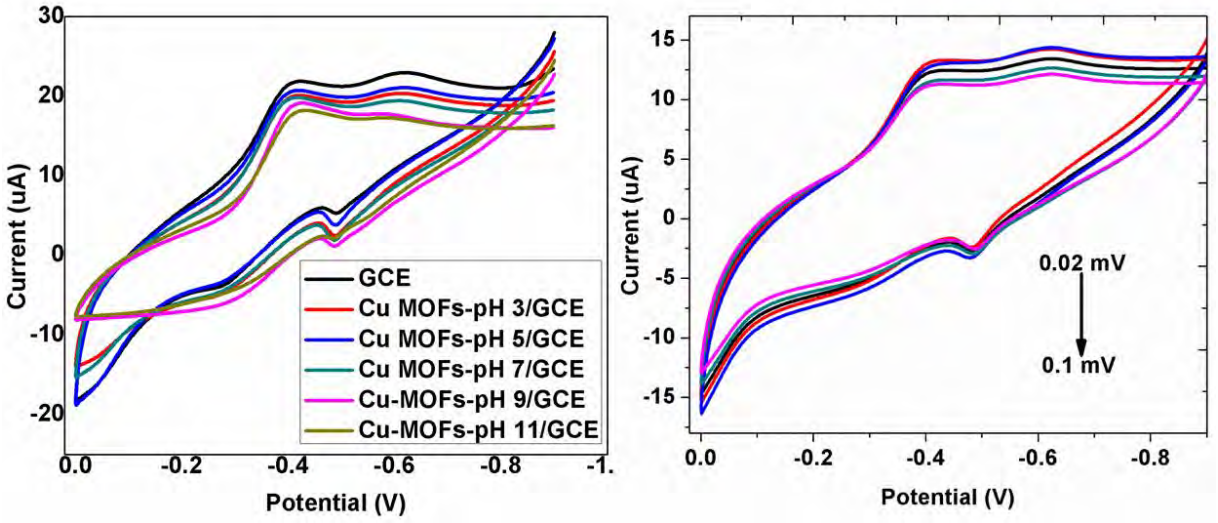

Figure 5:7 (A) Cyclic voltammograms of bare GCE, and Cu-MOFs/GCE in 0.1 mM β−Hematin; (B) Cyclic voltammograms of Cu-MOFs (pH 7)/GCE with change in scan rate

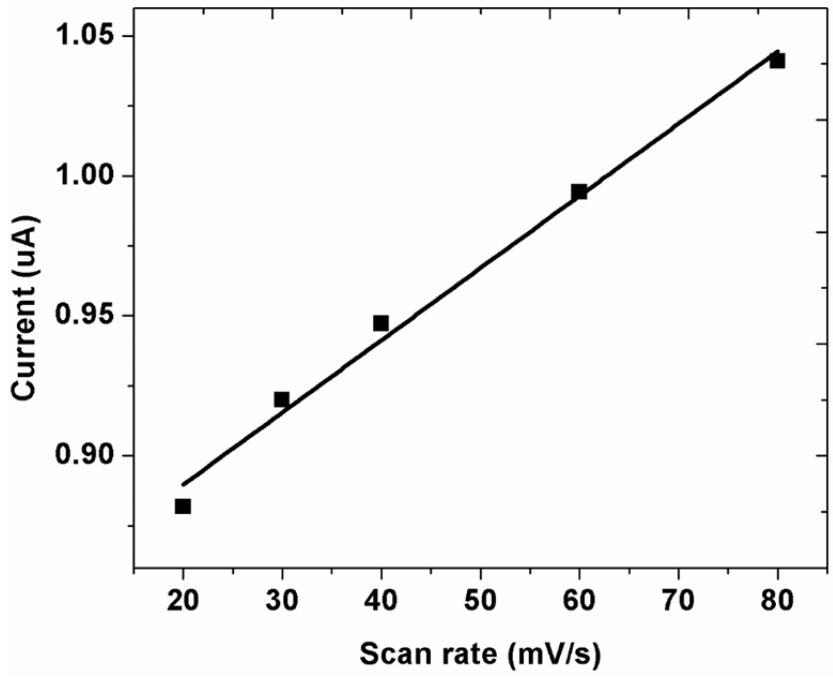

Figure 5:8 Relation between scan rate and current for Cu-MOFs (pH 7)/GCE in β−Hematin

Table 5:2 CV data obtained for Cu-MOFs/GCE in 0.1 mM β−Hematin

Electrode	**Current (µA)**
GCE	1.411
Cu-MOFs pH 3/GCE	1.665
Cu-MOFs pH 5/GCE	2.256
Cu-MOFs pH 7/GCE	2.379
Cu-MOFs pH 9/GCE	1.337
Cu-MOFs pH 11/GCE	1.247

5.4.5 Analytical performance

The analytical performance of Cu-MOFs (pH 7)/GCE was investigated using Differential Pulse Voltammetry (DPV) (Figure 5:9A) under optimum conditions (pulse amplitude 50 mV, step potential 5mV, pulse width 40 ms, sampling width 0.0167 s and pulse period 0.5 s). A potential window of -0.4 to -0.95 V was used. A linear relationship in the range of 0.05 to 0.45 mM was observed between peak current and concentration (Figure 5:9B). The linear equation of the calibration curve was calculated to be

$$Ip= 0.00136C + 0.4432 \quad (3)$$

Where C= concentration of β−Hematin and Ip= current. The limit of detection was calculated to be 4.08 µM. This is attributed to the large volume to surface ratio of Cu-MOFs. To the best of our knowledge, this is the second study to report on the electrochemical detection and quantification of β−Hematin. The present study shows good sensitivity compared to the previously reported work by Obisesan et al. [12].

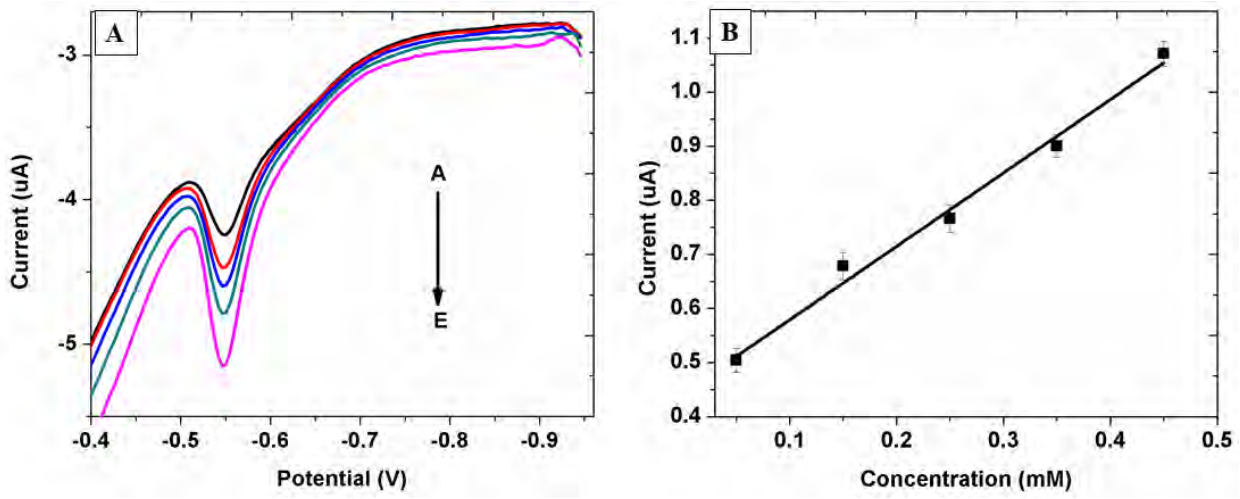

Figure 5:9 (A) DPV voltammograms of Cu-MOFs (pH 7)/GCE in different concentrations of β−Hematin; (B) calibration plots for β−Hematin

5.4.6 Interference and reproducibility

Under optimum conditions, Differential Pulse Voltammetry (DPV) was used to investigate the selectivity of Cu-MOFs (pH 7)/GCE towards 0.1 mM β−Hematin in the presence of 100 fold dilution of interfering agents such as cysteine, ascorbic acid, dopamine, uric acid and glucose. As shown in Figure 5:10A-B, β−Hematin was successfully detected in the presence of these interfering agents, and the deviation was within the accepted tolerance of 10%. This indicates that the modified electrode is selective towards β−Hematin. The reproducibility of the modified electrode was determined using three identically prepared electrodes (Figure 5:11). The relative standard deviation was calculated to be 4.38 % (n=3). Thus the modified electrode showed good reproducibility.

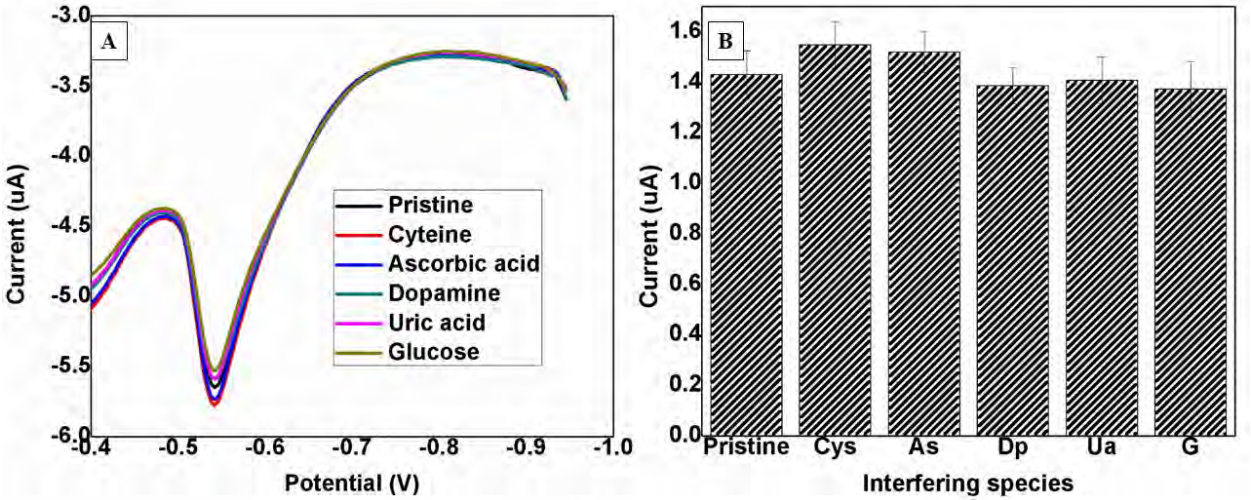

Figure 5:10 DPV voltammograms (A), (B) column graph of β−Hematin with different interfering species

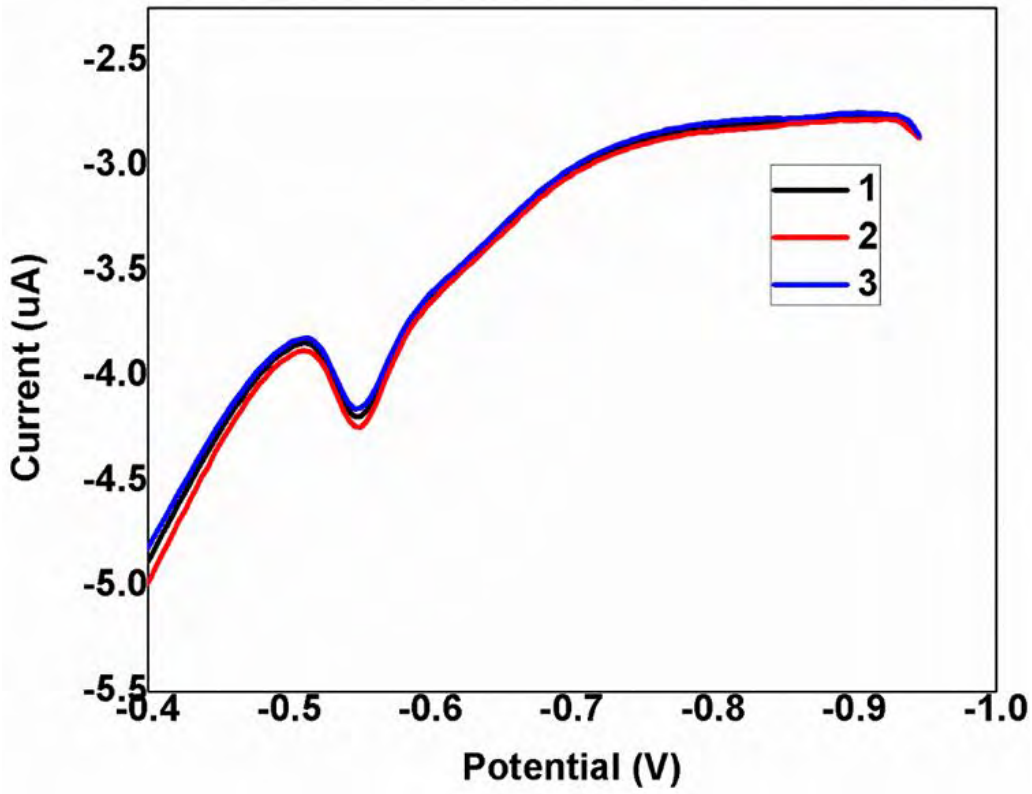

Figure 5:11 DPV voltammograms for reproducibility studies

5.5 SUB-CONCLUSION

The influence of pH on the synthesis of Cu-MOFs nanorods using an amorphous MOF-mediated recrystallization approach (AMMRA) was successfully investigated. SEM and TEM were used to study the morphology of Cu-MOFs. The formation of Cu-MOFs was confirmed by XRD spectroscopy. Electrochemical detection and quantification of β−Hematin were carried out using Cu-MOFs (pH 7)/GCE. A detection limit of 4.08 μM with a linear range of 0.05 to 0.45 mM was obtained. The feasibility of the modified electrode was investigated in some organic and inorganic interfering species. The modified electrode showed good sensitivity and reproducibility compared to the previously reported work by Obisesan et al. [12]. Thus this sensor can be further developed, optimised and used for early diagnosis of malaria in low resource settings. Since malaria affects most under developed countries, the present study demonstrated the use of cheap biomarkers (β−Hematin) for the diagnosis of malaria. Therefore more diagnostic tools can be developed at a lower cost.

5.6 REFERENCES

[1] M. Chauhan, S.K. Bhardwaj, G. Bhanjana, R. Kumar, N. Dilbaghi, S. Kumar, G.R. Chaudhary, Chapter 3 - Conducting Polymers and Metal-Organic Frameworks as Advanced Materials for Development of Nanosensors, in: A. Deep, S.B.T.-A. in N. for B. and E.A. Kumar (Eds.), Elsevier, 2019: pp. 43–62. https://doi.org/https://doi.org/10.1016/B978-0-12-817456-2.00003-6.

[2] R. Seetharaj, P. V Vandana, P. Arya, S. Mathew, Dependence of solvents, pH, molar ratio and temperature in tuning metal organic framework architecture, Arab. J. Chem. 12 (2019) 295–315. https://doi.org/https://doi.org/10.1016/j.arabjc.2016.01.003.

[3] L. Zou, C.-C. Hou, Z. Liu, H. Pang, Q. Xu, Superlong Single-Crystal Metal–Organic Framework Nanotubes, J. Am. Chem. Soc. 140 (2018) 15393–15401. https://doi.org/10.1021/jacs.8b09092.

[4] H. Jiang, Q. Wang, H. Wang, Y. Chen, M. Zhang, Temperature effect on the morphology and catalytic performance of Co-MOF-74 in low-temperature NH3-SCR process, Catal. Commun. 80 (2016) 24–27. https://doi.org/https://doi.org/10.1016/j.catcom.2016.03.013.

[5] L. Luo, G.-C. Lv, P. Wang, Q. Liu, K. Chen, W.-Y. Sun, pH-Dependent cobalt(ii)

frameworks with mixed 3,3′,5,5′-tetra(1H-imidazol-1-yl)-1,1′-biphenyl and 1,3,5-benzenetricarboxylate ligands: synthesis, structure and sorption property, CrystEngComm. 15 (2013) 9537–9543. https://doi.org/10.1039/C3CE41056K.

[6] F. Yuan, J. Xie, H.-M. Hu, C.-M. Yuan, B. Xu, M.-L. Yang, F.-X. Dong, G.-L. Xue, Effect of pH/metal ion on the structure of metal–organic frameworks based on novel bifunctionalized ligand 4′-carboxy-4,2′:6′,4″-terpyridine, CrystEngComm. 15 (2013) 1460–1467. https://doi.org/10.1039/C2CE26171E.

[7] F. Ming, J. Hou, D. Huo, J. Zhou, M. Yang, C. Shen, S. Zhang, C. Hou, Copper-based metal–organic framework nanoparticles for sensitive fluorescence detection of ferric ions, Anal. Methods. 11 (2019) 4382–4389. https://doi.org/10.1039/C9AY01093A.

[8] Y. Lin, C. Kong, L. Chen, Direct synthesis of amine-functionalized MIL-101(Cr) nanoparticles and application for CO2 capture, RSC Adv. 2 (2012) 6417–6419. https://doi.org/10.1039/C2RA20641B.

[9] P. Huo, Z. Li, C. Fan, S. Pu, Amino-functionalized copper-based metal–organic frameworks for highly selective and sensitive detection of hypochlorite, New J. Chem. 44 (2020) 19753–19758. https://doi.org/10.1039/D0NJ04256K.

[10] T.J. Egan, E. Hempelmann, W.W. Mavuso, Characterisation of synthetic β-haematin and effects of the antimalarial drugs quinidine, halofantrine, desbutylhalofantrine and mefloquine on its formation, J. Inorg. Biochem. 73 (1999) 101–107. https://doi.org/https://doi.org/10.1016/S0162-0134(98)10095-8.

[11] D.S. Bohle, R.E. Dinnebier, S.K. Madsen, P.W. Stephens, Characterization of the products of the heme detoxification pathway in malarial late trophozoites by X-ray diffraction., J. Biol. Chem. 272 (1997) 713–716. https://doi.org/10.1074/jbc.272.2.713.

[12] O.R. Obisesan, A.S. Adekunle, J.A.O. Oyekunle, T. Sabu, T.T.I. Nkambule, B.B. Mamba, Development of Electrochemical Nanosensor for the Detection of Malaria Parasite in Clinical Samples., Front. Chem. 7 (2019) 89. https://doi.org/10.3389/fchem.2019.00089.

[13] C.D. Fitch, P. Kanjananggulpan, The state of ferriprotoporphyrin IX in malaria pigment., J.

Biol. Chem. 262 (1987) 15552–15555.

[14] E.B. Samson, B.S. Goldschmidt, P.J.D. Whiteside, A.S.M. Sudduth, J.R. Custer, B. Beerntsen, J.A. Viator, Photoacoustic spectroscopy of β-hematin, J. Opt. 14 (2012) 65302. https://doi.org/10.1088/2040-8978/14/6/065302.

[15] S. Zhang, G.S. Gerhard, Heme Mediates Cytotoxicity from Artemisinin and Serves as a General Anti-Proliferation Target, PLoS One. 4 (2009) e7472. https://doi.org/10.1371/journal.pone.0007472.

[16] T.J. Egan, W.W. Mavuso, K.K. Ncokazi, The Mechanism of β-Hematin Formation in Acetate Solution. Parallels between Hemozoin Formation and Biomineralization Processes, Biochemistry. 40 (2001) 204–213. https://doi.org/10.1021/bi0013501.

[17] A.F. Slater, W.J. Swiggard, B.R. Orton, W.D. Flitter, D.E. Goldberg, A. Cerami, G.B. Henderson, An iron-carboxylate bond links the heme units of malaria pigment, Proc. Natl. Acad. Sci. U. S. A. 88 (1991) 325–329. https://doi.org/10.1073/pnas.88.2.325.

[18] R.-P. Ye, L. Lin, C.-C. Chen, J.-X. Yang, F. Li, X. Zhang, D.-J. Li, Y.-Y. Qin, Z. Zhou, Y.-G. Yao, Synthesis of Robust MOF-Derived Cu/SiO2 Catalyst with Low Copper Loading via Sol–Gel Method for the Dimethyl Oxalate Hydrogenation Reaction, ACS Catal. 8 (2018) 3382–3394. https://doi.org/10.1021/acscatal.8b00501.

[19] J. Khan, N. Iqbal, A. Asghar, T. Noor, Novel amine functionalized metal organic framework synthesis for enhanced carbon dioxide capture, Mater. Res. Express. 6 (2019) 105539. https://doi.org/10.1088/2053-1591/ab3ff8.

CHAPTER SIX

Electrospun polyethylene oxide-silica-Co_3O_4 nanofibers for electrochemical detection of *Plasmodium falciparum* histidine-rich protein II

Graphical Abstract

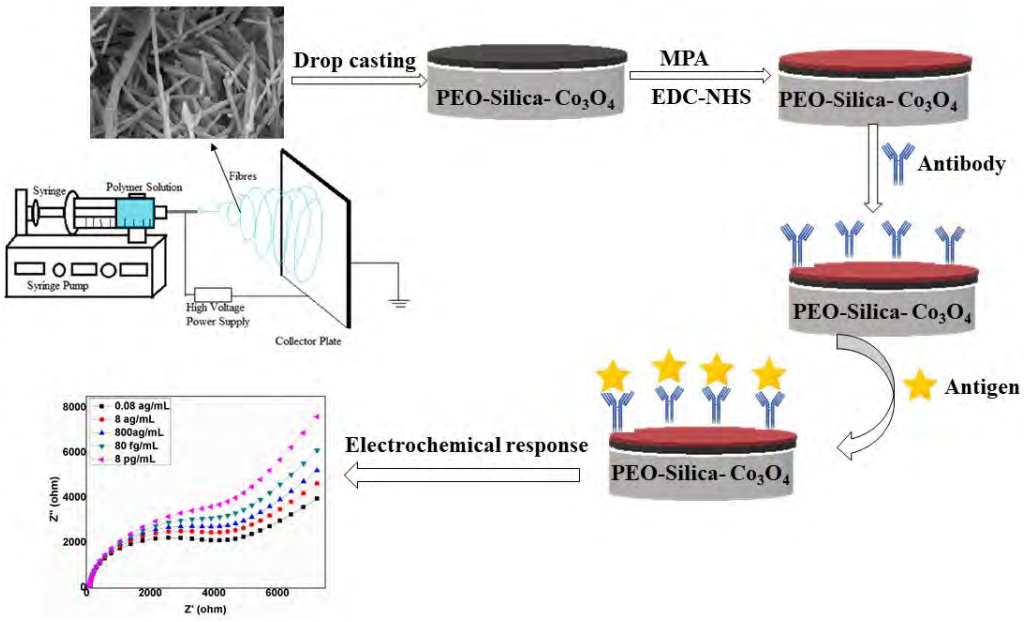

6.1 ABSTRACT

Malaria is one of the most common parasitic disease, which has become a great public health problem. In 2020 an estimated 229 million cases of malaria were reported worldwide, 409 000 cases resulted in death. This study was aimed at developing a rapid and sensitive electrochemical biosensor for the detection of *Plasmodium falciparum* histidine-rich protein 2 (P*f*HRP2). Polyethylene oxide silica nanofibers incorporated with cobalt oxide nanoparticles were fabricated using the electrospinning technique. These nanofibers were characterized using Scanning Electron Microscopy (SEM), Energy-Dispersive X-Ray Spectroscopy (EDX), Fourier Transform Infrared Spectroscopy (FTIR), and X-Ray Diffraction Spectroscopy (XRD). The nanofibers were used to modify a glassy carbon electrode. The modified electrode was functionalized with a self-assembled monolayer of mercaptopropionic acid and Anti-*Pf*HRP2 immobilized with well-established EDC-NHS crosslinking chemistry. Cyclic Voltammetry (CV) and Electrochemical Impendence Spectroscopy (EIS) were used to characterize the modified electrode (Anti-P*f*HRP2/PEO-Silica-Co_3O_4/GCE). EIS was further used to study the electrochemical behavior of (Anti-P*f*HRP2/PEO-Silica-Co_3O_4/GCE towards P*f*HRP2. A detection limit of 1.2×10^{-17} g/mL and 1.83×10^{-17} g/mL was obtained for P*f*HRP2 in phosphate buffer saline and sheep blood serum respectively. The sensor showed good stability, reproducibility, selectivity, and sensitivity, thus it can be used for the diagnosis of malaria in low resource settings.

Keywords: Polyethylene oxide, silica, Nanofibers, *Plasmodium falciparum* histidine-rich protein 2, Immunosensor

6.2 INTRODUCTION

Diseases that are caused by parasites, viruses, and bacteria are a major concern for human health globally. Malaria is one of the serious vector-borne diseases in tropical and subtropical countries. Malaria is caused by a protozoan parasite that belongs to the *Plasmodium* genus. This parasite is vectored by the female mosquitoes of genus *Anopheles* and is transmitted to humans through the mechanism of blood-sucking while feeding [1–3]. In 2019 an estimated 229 million malaria cases were reported globally with 409 000 deaths [4]. Most cases are due to *Plasmodium falciparum*, the high mortality rate is mostly reported in developing countries; this is mainly due to the use of conventional detection methods for malaria with poor sensitivity and the presence of counterfeits antimalarial drugs. As a result treatment of affected patients is delayed. Conventional methods are expensive and carry some disadvantages such as multi-step analysis, they require skilled personnel for operation, and are time-consuming [5–7].

Due to some of the drawbacks of conventional methods, a rapid ultrasensitive diagnostic kit for early detection of malaria is needed, especially in developing and tropical countries. The commonly used malaria biomarkers in diagnostic tools include *Plasmodium falciparum* Lactate Dehydrogenase (*Pf*LDH) [8–10], *Plasmodium falciparum* Histidine-Rich Protein 2 (*Pf*HRP2) [11–13], *Plasmodium falciparum* Glutamate dehydrogenase[14,15], hemozoin [16,17], and aldolase [11,18]. However, *Pf*HRP2 is frequently used because of its unique structure that has multiple epitope copies on a single protein [19]. This results in high-avidity interaction with antibodies. The selectivity and sensitivity of diagnostic tools can be improved by the use of various nanomaterials. Among these materials; polymer nanofibers have gained interest in electrochemical biosensors. This is due to their unique properties such as extremely long length, complex pore structures, high surface area, good surface modification, and controllable surface conformation [20–22].

An immunosensor for early diagnosis of malaria with a detection limit of 0.01 ng/mL was reported by Gikunoo et al [23]. Carbon nanofibers grown on glass micro balloons were used. The method used by Gikunoo et al [23] to synthesis carbon nanofibers is complex. Paul et al [24] developed an electrochemical biosensor for detection of *Plasmodium falciparum* histidine-rich protein 2 (*Pf*HRP2) using copper doped zinc oxide nanofibers fabricated by electrospinning method. A detection limit of 6.8 ag/mL was obtained, this was attributed to the high isoelectric point of zinc oxide and its high diffusion coefficient. The doping of zinc oxide with copper resulted in improved

conductivity and sensitivity. The sensitivity and selectivity of electrochemical biosensors for malaria diagnosis can be improved by using porous biocompatible nanofibers with good electrocatalytic properties. This study focuses on the preparation of polyethylene oxide silica nanofibers incorporated with cobalt oxide nanoparticles using the electrospinning method.

The unique properties of silica nanofibers such as high surface-to-volume ratio, high porosity, high reactivity excellent biocompatibility, and surfaces that can be easily functionalized make them suitable to be used in biosensors. The presence of polyethylene oxide improves the ability of silica to form nanofibers through the electrospinning method. Patel et al [25] reported the formation of beaded morphology when pure silica solution was electrospun without the polymer. While the incorporation of cobalt oxide nanoparticles improves the charge density which results in stronger elongation forces exerted on the polymer jet thus the formation of the nanofibers is favoured. Cobalt oxide nanoparticles also have good electrocatalytic properties.

The polyethylene oxide silica nanofibers incorporated with cobalt oxide nanoparticles nanofibers were used to develop a simple, rapid, low-cost, and sensitive method for the early detection of *Pf*HRP2. To the best of our knowledge, this is the first study the report the application of electrospun nanofibers incorporated with cobalt oxide nanoparticles for electrochemical detection of *Pf*HRP2.

6.3 EXPERIMENTAL

6.3.1 Apparatus and chemicals

Potassium ferricyanide, polyethylene oxide, colloidal silica gel, Mercaptopropionic acid, N-(3-dimethylaminopropyl)-N′ ethylcarbodiimide hydrochloride (EDC, crystalline), ethanol, N-hydroxysuccinimide (NHS), bovine serum albumin, and phosphate buffered saline tablet were purchased from Sigma Aldrich (South Africa). *Plasmodium falciparum* histidine-rich protein 2 antibody (Anti-P*f*HRP2) and *Plasmodium falciparum* histidine-rich protein 2 antigen were purchased from MyBioSource INC (USA). Elemental composition and morphological studies were done using Energy-Dispersive X-Ray Spectroscopy (EDX) and Field Emission Scanning Electron Microscopy (FE-SEM) (ZEISS ultra plus, Germany), respectively. X-ray diffraction patterns (XRD) were recorded using a multipurpose Bruker AXS D8 advance diffractometer (Germany) at 40 kV and 40 mA. The functional groups were confirmed by Fourier Transform Infrared Spectroscopy (Bruker® Alpha-P ATR–FT-IR, Germany). CHI660E electrochemical

workstation (CH instrument, USA) and a standard three-electrode system were used for all electrochemical measurements. Ag/AgCl/NaCl (3.00 $molL^{-1}$), glassy carbon electrode (3.00 mm), and platinum wire were used as a reference, working and counter electrode respectively. Distilled water was used throughout the experiment. The synthesis of cubic cobalt oxide nanoparticles with an average size of 4 nm was reported in our previous work [26].

6.3.2 Synthesis of Polyethylene-silica-cobalt oxide (PEO-Silica-Co_3O_4) nanofibers

PEO-Silica-Co_3O_4 nanofibers were prepared using the electrospinning method as adopted from Shah et al [27] with slight modification. 5% PEO solution was prepared by dissolving 5 g PEO powder in 38 g distilled water, the solution was stirred for 10 minutes. 40 g colloidal silica (30%) was slowly added to the PEO solution, the mixture was stirred for 2 hours. 0.8 g cubic cobalt oxide nanoparticles with an average size of 4 nm were added and the mixture was further stirred for 2 hours. The mixture was electrospun and the following parameters were used; applied voltage 25 KV, the distance between the nozzle tip and ground collector 10 cm. A similar procedure was followed for PEO-Silica nanofibers without the addition of cubic cobalt oxide nanoparticles. PEO-Silica-Co_3O_4 and PEO-Silica nanofibers were calcined at 350 ℃ for 3 hours.

6.3.3 Fabrication of PEO-Silica-Co_3O_4 modified electrode

The alumina slurry with the size of 0.05 Microns was used to polish the surface of the glassy carbon electrode (GCE), followed by rinsing with distilled water to remove any adsorbed alumina particles. A suspension of 5 µL PEO-Silica-Co_3O_4 was drop cast on the surface of the clean GCE. The electrode was dried under an IR lamp for 15 min. Mercaptopropionic acid (MPA) treatment was carried out by drop-casting 5 µL of 10 mM MPA prepared in ethanol into the modified. The electrode was allowed to dry at room temperature before antibody immobilization.

6.3.4 Anti-*Pf*HRP2 immobilization

Monoclonal Anti-*Pf*HRP2 was chemically attached to PEO-Silica-Co_3O_4 MPA functionalized electrode surface using well-established EDC-NHS crosslinking chemistry. Onto the modified electrode 5 µL of Anti-P*f*HRP2 (0.15 mg/mL) was drop casted and the electrode was stored at 4 ℃ for 24 hours. The electrode was then washed with distilled water to remove unbound antibodies. This was followed by treatment with BSA solution (1% wt) to block nonspecific sites. The electrode was kept at 4 ℃ when not in use.

6.3.5 Interaction of *Pf*HRP2 antigen with the modified electrode

The desired dilutions of P*f*HRP2 antigen (0.08 ag/mL - 80 fg/mL) were prepared in 0.01 M phosphate buffer saline (PBS) (pH 7.4). The P*f*HRP2 solution was kept in ice during the experiments to avoid their aggregation. 5 µL of the P*f*HRP2 antigen was drop casted onto the modified electrode and incubated for 60 min at room temperature. The modified electrode was rinsed with distilled water to remove any unbounded P*f*HRP2 antigen.

6.3.6 Preparation of serum samples

The sheep blood serum samples were collected from Professor Thirumala Govender laboratory at the University of Kwazulu Natal, Westville campus South Africa. To minimize the matrix effect, the serum samples were diluted 10 times with 0.01 M phosphate buffer solution (pH 7.4). The modified electrode was then used to detect and quantify *Pf*HRP2 in sheep blood serum samples. 2.5 mM $[Fe(CN)_6]^{3-/-4}$ was used as a redox couple.

6.4 RESULTS AND DISCUSSION

6.4.1 Characterization of PEO-Silica-Co_3O_4 nanofibers

Energy Dispersive X-Ray Spectroscopy (EDX) was used to confirm the presence of cobalt oxide nanoparticles in the nanofibers (Figure 6:1A-B). The elemental composition for carbon, oxygen, silicon, and cobalt was found to be 12.09, 46.35, 41.31, 0.22 %, and 51.65, 48.01, 0.34% for PEO-Silica-Co_3O_4 before and after calcination respectively. To confirm the presence of PEO and silica in the nanofibers Fourier Transform Infrared Spectroscopy (FTIR) was used. PEO-Silica before calcination (Figure 6:2) showed peaks at 782, 965, 1100 cm^{-1} which are attributed to Si-O-Si symmetric stretching, Si-O-H stretching, and Si-O-Si asymmetric stretching vibrations respectively of silica. The peaks at 2877, 1100, 1300-1400 cm^{-1} are due to C-H asymmetric stretching of CH_2, C-O-C stretching vibration, C-H swinging vibration in CH_2 respectively of PEO. The peak at 3400 cm^{-1} is due to moisture. After calcination, only peaks belonging to Silica were observed thus the PEO was completely removed. The addition of cobalt oxide nanoparticles to the PEO silica solution before electrospinning resulted in a slight shift in peak position for both PEO and silica. After calcination, the PEO was completely removed. The XRD patterns of the fabricated nanofibers are shown in Figure 6:3, an amorphous peak at 23 was observed. This is a characteristic peak of silica. The silica peak overlaps with the PEO characteristic peaks. The incorporation of cobalt nanoparticles improved the crystallinity of silica as shown in Figure 6:4.

The presence of cobalt oxide nanoparticles was confirmed by the peaks at 2Θ 19.66, 31.20, 36.05, 45.86, 54.59, 59.71, and, 65.01 these peaks are attributed to (111), (220), (311), (222), (400), (511) and (440) planes respectively of face-centered cubic structure (JCPD: 042-1467).

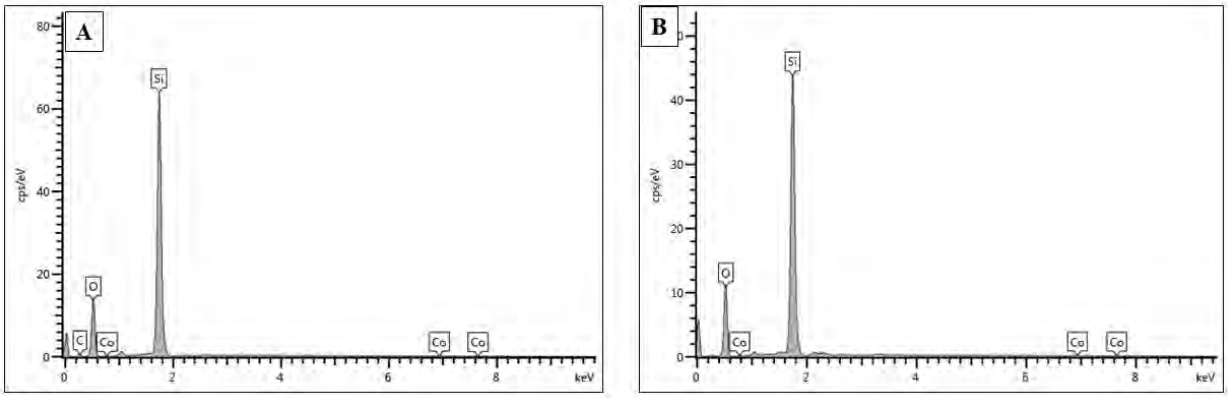

Figure 6:1 EDX of (A) PEO-Silica-Co_3O_4 before (B) PEO-Silica-Co_3O_4 after calcination

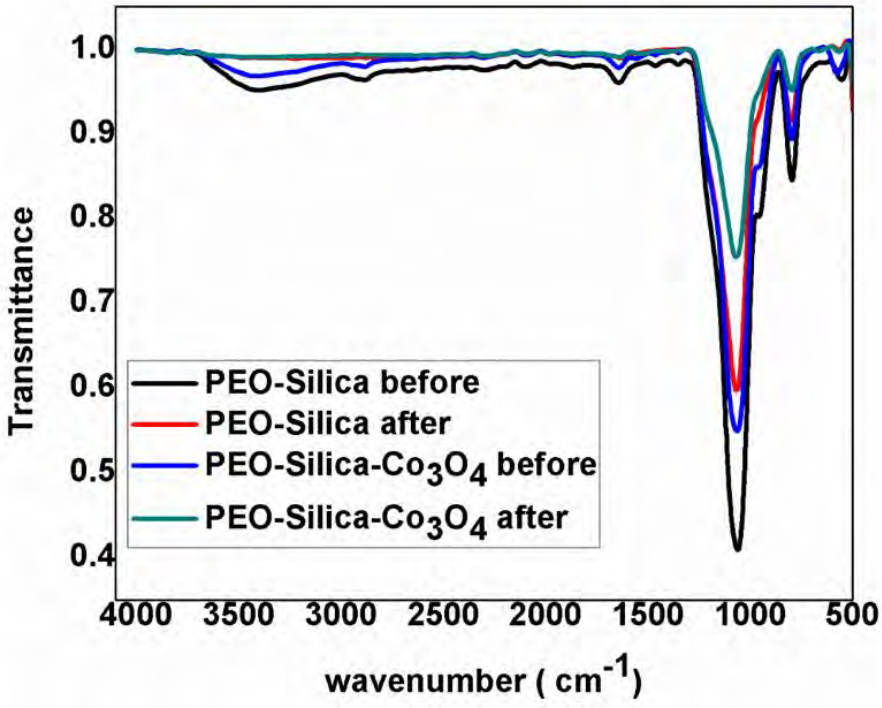

Figure 6:2 FTIR spectra of PEO-silica and PEO-Silica-Co_3O_4 before and after calcination

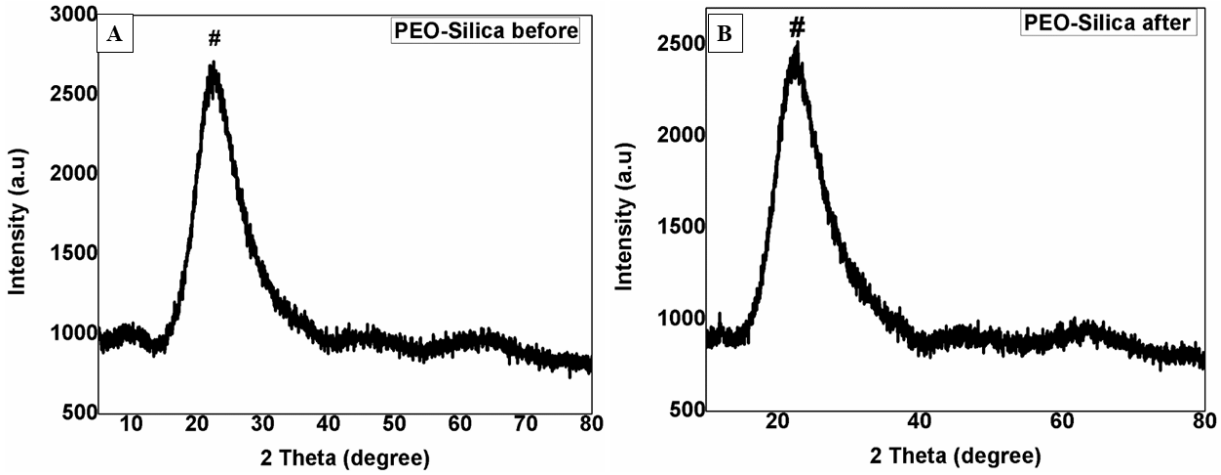

Figure 6:3 XRD spectra of (A) PEO-Silica before, (B) PEO-Silica after calcination

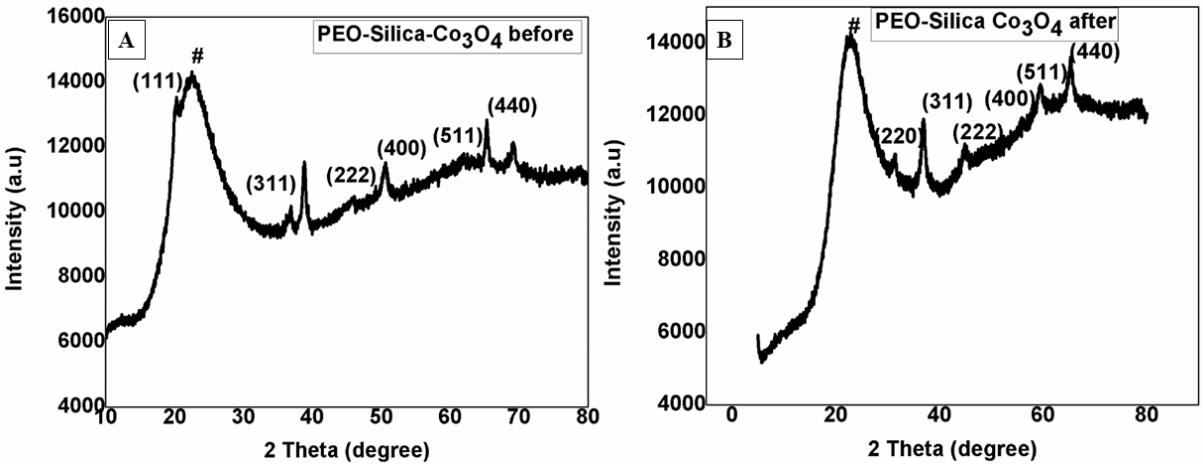

Figure 6:4 (A) PEO-Silica-Co_3O_4 before, (B) PEO-Silica-Co_3O_4 after calcination

The morphological studies of the prepared nanofibers were done using Scanning Electron Microscopy (SEM) as shown in Figure 6:5. Nanofibers with sharp edges (Figure 6:5A) with an average diameter of 248 nm were obtained for PEO-Silica before calcination (Figure 6:6A). The presence of PEO improves the ability of silica to form nanofibers through the electrospinning technique. Patel et al [25] reported the formation of beaded morphology when pure silica solution was electrospun without the polymer. This was attributed to the low molecular weight and low viscosity of the sol-gel silicates in the spinning solution. After calcination (Figure 6:5B) the diameter of the nanofibers decreased from 248 nm to 224 nm (Figure 6:6B), this is mainly due to the removal of PEO. It also observed that the nanofibers retained their morphology post

calcination. The incorporation of cobalt oxide nanoparticles into PEO-silica solution before electrospinning resulted in the formation of long nanofibers with no sharp edges (Figure 6:5C). An average diameter of 237 nm (Figure 6:6C) was obtained. This is due to improved charge density which results in stronger elongation forces exerted on the polymer jet thus the formation of the nanofibers is favoured. Also, the addition of cobalt oxide nanoparticles plays a crucial role in controlling the morphology of the nanofibers. After calcination, the nanofibers retained their morphology (Figure 6:5D) however a decrease in diameter from 237 nm to 195 nm (Figure 6:6D) was observed.

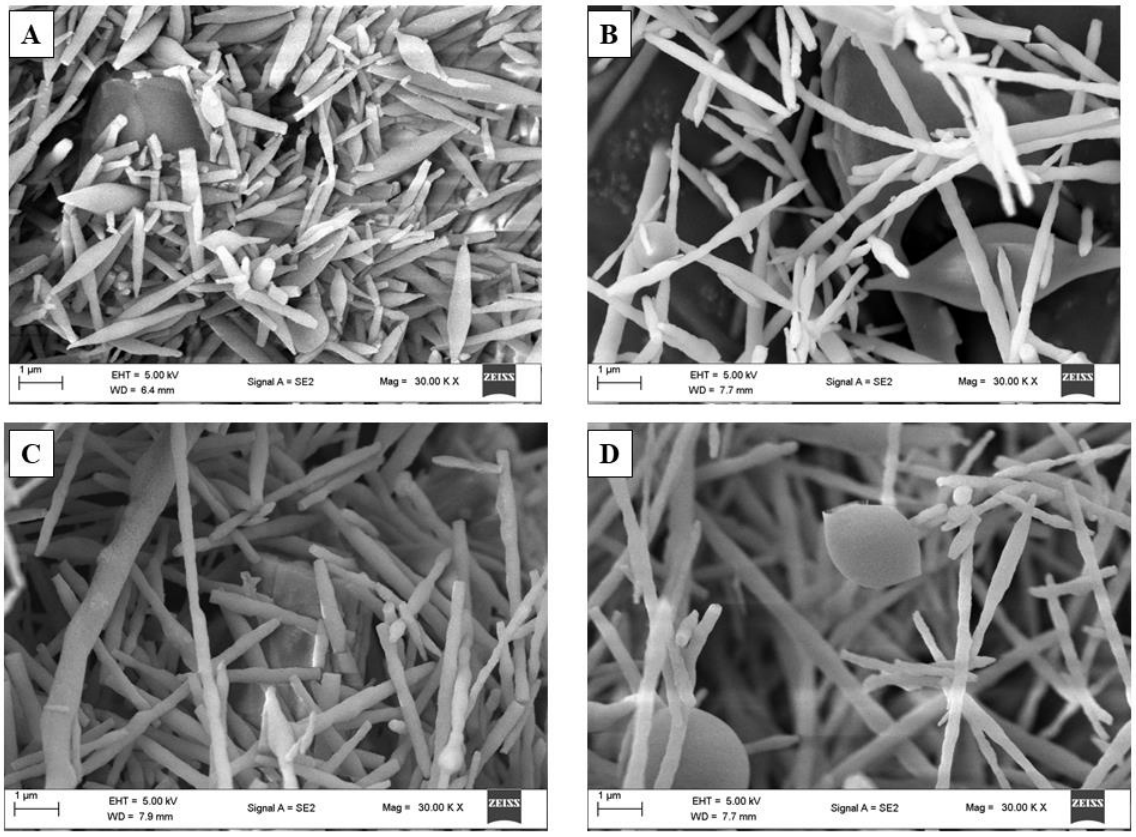

Figure 6:5 SEM images of (A) PEO-Silica before, (B) PEO-silica after calcination, (C) PEO silica-Co3O4 before, (D) PEO silica-Co_3O_4 after calcination

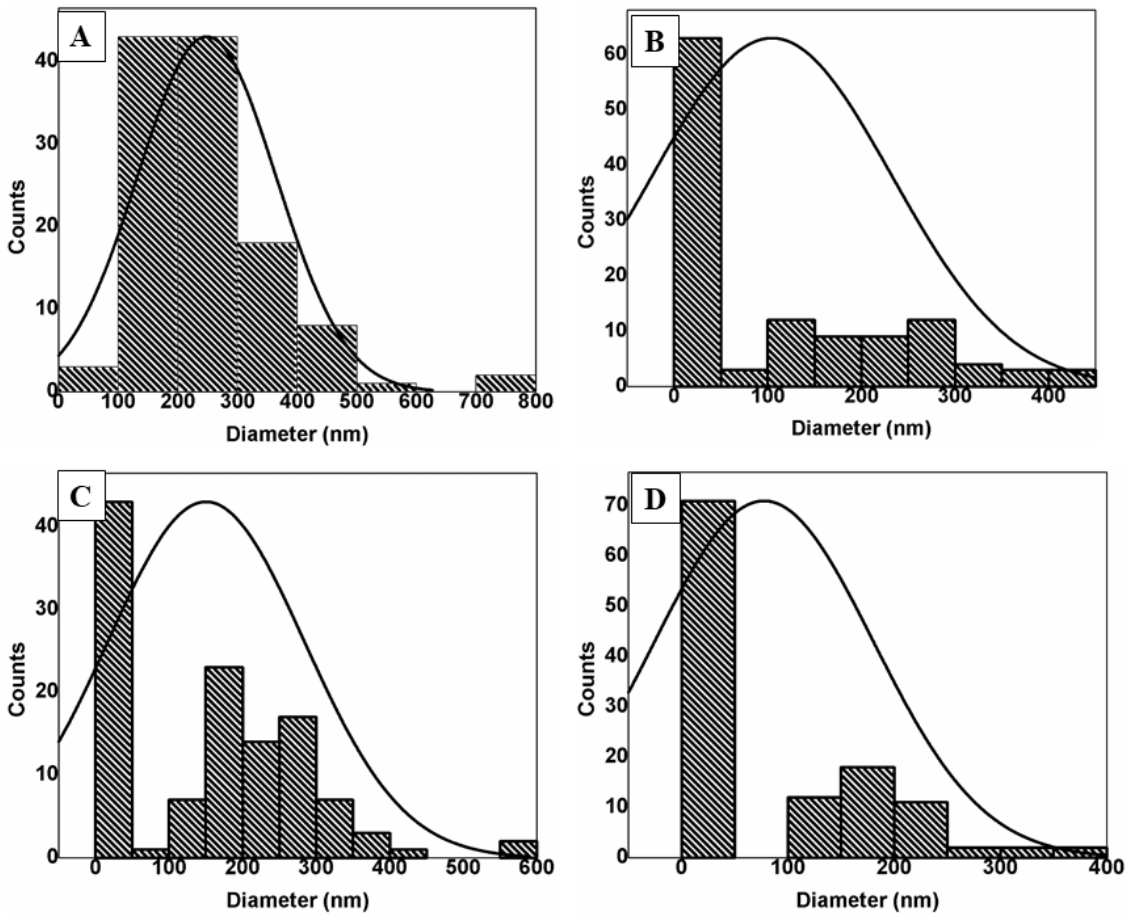

Figure 6:6 Histogram based on SEM images of (A) PEO-Silica before, (B) PEO-Silica after calcination, (C) PEO-Silica-Co_3O_4 before, (D) PEO-Silica-Co_3O_4 after calcination

6.4.2 Electrochemical characterization

The electrochemical characterization of the modified electrode was done using cyclic voltammetry as shown in Figure 6:7A. 2.5 mM $[Fe(CN)_6]^{3-}/[Fe(CN)_6]^{4-}$ in 0.1 M KCl was used as the electrolyte. When the uncalcined PEO-Silica/GCE was used an oxidation peak current of 3.37 µA was obtained. This is due to the insulating nature of PEO. However, after calcination, an increase in current was observed (3.93 µA). This is due to the removal of PEO during calcination thus the electron transfer rate is improved since only silica nanofibers remained. A further increase in oxidation peak current of (3.50 µA) and (4.06 µA) was obtained for uncalcined PEO-Silica-Co_3O_4/GCE and calcined PEO-Silica-Co_3O_4/GCE respectively. This increase is attributed to the addition of cobalt oxide nanoparticles and the removal of PEO. As indicated in Table 6:1, the ratio of Ipa/Ipc was calculated to be ~ 1 for all the modified electrodes, thus a reversible electrochemical

process was observed. The peak-to-peak potential (ΔEp) was found to decrease when the calcined nanofibers were used. This indicates a faster electron transfer rate.

Table 6:1 CV data obtained for the modified electrode in 2.5 mM $[Fe(CN)_6]^{3-/-4}$

Electrode	**Ipa (µA)**	**Ipc (µA)**	**Ipa/Ipc**	**Epa (mV)**	**Epc (mV)**	**ΔEp (mV)**
PEO-Silica/GCE before	3.37	3.43	0.98	328	186	142
PEO-Silica/GCE after	3.93	3.83	1.03	303	205	98
PEO-Silica-Co_3O_4/GCE before	3.50	3.56	0.98	315	193	122
PEO-Silica-Co_3O_4/GCE after	4.06	4.05	1.00	307	202	105

Electrochemical Impendence Spectroscopy (EIS) was used to further investigate the electrocatalytic properties of all the modified electrodes (Figure 6:7B). EIS measurements were taken at a frequency range of 1-10000 Hz with 5 mV amplitude. The EIS data was fitted using Randles equivalent circuit (Figure 6:7B inset). The values for each element of the Randles equivalent circuit are given in Table 6:2. As shown in Figure 6:7B a semi-circle with the charge resistance transfer (Rct) value of 873.7 Ω, 476.5 Ω, 680.1 Ω, 382.6 Ω was obtained for PEO-Silica before/GCE, PEO-Silica after/GCE, PEO-Silica- Co_3O_4 before/GCE, and PEO-Silica- Co_3O_4 after/GCE respectively. Where before and after represent uncalcined and calcined nanofibers. A decrease in Rct after calcination was observed. This is due to the removal of PEO and the addition of cobalt oxide nanoparticles. These results are in agreement with the cyclic voltammetry data in figure 6:7A.

Table 6:2 EIS data obtained for the modified electrode in 2.5 mM $[Fe(CN)_6]^{3-/-4}$

Electrode	Resistance of the electrolyte solution (Ω)	Charge-transfer resistance (Ω)	Warburg impedance (Ω)	Double layer capacitance (Farad)
PEO-Silica before/GCE	37.7	873.7	0.0002938	8.404×10^{-7}
PEO-Silica after/GCE	29.16	476.5	0.0003948	6.962×10^{-7}
PEO-Silica- Co_3O_4 before/GCE	25.84	680.1	0.0003104	9.557×10^{-7}
PEO-Silica- Co_3O_4 after/GCE after	30.15	382.6	0.0002854	7.092×10^{-7}

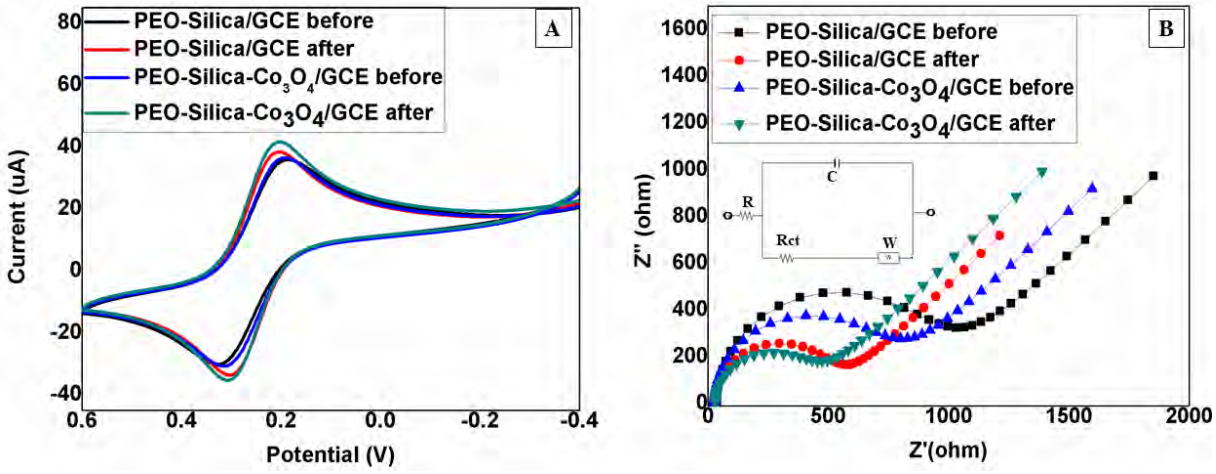

Figure 6:7 (A) Cyclic voltammetry (B) Electrochemical impendence spectroscopy of PEO-Silica and PEO-Silica-Co_3O_4 before and after calcination in 2.5 mM $[Fe(CN)_6]^{3-/-4}$

6.4.3 *Pf*HRP2 antibody optimization

The concentration of the antibody plays a crucial role in the sensitivity and selectivity of the biosensor. EIS was used to optimize the concentration of the *Pf*HRP2 antibody. A range of 0.1-0.3 mg/mL was used. The increase in the concentration of the antibody resulted in an increased charge-transfer resistance (Rct) as shown in Figure 6:8A. A slight increase in Rct value of 2371 Ω, 2500 Ω and 2790 Ω was obtained for 0.1, 0.15 and 0.2 mg/mL respectively (Figure 6:8B). However, a further increase in the concentration of the antibody resulted in an increase in the Rct values to 2924 Ω and 3133 Ω for 0.25 and 0.3 mg/mL respectively. Thus, 0.15 mg/mL was selected as the

optimum concentration since there was less variation between the triplicate readings as indicated by the error bars in Figure 6:8B.

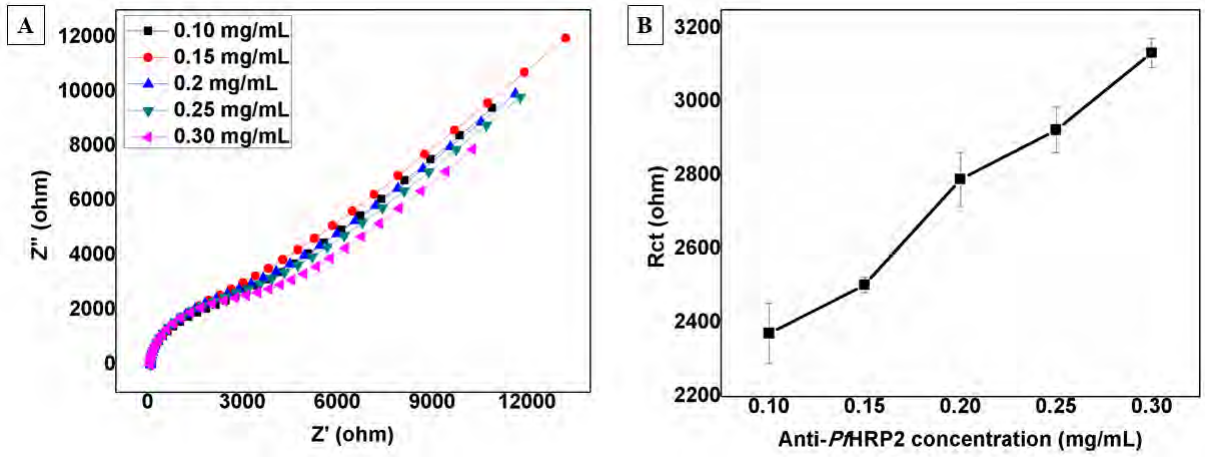

Figure 6:8 (A) EIS spectra of PEO-Silica-Co_3O_4/GCE with different concentrations of *Pf*HRP2 antibody in 0.01 M phosphate saline buffer (pH 7.4) and 2.5 mM $[Fe(CN)_6]^{3-/-4}$ (B) Plot of *Pf*HRP2 antibody concentration vs Rct

6.4.4 Electrochemical behaviour

Electrochemical Impendence Spectroscopy (EIS) was further used to confirm the surface modification of the glassy carbon electrode (GCE) as shown in Figure 6:9A, 0.01 M phosphate saline buffer (pH 7.4), and 2.5 mM $[Fe(CN)_6]^{3-/-4}$ were used as electrolyte and redox probe. An Rct value of 593 Ω, 0.001 Ω, and 2500 Ω was obtained for GCE, PEO-Silica-Co_3O_4 after/GCE and Anti-*Pf*HRP2/PEO-Silica-Co_3O_4 after /GCE respectively. Modification of GCE with PEO-Silica-Co_3O_4 after resulted in a decrease in Rct value, this is due to the unique properties of the nanocomposites such as high surface to volume ratio, good electrocatalytic activity, and enhancement of electron transfer rate. The increase in Rct value after surface functionalization of PEO-Silica-Co_3O_4 after /GCE confirmed the attachment of anti-*Pf*HRP2. The analytical performance of the Anti-*Pf*HRP2/PEO-Silica-Co_3O_4 after /GCE towards *Pf*HRP2 antigen was investigated using EIS (Figure 6:9B). The Rct value was found to be directly proportional to the concentration of the *Pf*HRP2 antigen. A linear relationship between log[HRP2] and (Ra-Ro)/Ro in the range of log(-19) – log (-11) was observed, where Ra and Ro represent Rct of PEO-Silica-Co_3O_4 after/GCE with anti-*Pf*HRP2 and Rct of Anti-*Pf*HRP2/PEO-Silica-Co_3O_4 after /GCE with

*Pf*HRP2 antigen respectively (Figure 6:10). The limit of detection was calculated to be 1.2×10^{-17} g/mL. The current study was compared with previously reported literature as shown in Table 6:3.

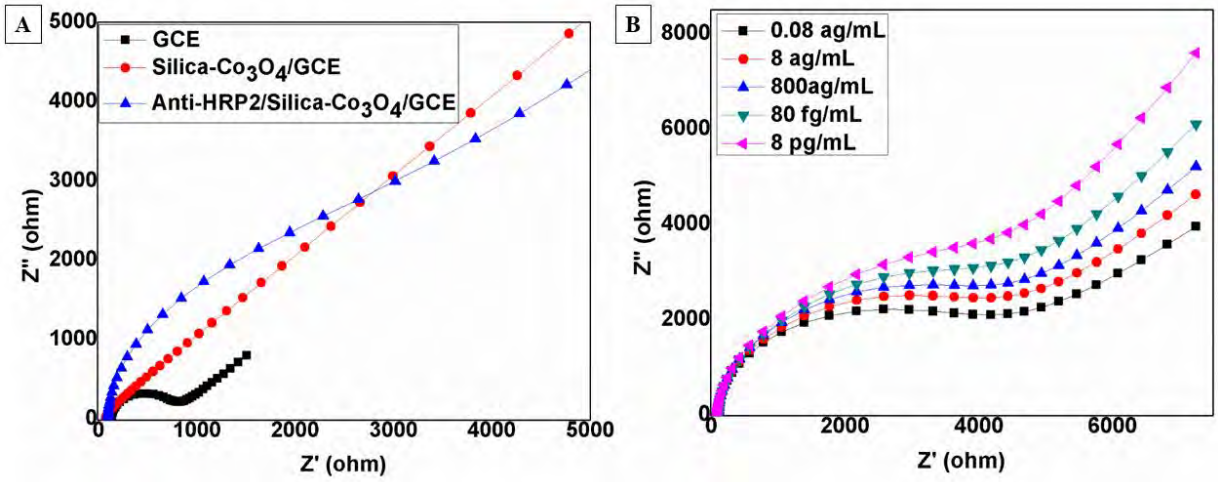

Figure 6:9 (A) EIS spectra of GCE bare, PEO-Silica-Co_3O_4 after/GCE and anti-*Pf*HRP2/PEO Silica-Co_3O_4 after/GCE in 0.01 M phosphate saline buffer (pH 7.4), and $[Fe(CN)_6]^{3-/-4}$ (B) EIS spectra of anti-*Pf*HRP2/PEO Silica-Co_3O_4 after/GCE with change in concentration of *Pf*HRP2 antigen in phosphate saline buffer (pH 7.4), and $[Fe(CN)_6]^{3-/-4}$

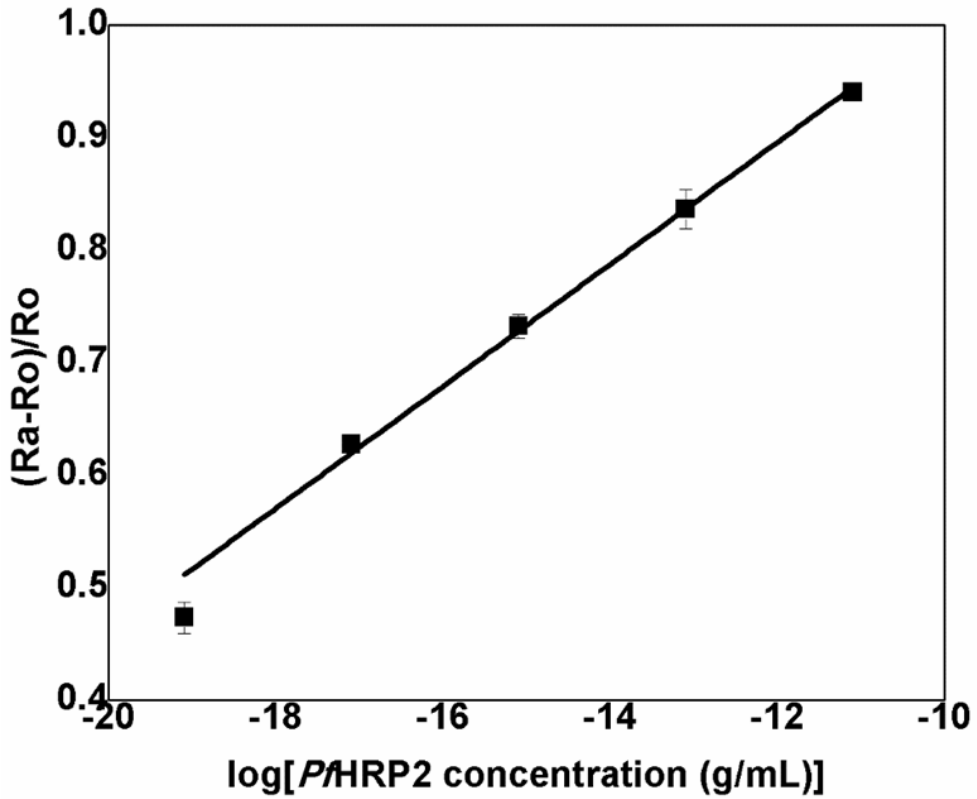

Figure 6:10 Plot of log[*Pf*HRP2 antigen concentration] vs (Ra-Ro)/Ro

Table 6:3 A comparison of the present study with other reported methods for the electrochemical determination of *Pf*HRP2

Biosensor	**Biomarker**	**LOD**	**Ref**
Nano-Au/MWCNT/SPEs	*Pf*HRP2	8 ng/mL in diethanolamine buffer	[28]
GCE/fCZnONF/Anti-HRP2	*Pf*HRP2	6.8 ag/mL in phosphate saline buffer	[24]
MWCNTs-ZnO nanofibers based chemiresistive biosensor for detection of malaria	PfHRP2	0.97 fg/mL	[29]
electrochemical platform integrated with a mobile phone		16 ng/mL	[30]
Anti-*Pf*HRP2/PEO-Silica- Co_3O_4 after /GCE	*Pf*HRP2	1.2×10^{-17} g/mL in phosphate saline buffer and 1.83×10^{-17} g/mL in sheep blood serum	Present work

6.4.5 Real sample, reproducibility, and stability studies

The practical applicability of the Anti-*Pf*HRP2/PEO-Silica-Co_3O_4 after /GCE was investigated in sheep blood serum (Figure 6:11), the preparation method is mentioned in section 6:2.6. A linear relationship between log [HRP2] and (Ra-Ro)/Ro was observed and the detection limit was calculated to be 1.83×10^{-17} g/mL. A bias between the limit of detection (LOD) in saline buffer and sheep blood serum of found to be less than 34% thus the modified electrode is selective and sensitive to *Pf*HRP2. The reproducibility studies were conducted in saline buffer using three identically prepared electrodes (Figure 6:12A) and a relative standard deviation of 2.45 % was obtained. The modified electrode was also found to be stable for 7 days (figure 6:12B).

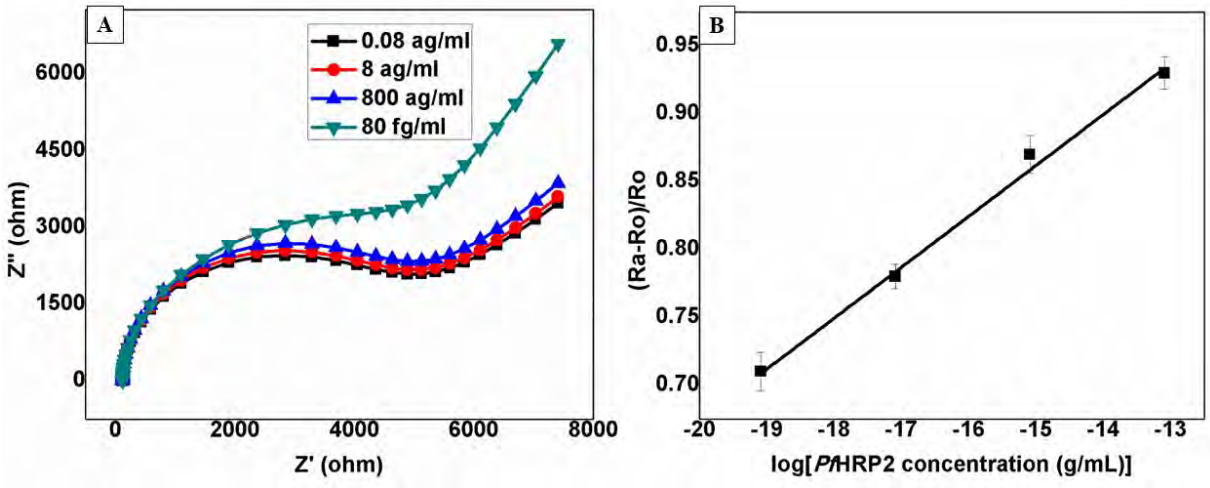

Figure 6:11 (A) EIS spectra of Anti-*Pf*HRP2/PEO-Silica-Co_3O_4 after/GCE with *Pf*HRP2 antigen in diluted blood sheep serum (B) Plot of log[*Pf*HRP2 antigen concentration] vs (Ra-Ro)/Ro

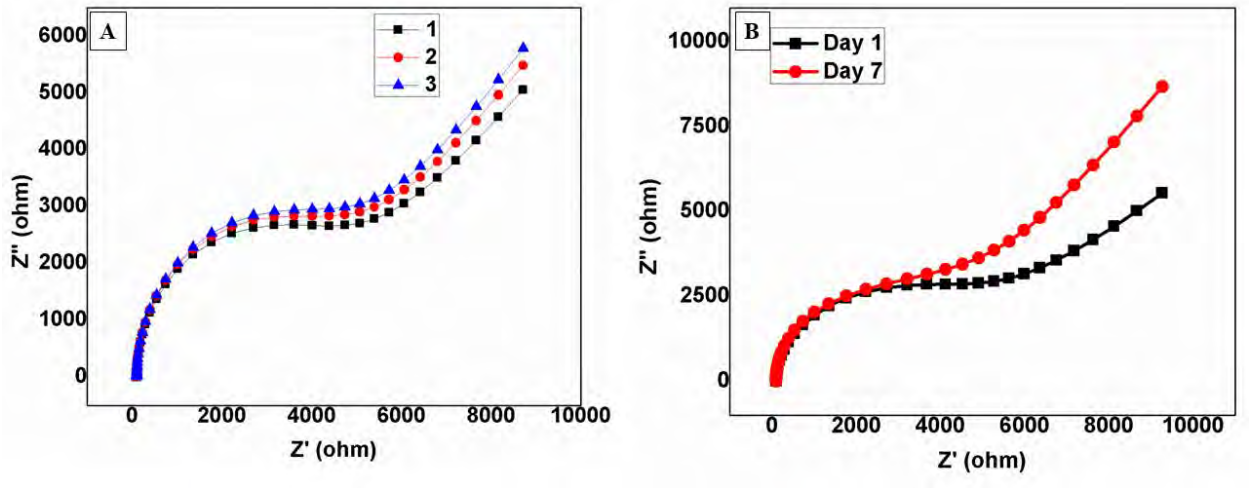

Figure 6:12 (A) EIS spectra of PEO-Silica-Co3O4 after/GCE in PfHRP2 for reproducibility (B) Stability studies

6.5 SUB-CONCLUSION

Scanning electron microscopy confirmed the fabrication of polyethylene oxide silica nanofibers incorporated with cobalt oxide using the electrospinning technique. X-Ray Diffraction Spectroscopy and Fourier Transform Infrared Spectroscopy confirmed the removal of polyethylene oxide post calcination. *Plasmodium falciparum* histidine-rich protein 2 was detected using Anti-*Pf*HRP2/PEO-Silica-Co_3O_4/GCE. The practical applicability of the sensor was evaluated in sheep blood serum and a detection limit of 1.83×10^{-17} g/mL was obtained. The sensor showed good stability, reproducibility, selectivity, and sensitivity in phosphate buffer saline and sheep blood serum. Thus it can be used for the diagnosis of malaria in low resource settings.

6.6 REFERENCES

[1] A. Rossati, O. Bargiacchi, V. Kroumova, M. Zaramella, A. Caputo, P.L. Garavelli, Climate, environment and transmission of malaria., Le Infez. Med. 24 (2016) 93–104.

[2] E. Meibalan, M. Marti, Biology of Malaria Transmission, Cold Spring Harb. Perspect. Med. 7 (2017) a025452. https://doi.org/10.1101/cshperspect.a025452.

[3] D.E. Loy, W. Liu, Y. Li, G.H. Learn, L.J. Plenderleith, S.A. Sundararaman, P.M. Sharp, B.H. Hahn, Out of Africa: origins and evolution of the human malaria parasites Plasmodium falciparum and Plasmodium vivax, Int. J. Parasitol. 47 (2017) 87–97.

https://doi.org/10.1016/j.ijpara.2016.05.008.

[4] WHO, World malaria report 2020: 20 years of global progress and challenges, Geneva, 2020. https://www.who.int/publications/i/item/9789240015791.

[5] N. Tangpukdee, C. Duangdee, P. Wilairatana, S. Krudsood, Malaria diagnosis: a brief review., Korean J. Parasitol. 47 (2009) 93–102. https://doi.org/10.3347/kjp.2009.47.2.93.

[6] S. Kasetsirikul, J. Buranapong, W. Srituravanich, M. Kaewthamasorn, A. Pimpin, The development of malaria diagnostic techniques: a review of the approaches with focus on dielectrophoretic and magnetophoretic methods, Malar. J. 15 (2016) 358. https://doi.org/10.1186/s12936-016-1400-9.

[7] A. Mbanefo, N. Kumar, Evaluation of Malaria Diagnostic Methods as a Key for Successful Control and Elimination Programs, Trop. Med. Infect. Dis. 5 (2020) 102. https://doi.org/10.3390/tropicalmed5020102.

[8] W.-X. Wang, Y.-W. Cheung, R.M. Dirkzwager, W.-C. Wong, J.A. Tanner, H.-W. Li, Y. Wu, Specific and sensitive detection of Plasmodium falciparum lactate dehydrogenase by DNA-scaffolded silver nanoclusters combined with an aptamer, Analyst. 142 (2017) 800–807. https://doi.org/10.1039/C6AN02417C.

[9] M.S. Gomez, R.C. Piper, L.A. Hunsaker, R.E. Royer, L.M. Deck, M.T. Makler, D.L. Vander Jagt, Substrate and cofactor specificity and selective inhibition of lactate dehydrogenase from the malarial parasite P. falciparum, Mol. Biochem. Parasitol. 90 (1997) 235–246. https://doi.org/https://doi.org/10.1016/S0166-6851(97)00140-0.

[10] C.F. Markwalter, K.M. Davis, D.W. Wright, Immunomagnetic capture and colorimetric detection of malarial biomarker Plasmodium falciparum lactate dehydrogenase., Anal. Biochem. 493 (2016) 30–34. https://doi.org/10.1016/j.ab.2015.10.003.

[11] P. Jain, B. Chakma, S. Patra, P. Goswami, Potential Biomarkers and Their Applications for Rapid and Reliable Detection of Malaria, Biomed Res. Int. 2014 (2014) 852645. https://doi.org/10.1155/2014/852645.

[12] C.H. Leow, M. Jones, Q. Cheng, S. Mahler, J. McCarthy, Production and characterization

of specific monoclonal antibodies binding the Plasmodium falciparum diagnostic biomarker, histidine-rich protein 2, Malar. J. 13 (2014) 277. https://doi.org/10.1186/1475-2875-13-277.

[13] C.P. Gulka, J.D. Swartz, J.R. Trantum, K.M. Davis, C.M. Peak, A.J. Denton, F.R. Haselton, D.W. Wright, Coffee rings as low-resource diagnostics: detection of the malaria biomarker Plasmodium falciparum histidine-rich protein-II using a surface-coupled ring of Ni(II)NTA gold-plated polystyrene particles., ACS Appl. Mater. Interfaces. 6 (2014) 6257–6263. https://doi.org/10.1021/am501452k.

[14] L.D. Kori, N. Valecha, A.R. Anvikar, Glutamate dehydrogenase: a novel candidate to diagnose Plasmodium falciparum through rapid diagnostic test in blood specimen from fever patients, Sci. Rep. 10 (2020) 6307. https://doi.org/10.1038/s41598-020-62850-x.

[15] C. Werner, M.T. Stubbs, R.L. Krauth-Siegel, G. Klebe, The Crystal Structure of Plasmodium falciparum Glutamate Dehydrogenase, a Putative Target for Novel Antimalarial Drugs, J. Mol. Biol. 349 (2005) 597–607. https://doi.org/https://doi.org/10.1016/j.jmb.2005.03.077.

[16] O. Rifaie-Graham, J. Pollard, S. Raccio, S. Balog, S. Rusch, M.A. Hernández-Castañeda, P.-Y. Mantel, H.-P. Beck, N. Bruns, Hemozoin-catalyzed precipitation polymerization as an assay for malaria diagnosis, Nat. Commun. 10 (2019) 1369. https://doi.org/10.1038/s41467-019-09122-z.

[17] M.C. Hegg, Malaria Diagnostic Platform, Hemozoin Detection BT - Encyclopedia of Malaria, in: P.G. Kremsner, S. Krishna (Eds.), Springer New York, New York, NY, 2016: pp. 1–10. https://doi.org/10.1007/978-1-4614-8757-9_110-1.

[18] N.S. Gopal, R. Raychaudhuri, Detection of *Plasmodium* Aldolase Using a Smartphone and Microfluidic Enzyme Linked Immunosorbent Assay, Malar. Res. Treat. 2017 (2017) 9062514. https://doi.org/10.1155/2017/9062514.

[19] C.F. Markwalter, L. Mudenda, M. Leelawong, D.W. Kimmel, A. Nourani, S. Mbambara, P.E. Thuma, D.W. Wright, Evidence for histidine-rich protein 2 immune complex formation in symptomatic patients in Southern Zambia, Malar. J. 17 (2018) 256.

https://doi.org/10.1186/s12936-018-2400-8.

[20] J. Horne, L. McLoughlin, B. Bridgers, E.K. Wujcik, Recent developments in nanofiber-based sensors for disease detection, immunosensing, and monitoring, Sensors and Actuators Reports. 2 (2020) 100005. https://doi.org/https://doi.org/10.1016/j.snr.2020.100005.

[21] C. Cleeton, A. Keirouz, X. Chen, N. Radacsi, Electrospun Nanofibers for Drug Delivery and Biosensing, ACS Biomater. Sci. Eng. 5 (2019) 4183–4205. https://doi.org/10.1021/acsbiomaterials.9b00853.

[22] S. Sundera Murthe, M.S. Mohamed Saheed, V. Perumal, M.S. Mohamed Saheed, N.M. Mohamed, 11 - Electrospun Nanofibers for Biosensing Applications, in: S.C.B. Gopinath, T.B.T.-N. for B.T. Lakshmipriya (Eds.), Micro Nano Technol., Elsevier, 2019: pp. 253–267. https://doi.org/https://doi.org/10.1016/B978-0-12-813900-4.00011-7.

[23] E. Gikunoo, A. Abera, E. Woldesenbet, A novel carbon Nanofibers grown on glass microballoons immunosensor: A tool for early diagnosis of Malaria, Sensors (Switzerland). 14 (2014) 14686–14699. https://doi.org/10.3390/s140814686.

[24] K. Brince Paul, S. Kumar, S. Tripathy, S.R.K. Vanjari, V. Singh, S.G. Singh, A highly sensitive self assembled monolayer modified copper doped zinc oxide nanofiber interface for detection of Plasmodium falciparum histidine-rich protein-2: Targeted towards rapid, early diagnosis of malaria, Biosens. Bioelectron. 80 (2016) 39–46. https://doi.org/https://doi.org/10.1016/j.bios.2016.01.036.

[25] A.C. Patel, S. Li, C. Wang, W. Zhang, Y. Wei, Electrospinning of Porous Silica Nanofibers Containing Silver Nanoparticles for Catalytic Applications, Chem. Mater. 19 (2007) 1231–1238. https://doi.org/10.1021/cm061331z.

[26] Z. Nate, A.A.S. Gill, R. Chauhan, R. Karpoormath, Polyaniline-cobalt oxide nanofibers for simultaneous electrochemical determination of antimalarial drugs: Primaquine and proguanil, Microchem. J. 160 (2021) 105709. https://doi.org/10.1016/j.microc.2020.105709.

[27] H. V. Shah, J.R. Sandy, A.J. Ireland, B. Su, Elec tros pinning of 2D and 3D silica nanofibres

from a colloidal solution, Ceram. - Silikaty. 56 (2012) 112–116.

[28] M.K. Sharma, V.K. Rao, G.S. Agarwal, G.P. Rai, N. Gopalan, S. Prakash, S.K. Sharma, R. Vijayaraghavan, Highly sensitive amperometric immunosensor for detection of Plasmodium falciparum histidine-rich protein 2 in serum of humans with malaria: comparison with a commercial kit., J. Clin. Microbiol. 46 (2008) 3759–3765. https://doi.org/10.1128/JCM.01022-08.

[29] B. Paul, A.K. Panigrahi, V. Singh, S.G. Singh, A multi-walled carbon nanotube-zinc oxide nanofiber based flexible chemiresistive biosensor for malaria biomarker detection, Analyst. 142 (2017) 2128–2135. https://doi.org/10.1039/c7an00243b.

[30] P.B. Lillehoj, M.-C. Huang, N. Truong, C.-M. Ho, Rapid electrochemical detection on a mobile phone, Lab Chip. 13 (2013) 2950–2955. https://doi.org/10.1039/C3LC50306B.

CHAPTER SEVEN

7.1 SUMMARY AND CONCLUSION

This thesis is based on the synthesis of various nanomaterials such as nanofibers, carbon nanotubes, metal nanoparticles, nanostructured conducting polymers, and metal-organic frameworks. These materials were used to develop electrochemical sensors for the detection and quantification of malaria biomarkers (β−Hematin, *Plasmodium falciparum* histidine-rich protein 2) and antimalarial drugs (primaquine and proguanil).

Since quality control of pharmaceutical drugs is still a challenge in most developing countries. The first focus of this thesis was to develop rapid, selective, and sensitive methods for the quantification of selected antimalarial drugs. In this thesis, it was demonstrated in chapters 3 and 4 that the selectivity and sensitivity of the glassy carbon electrode towards proguanil and primaquine can be improved by modifying the glassy carbon electrode with multiwall carbon nanotubes incorporated with iron oxide and polyaniline-cobalt oxide nanocomposites. The method used to synthesis multiwall carbon nanotubes is novel. The modified electrodes in chapter 3 showed acceptable sensitivity and selectivity towards proguanil in the presence of different sample matrix such as urine and pharmaceutical formulation. Thus, the developed method can be used as a substitute for conventional quality control methods. Also, the modified electrode in chapter 4 showed good selectivity, reproducibility, and sensitivity in the presence of human urine and different organic and inorganic interfering species. As far as we could know, this is the first study to report the simultaneous electrochemical detection of proguanil and primaquine.

The second phase of this thesis was based on the development of electrochemical biosensors for the early detection of malaria. In chapter 5 the surface of a glassy carbon electrode was modified with copper metal-organic frameworks to improve its selectivity and sensitivity towards β−Hematin. The modified electrode was found to be selective and sensitive to β−Hematin in the presence of various interfering species. Since β−Hematin is structurally and chemically similar to hemozoin this method can be further developed, optimized, and used for early diagnosis of malaria in low resource settings. Since *Plasmodium falciparum* is the most dominant malaria species in Africa, a biosensor that is specific to this species was developed in chapter 6. The biosensor was found to be sensitive and selective towards *Plasmodium falciparum* histidine-rich protein 2) with low detection limits in phosphate buffer and blood sheep serum.

The work described in this thesis is multidisciplinary since it involves chemistry, material science, nanotechnology, and electrochemistry therefore it will be relevant to various scientists that are working in these areas. This work will also contribute to the existing body of knowledge through research publications that can be accessed by scholars and industry experts.

7.2 FUTURE WORK

- The novel flame synthesis method that was reported in this thesis to produce multiwall carbon nanotubes incorporated with iron oxide nanoparticles can be further used to synthesis other nanocomposites. This can be achieved by changing the carbon precursor from ferrocene to other metallocenes such as ruthenocene and cobaltocene.
- In this thesis, amino-functionalized copper metal-organic frameworks were synthesized using the amorphous MOF-mediated recrystallization approach where the effect of pH on the morphology was investigated. The effect of other parameters such as temperature, concentration, time, and solvent can be investigated. Also, the amino-functionalized copper metal-organic frameworks can be used as precursors to synthesis super long Cu-MOFs nanotubes that can be used in various applications.
- In this thesis, it was demonstrated that the glassy carbon electrode modified with amino-functionalized copper metal-organic frameworks is sensitive to β−Hematin. Since β−Hematin is structurally and chemically similar to hemozoin, a custom-made electrode can be developed to directly detect hemozoin in malaria-infected patients.
- Based on the results that were obtained in the development of an electrochemical biosensor for the detection of *Plasmodium falciparum* histidine-rich protein. A point of care device can be developed, optimized, and used for early diagnosis of malaria in low resource settings. Also, a further modification of PEO-Silica-Co_3O_4 nanofibers can result in the development of another electrochemical method for the detection of other malaria biomarkers such as *Plasmodium falciparum* lactate dehydrogenase.
- The unique properties of the calcined PEO-Silica-Co_3O_4 nanofibers make them suitable to be used in wastewater treatment.

7.3 APPENDIX

7.3.1 Appendix 1 supplementary information for chapter 3

Supplementary information

A simple *In-situ* flame synthesis of nanocomposite (MWCNTs-Fe_2O_3) for electrochemical sensing of proguanil in pharmaceutical formulation

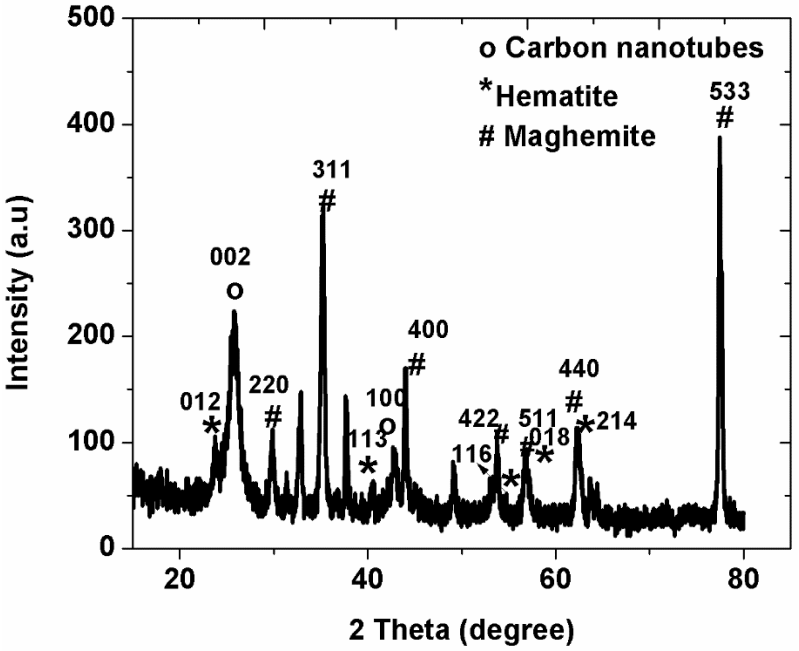

Figure 3:S1 XRD pattern of MWCNTs-iron oxide nanocomposite.

Table 3:S1 Elements of the fitted EIS data using Randles equivalent circuit.

Equivalent circuit parameters	**Resistance of the electrolyte solution (Ω)**	**Charge-transfer resistance Ω**	**Warburg impedance Ω**	**Double layer capacitance (Farad)**
GCE	16.16	222.2	0.0004534	4.94×10^{-7}
Error (%)	0.17	0.018	0.024	0.014
MWCNTs-iron oxide/GCE	19.38	0.001	0.0001843	1.051×10^{-5}
Error (%)	0.01	0.012	0.006	0.012

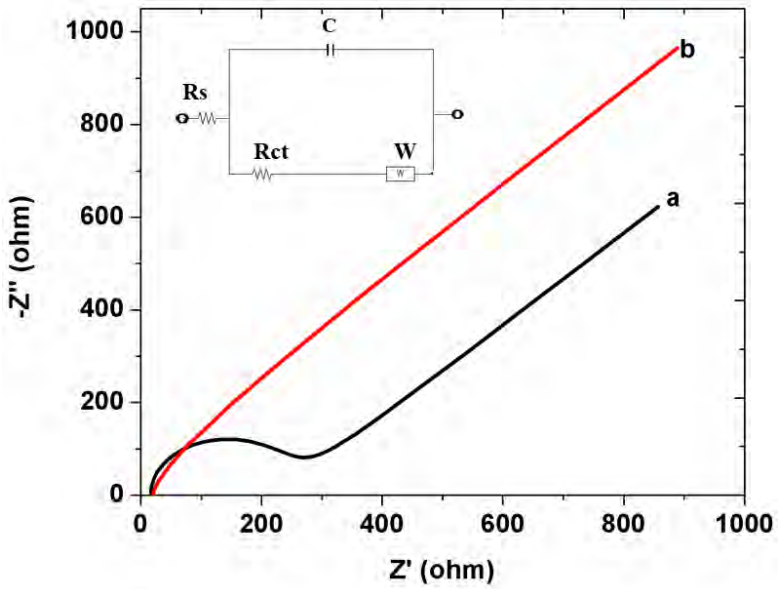

Figure 3:S2 EIS measurement in 2.5 mM $Fe(CN)_6]^{3-}$/$[Fe(CN)_6]^{4-}$ at (a) bare GCE and (b) MWCNTs-iron oxide/GCE. The inset shows the Randles equivalent circuit (C, W, Rct and Rs represents the double layer capacitance, Warburg impedance, charge-transfer resistance and resistance of the electrolyte solution respectively).

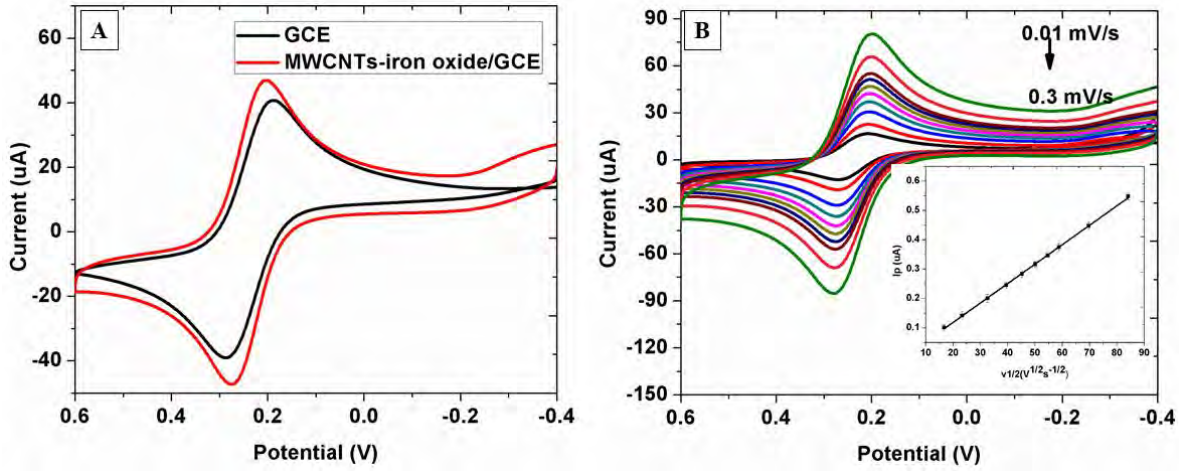

Figure 3:S3: (A) Cyclic voltammograms of $Fe(CN)_6]^{3-}$/$[Fe(CN)_6]^{4-}$ (2.5 mM) in KCl solution (0.1 M) at bare GCE and MWCNTs-iron oxide/GCE at 100 mV/s. (B) Cyclic voltammograms of $Fe(CN)_6]^{3-}$/$[Fe(CN)_6]^{4-}$ (2.5 mM) in KCl solution (0.1 M) at MWCNTs-iron oxide/GCE at varying scan rates. (Inset displays a plot of peak current versus square root of scan rate).

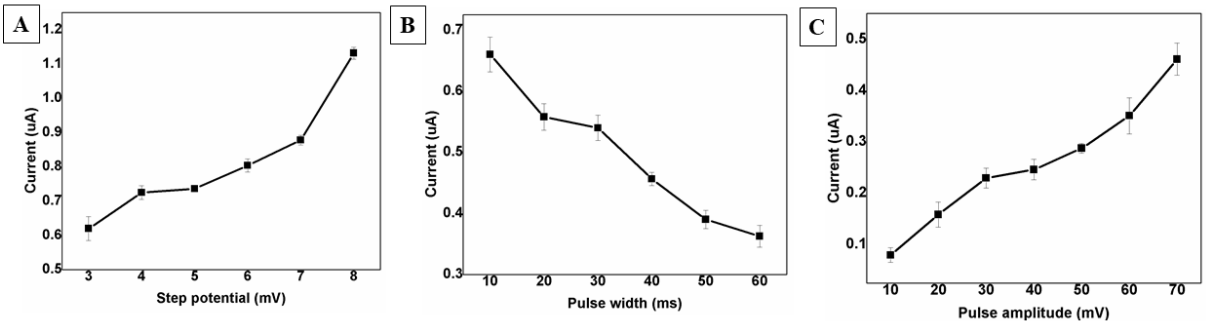

Figure 3:S4: Effect of DPV parameters (A) Potential step (B) Pulse width (C) Pulse amplitude on proguanil (pH 5.5) peak current recorded at MWCNTs-iron oxide/GCE.

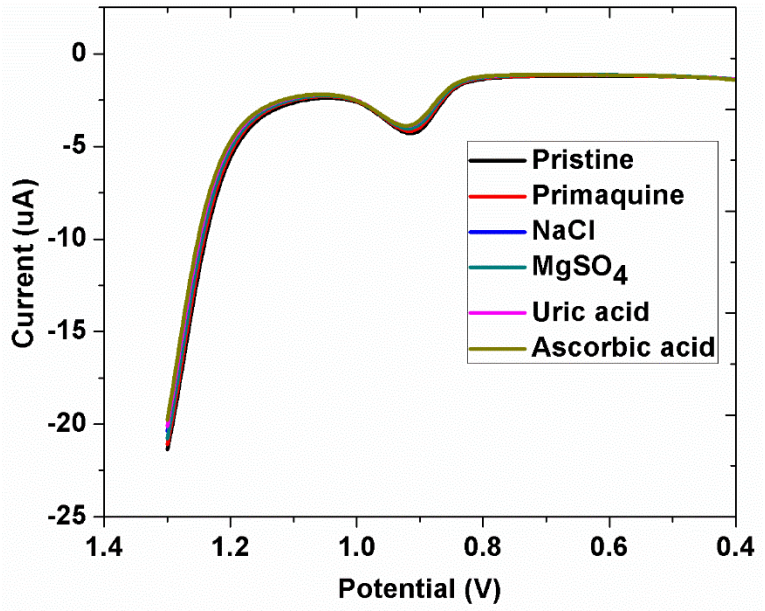

Figure 3:S5: DP voltammograms of proguanil in different interfering species.

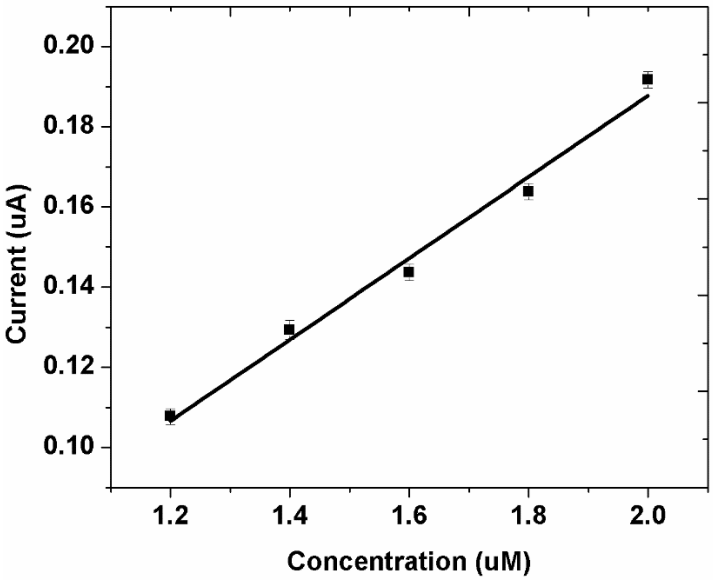

Figure 3:S6: Standard addition curve of Proguanil in the pharmaceutical sample

7.3.2 Appendix 2 supplementary information for chapter 4

Supplementary information

Polyaniline-cobalt oxide nanofibers for simultaneous electrochemical determination of antimalarial drugs: primaquine and proguanil

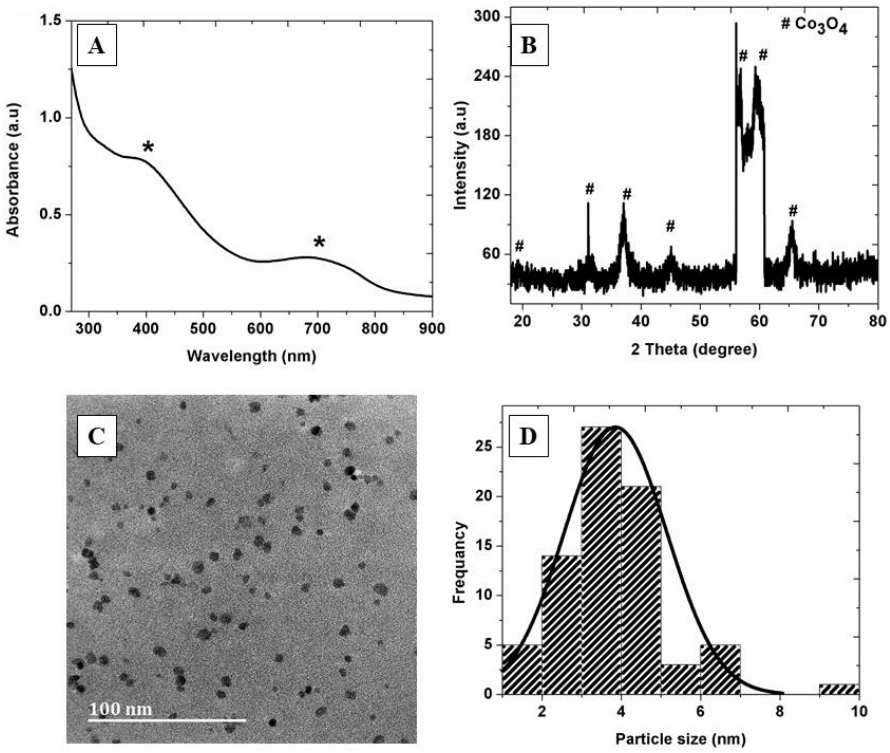

Figure 4:S1: (A) Uv-vis spectrum, (B) XRD, (C) TEM and (D) Histogram of Cobalt oxide nanoparticles.

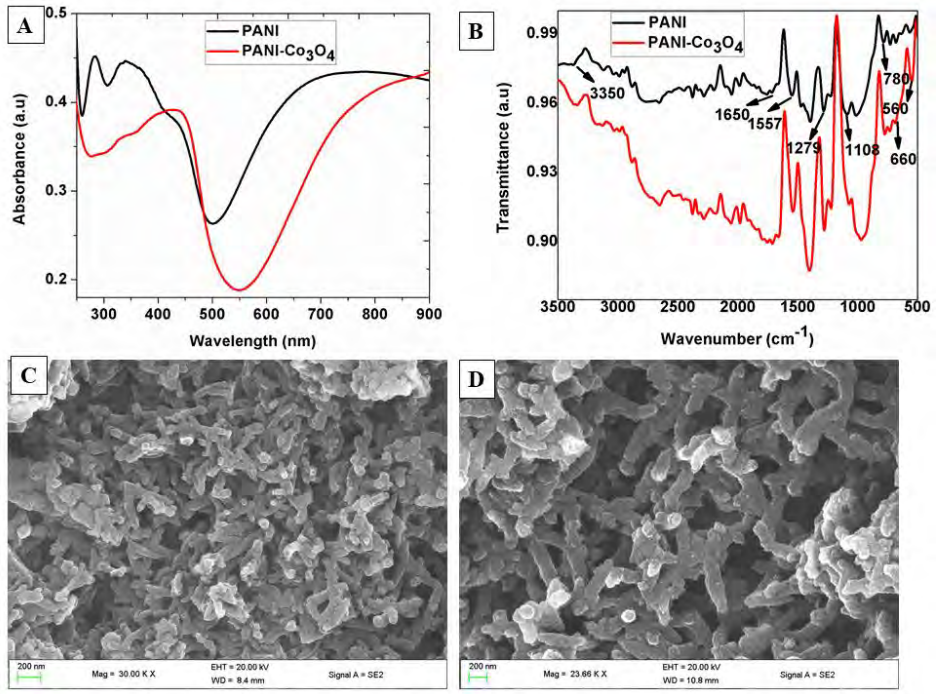

Figure 4:S2: (A) Uv-vis spectra of PANI and PANI-Co_3O_4, (B) Structural characterization of PANI and PANI-Co_3O_4, (C) Morphological studies of PANI and (D) PANI-Co_3O_4

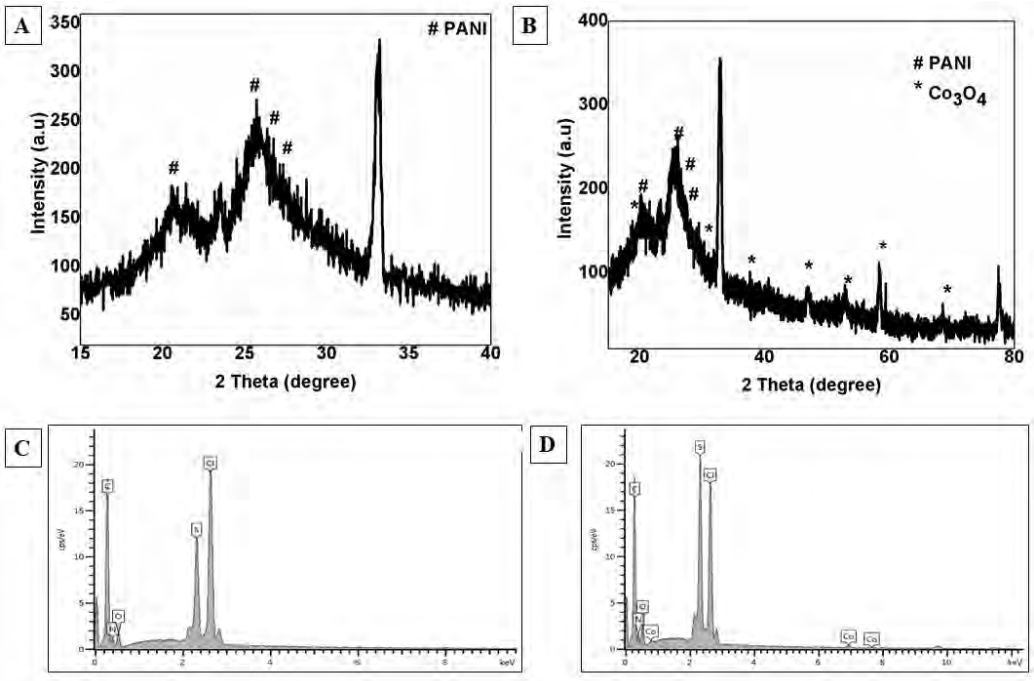

Figure 4:S3: X-ray differection pattern of (A) PANI , (B) PANI-Co_3O_4, and EDX analysis of (C) PANI and (D) PANI-Co_3O_4

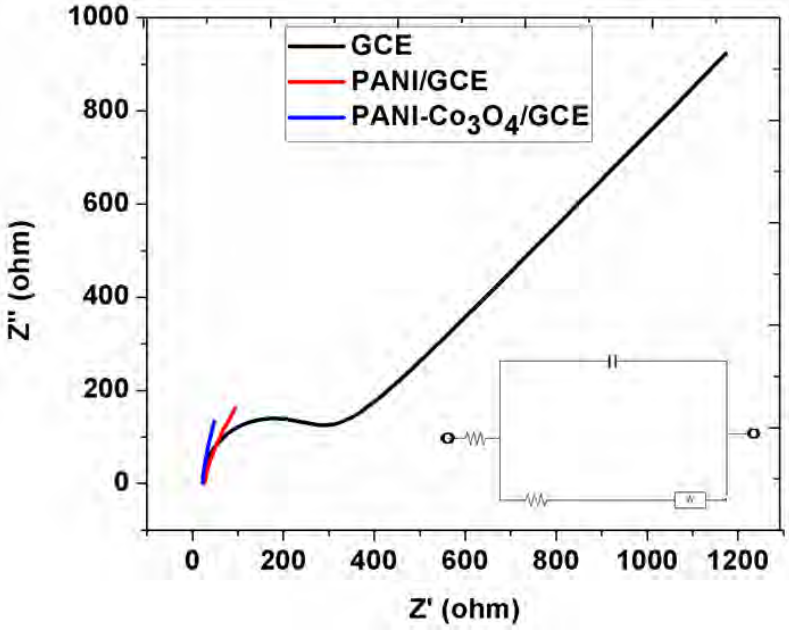

Figure 4:S4: EIS measurement in 2.50 mM $Fe(CN)_6]^{3-}$/$[Fe(CN)_6]^{4-}$. The inset shows the Randles equivalent circuit.

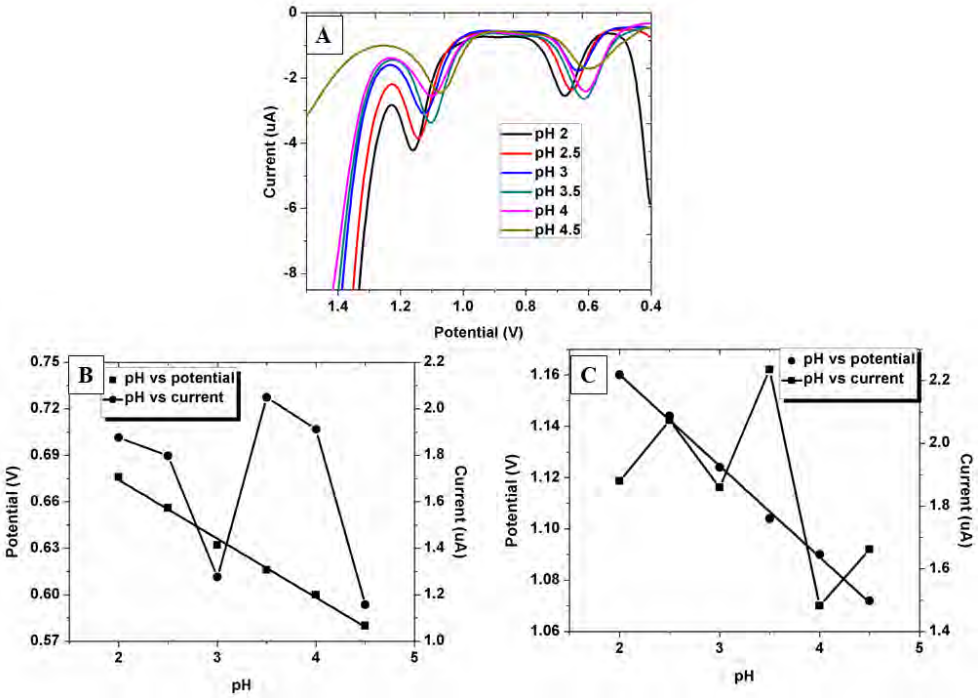

Figure: 4:S5: (A) Differential pulse voltammograms of primaquine and proguanil with different pH; (B-C) The plot of current vs pH and potential vs pH at PANI-Co_3O_4/GCE for primaquine and proguanil, respectively.

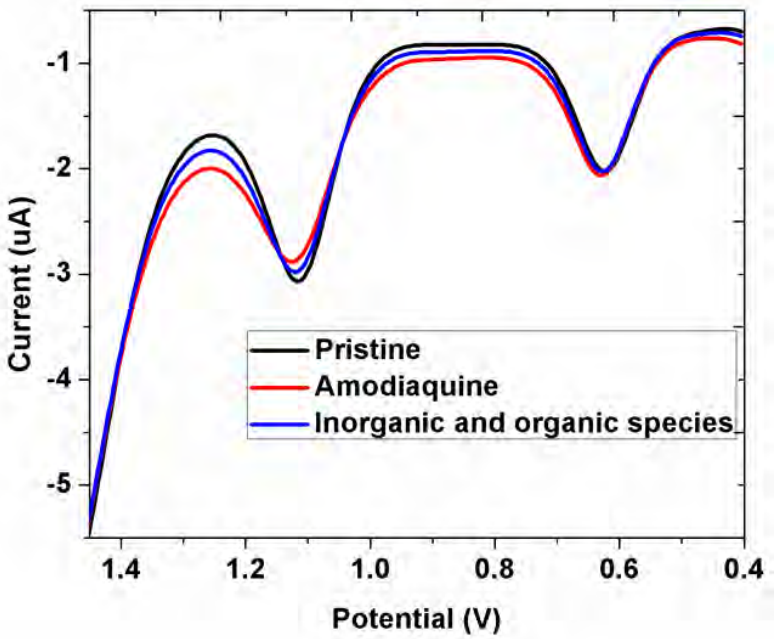

Figure 4:S6: DP voltammograms of primaquine and proguanil with different interfering species.

7.3.3 Appendix 3 published article

ARTICLE IN PRESS

Diamond & Related Materials xxx (xxxx) xxx

Contents lists available at ScienceDirect

Diamond & Related Materials

journal homepage: www.elsevier.com/locate/diamond

A simple in-situ flame synthesis of nanocomposite (MWCNTs-Fe_2O_3) for electrochemical sensing of proguanil in pharmaceutical formulation

Zondi Nate, Atal A.S. Gill, Suraj Shinde, Ruchika Chauhan, Shaukatali N. Inamdar, Rajshekhar Karpoormath*

Department of Pharmaceutical Chemistry, College of Health Sciences, University of KwaZulu Natal, Westville Campus, Durban 4000, South Africa

ARTICLE INFO

Keywords:
Proguanil
Carbon nanotubes
Iron oxide nanoparticles
Flame synthesis
Differential pulse voltammetry

ABSTRACT

Multiwall carbon nanotubes incorporated with iron oxide nanoparticles (MWCNTs-iron oxide) were prepared using a cheap, facile in-situ flame synthesis method. The nanocomposites were characterized using scanning electron microscopy, energy-dispersive X-ray spectroscopy, transmission electron microscopy, X-ray powder diffractometry, and Raman spectroscopy. MWCNTs-iron oxide nanocomposite was used to fabricate a sensitive electrochemical sensor for the detection and quantification of proguanil. The fabrication of the sensor was done by modifying a glassy carbon electrode with multiwall carbon nanotubes-iron oxide nanocomposite (MWCNTs-iron oxide). Differential pulse voltammetry (DPV) and cyclic voltammetry (CV) were used to study the electrochemical oxidation of proguanil. The selectivity of the sensor was investigated in the presence of organic and inorganic interfering agents. Furthermore, spiked human urine samples and pharmaceutical formulation were used to evaluate the utility of the sensor. A detection limit of 1.96×10^{-8} M was obtained under optimum conditions. MWCNTs-iron oxide nanocomposite can, therefore, be used to fabricate electrochemical sensors for quality control purposes.

1. Introduction

The application of carbon nanotubes in different fields, such as energy management, chemical sensors, and clinical diagnostic tools is increasing. This is mainly due to their unique physical and chemical properties. Some of these properties include a high surface area to volume ratio, ultra-lightweight, fast electron transfer rate, and biocompatibility [1–4]. In the past two decades, the properties of carbon nanotubes have been improved by the incorporation of metal oxide nanoparticles such as iron oxide and zinc oxide [5–8]. Also, other studies have reported the synthesis of carbon nanotubes with conducting polymers and metal nanoparticles [9–11]. Various methods, such as flame pyrolysis [12,13], arc discharge [14], laser ablation [15], sol-gel [16], and chemical vapor deposition [16,17] have been reported for the synthesis of different carbon nanotubes composites. However, most of these methods require sophisticated instrumentation, further purification steps, and are time-consuming. A cheap simple method is needed for the synthesis of carbon nanotubes. The ability of the flame to provide the required heat and chemical reaction environment for the production of carbon nanotubes makes flame pyrolysis to be among the frequently used methods. This approach is economical, simpler and fast for making carbon nanotubes. Inamdar et al. [18] used a simple flame synthesis method to prepare maghemite nanoparticles. In another study by Bhattacharjya et al. [19], N-doped carbon particles were synthesized by direct burning of acetonitrile as nitrogen and carbon source.

Therefore in the present work, a simple, less time consuming, cheap method for synthesis of carbon nanotubes with iron oxide nanoparticles is reported. These methods allow for a direct one step synthesis of the MWCNTs-iron oxide nanocomposites, thus no further purification step is required. Iron oxide nanoparticles possess good adsorption affinity, biocompatibility and high electrocatalytic activity [20,21]. These properties are different from their bulk counterparts. However iron oxide nanoparticles have some drawbacks that limit their application in electrochemical sensors. These include poor dispersibility and high degree of agglomeration [20]. To overcome these drawbacks, iron oxide nanoparticles are incorporated into multiwall carbon nanotubes. Also, the synergistic effect of iron oxide nanoparticles and multiwall carbon nanotubes improves the electrocatalytic activity of the nanocomposite [22]. The presence of iron oxide nanoparticles will improve the selectivity of the sensor since it has high affinity to towards amine functional

* Corresponding author at: Department of Pharmaceutical Chemistry, College of Health Sciences, University of KwaZulu Natal, Durban 4000, South Africa.
E-mail address: karpoormath@ukzn.ac.za (R. Karpoormath).

https://doi.org/10.1016/j.diamond.2020.108178
Received 28 August 2020; Received in revised form 9 November 2020; Accepted 9 November 2020
Available online 16 November 2020
0925-9635/

Please cite this article as: Zondi Nate, *Diamond & Related Materials*, https://doi.org/10.1016/j.diamond.2020.108178

groups. In this method, ethanol, atmospheric air, and cold water were used as the source of fuel, oxidizer, and cooling system, respectively. Ferrocene was selected as a precursor because of its dual function; it acts as a source of iron (Fe) and carbon. The process for the formation of MWCNTs-iron oxide nanocomposite begins at temperatures above 400 °C, where ferrocene is vaporized to hydrocarbons (CH_4 and C_5H_6) and Fe [23,24]. In this reaction, the π electrons of C_5H_6 interact with Fe atoms. As the temperature increases above 500 °C, the formation of MWCNTs-iron oxide nanocomposite takes place during the carbonization process [25]. Further, the synthesized nanocomposite was employed to carry out electrochemical detection of proguanil in human urine and pharmaceutical samples.

Proguanil is an antimalarial drug that is used in combination with other drugs. Among these, a synergistic combination of proguanil with atovaquone is widely used for malaria treatment in high-income countries. The high-cost factor of proguanil has contributed to a prevalence of counterfeit antimalarial drugs in Sub-Saharan Africa. Hence, there is a need to trace or encounter such counterfeit drugs available in the markets. Proguanil plays a significant role in the treatment of malaria; its function is to stop the reproduction of the parasite in the red blood cells by inhibiting the folic acid metabolism [26]. To achieve this, the active metabolite of the drug binds with dihydrofolate reductase (DHFR) enzyme of the parasite.

Several analytical methods have been reported for the detection and quantification of pharmaceutical drugs. These methods include; High-performance liquid chromatography [27–29], capillary electrophoresis [30–32], micellar electrokinetic chromatography [33,34], electrochemical [35,36], and spectroscopic methods. Most of these methods require tedious sample extraction processes and are time-consuming. Therefore, there is a need to develop a fast, sensitive, and selective method for qualitative and quantitative analysis of proguanil. As far as we could possibly know, just two investigations are reported for the electroanalytical detection of proguanil. A few notable limitations of the electrochemical methods include slow electron transfer, low selectivity, and sensitivity. Hence there is a need to modify the bare electrodes to avoid such limitations mentioned above. The use of nanocomposites carbon nanotubes with nanoparticle would be beneficial in this regard because of their enhanced electrical conductivity, high surface area, and fast electron transfer rate, which ultimately improve the selectivity and sensitivity of the modified electrode [37,38].

2. Experimental

2.1. Apparatus and chemicals

Field emission scanning microscopy (FE-SEM) (ZEISS ultra plus, Germany) and transmission electron microscopy (TEM) (JEOL 101, USA) were used for morphological studies of the nanocomposite. For SEM analysis, aluminium stub sample holder was coated with carbon tape. The nanocomposite was then added on to the carbon tape and it was gold coated three times. Prior to TEM analysis, the nanocomposite was dispersed in ethanol and sonicated for 15 min. A copper grid was immersed into the solution. The gird was dried under IR lamp. The elemental composition was determined using Energy-dispersive X-ray spectroscopy (EDX). A Bruker D2 diffractometer at 40 kV and 50 mA was used to record the X-ray diffraction patterns (XRD). The measurements were taken at high angle 2θ in a range of 5°–90° with a scan speed of 0.01° 2θ s^{-1} using a secondary graphite monochromated Co K alpha radiation (l = 1.7902 A°). Raman spectroscopy studies were done using a DeltaNu Advantage 532 high performance Raman spectrometer with a 532 nm solid state frequency doubled Nd:YAG laser with a peak power of 200 mW and a 35 μ m diameter focused beam. Its resolution ranges from 8 to 10 cm^{-1} and the spectral range from 200 to 3400 cm^{-1}. CHI660E electrochemical workstation (CH instrument, USA) and a conventional three-electrode system were used for all electrochemical measurements. A glassy carbon electrode (3.0 mm), platinum wire and

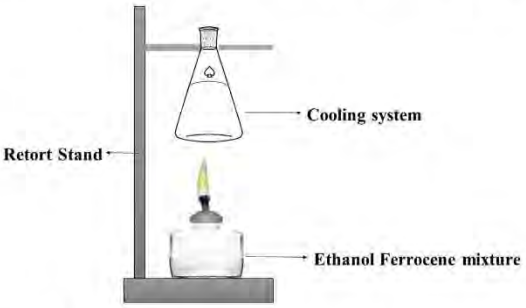

Fig. 1. Flame synthesis of MWCNTs-iron oxide nanocomposite.

Ag/AgCl/KCl (3.0 $molL^{-1}$) were used as working, counter, and the reference electrode, respectively. pH measurements were performed using the EXTECH PH60 pH meter (China). Ferrocene, ethanol, potassium ferricyanide, proguanil, and primaquine were purchased from Sigma Aldrich. Monosodium dihydrogen orthophosphate and sodium phosphate dibasic were purchased from Merck. Deionized water was used throughout the experiment.

2.2. Flame synthesis of MWCNTs-iron oxide nanocomposite

The experimental setup used in this study is shown in Fig. 1. Briefly, 0.5 g of ferrocene in ethanol was stirred for 30 min at room temperature. The mixture was transferred in a glassy spirit lamp with a cotton wick and ignited. After 4 h, MWCNTs-iron oxide nanocomposites were collected at the bottom of the cotton wick.

2.3. Fabrication of MWCNTs-iron oxide modified electrode

0.05 Microns of alumina slurry was used to polish the surface of the glassy carbon electrode (GCE) followed by washing with deionized water to remove any adsorbed alumina particles. A suspension of 5 μL (1 $mg.mL^{-1}$) MWCNTs-iron oxide was drop cast on the surface of the clean GCE. The electrode was dried under an IR lamp for 15 min. The modified electrode denoted (MWCNTs-iron oxide/GCE) was utilized for all electrochemical measurements. All electrochemical measurements were done using CHI660E electrochemical workstation. Electrochemical impendence spectroscopy measurements were taken at frequency range of 1–10,000 Hz with 5 mV amplitude. 2.5 mM $[Fe(CN)_6]^{3-}/[Fe(CN)_6]^{4-}$ in 0.1 M KCl was used.

2.4. Preparation of pharmaceutical and human urine samples

Proguanil tablets (Mozitec) containing 100 mg proguanil hydrochloride were finely powdered using a mortar and pestle. A suitable stock solution was prepared using powdered tablets. DPV of proguanil in the presence of pharmaceutical excipients were recorded by using diluted aliquots that are within the linear concentration range.

Urine sample was diluted 100 times with 0.1 M phosphate buffer (PB) (pH 5.5) to reduce the matrix effects. The sample was spiked with proguanil prior to analysis. MWCNTs-iron oxide/GCE was then used to detect proguanil in spiked urine samples.

3. Results and discussion

3.1. Morphological characterization

The formation of MWCNTs-iron oxide nanocomposite was confirmed by Raman spectroscopy as shown in Fig. 2A. The peaks at 1338 and 1604 cm^{-1} were attributed to D and G band respectively. The D band is

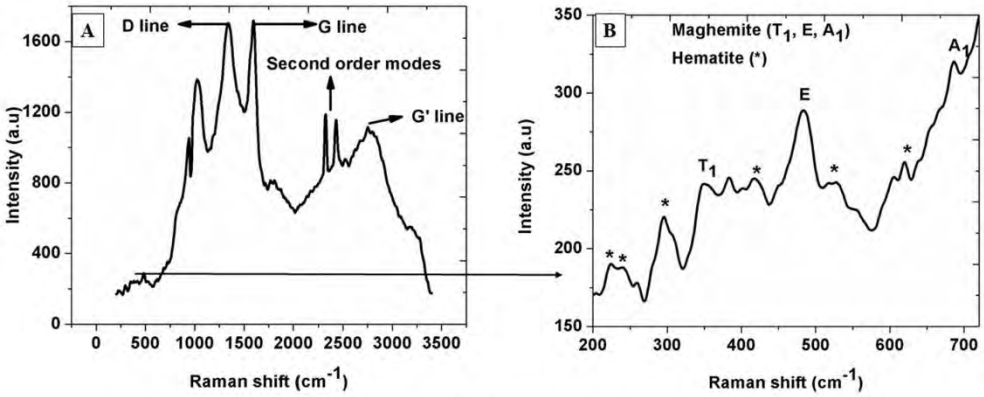

Fig. 2. Raman spectra of MWCNTs-iron oxide nanocomposite.

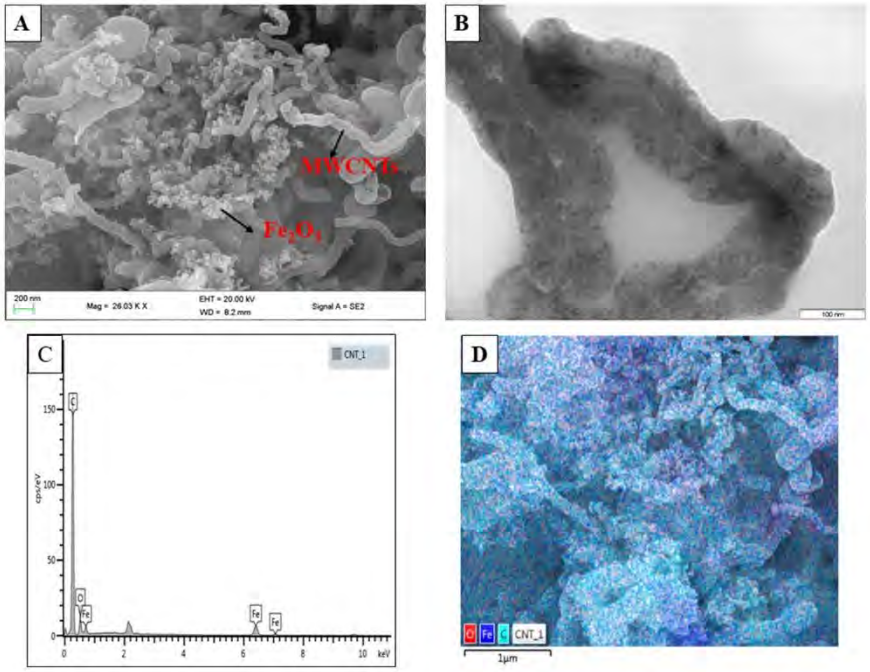

Fig. 3. (A) SEM, (B) TEM, (C) EDX and (D) EDX mapping of MWCNTs-iron oxide nanocomposite.

due to the defects in the sidewalls and ends of MWCNTs, while the G band is mainly due to the tangential stretching of the carbon-carbon bond. Second-order modes at 2301–2445 cm^{-1} and the G' (2759 cm^{-1}) were also observed. The structural quality of MWCNTs was estimated using the intensity ratio of the Raman D and G band (I_d/I_g) [39]. Both the D and G band were found to have similar intensities; thus, the density of defects was estimated to be high. The (I_d/I_g) ratio was found to be 0.98, the high (I_d/I_g) is attributed to the growth in multiple layers of MWCNTs. Raman spectroscopy was further used to confirm the presence of iron oxide in the MWCNTs- nanocomposite. The bands at 350, 482 and 686 cm^{-1} are assigned to maghemite nanoparticles [40]. While bands at 221, 240, 297, 416, 525, 620 cm^{-1} are assigned to hematite nanoparticles [41], as shown in Fig. 2B.

The morphological analysis of MWCNTs-iron oxide nanocomposite was studied using FE-SEM, as shown in Fig. 3A. Carbon nanotubes with an average diameter of 84 nm were obtained. The presence of iron oxide particles around the MWCNT was also observed. The presence of small iron oxide nanoparticles on the surface of MWCNTs were also confirmed with TEM (Fig. 3B). EDX analysis was used to confirm the presence of carbon (81.27 Wt%), iron (4.19 Wt%), and oxygen (14.54 Wt%). No peaks of impurities were observed (Fig. 3C). Iron oxide nanoparticles were evenly distributed on the surface of CNT, as shown in Fig. 3D.

Table 1
CV data obtained for MWCNTs-iron oxide/GCE electrode in 2.5 mM $[Fe(CN)_6]^{-3/-4}$.

Electrode	Ipa (μA)	Ipc (μA)	Ipa/Ipc	Epa (mV)	Epc (mV)	ΔEp (mV)
GCE	4.45	4.39	1.01	288	188	100
GCE/MWCNTs iron oxide	4.98	4.78	1.04	274	202	72

The XRD pattern of MWCNTs-iron oxide nanocomposite is shown in Fig. S1. Two distinct diffraction peaks at 2Θ 26 and 42.7 were indexed to (002) and (100) plane of graphite structure [42]. The other peaks at 2Θ 29, 35, 43, 53, 56, 62 and 77 are indexed to (220), (311), (400), (422), (511), (440) and (533) plane of cubic maghemite (JCPDS: 01-089-3850). As confirmed in the Raman spectroscopy, peaks of hematite were also observed in the XRD patterns at 2Θ 23.94, 40.33, 54.77, 56.95 and 62.48. These peaks were assigned to (012), (113), (116), (018), and (214) plane of rhombohedral hematite (JCPDS: 00-033-0664). The area ratio of the crystalline peak to all peaks was used to estimate the degree of crystallinity [43]. The percentage crystallinity values for MWCNTs, maghemite, and hematite nanoparticles were found to be 34.63, 7.89, and 13.69% respectively.

3.2. Electrochemical characterization

To investigate the electron transfer properties of the modified electrode; electrochemical impendence spectroscopy (EIS) studies were done. $[Fe(CN)_6]^{3-}/[Fe(CN)_6]^{4-}$ (2.5 mM) in 0.1 KCl was used as the electrolyte. A frequency range of 1–10,000 Hz with 5 mV amplitude was used to take the measurements. EIS data was fitted using Randles equivalent circuit (Fig. S2 inset). The values for each element of the Randles equivalent circuit are given in Table S1. As shown in Fig. S2, a well-defined semi-circle with charge transfer resistance (Rct) value of 222.2 Ω was obtained for the bare GCE. This high Rct value suggests that the diffusion of $[Fe(CN)_6]^{3-}/[Fe(CN)_6]^{4-}$ towards the electrode is low. Thus to improve this Rct value, it is necessary to modify the electrode with MWCNTs-iron oxide nanocomposite. Upon modification with MWCNTs-iron oxide nanoparticles; the semi-circle diminished, and the Rct value of 0.001 Ω was obtained. The decrease in Rct value signifies a high electron rate transfer between the modified electrode and the $[Fe(CN)_6]^{3-}/[Fe(CN)_6]^{4-}$. This is attributed to the unique properties of carbon nanotubes and iron oxide nanoparticles, such as high surface area and good conductivity.

Cyclic voltammetry (CV) was used to investigate further the electron transport properties of MWCNTs-iron oxide nanocomposite-modified electrode using $[Fe(CN)_6]^{3-}/[Fe(CN)_6]^{4-}$ as the redox probe. A well-defined redox couple (Fig. S3A) that is due to $[Fe(CN)_6]^{3-}/[Fe(CN)_6]^{4-}$ was obtained for both the bare electrode and MWCNTs-iron oxide/GCE electrode. However, the current increased on the modified electrode compared to the bare electrode, as shown in Table 1, which can be attributed to the high surface area of nanocomposite. Thus more sites for electron transfer were available. Also, the ratio of the anodic and cathodic peak current (I_{pa}/I_{pc}) was calculated to be ~1.0 (Table 1). This indicates a reversible electrochemical process [44]. Peak to peak separation potential (ΔEp) for bare and MWCNTs-iron oxide/GCE electrodes were found to be 100 mV and 72 mV, respectively. The decrease in ΔEp indicates a faster electron transfer rate at the modified electron.

Randles Sevcik equation was used to calculate the effective surface area of the bare and modified electrode at 2.5 mM $Fe(CN)_6]^{3-}/[Fe(CN)_6]^{4-}$ solution while varying the scan rate as shown in Fig. S3B. The inset on S3B displays a plot of peak current versus square root of scan rate with a linear regression $Ip = 0.0065\sqrt{v} - 0.015$

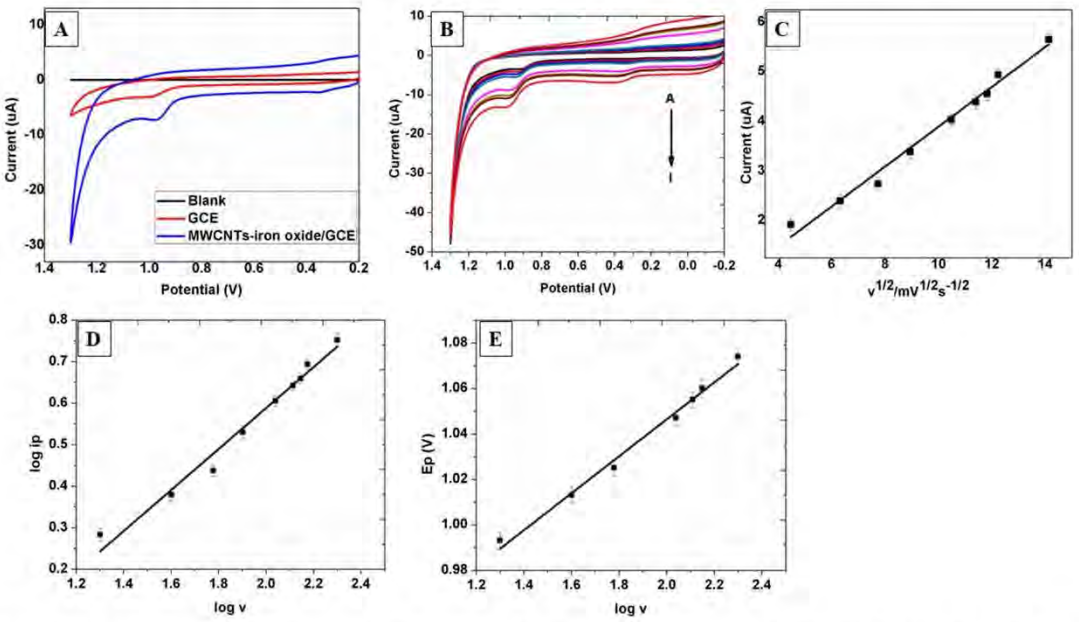

Fig. 4. (A) Cyclic voltammograms of MWCNTs-iron oxide/GCE in plain electrolyte, bare GCE and MWCNTs-iron oxide/GCE in 0.1 mM proguanil (pH 5.5) at a scan rate of 100 mV/s; (B) Cyclic voltammograms of MWCNTs-iron oxide/GCE with change in scan rate; (C) Relation between square root of scan rate and current for MWCNTs-iron oxide/GCE in proguanil (0.1 M); (D) Relation between log v and log ip (E) plot between peak potential vs log of scan rate for MWCNTs-iron oxide/GCE in proguanil (0.1 M).

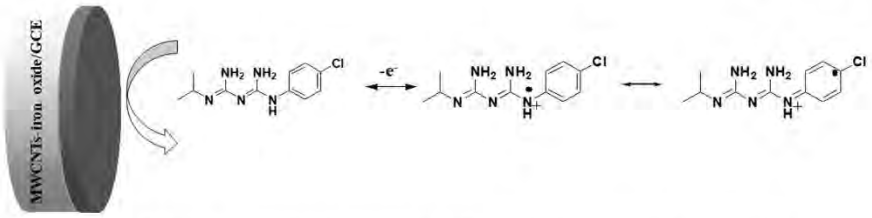

Fig. 5. Schematic representation of a plausible mechanism for electrochemical detection of proguanil.

$$I_p = 2{\cdot}69 \times 10^5 A \sqrt{D} \left(\sqrt{n}\right)^3 \sqrt{\gamma}\, C_0 \quad (1)$$

where Ip represent the peak current, n = number of electrons involved in the charge transfer (n = 1), D = diffusion coefficient (D = 7.6 × 10^{-6} cm^2s^{-1}), A = effective surface area (cm^2), C = concentration of [Fe $(CN)_6]^{3-}$/$[Fe(CN)_6]^{4-}$ ($mol.cm^{-3}$) and υ = is the scan rate ($V.s^{-1}$). The effective surface area was calculated to be 0.0324 and 0.040 cm^2 for bare and MWCNTs-iron oxide modified electrode respectively.

3.3. Electrochemical behavior of proguanil at MWCNTs-iron oxide/GCE

CV was used to investigate the electrochemical behavior of MWCNTs-iron oxide/GCE electrode towards 0.1 mM proguanil in 0.1 mM PBS at pH 5.5, as illustrated in Fig. 4A. One anodic peak at 1.02 V and 1.0 V was observed for GCE and MWCNTs-iron oxide/GCE respectively. No peaks were observed for MWCNTs-iron oxide/GCE in plan electrolyte. The anodic peak indicates that proguanil undergoes one irreversible oxidation process; thus, no reverse peak was obtained. A plausible mechanism for the electrochemical detection of proguanil is shown in Fig. 5. The anodic peak at 1.0 V is due to the irreversible oxidation 4-Chloroaniline moiety in proguanil. The MWCNTs-iron oxide/GCE showed better sensitivity towards proguanil compared to bare GCE. This is attributed to the unique properties of the synthesized nanocomposite such as high electrocatalytic activity and good conductivity; thus the electron transfer rate is enhanced. The high surface to volume ratio and good affinity of iron oxide nanoparticles towards amine functional groups that are present in proguanil improves the sensitivity and selectivity of the sensor.

The effect of scan rate was conducted to investigate the electrochemical reaction mechanism of proguanil. Cyclic voltammograms (Fig. 4B) were recorded with different scan rates (20–200 $mV.s^{-1}$). A linear relationship between peak currents and square root of scan rate was observed (Fig. 4C). This relationship is represented by the equation Ip = $0.4014v^{1/2}$ − 0.124 (R^2 = 0.9842). Therefore the oxidation of proguanil at MWCNTs-iron oxide/GCE is a diffusion controlled process [45]. This was further confirmed by the linear relation between the logarithm of scan rate and logarithm of peak current (Fig. 4D) (log Ip = 0.486logv − 0.386 (R^2 = 0.9761)). The slope was found to be 0.49 thus it is close to the theoretical value of a diffusion controlled process [46]. The potential of the oxidation peak was also influenced by the change in scan rate. The peak potential shifted to more positive values as the scan rate was increased (Fig. 4E). This further confirms the irreversibility of the oxidation process. The linear relationship between log v and Ep can be expressed as Ep = 0.081logv + 0.884 (R^2 = 0.9892).

The number of electrons involved in the oxidation of proguanil was calculated using the Laviron equation, which defines the relationship between Ep and logv as:

$$Ep = E^{\circ} + \left[2.303\frac{RT}{\alpha nF}\right][log(RTk^{\circ}/\alpha nF)] + \left[\left(2.303\frac{RT}{\alpha nF}\right) log v\right] \quad (2)$$

where E^o = formal redox potential, n = number of electrons involved K^o = standard rate constant of the surface reaction, α = electron transfer coefficient. Other symbols have their usual meaning [47]. As illustrated in Fig. 4E, a linear relationship was observed between Ep and logv, which is represented by the equation Ep = 0.081logv + 0.884 (R^2 = 0.9892). The value of αn was calculated by using the following constants; R = 8.314 JK mol, T = 298 K, and F = 96,480 C mol^{-1}. The value of α was then calculated using the Bard and Faulkner equation below:

$$\alpha = 47.7/\left(E_p - E_{p^{1/2}}\right) \quad (3)$$

where $Ep_{1/2}$ is half of the peak potential. The number of electrons (n) involved in the oxidation of proguanil was found to be ~1.

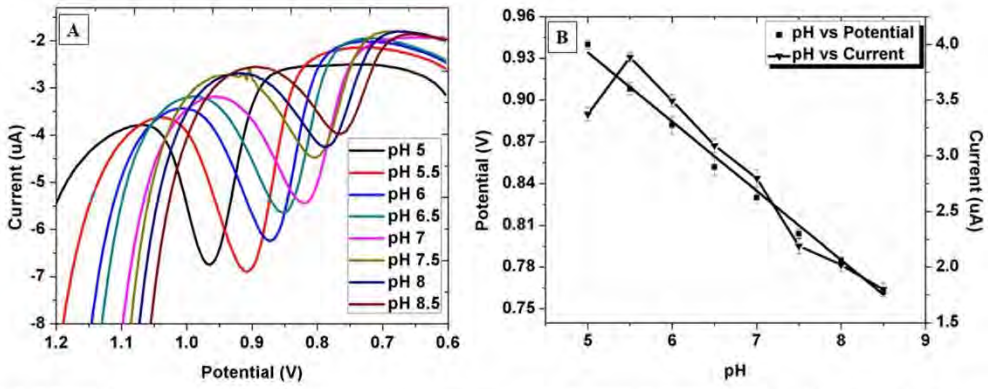

Fig. 6. Differential pulse voltammograms of proguanil with different pH; (B) The plot of current vs pH and potential vs pH at MWCNTs-iron oxide/GCE.

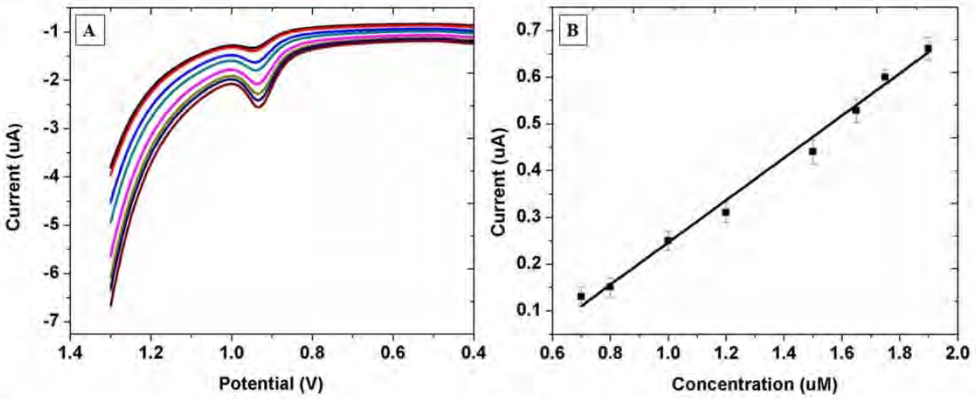

Fig. 7. (A) DP voltammograms of proguanil at different concentrations in 0.1 M PBS (pH 5.5); (B) calibration plots for proguanil in 0.1 M PBS (pH 5.5) MWCNTs-iron oxide/GCE.

3.4. DPV optimization and influence of pH

Before differential pulse voltammetry (DPV) analysis, parameters such as step potential, pulse width, and pulse amplitude were optimized (Fig. S4). All Measurements were done three times. A pulse amplitude of 50 mV and a pulse width of 50 ms was used while varying the step potential (3–8 mV). An increase in current with the potential step was observed (Fig. S4A). This is due to a faster change in potential, thus a larger scan rate. The most repeatable peak current was obtained at 5 mV. A pulse amplitude of 50 mV and the optimum step potential (5 mV) was used to investigate the effect of pulse width (10–60 ms). A decrease in peak current with an increase in pulse width was observed (Fig. S4B). This is due to a decrease in scan rate; the most repeatable current was obtained at 40 ms. The pulse width (40 ms) and potential step (5 mV) were used to study the influence of pulse amplitude (10–70 mV). An increase in current with pulse amplitude was observed (Fig. S4C). The most repeatable pulse amplitude was found to be 50 mV. The effect of pH on the oxidation of 0.1 mM proguanil in 0.1 M PBS was investigated using differential pulse voltammetry (DPV), as shown in Fig. 6A. A pH range of 5–8.5 was selected. A linear relationship between Ep vs pH was observed (Fig. 6B). The linear regression is shown below:

$$Ep = 1.185 - 0.05pH \quad (4)$$

Since the slope is close to the theoretical Nernstian value of 0.059 V/pH at 25 °C; an equal number of protons and electrons are involved in the electro-oxidation of proguanil at MWCNTs-iron oxide/GCE [48]. The peak potential shifted towards less positive potentials as the solution became more basic. This indicates the presence of a proton-coupled electron transfer reaction. The optimum pH was 5.5, and it was used for all further studies.

3.5. Analytical performance

DPV was used under optimum conditions to investigate the analytical performance of MWCNTs-iron oxide/GCE (Fig. 7A). A linear relationship between the peak current and concentration was observed in the range of 0.7×10^{-6}–1.9×10^{-6} M (Fig. 7B). The equation below represents the corresponding linear regression:

$$Ip = 0.4479C - 0.0204 \quad (5)$$

where C = concentration of proguanil and Ip = peak current. The relation between 3S/N and 10S/N was used to calculate the limit of detection (LOD) and limit of quantification (LOQ) respectively. The LOD and LOQ for proguanil at GCE/MWCNTs-iron oxide were calculated to be 1.96×10^{-8} M and 6.54×10^{-8} M respectively. The present work was compared with other reported electroanalytical methods for detection of proguanil (Table 2). The proposed method shows better sensitivity for detection of proguanil.

Table 2
A comparison of the present study with other reported methods for electrochemical determination of proguanil.

Electrode	Concentration range ($mol.L^{-1}$)	LOD ($mol.L^{-1}$)	Ref
Renewable silver amalgam film	1×10^{-7}–6×10^{-6}	2.9×10^{-8}	[49]
CWE/phosphotungstic acid	1×10^{-5}–1×10^{-2}	1×10^{-6}	[26]
MWCNTs iron oxide/GCE	0.7×10^{-6}–1.9×10^{-6}	1.96×10^{-8}	Present work

Table 3
Results from proguanil tablet at MWCNTs-iron oxide/GCE.

S no	Expected (μM)	Detected	Recovery	Bias (%)	RSD (%) (n = 3)
1	1.2	1.2093	100.8	0.8	0.26
2	1.4	1.423	101.6	1.6	0.83
3	1.6	1.5646	97.8	2.2	0.52
4	1.8	1.7631	98	2	1.23
5	2	2.0384	101.92	1.92	0.33

3.6. Interference study and reproducibility

The selectivity of MWCNTs-iron oxide/GCE towards proguanil was investigated in the presence of 200 fold concentration of primaquine, inorganic (Na^+, Mg^{2+}, Cl^- SO_4) and organic (uric acid, ascorbic acid) interfering species using DPV under optimum conditions (Fig. S5). The peak current slightly decreased in the presence of interfering species. The deviation was less than the accepted tolerance of 5%. Thus the proposed sensor showed good selectivity towards proguanil. The reproducibility of the sensor was evaluated using three identically prepared electrodes. The relative standard deviation was calculated to be 2.4%, this demonstrate good reproducibility.

Table 4
Recovery results for proguanil in spiked human urine sample at MWCNTs-iron oxide/GCE.

S no	Amount added (μM)	Found (μM)	Recovery (%)	Bias (%)
1	2.00	1.98	99.0	1
2	2.50	2.54	101.6	1.6
3	3.00	3.12	104.0	4

3.7. Real sample analysis

DPV studies were carried out under optimum conditions to determine the content of proguanil in commercially available pharmaceutical tablets. The proposed sensor demonstrated good selectively towards proguanil in the presence of pharmaceutical excipients (Table 3). The recovery percentages were calculated using standard addition method (Fig. S6). A bias of less than 2.3% was obtained. Additionally proguanil was determined in 100 fold dilution of human urine under optimum conditions. The recovery results were found to be in the range of 99–104% (Table 4). The proposed sensor is selective and practically applicable for the analysis of proguanil in pharmaceutical formulations and urine samples.

4. Conclusions

A simple method for in-situ flame synthesis of MWCNTs-iron oxide nanocomposite was successfully developed. Raman spectroscopy and X-ray diffraction confirmed the presence of MWCNTs and iron oxide nanoparticles in the composite material. SEM and TEM images proved the formation of MWCNTs-iron oxide nanocomposite. Electrochemical detection of proguanil was carried out using MWCNTs-iron oxide/GCE. A detection limit of 1.96×10^{-8} M with a linear range of 0.7×10^{-6}–1.9×10^{-6} M was obtained, this was found to be better when compared with the reported literature. The modified electrode showed satisfactory selectivity and sensitivity towards proguanil in the presence of different sample matrix such as pharmaceutical formulation and urine sample. Thus, MWCNTs-iron oxide nanocomposites have proven to be useful in the fabrication of electrochemical sensor for quality control purposes.

CRediT authorship contribution statement

Zondi Nate: Conceptualization, Methodology, Investigation, Writing - Original Draft.

Rajshekhar Karpoormath: Supervision, Funding acquisition, Resources.

Atal A.S. Gill: Conceptualization, Validation.

Suraj Shinde: Validation.

Shaukatali N. Inamdar: Validation.

Ruchika Chauhan: Supervision.

Declaration of competing interest

The authors declare that they have no known competing financial interests or personal relationships that could have appeared to influence the work reported in this paper.

Acknowledgement

The authors are grateful for the financial support from the National Research Foundation-South Africa (NRF-SA) (Grant No 121804, 103728 and 112079) and College of Health Sciences, University of KwaZulu-Natal (CHS-UKZN). Furthermore authors would also like to acknowledge Nano-technology for sustainable development platform of UKZN and UKZN microscopy & microanalysis unit.

Appendix A. Supplementary data

Supplementary data to this article can be found online at https://doi.org/10.1016/j.diamond.2020.108178.

References

[1] N. Anzar, R. Hasan, M. Tyagi, N. Yadav, J. Narang, Carbon nanotube - a review on synthesis, properties and plethora of applications in the field of biomedical science, Sensors Int. 1 (2020) 100003, https://doi.org/10.1016/j.sintl.2020.100003.
[2] R.H. Baughman, A.A. Zakhidov, W.A. de Heer, Carbon nanotubes—the route toward applications, Science. 297 (2002) 787–792, https://doi.org/10.1126/science.1060928.
[3] J. Li, R. Yuan, Y. Chai, X. Che, Fabrication of a novel glucose biosensor based on Pt nanoparticles-decorated iron oxide-multiwall carbon nanotubes magnetic composite, J. Mol. Catal. B Enzym. 66 (2010) 8–14, https://doi.org/10.1016/j.molcatb.2010.03.005.
[4] N.P. Shetti, D.S. Nayak, S.J. Malode, R.R. Kakarla, S.S. Shukla, T.M. Aminabhavi, Sensors based on ruthenium-doped TiO2 nanoparticles loaded into multi-walled carbon nanotubes for the detection of flufenamic acid and mefenamic acid, Anal. Chim. Acta 1051 (2019) 58–72, https://doi.org/10.1016/j.aca.2018.11.041.
[5] Y.X. C., Y.J. L., J.J. H., K. Li, Y.Z. X., W. Zhang, L.T. J., Amperometric tyrosinase biosensor based on Fe3O4 nanoparticles-coated carbon nanotubes nanocomposite for rapid detection of coliforms, Electrochim. Acta 54 (2009) 2588–2594, https://doi.org/10.1016/j.electacta.2008.10.072.
[6] Y. Fan, F. Su, K. Li, C. Ke, Y. Yan, Carbon nanotube filled with magnetic iron oxide and modified with polyamidoamine dendrimers for immobilizing lipase toward application in biodiesel production, Sci. Rep. 7 (2017) 45643, https://doi.org/10.1038/srep45643.
[7] J. de O. Marques Neto, C.R. Bellato, D. de C. Silva, Iron oxide/carbon nanotubes/chitosan magnetic composite film for chromium species removal, Chemosphere 218 (2019) 391–401, https://doi.org/10.1016/j.chemosphere.2018.11.080.
[8] M. Madhusudhana Reddy, G. Ramanjaneya Reddy, K. Chennakesavulu, E. Sundaravadivel, S.S. Prasath, A.M. Rabel, J. Sreeramulu, Synthesis of zinc oxide and carbon nanotube composites by CVD method: photocatalytic studies, J. Porous. Mater. 24 (2017) 149–156, https://doi.org/10.1007/s10934-016-0247-3.
[9] E.M. Elnaggar, K.I. Kabel, A.A. Farag, A.G. Al Gamal, Comparative study on doping of polyaniline with graphene and multi-walled carbon nanotubes, J. Nanostructure Chem. 7 (2017) 75–83, https://doi.org/10.1007/s40097-017-0217-6.
[10] L.M. Hoyos-Palacio, D.P. Cuesta Castro, I.C. Ortiz-Trujillo, L.E. Botero Palacio, B. J. Galeano Upegui, N.J. Escobar Mora, J.A. Carlos Cornelio, Compounds of carbon nanotubes decorated with silver nanoparticles via in-situ by chemical vapor deposition (CVD), J. Mater. Res. Technol. 8 (2019) 5893–5898, https://doi.org/10.1016/j.jmrt.2019.09.062.
[11] Z. Yang, L. Tang, J. Ye, D. Shi, S. Liu, M. Chen, Hierarchical nanostructured α-Fe2O3/polyaniline anodes for high performance supercapacitors, Electrochim. Acta 269 (2018) 21–29, https://doi.org/10.1016/j.electacta.2018.02.144.
[12] G. Zhao, H.-Y. Liu, X. Du, H. Zhou, Z. Pan, Y.-W. Mai, Y.-Y. Jia, W. Yan, Flame synthesis of carbon nanotubes on glass fibre fabrics and their enhancement in electrical and thermal properties of glass fibre/epoxy composites, Compos. Part B Eng. 198 (2020) 108249, https://doi.org/10.1016/j.compositesb.2020.108249.
[13] H. Hong, N.K. Memon, Z. Dong, B.H. Kear, S.D. Tse, Flame synthesis of gamma-iron-oxide (γ-Fe2O3) nanocrystal films and carbon nanotubes on stainless-steel substrates, Proc. Combust. Inst. 37 (2019) 1249–1256, https://doi.org/10.1016/j.proci.2018.06.098.
[14] N. Arora, N.N. Sharma, Arc discharge synthesis of carbon nanotubes: comprehensive review, Diam. Relat. Mater. 50 (2014) 135–150, https://doi.org/10.1016/j.diamond.2014.10.001.
[15] R.A. Ismail, M.H. Mohsin, A.K. Ali, K.I. Hassoon, S. Erten Ela, Preparation and characterization of carbon nanotubes by pulsed laser ablation in water for optoelectronic application, Phys. E Low-Dimensional Syst. Nanostructures. 119 (2020) 113997, https://doi.org/10.1016/j.physe.2020.113997.
[16] B.V. Basheer, J.J. George, S. Siengchin, J. Parameswaranpillai, Polymer grafted carbon nanotubes—synthesis, properties, and applications: a review, Nano-Structures & Nano-Objects 22 (2020), https://doi.org/10.1016/j.nanoso.2020.100429, 100429.
[17] R. Andrews, D. Jacques, D. Qian, T. Rantell, Multiwall carbon nanotubes: synthesis and application, Acc. Chem. Res. 35 (2002) 1008–1017, https://doi.org/10.1021/ar010151m.
[18] S.N. Inamdar, S.K. Haram, Synthesis and characterization of uncapped gamma-Fe2O3 nanoparticles prepared by flame pyrolysis of ferrocene in ethanol, J. Nanosci. Nanotechnol. 6 (n.d.) 2155–2158. https://www.ingentaconnect.com/content/asp/jnn/2006/00000006/00000007/art00042.
[19] D. Bhattacharjya, H.-Y. Park, M.-S. Kim, H.-S. Choi, S.N. Inamdar, J.-S. Yu, Nitrogen-doped carbon nanoparticles by flame synthesis as anode material for rechargeable lithium-ion batteries, Langmuir. 30 (2014) 318–324, https://doi.org/10.1021/la403366e.
[20] N.P. Shetti, D.S. Nayak, G.T. Kuchinad, R.R. Naik, Electrochemical behavior of thiosalicylic acid at γ Fe2O3 nanoparticles and clay composite carbon electrode, Electrochim. Acta 269 (2018) 204–211, https://doi.org/10.1016/j.electacta.2018.02.170.
[21] G. Manasa, A.K. Bhakta, Z. Mekhalif, R.J. Mascarenhas, Voltammetric study and rapid quantification of resorcinol in hair dye and biological samples using

ultrasensitive maghemite/MWCNT modified carbon paste electrode, Electroanalysis 31 (2019) 1363–1372, https://doi.org/10.1002/elan.201900143.
[22] V. Erady, R.J. Mascarenhas, A.K. Satpati, S. Detriche, Z. Mekhalif, J. Dalhalle, A. Dhason, Sensitive detection of ferulic acid using multi-walled carbon nanotube decorated with silver nano-particles modified carbon paste electrode, J. Electroanal. Chem. 806 (2017) 22–31, https://doi.org/10.1016/j.jelechem.2017.10.045.
[23] Wulan, Praswasti PDK, Rivai, Ghassan Tsabit, Synthesis of carbon nanotube using ferrocene as carbon source and catalyst in a vertical structured catalyst reactor, E3S Web Conf. 67 (2018), https://doi.org/10.1051/e3sconf/20186703038, 3038.
[24] C.S. Yah, G.S. Simate, K. Moothi, M.K. S, S.E. Iyuke, Synthesis of large carbon nanotube from ferrocene:The chemical vapour deposition process, Trends Appl. Sci. Res. 6 (2011) 1270–1279.
[25] T.M. Keller, M. Laskoski, S.B. Qadri, Ferrocene catalyzed carbon nanotube formation in carbonaceous solid, J. Phys. Chem. C 111 (2007) 2514–2519, https://doi.org/10.1021/jp0665527.
[26] F.M. Abdel Haleem, M. Saad, M.S. Rizk, Development of new potentiometric sensors for the determination of proguanil hydrochloride in serum and urine, Chin. Chem. Lett. 27 (2016) 857–863, https://doi.org/10.1016/j.cclet.2016.01.027.
[27] S. Kombath, I.B. Balde, S. Carret, S. Kabiche, S. Cisternino, J.E. Fontan, J. Schlatter, Stability-indicating HPLC assay for determination of idebenone in pharmaceutical forms, J. Anal. Methods Chem. 2015 (2015) 6–11, https://doi.org/10.1155/2015/835986.
[28] N.M. Hosny, K. Huddersman, S.M. El-Gizawy, N.N. Atia, New approach for simultaneous analysis of commonly used antigout drugs by HPLC/UV method; application in pharmaceutical and biological analysis, Microchem. J. 147 (2019) 717–728, https://doi.org/10.1016/j.microc.2019.03.080.
[29] Y.S. Endoh, H. Yoshimura, N. Sasaki, Y. Ishihara, H. Sasaki, S. Nakamura, Y. Inoue, M. Nishikawa, High-performance liquid chromatographic determination of pamaquine, primaquine and carboxy primaquine in calf plasma using electrochemical detection, J. Chromatogr. B Biomed. Sci. Appl. 579 (1992) 123–129, https://doi.org/10.1016/0378-4347(92)80370-6.
[30] M. Heller, L. Vitali, M.A. Siqueira, A.V.F. Sako, M. Piovezan, G.A. Micke, Capillary electrophoresis with UV detection to determine cocaine on circulated banknotes, ISRN Anal. Chem. 2013 (2013) 489705, https://doi.org/10.1155/2013/489705.
[31] M. Rambla Alegre, J. Peris Vicente, J. Esteve Romero, M. E. Capella Peiró, D. Bose, Capillary electrophoresis determination of antihistamines in serum and pharmaceuticals, Anal. Chim. Acta 666 (2010) 102–109, https://doi.org/10.1016/j.aca.2010.03.041.
[32] Y. Huang, W. Pan, M. Guo, S. Yao, Capillary electrophoresis with end-column electrochemiluminescence for the analysis of chloroquine phosphate and the study on its interaction with human serum albumin, J. Chromatogr. A 1154 (2007) 373–378, https://doi.org/10.1016/j.chroma.2007.02.029.
[33] R.B. Taylor, R.G. Reid, A.S. Low, Analysis of proguanil and its metabolites by application of the sweeping technique in micellar electrokinetic chromatography, J. Chromatogr. A 916 (2001) 201–206, https://doi.org/10.1016/S0021-9673(00)01035-9.
[34] M.E. El-Kommos, N.A. Mohamed, A.F. Abdel Hakiem, Selective micellar electrokinetic chromatographic method for simultaneous determination of some pharmaceutical binary mixtures containing non-steroidal anti-inflammatory drugs, J. Pharm. Anal. 3 (2013) 53–60, https://doi.org/10.1016/j.jpha.2012.07.005.
[35] A. Afkhami, H. Ghaedi, T. Madrakian, M. Ahmadi, H. Mahmood-Kashani, Fabrication of a new electrochemical sensor based on a new nano-molecularly imprinted polymer for highly selective and sensitive determination of tramadol in human urine samples, Biosens. Bioelectron. 44 (2013) 34–40, https://doi.org/10.1016/j.bios.2012.11.030.
[36] T.E. Chiwunze, V.N. Palakollu, A.A.S. Gill, F. Kayamba, N.B. Thapliyal, R. Karpoormath, A highly dispersed multi-walled carbon nanotubes and poly (methyl orange) based electrochemical sensor for the determination of an anti-malarial drug: Amodiaquine, Mater. Sci. Eng. C Mater. Biol. Appl. 97 (2019) 285–292, https://doi.org/10.1016/j.msec.2018.12.018.
[37] A.A. Ensafi, H. Karimi-Maleh, A voltammetric sensor based on modified multiwall carbon nanotubes for cysteamine determination in the presence of tryptophan using p-aminophenol as a mediator, Electroanalysis 22 (2010) 2558–2568, https://doi.org/10.1002/elan.201000270.
[38] N. Sattaralmady, H. Heli, An electrocatalytic transducer for l cysteine detection based on cobalt hexacyanoferrate nanoparticles with a core–shell structure, Anal. Biochem. 409 (2011) 74–80, https://doi.org/10.1016/j.ab.2010.09.032.
[39] L. Thi Mai Hoa, Characterization of multi walled carbon nanotubes functionalized by a mixture of HNO3/H2SO4, Diam. Relat. Mater. 89 (2018) 43–51, https://doi.org/10.1016/j.diamond.2018.08.008.
[40] Y. El Mendili, J.-F. Bardeau, N. Randrianantoandro, J.-M. Greneche, F. Grasset, Structural behavior of laser-irradiated γ-Fe(2)O(3) nanocrystals dispersed in porous silica matrix: γ-Fe(2)O(3) to α-Fe(2)O(3) phase transition and formation of ε-Fe(2)O(3), Sci. Technol. Adv. Mater. 17 (2016) 597–609, https://doi.org/10.1080/14686996.2016.1222494.
[41] L. Slavov, M.V. Abrashev, T. Merodiiska, C. Gelev, R.E. Vandenberghe, I. Markova-Deneva, I. Nedkov, Raman spectroscopy investigation of magnetite nanoparticles in ferrofluids, J. Magn. Magn. Mater. 322 (2010) 1904–1911, https://doi.org/10.1016/j.jmmm.2010.01.005.
[42] K.S. Khashan, G.M. Sulaiman, R. Mahdi, A. kadhim, The effect of laser energy on the properties of carbon nanotube—iron oxide nanoparticles composite prepared via pulsed laser ablation in liquid, Mater. Res. Express. 5 (2018), https://doi.org/10.1088/2053-1591/aadabc, 105004.
[43] H. Park, T. Kim, J. Huh, M. Kang, J.E. Lee, H. Yoon, P.E.T. Al, Anisotropic growth control of polyaniline nanostructures and their morphology-dependent electrochemical characteristics, (2012) 7624–7633.
[44] O.R. Obisesan, A.S. Adekunle, J.A.O. Oyekunle, T. Sabu, T.T.I. Nkambule, B. B. Mamba, Development of electrochemical nanosensor for the detection of malaria parasite in clinical samples, Front. Chem. 7 (2019) 89, https://doi.org/10.3389/fchem.2019.00089.
[45] Allen J. Bard, L.R., Faulkner, Electrochemical Methods: Fundamentals and Applications, 2nd edition, John Wiley & Sons, Ltd, New York, 1980.
[46] David K. Gosser, Cyclic Voltammetry: Simulation and Analysis of Reaction Mechanisms, VCH, New York, 1993.
[47] E. Laviron, General expression of the linear potential sweep voltammogram in the case of diffusionless electrochemical systems, J. Electroanal. Chem. Interfacial Electrochem. 101 (1979) 19–28, https://doi.org/10.1016/S0022-0728(79)80075-3.
[48] L. Zhang, J. Zhang, 3D hierarchical bayberry-like Ni@carbon hollow nanosphere/rGO hybrid as a new interesting electrode material for simultaneous detection of small biomolecules, Talanta. 178 (2018) 608–615, https://doi.org/10.1016/j.talanta.2017.09.086.
[49] S. Smarzewska, S. Skrzypek, W. Ciesielski, Voltammetric determination of proguanil in malarone and spiked urine with a renewable silver amalgam film electrode, Electroanalysis. 24 (2012) 1966–1972, https://doi.org/10.1002/elan.201200312.

7.3.4 Appendix 4 published article

Microchemical Journal 160 (2021) 105709

Contents lists available at ScienceDirect

Microchemical Journal

journal homepage: www.elsevier.com/locate/microc

Polyaniline-cobalt oxide nanofibers for simultaneous electrochemical determination of antimalarial drugs: Primaquine and proguanil

Zondi Nate, Atal A.S. Gill, Ruchika Chauhan, Rajshekhar Karpoormath*

Department of Pharmaceutical Chemistry, College of Health Sciences, University of KwaZulu-Natal, Westville Campus, Durban 4000, South Africa

ARTICLE INFO

Keywords:
Primaquine
Proguanil
Simultaneous detection
Cobalt oxide
Polyaniline nanofibers

ABSTRACT

Quality control of antimalarial drugs is essential due to the prevalence of counterfeit medicines. In this work, polyaniline-cobalt oxide nanofibers were synthesized using precipitation oxidation and interfacial polymerization. The nanocomposites were characterized using UV–Vis spectroscopy, Fourier transform infrared spectroscopy (FTIR), transmission electron microscopy (TEM), scanning electron microscopy (SEM), Energy-dispersive X-ray spectroscopy (EDX), and X-ray diffraction (XRD). Morphological studies confirmed the formation of PANI nanofibers. The presence of Co_3O_4 in the composite was confirmed by XRD and EDX. Differential pulse voltammetry (DPV) and cyclic voltammetry (CV) were used to study the simultaneous electrochemical detection of primaquine and proguanil using a glassy carbon electrode modified with polyaniline nanofibers incorporated with cobalt oxide nanoparticles (PANI-Co_3O_4/GCE). The optimum pH for the response of the sensor was found to be 3.5 for both drugs. A limit of detection (LOD) of 2.07 nM and 1.42 nM with a linear range of 0.020–0.036 and 0.016–0.028 mM was obtained for primaquine and proguanil, respectively. Additionally, the practical applicability of PANI-Co_3O_4/GCE was studied in human urine with different interfering agents, good recovery of both drugs ranging within 94–105% was achieved. PANI-Co_3O_4 nanocomposite can therefore be used to fabricate electrochemical sensors for quality control purposes.

1. Introduction

Malaria is one of the most common protozoan parasitic diseases, which has become a great public health concern in tropical and sub-tropical areas [1–3]. In 2017 an estimated 219 million malaria cases were reported worldwide; 435,000 cases resulted in death [4]. Most malaria cases in Africa are due to *Plasmodium falciparum*, while in the North and South America regions, *Plasmodium vivax* is dominant [4–7]. The application of combination therapy in the treatment of malaria due to *Plasmodium falciparum*, *Plasmodium vivax*, and *Plasmodium ovale* is increasing. A combination of primaquine and proguanil is usually recommended to treat uncomplicated malaria due to *Plasmodium vivax* [8]. N-(6-methoxyquinolin-8-yl)pentane-1,4-diamine, commonly known as primaquine (Fig. 1A), is an FDA approved antimalarial drug. Its main function is to eliminate hypnozoites and schizonts of *Plasmodium ovale* and *Plasmodium vivax* [9–11]. Another antimalarial drug that is mostly used is (1E)-1-[amino-(4-chloroanilino)methylidene]-2-propan-2-yl guanidine commonly known as proguanil (Fig. 1B). This drug effectively treats *Plasmodium vivax* when combined with other antimalarial drugs such as atovaquone and primaquine. Proguanil plays a crucial role in treating malaria; its function is to stop the reproduction of the parasite in the red blood cells by inhibiting folic acid metabolism [12].

Quality control of these antimalarial drugs is essential due to the prevalence of counterfeit drugs [13–15]. Different analytical methods have been reported for qualitative and quantitative analysis of primaquine and proguanil. These methods include ultra-performance liquid chromatography [16,17], capillary electrophoresis [18,19] and mass spectrometry [20,21]. However, these methods involve multi-step analysis procedures, which are time-consuming. Electrochemical methods are gaining interest in pharmaceutical drug analysis because they are rapid, sensitive, and selective to the targeted drug. Several electrochemical methods have been reported to detect primaquine and proguanil; however, these methods focus on individual detection [10,11,22]. To the best of our knowledge, this is the first study to report on the simultaneous electrochemical detection of primaquine and proguanil. This approach is less time consuming and economical since two analytes are analyzed at the same time.

The low cost, thermal stability, high conductivity, and its ability to

* Corresponding author.
E-mail address: karpoormath@ukzn.ac.za (R. Karpoormath).

https://doi.org/10.1016/j.microc.2020.105709
Received 20 August 2020; Received in revised form 1 November 2020; Accepted 2 November 2020
Available online 6 November 2020

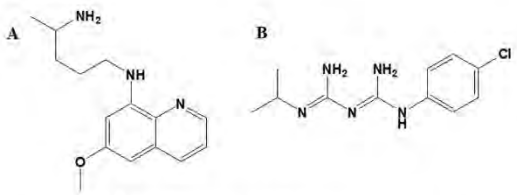

Fig. 1. (A) Primaquine and (B) Proguanil structure.

form nanostructured nanoparticles makes polyaniline to be amongst the commonly used conducting polymers [23]. In recent years, the application of nanostructured conducting polymers such as polyaniline in electrochemical sensors is increasing. This is due to their unique physical and chemical properties that are different from their bulk counterparts. These properties include high surface to volume ratio, flexibility, high porosity, and fast electron transfer rate [24,25]. The morphology of nanostructured polyaniline plays a crucial role in their application in electrochemical sensors. Nanofibers have more active sites available than other morphologies; thus, the sensor's sensitivity is improved since the interaction between the analytes and the polymer occurs close to the underlying electrode [26]. Park et al [27] investigated the effect of shape on the electrochemical properties of nanostructured polyaniline. Nanofibers, nanorods, and nanospheres were used for electrochemical applications. Faster electron kinetics were obtained for nanofibers compared with nanorods and nanospheres. The electrical properties of polyaniline nanofibers can be improved by incorporating metal nanoparticles such as cobalt oxide, silver, and gold [28–31]. Cobalt oxide is a p-type semiconducting material that has good electrocatalytic activity. Co_3O_4 facilitates the oxidation of different pharmaceutical drugs by its ability to change oxidation states [32,33]. Sandhya et al [34] improved PANI shrubs' electron transfer rate by incorporating cobalt oxide nanoparticles.

Several methods have been reported for the synthesis of polyaniline nanostructures [35–38]. In this study, an interfacial polymerization method was used to synthesize well-defined polyaniline nanofibers incorporated with cobalt oxide nanoparticles. The addition of cobalt oxide nanoparticles into polyaniline nanofibers provides several advantages such as good conductivity, higher surface area, and better catalytic activity. The solubility of the nanocomposite is also improved. This study presents a method for synthesizing polyaniline nanofibers incorporated with cobalt oxide nanoparticles (PANI-Co_3O_4). The prepared nanocomposite was used to modify a glassy carbon electrode (GCE) for simultaneous electrochemical detection of primaquine and proguanil.

2. Experimental

2.1. Apparatus and chemicals

The optical properties were studied using a UV spectrophotometer (UV-1800, Shimadzu, South Africa). The functional groups of PANI were confirmed by Fourier transform infrared spectroscopy (Bruker® Alpha-P ATR–FT-IR, Germany). Morphological studies were done using transmission electron microscopy (TEM) (JEOL 101, USA) and field emission scanning microscopy (FE-SEM) (ZEISS ultra plus, Germany). The elemental composition of the nanocomposite was recorded using Energy-dispersive X-ray spectroscopy (EDX). X-ray diffraction patterns were recorded using a Bruker D2 diffractometer at 40.00 kV and 50.00 mA. The measurements were taken at high angle 2θ in a range of 5–90 with a scan speed of 0.01° 2θ s^{-1} using secondary graphite monochromated Co K alpha radiation (l = 1.79 A). CHI660E electrochemical workstation (CH instrument, USA) and a standard three-electrode system were used for all electrochemical measurements. A glassy carbon electrode (3.00 mm), platinum wire, and Ag/AgCl/NaCl (3.00 $molL^{-1}$) were used as working, counter, and reference electrode respectively. pH measurements were performed using the EXTECH PH60 pH meter (China). All the chemicals used in this study were purchased from Sigma Aldrich. Throughout the experiment distilled water was used.

2.2. Synthesis of cobalt oxide nanoparticles

For the synthesis of cobalt oxide nanoparticles, the precipitation oxidation method was used with slight modification [39]. Briefly, two solutions were prepared; solution A was made by dissolving 5.00 g of cobalt acetate in 20 ml water and 0.91 g hydrogen peroxide. Solution B was prepared by adding 100 ml water to 1.27 g sodium hydroxide (NaOH) followed by the addition of 20 ml butanol. Solution A was added to solution B, and the mixture was stirred for 16 h at 85 °C. After 16 h, the mixture was washed with 2.00 M hydrochloric acid (HCl) to dissolve the unreacted cobalt hydroxide. The product was further centrifuged with methanol and dried at room temperature.

2.3. Synthesis of polyaniline-cobalt oxide (PANI-Co_3O_4) nanocomposite

For the synthesis of PANI-Co_3O_4 nanocomposite, interfacial polymerization was used with some modifications, two solutions were used [38]. Solution A was made up of 4.00 mmol ammonium persulfate in 20 ml HCl and solution B was made up of 4.00 mmol aniline in 20 ml chloroform. 6 mg of Co_3O_4 nanoparticles powder with an average size of 4 nm was added to Solution B. The mixture was stirred for 5 min; solution A was then added to the mixture. The mixture was left undisturbed at room temperature for 24 h. After 24 h, a green precipitate was filtered and dried at room temperature. The same procedure was followed for the synthesis of PANI nanofibers without the addition of Co_3O_4 nanoparticles. A yield of 67% and 63% was obtained for PANI and PANI-Co_3O_4, respectively.

2.4. Fabrication of PANI-Co_3O_4 modified electrode

The surface of the glassy carbon electrode (GCE) was mechanically polished using 0.05 μm of alumina slurry followed by rinsing with distilled water to remove any adsorbed alumina particles. A suspension of 5 μL PANI-Co_3O_4 was drop cast on the surface of the clean GCE. The electrode was dried under an IR lamp for 30 min. The modified electrode denoted (PANI-Co_3O_4/GCE) was used for all electrochemical measurements. All electrochemical measurements were done using the CHI660E electrochemical workstation. Electrochemical impendence spectroscopy measurements were taken at a frequency range of 1–10000 Hz with 5 mV amplitude. 2.5 mM $[Fe(CN)_6]^{3}$ /$[Fe(CN)_6]^{4}$ in 0.1 M KCl was used. Cyclic voltammetry and differential pulse voltammetry measurements were taken using a potential window of 0 to 1.5 V and scan rate of 0.1 V in phosphate buffer pH 3.5

2.5. Preparation of urine samples

The prepared PANI-Co_3O_4/GCE electrode was tested in real samples; urine samples were collected from a healthy laboratory personnel. The sample was diluted 100 times with 0.1 M phosphate buffer (pH 3.5) to reduce the matrix effect. The diluted samples were spiked with different concentrations of primaquine and proguanil before analysis. The PANI-Co_3O_4/GCE was then used to simultaneously detect primaquine and proguanil in spiked urine samples.

3. Results and discussion

3.1. Material characterization

The optical properties of cobalt oxide nanoparticles were studied using Uv–vis spectroscopy, as shown in figure S1A. Two absorption

peaks at 410 nm and 700 nm were obtained. These peaks are blue-shifted compared to the bulk cobalt oxide which absorbs at 554 nm and 838 nm [40,41]. The peaks at 410 and 700 nm are due to $O^{2-} \rightarrow Co^{2+}$ and $O^{2-} \rightarrow Co^{3+}$ transitions, respectively. Figure S1B shows the X-ray diffraction pattern of cobalt oxide nanoparticles. The peaks at 2θ 19.66, 31.20, 36.05, 45.86, 54.59, 59.71, 65.01 are attributed to (1 1 1), (2 2 0), (3 1 1), (2 2 2), (4 0 0), (5 1 1) and (4 4 0) planes respectively of face-centered cubic structure (JCPD: 042–1467). No peaks of impurities were obtained; thus, the prepared cobalt oxide nanoparticles are of high purity. The size and shape of cobalt oxide nanoparticles were confirmed by TEM, as shown in figure S1C. Cubic particles with an average size of 4.00 nm and narrow size distribution (figure S1D) were obtained. The smaller size of Co_3O_4 nanoparticles provides a higher surface area; this leads to better electro-catalytic activity. Also, the shape of Co_3O_4 nanoparticles plays a crucial role in their properties since different Miller indices are found in various shapes.

The oxidation levels of the polyaniline nanocomposite were investigated using Uv–vis spectroscopy as shown in figure S2A. Absorption peaks at 286, 340, and 435 nm were obtained for both the pristine PANI and PANI-Co_3O_4 nanocomposite. These peaks are attributed to π-π* (phenyl ring), π-π* (within benzenoid segment) and polaron- π* transition, respectively. The presence of the 435 nm peak confirms the formation of emeraldine salt PANI [42]. The slight hyper-chromic shift in PANI-Co_3O_4 is due to the presence of cobalt oxide. Figure S2B shows the FTIR spectra of PANI and PANI-Co_3O_4 nanocomposite. The peak at 780 is attributed to (C–H out of plane bending vibration), 1108 (C–H stretch from both quinoid and benzenoid rings), 1279 (C-N stretching mode of secondary aromatic amines), 1557 (C–C bond in quinoid), 1650 (C–C bond in benzenoid ring) and 3350 cm^{-1} (N–H stretching). The addition of cobalt oxide resulted in a peak at 560 and 660 cm^{-1}, these are attributed to metal oxide stretching vibration of the Co^{3+}-O and Co^{2+}-O bands, respectively. Also cobalt oxide interacts with PANI through the qunoid ring and N–H groups, this is shown by a slight shift in peak position to lower wavenumbers. Figure S2C-D shows the SEM images of PANI and PANI-Co_3O_4, nanofibers with an average diameter of 60 nm, and 118 nm, respectively, were obtained. The presence of cobalt oxide nanoparticles did not affect the morphology of PANI nanofibers.

Figure S3A-B shows the XRD pattern of PANI and PANI-Co_3O_4 nanocomposite, the peaks at 2θ 20.73, 25.81, 26.38, and 27.30 are indexed to (0 2 0), (2 2 0), (1 1 1), and (1 2 1) planes of conducting PANI [42]. Additionally, cobalt oxide peaks that correspond to a face-centered cubic structure (JCPD: 042–1467) were present in PANI-Co_3O_4. The presence of Co_3O_4 did not affect the crystal structure of PANI. The sharp peak at 2θ 33.3 might be due to the metal sample holder [43]. The area ratio of the crystalline peak to all peaks was used to estimate the degree of crystallinity [44]. The percentage crystallinity values for PANI and PANI-Co_3O_4 were found to be 6.40% and 7.79%, respectively. EDX analysis (figure S3C-D) was done to confirm the presence of C (32.79), N (14.16), O (10.57), S (5.90), Cl (6.16), and Co (0.41) in PANI and PANI-Co_3O_4.

3.2. Electrochemical characterization

The electrochemical impedance spectroscopy (EIS) was used for electrochemical characterization of the modified electrode. (EIS) measurements were taken at a frequency range of 1–10000 Hz with a 5 mV amplitude, as shown in figure S4. The charge resistance transfer (Rct) values for bare GCE, PANI, and PANI-Co_3O_4 were found to be 239.40 Ω, 0.001 Ω, and 0.001 Ω, respectively. These Rct values were obtained from the EIS plot using the standard Randles equivalent circuit (figure inset). The high Rct value for the bare GCE suggests that the diffusion of $[Fe(CN)_6]^{3-}$/$[Fe(CN)_6]^{4-}$ towards the electrode is low. Thus there is low electro-catalytic activity. The electrode surface was improved by modification with PANI and PANI-Co_3O_4. The semi-circle that was observed in the bare GCE diminished thus a low Rct value was obtained. The decrease in Rct value signifies a high electron transfer rate between the modified electrode and $[Fe(CN)_6]^{3-}$/$[Fe(CN)_6]^{4-}$. The decrease in Rct value is attributed to the conducting nature of PANI and the high electro-catalytic activity of Co_3O_4 nanoparticles.

3.3. Electrochemical behavior

The electrochemical behavior of 0.10 mM primaquine and proguanil in 0.10 M phosphate buffer solution (pH 3.50) at GCE, PANI/GCE, and PANI-Co_3O_4/GCE was investigated by cyclic voltammetry, as shown in Fig. 2A. A potential window of 0 to 1.50 V was used. No peaks were observed at bare GCE; upon modification with PANI anodic peaks at 0.56 V and 1.20 V were obtained. These anodic peaks are attributed to the oxidation of primaquine and proguanil respectively. No corresponding reduction peak was observed for both drugs; therefore, the electrode process is an irreversible reaction. A plausible mechanism for the simultaneous electrochemical detection of primaquine and proguanil is shown in Fig. 3. The anodic peaks at 0.56 V and 1.20 V are due to the irreversible oxidation of 7-methoxyamino quinolone and 4-Chloroaniline moiety in primaquine and proguanil, respectively. The introduction of Co_3O_4 nanoparticles during the chemical polymerization of PANI enhanced the electrochemical performance of the composite; as a result, an increase in anodic peak current was observed at PANI-Co_3O_4/GCE. This increase in peak current is due to fast electron transfer kinetics of the modified electrode.

CV was further used to investigate the effect of scan rate on the oxidation of primaquine and proguanil at PANI-Co_3O_4/GCE, as shown in Fig. 2B. CV voltammograms were recorded by changing the scan rate from 30 to 120 mV/s. An increase in peak current with scan rate was observed. As shown in Fig. 2C-D, a linear relationship between peak current and root of scan rate was observed. Therefore the simultaneous oxidation of primaquine and proguanil at PANI-Co_3O_4/GCE is a diffusion-controlled process [45]. The equation for peak current vs root of scan rate can be expressed as:

$$Ip = 0.01x + 0.17 \quad (R^2 = 0.99) \tag{1}$$

$$Ip = 0.40x + 3.10 \quad (R^2 = 0.98) \tag{2}$$

3.4. Influence of pH

The influence of pH on the oxidation of primaquine and proguanil at PANI-Co_3O_4/GCE was investigated using differential pulse voltammetry (DPV), as shown in figure S5A. The anodic peak current for primaquine decreased between pH 2.00 and pH 3.00. An increase in peak current at pH 3.50 was observed. The current continued to decrease between pH 4.00 and pH 4.50, as shown in figure S5B. In the case of proguanil, the anodic peak was found to alternate with a change in pH (figure S5C); the optimum current was also obtained at pH 3.50. For both drugs, the peak potential shifted towards less positive potential as the solution became less acidic. This indicates the presence of a proton-coupled electron transfer reaction. The linear relationship between pH and Ep (V) is expressed using the following regression equation:

$$Ep(V) = -0.040x + 0.750 \quad (R^2 = 0.99)\ \text{primaquine} \tag{3}$$

$$Ep(V) = -0.034x + 1.231 \quad (R^2 = 0.99)\ \text{proguanil} \tag{4}$$

The slope of Ep (V) vs pH for both primaquine and proguanil was calculated to be 0.04 and 0.03 V/pH, respectively. The slope values are biased from the Nernstain slope of 0.059 V/pH. Thus the simultaneous electro-catalytic oxidation of primaquine and proguanil is more complex. The slope values also indicate that an unequal number of protons and electrons are involved in the oxidation of both drugs at PANI-Co_3O_4/GCE.

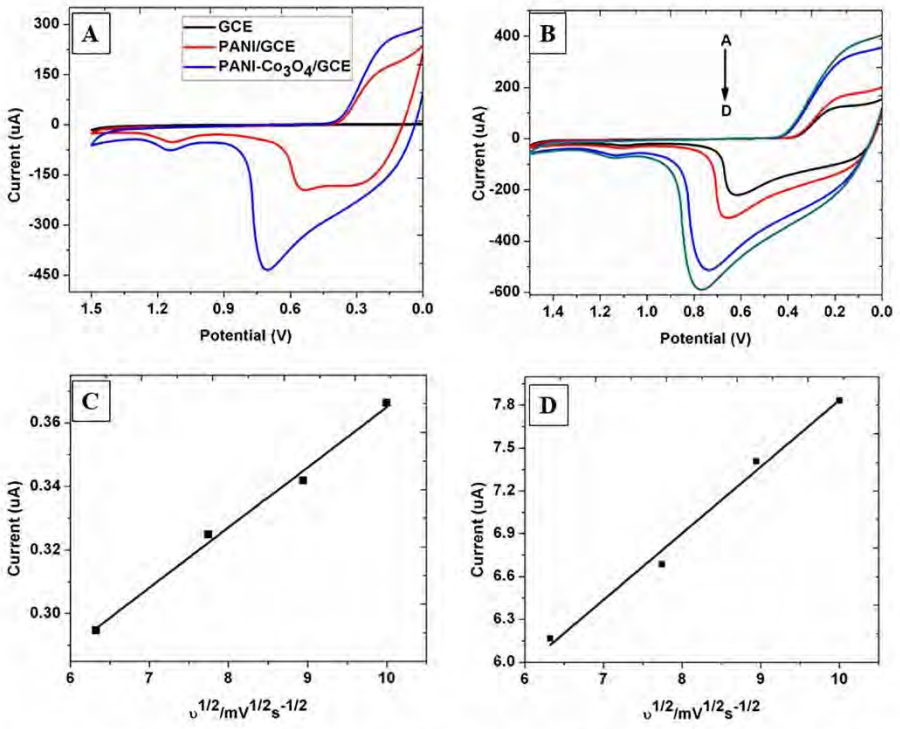

Fig. 2. (A) Cyclic voltammograms of bare GCE, PANI and PANI-Co_3O_4/GCE in 0.1 mM proguanil and primaquine (pH 3.5) at a scan rate of 100 mV/s; (B) Cyclic voltammograms of PANI-Co_3O_4/GCE with change in scan rate; (C-D) Relation between scan rate and current for PANI-Co_3O_4/GCE in primaquine and proguanil.

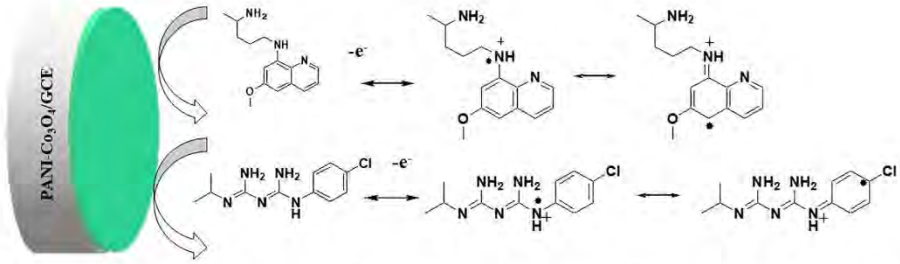

Fig. 3. Schematic representation of a plausible mechanism for simultaneous electrochemical detection of primaquine and proguanil.

3.5. Analytical performance

The analytical performance of PANI-Co_3O_4/GCE for simultaneous detection of primaquine and proguanil was investigated using differential pulse voltammetry (DPV) under optimum conditions (Fig. 4A and C). When the concentration of proguanil was kept constant, a linear relationship between current and primaquine concentration was observed in the range of 0.020–0.036 mM (Fig. 4B) with a limit of detection (LOD) of 2.07 nM. When the primaquine concentration was kept constant while varying the concentration of proguanil, a linear relationship in the range of 0.016–0.028 mM (Fig. 4D) with LOD of 1.42 nM was obtained. The equations below represent the corresponding linear regression:

$$Ip = 12.05C - -0.07 \quad (R^2 = 0.99)\ \text{primaquine} \tag{5}$$

$$Ip = 6.10C + 0.59 \quad (R^2 = 0.99)\ \text{proguanil} \tag{6}$$

Where C = Concentration of the drug and Ip = peak current. To the best of our knowledge, this is the first study to report on the simultaneous electrochemical detection of primaquine and proguanil. However, the present work was compared with previously reported studies for the detection of primaquine and proguanil separately (table 1). The proposed method shows good sensitivity for the simultaneous detection of the selected drugs.

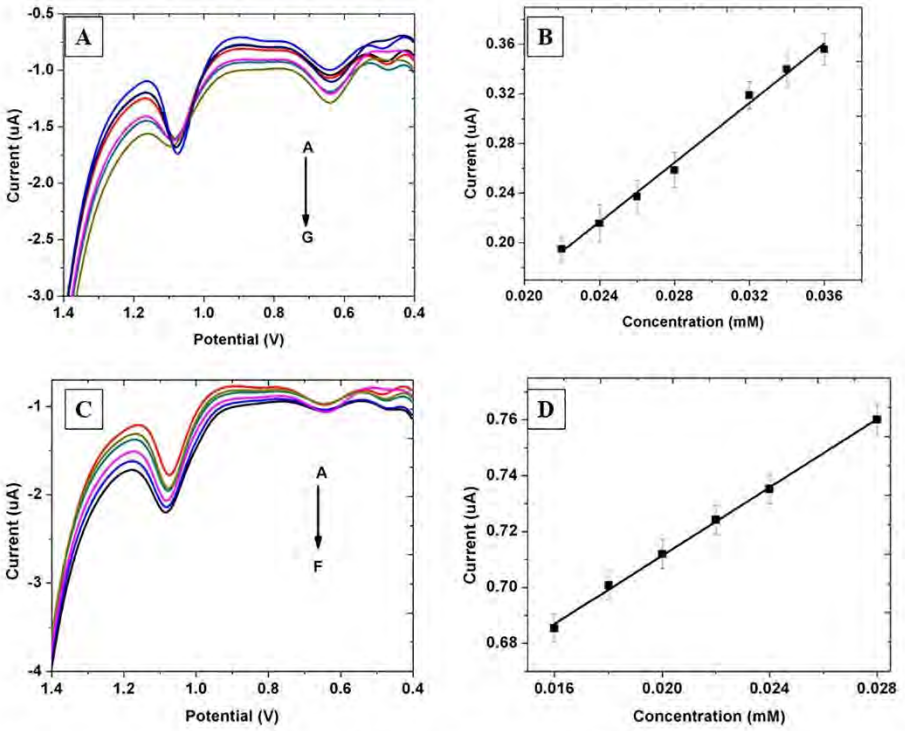

Fig. 4. (A and C) DP voltammograms of primaquine and proguanil at different concentrations in 0.10 M PBS (pH 3.50); (B and D) calibration plots for primaquine and proguanil in 0.10 M PBS (pH 3.50) PANI-Co_3O_4/GCE respectively.

Table 1
A comparison of the present study with other reported methods for the electrochemical determination of primaquine and proguanil.

Electrode	Concentration range ($molL^{-1}$)	Analyte	LOD ($mol.L^{-1}$)	Ref
Renewable silver amalgam film	1×10^{-7}-6×10^{-6}	proguanil	2.9×10^{-8}	[22]
CWE/ phosphotugnestic acid	1×10^{-5}-1×10^{-2}	proguanil	1×10^{-6}	[12]
Cu-NW/CPE	22.4×10^{-7}-22.7×10^{-6}	primaquine	0.96×10^{-6}	[46]
GCE	3×10^{-5}-1×10^{-4}	primaquine	1.62×10^{-5}	[47]
AuNn/GCE	1×10^{-8}-1×10^{-6}	primaquine	3.52×10^{-9}	[10]
PANI-Co_3O_4/GCE	2×10^{-5}-3.6×10^{-5} 1.6×10^{-5}-2.8×10^{-5}		2.07×10^{-9} 1.42×10^{-9}	Present work

3.6. Interference, reproducibility, and real sample

The selectivity of PANI-Co_3O_4/GCE towards primaquine and proguanil was investigated using DPV, as shown in figure S6. A 200-fold dilution of amodiaquine, a mixture of organic (ascorbic acid, glucose, citric acid, and uric acid) and inorganic (K^+, Cl^-, Mg^{2+}, SO_4^{2-} and Na^+) species were used as interfering agent. During the simultaneous detection of primaquine and proguanil, the modified electrode was found to be selective to primaquine with a deviation that is within the accepted tolerance of 5%. There was interference of more than 5% in the case of proguanil. The reproducibility of the modified electrode was evaluated using four identically prepared electrodes. Relative standard deviations of 1.90% and 2.30% were obtained for primaquine and proguanil, respectively. Thus the modified electrode shows good reproducibility. The practical applicability of the modified electrode was evaluated using a 100-fold dilution of human urine. As shown in tables 2 and 3, the recovery results were found to be in the range of 95–104 % and 94.40–105.00% for primaquine and proguanil, respectively.

4. Conclusion

Precipitation-oxidation and interfacial polymerization methods were successfully employed to prepare PANI-Co_3O_4 nanocomposite. X-ray diffraction spectroscopy and energy-dispersive X-ray spectroscopy confirmed the presence of cobalt oxide nanoparticles in the composite material. The formation of PANI nanofibers was confirmed by SEM. Simultaneous electrochemical detection of primaquine and proguanil was done using PANI-Co_3O_4/GCE. A detection limit of 2.07 nM and 1.42 nM was obtained for primaquine and proguanil, respectively. Additionally, the practical applicability of the modified electrode was

Table 2
Recovery results for primaquine in the spiked human urine sample.

S No	Amount added (mM)	Found (mM)	Recovery (%)	Bias (%)
1	0.02	0.019	95.00	5
2	0.025	0.026	104.00	4
3	0.03	0.031	103.30	3.3

Table 3
Recovery results for proguanil in the spiked human urine sample.

S No	Amount added (uM)	Found (uM)	Recovery (%)	Bias (%)
1	0.018	0.017	94.40	5.6
2	0.020	0.021	105.00	5
3	0.022	0.023	104.50	4.5

evaluated in human urine and in the presence of different interfering agents. The modified electrode showed good reproducibility, selectivity, and sensitivity. Thus, PANI-Co_3O_4 nanocomposite can be used to fabricate electrochemical sensors for quality control purposes. As far as we could possibly know, this is the first study to report simultaneous electro-oxidation of primaquine and proguanil.

CRediT authorship contribution statement

Zondi Nate: Conceptualization, Methodology, Investigation, Writing - original draft. **Atal A.S. Gill:** Conceptualization, Validation. **Ruchika Chauhan:** Supervision. **Rajshekhar Karpoormath:** Supervision, Funding acquisition, Resources.

Declaration of Competing Interest

The authors declare that they have no known competing financial interests or personal relationships that could have appeared to influence the work reported in this paper.

Acknowledgement

The authors are grateful for the financial support from the National Research Foundation- South Africa (NRF-SA) (Grant No 121804, 103728 and 112079) and College of Health Sciences, University of KwaZulu-Natal (CHS-UKZN). Furthermore authors would also like to acknowledge Nano-technology for sustainable development platform of UKZN and UKZN microscopy & microanalysis unit.

Appendix A. Supplementary data

Supplementary data to this article can be found online at https://doi.org/10.1016/j.microc.2020.105709.

References

[1] G. Figueroa-Miranda, L. Feng, S.C.C. Shiu, R.M. Dirkzwager, Y.W. Cheung, J. A. Tanner, M.J. Schöning, A. Offenhäusser, D. Mayer, Aptamer-based electrochemical biosensor for highly sensitive and selective malaria detection with adjustable dynamic response range and reusability, Sensors Actuators, B Chem. 255 (2018) 235–243, https://doi.org/10.1016/j.snb.2017.07.117.
[2] B. Kumar, V. Bhalla, R.P. Singh Bhadoriya, C.R. Suri, G.C. Varshney, Label-free electrochemical detection of malaria infected red blood cells, RSC Adv. 6 (2016) 75862–75869, https://doi.org/10.1039/c6ra07665c.
[3] M.E. Casas, M. Hansen, K.A. Krogh, B. Styrishave, E. Björklund, Analytical sample preparation strategies for the determination of antimalarial drugs in human whole blood, plasma and urine, J. Chromatogr. B Anal. Technol. Biomed, Life Sci. 962 (2014) 109–131, https://doi.org/10.1016/j.jchromb.2014.02.048.
[4] WHO, World Malaria Report 2018, Geneva, 2018.
[5] D.E. Loy, W. Liu, Y. Li, G.H. Learn, L.J. Plenderleith, S.A. Sundararaman, P. M. Sharp, B.H. Hahn, Out of Africa: origins and evolution of the human malaria parasites Plasmodium falciparum and Plasmodium vivax, Int. J. Parasitol. 47 (2017) 87–97, https://doi.org/10.1016/j.ijpara.2016.05.008.
[6] WHO, World malaria report 2017, Geneva, 2017.
[7] WHO, World malaria report in 2015, Geneva, 2015.
[8] J. Recht, E.A. Ashley, N.J. White, Use of primaquine and glucose-6 phosphate dehydrogenase deficiency testing: Divergent policies and practices in malaria endemic countries, PLoS Negl. Trop. Dis. 12 (2018), e0006230, https://doi.org/10.1371/journal.pntd.0006230.
[9] D.R. Hill, J.K. Baird, M.E. Parise, L.S. Lewis, E.T. Ryan, A.J. Magill, Primaquine: Report from CDC expert meeting on malaria chemoprophylaxis I, Am. J. Trop. Med. Hyg. 75 (2006) 402–415, https://doi.org/10.4269/ajtmh.2006.75.402.
[10] N.B. Thapliyal, T.E. Chiwunze, R. Karpoormath, S. Cherukupalli, Fabrication of highly sensitive gold nanourchins based electrochemical sensor for nanomolar determination of primaquine, Mater. Sci. Eng. C. 74 (2017) 27–35, https://doi.org/10.1016/j.msec.2016.12.126.
[11] M.J. Pedrozo-Peñafiel, J.M.S. Almeida, C.A.T. Toloza, D.G. Larrudé, W.F. Pacheco, R.Q. Aucelio, Square-wave voltammetric determination of primaquine in urine using a multi-walled carbon nanotube modified electrode, Microchem. J. 150 (2019), 104201, https://doi.org/10.1016/j.microc.2019.104201.
[12] T.D. If, F.M.A. Td, M. Saad, T.D. If, M.S. Rizk, Development of new potentiometric sensors for the determination of proguanil hydrochloride in serum and urine 27 (2016) 857–863.
[13] K. Karunamoorthi, The counterfeit antimalarial is a crime against humanity: a systematic review of the scientific evidence, Malar. J. 13 (2014) 209, https://doi.org/10.1186/1475-2875-13-209.
[14] L. Mhando, M.B. Jande, A. Liwa, S. Mwita, K.J. Marwa, Public Awareness and Identification of Counterfeit Drugs in Tanzania: A View on Antimalarial Drugs, Adv. Public Heal. 2016 (2016) 6254157, https://doi.org/10.1155/2016/6254157.
[15] WHO, A study on the public health and socioeconomic impact of substandard and falsified medical products, Geneva, 2017.
[16] T.A. Miranda, P.H.R. Silva, G.A. Pianetti, I.C. César, Simultaneous quantitation of chloroquine and primaquine by UPLC-DAD and comparison with a HPLC-DAD method, (2015) 1–7. https://doi.org/10.1186/s12936-015-0570-1.
[17] V.G. Dongre, P.P. Karmuse, P.P. Rao, A. Kumar, Development and validation of UPLC method for determination of primaquine phosphate and its impurities, J. Pharm. Biomed. Anal. 46 (2008) 236–242, https://doi.org/10.1016/j.jpba.2007.09.012.
[18] M. Heller, L. Vitali, M.A. Siqueira, A.V.F. Sako, M. Piovezan, G.A. Micke, Capillary Electrophoresis with UV Detection to Determine Cocaine on Circulated Banknotes, ISRN Anal. Chem. 2013 (2013) 1–7, https://doi.org/10.1155/2013/489705.
[19] M. Rambla-alegre, J. Peris-vicente, J. Esteve-romero, M. Capella-peiró, D. Bose, Analytica Chimica Acta Capillary electrophoresis determination of antihistamines in serum and pharmaceuticals, 666 (2010) 102–109. https://doi.org/10.1016/j.aca.2010.03.041.
[20] I. Brondz, D. Mantzilas, U. Klein, D. Ekeberg, E. Hvattum, M.N. Lebedeva, F. S. Mikhailitsyn, G.D. Souleimanov, J. Røe, Nature of the main contaminant in the anti malaria drug primaquine diphosphate: A qualitative isomer analysis, J. Chromatogr. B Anal. Technol. Biomed, Life Sci. 800 (2004) 211–223, https://doi.org/10.1016/j.jchromb.2003.09.042.
[21] K. Na, B. Etienne, A. Guirou, Determination of Primaquine in Whole Blood and Finger Pricked Capillary Blood Dried on Filter Paper Using HPLC and LCMS / MS (2014) 561–569, https://doi.org/10.1007/s10337-014-2639-3.
[22] S. Smarzewska, S. Skrzypek, W. Ciesielski, Voltammetric Determination of Proguanil in Malarone and Spiked Urine with a Renewable Silver Amalgam Film Electrode, Electroanalysis. 24 (2012) 1966–1972, https://doi.org/10.1002/elan.201200312.
[23] H. Wang, P.-H. Yang, H.-H. Cai, J. Cai, Constructions of polyaniline nanofiber-based electrochemical sensor for specific detection of nitrite and sensitive monitoring of ascorbic acid scavenging nitrite, Synth. Met. 162 (2012) 326–331, https://doi.org/10.1016/j.synthmet.2011.12.013.
[24] R. Li, Z. Chen, J. Li, C. Zhang, Q. Guo, Effective synthesis to control the growth of polyaniline nanofibers by interfacial polymerization, Synth. Met. 171 (2013) 39–44, https://doi.org/10.1016/j.synthmet.2013.02.020.
[25] Y. Shen, Z. Qin, T. Li, F. Zeng, Y. Chen, N. Liu, Boosting the supercapacitor performance of polyaniline nanofibers through sulfonic acid assisted oligomer assembly during seeding polymerization process, Electrochim. Acta. 356 (2020), 136841, https://doi.org/10.1016/j.electacta.2020.136841.
[26] C.O. Baker, X. Huang, W. Nelson, R.B. Kaner, Polyaniline nanofibers: broadening applications for conducting polymers, Chem. Soc. Rev. 46 (2017) 1510–1525, https://doi.org/10.1039/C6CS00555A.
[27] H.-W. Park, T. Kim, J. Huh, M. Kang, J.E. Lee, H. Yoon, Anisotropic Growth Control of Polyaniline Nanostructures and Their Morphology Dependent Electrochemical Characteristics, ACS Nano. 6 (2012) 7624–7633, https://doi.org/10.1021/nn3033425.
[28] M. Xu, Y. Song, Y. Ye, C. Gong, Y. Shen, L. Wang, L. Wang, A novel flexible electrochemical glucose sensor based on gold nanoparticles/polyaniline arrays/carbon cloth electrode, Sensors Actuators B Chem. 252 (2017) 1187–1193, https://doi.org/10.1016/j.snb.2017.07.147.
[29] Z. Lu, W. Dai, B. Liu, G. Mo, J. Zhang, J. Ye, J. Ye, One pot synthesis of dandelion-like polyaniline coated gold nanoparticles composites for electrochemical sensing applications, J. Colloid Interface Sci. 525 (2018) 86–96, https://doi.org/10.1016/j.jcis.2018.04.065.
[30] F.M. Zahed, B. Hatamluyi, F. Lorestani, Z. Es'haghi, Silver nanoparticles decorated polyaniline nanocomposite based electrochemical sensor for the determination of anticancer drug 5-fluorouracil, J. Pharm. Biomed. Anal. 161 (2018) 12–19. https://doi.org/https://doi.org/10.1016/j.jpba.2018.08.004.
[31] J. Lei, Y. Zhu, C. Shi, Q. Xu, X. Tao, Appropriate amount of polyaniline coated Co3O4 nanofibers and their excellent electrochemical properties, Phys. E Low-Dimensional Syst. Nanostructures. 117 (2020), 113836, https://doi.org/10.1016/j.physe.2019.113836.
[32] P.T. Mafuwe, M. Moyo, T. Mugadza, M. Shumba, S. Nyoni, Cobalt oxide nanoparticles anchored polyaniline-appended cobalt tetracarboxy phthalocyanine, modified glassy carbon electrode for facile electrocatalysis of amitrole, J. Solid State Electrochem. 23 (2019) 285–294, https://doi.org/10.1007/s10008-018-4131-8.
[33] M. Houshmand, A. Jabbari, H. Heli, M. Hajjizadeh, A.A. Moosavi-Movahedi, Electrocatalytic oxidation of aspirin and acetaminophen on a cobalt hydroxide nanoparticles modified glassy carbon electrode, J. Solid State Electrochem. 12 (2008) 1117–1128, https://doi.org/10.1007/s10008-007-0454-6.

[34] S. C.P, R. Baig F, S. Pillai, M. C, A. Aravind, S. J. Devaki, Polyaniline-cobalt oxide nano shrubs based electrodes for supercapacitors with enhanced electrochemical performance, Electrochim. Acta. 324 (2019) 134876. https://doi.org/https://doi.org/10.1016/j.electacta.2019.134876.

[35] T. Li, Y. Zhou, B. Liang, D. Jin, N. Liu, Z. Qin, M. Zhu, One-pot synthesis and electrochemical properties of polyaniline nanofibers through simply tuning acid–base environment of reaction medium, Electrochim. Acta. 249 (2017) 33–42, https://doi.org/10.1016/j.electacta.2017.07.177.

[36] J. Bhadra, N.J. Al-Thani, S. Karmakar, N.K. Madi, Photo-reduced route of polyaniline nanofiber synthesis with embedded silver nanoparticles, Arab. J. Chem. 12 (2019) 4848–4860, https://doi.org/10.1016/j.arabjc.2016.10.001.

[37] S. Chen, B. Liu, Y. Wang, H. Cheng, X. Zhang, S. Xu, H. Liu, W. Liu, C. Hu, Excellent Electrochemical Performances of Intrinsic Polyaniline Nanofibers Fabricated by Electrochemical Deposition, J. Wuhan Univ. Technol. Sci. Ed. 34 (2019) 216–222, https://doi.org/10.1007/s11595-019-2038-6.

[38] A. Abdolahi, E. Hamzah, Z. Ibrahim, S. Hashim, Synthesis of Uniform Polyaniline Nanofibers through Interfacial Polymerization, (2012) 1487–1494. https://doi.org/10.3390/ma5081487.

[39] E.L. Viljoen, M.J. Moloto, P.M. Thabede, Impact of acetate ions on the shape of Co3O4 nanoparticles, Dig. J. Nanomater. Biostructures. 12 (2017) 571–577.

[40] Q. Yuanchun, Z. Yanbao, W. Zhishen, Preparation of cobalt oxide nanoparticles and cobalt powders by solvothermal process and their characterization, Mater. Chem. Phys. 110 (2008) 457–462, https://doi.org/10.1016/j.matchemphys.2008.03.001.

[41] S. Farhadi, M. Javanmard, G. Nadri, Characterization of Cobalt Oxide Nanoparticles Prepared by the Thermal Decomposition of [Co(NH3)5(H2O)](NO3)3 Complex and Study of Their Photocatalytic Activity, Acta Chim. Slov. 63 (2016) 335–343.

[42] V. Kumar, R. Mahajan, I. Kaur, K.-H. Kim, Simple and Mediator-Free Urea Sensing Based on Engineered Nanodiamonds with Polyaniline Nanofibers Synthesized in Situ, ACS Appl. Mater. Interfaces. 9 (2017) 16813–16823, https://doi.org/10.1021/acsami.7b01948.

[43] X. Shang, M. De Luca, G. Pettinari, G. Bisognin, L. Amidani, E. Fonda, F. Boscherini, M. Berti, G. Ciatto, Quantitative determination of in clustering in In-rich InxGa1-xN thin films, J. Phys. D. Appl. Phys. 47 (2014), https://doi.org/10.1088/0022-3727/47/41/415301.

[44] H. Park, T. Kim, J. Huh, M. Kang, J.E. Lee, H. Yoon, P.E.T. Al, Anisotropic Growth Control of Polyaniline Nanostructures and Their Morphology Dependent Electrochemical Characteristics, (2012) 7624–7633.

[45] S.N. Prashanth, K.C. Ramesh, J. Seetharamappa, Electrochemical Oxidation of an Immunosuppressant, Mycophenolate Mofetil, and Its Assay in Pharmaceutical Formulations, Int. J. Electrochem. 2011 (2011) 1–7, https://doi.org/10.4061/2011/193041.

[46] M.H. Mashhadizadeh, M. Akbarian, Talanta Voltammetric determination of some antimalarial drugs using a carbon paste electrode modified with Cu (OH) 2 nanowire, 78 (2009) 1440–1445. https://doi.org/10.1016/j.talanta.2009.02.040.

[47] M.L.P.M. Arguelho, M. Valnice, B. Zanoni, R. Nelson, Electrochemical Oxidation and Voltammetric Determination of the Antimalaria Drug Primaquine, 2719 (2007). https://doi.org/10.1081/AL-200062218.